Theoretical and Experimental Approach Towards Generation of Thermal Scattering Law for Light Water

Jaiswal Vaibhav

To cite this version:

Jaiswal Vaibhav. Theoretical and Experimental Approach Towards Generation of Thermal Scattering Law for Light Water. Theoretical and/or physical chemistry. Université de Lille, 2018. English. NNT : 2018LILUR036 . tel-02390769

HAL Id: tel-02390769
https://hal.science/tel-02390769

Submitted on 3 Dec 2019

Université de Lille
Sciences de la Matière, du Rayonnement et de l'Environnement
École Doctorale 104

Thèse préparée à l'Institut de Radioprotection et de Sûreté Nucléaire (IRSN)
&
Laboratoire de Physique des Lasers, Atomes et Molécules (PhLAM)

pour obtenir le grade de

Docteur de l'Université de Lille

Spécialité : Constituants élémentaires et physique théorique

Obtention Théorique et Expérimentale des Lois de Diffusion Thermique de l'Eau Légère

---

présentée et soutenue publiquement par

Vaibhav JAISWAL

le 15 octobre 2018 devant un jury composé de

Alexander Kolesnikov	Oak Ridge National Laboratory, États Unis	Rapporteur
Fabienne Ribeiro	IRSN - Cadarache, France	Rapporteur
Cyrille De Saint Jean	CEA - Cadarache, France	Examinateur
Claude Mounier	CEA - Saclay, France	Examinateur
Valérie Vallet	Université de Lille, France	Directrice de thèse
Luiz Leal	IRSN - Fontenay-aux-Roses, France	Co-Directeur de thèse
Florent Réal	Université de Lille, France	Co-Directeur de thèse

University of Lille
Material Sciences, Radiation and Environment
Doctoral School 104

Thesis prepared at the Institute of Radioprotection and Nuclear Safety (IRSN)
&
Laboratory of Physics of Lasers, Atoms and Molecules (PhLAM)

for obtaining the degree of

Doctor of Philosophy

Speciality: Theoretical particle physics

Theoretical and Experimental Approach Towards Generation of Thermal Scattering Law for Light Water

presented and defended publicly by

Vaibhav JAISWAL

on 15 October 2018 in front of the jury composed of

Alexander Kolesnikov	Oak Ridge National Laboratory, United States	Reviewer
Fabienne Ribeiro	IRSN - Cadarache, France	Reviewer
Cyrille De Saint Jean	CEA - Cadarache, France	Examiner
Claude Mounier	CEA - Saclay, France	Examiner
Valérie Vallet	University of Lille, France	Thesis Director
Luiz Leal	IRSN - Fontenay-aux-Roses, France	Thesis Co-Director
Florent Réal	University of Lille, France	Thesis Co-Director

“ *The full performance of a Ferrari car can be achieved only if one uses the required high-end gasoline. In neutronics, its the accurate nuclear cross section data which drives the simulation tools.*”

Luiz C. Leal

Abstract

Safety analysis and design of nuclear systems rely on accurate computer simulation tools. These simulation tools take in basic nuclear data as an input to estimate the safety parameters of the nuclear systems and ensure its normal operation. In particular, precise knowledge of light water neutron scattering cross section data is important as light water is the most widely used moderator in thermal nuclear reactors, such as pressurized water reactors (PWRs). Since PWRs operate at temperature around 550 K and pressure around 150 bar, proper understanding of light water thermal cross section data at high temperatures and pressures is necessary.

In the thermal neutron energy region, the cross sections are governed by the structure and dynamics of the scattering material described by thermal scattering law (TSL). The TSL data for light water at several temperatures are available in the standard thermal scattering libraries. No information about the impact of pressure on the TSL data exists in these libraries. Until recently, the standard TSL data libraries for light water have relied mostly on physics model and experimental data measured in the 60s. One observes some discrepancies in these evaluations both at room temperature and reactor operating temperature (550 K). Experimental TSL, for high temperature and pressure, are very scarce. There is thus a need for reviewing the existing TSL evaluations and consequently performing new experiments, to develop new evaluations valid for a large range of temperature and pressure conditions of light water.

The research developed during this work, deals with the measurement and evaluation of TSL data for light water at high temperatures and pressures. To generate new TSL for light water, inelastic neutron scattering measurements were carried out at two time-of-flight (TOF) spectrometers, namely the IN4c and IN6, at the Institut Laue-Langevin (ILL), Grenoble, France. A corresponding set of molecular dynamics (MD) simulations were performed to complement the experimental data using two classical interaction models for water namely, a flexible non-polarizable TIP4P/2005f and a rigid polarizable TCPE model. Frequency spectra obtained from both TOF experiment and MD simulations at different temperatures and pressures have been analyzed and new TSL evaluations for light water have been developed.

A new module named as SAB module was developed in the existing IRSN nuclear data processing code, GAIA, with capabilities to generate TSL libraries for light water at the desired temperature requested by the user. The SAB module was validated on the French plutonium temperature effect experimental program, where TSL evaluations at exact temperatures of the experiment were necessary to observe a positive temperature effect.

The performance of the newly developed TSL evaluations, i.e. $S(\alpha,\beta)_{\text{JEFF-3.3-MOD}}$, $S(\alpha,\beta)_{\text{ILL}}$ and $S(\alpha,\beta)_{\text{TCPE}}$ were tested on a series of differential, double differential and total cross section measurements available in the literature. For further verification and validation of the new TSL data, critical benchmarks available in the International Handbook of Evaluated Criticality Safety Benchmark Experiments (ICSBEP Handbook), sensitive to TSL have been used. In addition, the new IRSN ^{16}O and ^{235}U evaluations along with ^{235}U Prompt Fission Neutron Spectrum (PFNS) from ENDF/B-VIII.0 were tested in conjunction with the new TSL evaluations.

The outcome of this study leads to a better interpretation of the impact of temperature and pressure on TSL in PWR applications. It is suggested that a similar study for nuclear reactors operating with different moderators (for instance heavy water, graphite, etc.,) should be conducted to investigate whether a similar behavior like the one observed in light water is seen.

Keywords: cross sections, thermal scattering law, time-of-flight, molecular dynamics, evaluations.

Résumé

L'es études de sûreté et la conception de nouveaux systèmes nucléaires nécessitent d'avoir recours à des outils de simulation efficaces. Ceux-ci dépendent des données nucléaires de base qui leur sont fournies, afin d'estimer au mieux les critères de sûreté des systèmes nucléaires et d'assurer leur bon fonctionnement. En particulier, une bonne connaissance des sections efficaces de l'eau légère est importante, car l'eau est le modérateur le plus employé dans les réacteurs nucléaires thermiques, comme les réacteurs à eau pressurisée (REP). Ces derniers fonctionnent à des températures et des pressions avoisinant 550 K et 150 bar, ce qui implique de connaître les sections efficaces de l'eau dans ces conditions.

Les sections efficaces neutroniques dans le domaine d'énergie thermique dépendent de la structure et de la dynamique du matériau diffusant, décrites par des lois de diffusion thermiques (thermal scattering law, TSL). Les TSL de l'eau légère sont consignées pour plusieurs températures dans des bibliothèques standard de diffusion thermique. Jusqu'à récemment, ces bibliothèques reposaient essentiellement sur des modèles physiques et des mesures expérimentales réalisées dans les années soixante, et des écarts peuvent être constatés dans ces évaluations à température ambiante et à la température de fonctionnement d'un réacteur (550K). Non seulement, les données expérimentales pour les TSL à hautes pressions et hautes températures sont rares, mais aucune information n'est disponible quant à l'impact de la pression sur les TSL. Par conséquent, il existe un réel besoin de revoir les évaluations des TSL existantes, et ainsi de proposer de nouvelles expériences, pour obtenir des bibliothèques indépendantes des modèles physiques et valides sur une large gamme de températures et de pressions.

Ce travail de recherche porte sur la mesure et l'évaluation de la loi de diffusion thermique de l'eau légère à hautes températures et hautes pressions. Pour produire de nouvelles TSL, des mesures de la diffusion inélastique des neutrons sur l'eau ont été effectuées à l'Institut Laue-Langevin (ILL) à Grenoble, à l'aide de deux spectromètres à temps de vol (TOF), IN4c et IN6. Afin de compléter ces mesures, des simulations de dynamique moléculaire (MD) ont été réalisées en s'appuyant sur deux modèles classiques d'interaction moléculaire, le modèle non polarisable TIP4P/2005f (utilisé dans le code GROMACS) et le modèle polarisable TCPE (utilisé dans le code PolarisMD). Les spectres de fréquence à différentes pressions et températures obtenus grâce aux mesures de temps de vol et aux simulations MD ont été exploités pour développer de nouvelles TSL pour l'eau légère.

Un nouveau module nommé SAB a été développé dans l'actuel code de traitement des données nucléaires de l'IRSN, GAIA, capable de produire des bibliothèques de diffusion thermique pour l'eau légère aux températures requises par l'utilisateur. Le module SAB a été validé sur le programme expérimental français d'étude de l'effet de la température sur le plutonium : afin d'observer une évolution positive de la réactivité avec la température, des bibliothèques de diffusion thermique aux températures exactes ont été nécessaires.

Les performances de ces nouvelles bibliothèques, i.e. $S(\alpha,\beta)_{\text{JEFF-3.3-MOD}}$, $S(\alpha,\beta)_{\text{ILL}}$ et $S(\alpha,\beta)_{\text{TCPE}}$ ont été testées sur une série de mesures de sections efficaces différentielles, double-différentielles et totales disponibles dans la littérature. Des benchmarks critiques de l'International Handbook of Evaluated Criticality Safety Benchmark Experiments (ICSBEP Handbook) ont également été utilisés. Enfin, les évaluations du ^{16}O et du ^{235}U de l'IRSN, ainsi que l'évaluation du ^{235}U PFNS de la bibliothèque ENDF/B-VIII.0 ont été utilisées conjuguées aux nouvelles TSL produites.

Les résultats de ces études permettent une meilleure compréhension de l'impact de la température et de la pression sur les TSL dans les applications liées à l'exploitation des REP. Il est suggéré qu'un travail comparable soit conduit pour les réacteurs nucléaires utilisant d'autres modérateurs que l'eau légère (eau lourde, graphite, etc.,), afin de savoir si des comportements similaires sont observés.

Mots-clés : sections efficaces, loi de diffusion thermique, évaluation de données nucléaires

Acknowledgments

I wish to thank all the people who contributed to help me achieve this research and accompanied its proper completion. First and foremost, I would like to thank Sophie Pignet and Eric Letang, past heads of the Laboratoire d'expertise et de recherche en Neutronique des Réacteurs (LNR) group and the Service de Netronique and Criticite (SNC) division, respectively, for giving me an opportunity to carry out research at IRSN. A special thanks is due to Stéphane Evo and Eric Dumonteil, for their constant efforts towards the development of the nuclear data project, 'INSIDER', of which my PhD project is a part.

A huge thanks and appreciation is reserved for Luiz Leal, my PhD supervisor, without whose contribution this work wouldn't have been possible. His kind support and motivation throughout this research, drove me to accomplish my task efficiently. Moreover, in addition to being one of the major international experts in his field, I wish to thank him for being such a friendly character at all times: working with him always becomes enjoyable.

I would also like to extend my deepest gratitude to my PhD director Valérie Vallet and my co-supervisor Florent Réal, two wonderful persons with whom I enjoyed working at the University of Lille. Their supervision and friendly guidance throughout my entire PhD work, especially on the work related to molecular dynamics simulations, is to be appraised. Thanks for various telephonic conversations, discussions over Skype and several parties that we shared together. It was fun learning the concepts of molecular dynamics simulations and the complexity of light water.

I am also grateful to Jacques Ollivier, Emmanuel Farhi, Yoann Calzavara and Stephane Rols from ILL, Grenoble for their valuable contribution in the inelastic neutron scattering measurements for light water. Without their support, the experiments wouldn't have been possible.

Special thanks to Gilles Noguere and Juan Pablo Scotta from CEA-Cadarache for having several discussions throughout this PhD work. The several meetings at CEA-Cadarache and exchanges we had over e-mails were fruitful and helped me in the successful completion of this work.

I'd also like to extend my deepest gratitude to all my colleagues of the SNC division for their welcoming spirit and my smooth integration into the team. In particular, I would like to thank Nicolas Leclaire, Raphaëlle Ichou, Frédéric Fernex and Bertrand Cochet for their constant support and providing their help throughout my PhD. Special thanks to Wim Haeck for sharing his experience on the previous experiments carried out at ILL. I am also grateful to all my colleagues from the PhLAM laboratory of the University of Lille with whom I shared several scientific discussions.

A big thanks to Alexander Kolesnikov, Fabienne Ribeiro, Cyrille De Saint Jean, Claude Mounier and the entire PhD committee for being so generous with their time in evaluating this work and providing great comments and suggestions.

A special thanks to Jose Ignacio Marquez Damian, Chris W. Chapman, Kemal Ramic, Emily Liu and Yaron Danon for their contribution in every possible way out, which allowed the successful completion of this research subject.

My journey so far would not have been interesting without Clément Jeannesson, with whom I shared my office. His friendly nature helped me know more about France and adapt to this beautiful culture. His French lessons will always be very useful for my day to day life in France.

I gratefully acknowledge Catherine Lamoureux and Florence Dallacasa for helping me with all the French administrative formalities starting from the security clearances to the management of all my missions during the entire duration of my PhD.

A warm expression of thanks to all my friends, especially Savneet Kaur, Riddhi Jani, Anupama Karnam, Sagar Uday Kumar, Mrinmoy Das, Neha Goyal and Shipra Sethi for making my stay in France enjoyable.

My success would not have been possible without the support of Shifali Singh. Your encouragement and motivation always kept me moving ahead.

And finally, I would like to thank my mom and dad to be supportive throughout these three years of my PhD in France. Managing the time difference between Indian and France and finding time to talk to me almost everyday, is to be appreciated.

Contents

3 Presently available TSL evaluations for light water 25

4 TOF inelastic neutron scattering experiment for light water 65

List of Figures

List of Tables

List of Abbreviations

PWR	**P**ressurized **W**ater **R**eactor
ENDF-6	**E**valuated **N**uclear **D**ata **F**ile- Version 6
TSL	**T**hermal **S**cattering **L**aw
ENDF/B	**E**valuated **N**uclear **D**ata **F**ile
JEFF	**J**oint **E**valuated **F**ission and **F**usion File
CENDL	**C**hinese **E**valuated **N**uclear **D**ata **L**ibrary
JENDL	**J**apanese **E**valuated **N**eutron **D**ata **L**ibrary
EXFOR	**Ex**perimental Nuclear Reaction data
MCNP	**M**onte **C**arlo **N** **P**article transport code
FWHM	**F**ull **W**idth at **H**alf **M**aximum
LAMP	**L**arge **A**array **M**anipulation **P**rogram
TOF	**T**ime **O**f **F**light
SCTA	**S**hort **C**ollision **T**ime **A**pproximation
ES	**E**gelstaff **S**chofield
MD	**M**olecular **D**ynamics
VACF	**V**elocity **A**uto **C**orrelation **F**unction

List of Symbols

E	Incident neutron energy	eV
E'	Scattered neutron energy	eV
$\vec{k}$	Incident neutron wave vector	Å^{-1}
$\vec{k'}$	Scattered neutron wave vector	Å^{-1}
ω	Energy	eV
$S(\vec{k},\omega)$	Dynamic structure factor	eV^{-1}
α	Alpha	Unitless
β	Beta	Unitless
$S(\alpha,\beta)$	Thermal scattering law	Unitless
$\frac{d^2\sigma}{d\Omega dE'}$	Double differential cross section	barn/eV/steradian
σ	Microscopic Cross section	barn
Σ	Macroscopic Cross section	cm^{-1}
Ω	Solid angle	steradian
μ	Angular cosine	Unitless
$\rho(\omega)$	Frequency spectrum	eV^{-1}
$\hbar\omega$	Energy transfer	eV
ω_c	weight of the continous band	Unitness
ω_t	Weight of the translational band	Unitness
ω_{E_1}	Weight of the first oscillator	Unitless

ω_{E_2}	Weight of the second oscillator	Unitless
k_{eff}	Effective multiplication factor	Unitless
N	Number density	m^{-3}
m_n	Mass of neutron	kg
k_B	Boltzmann constant	eV/K

Dedicated to my parents and Lord Sai ...

Chapter 1

Introduction

> “ *The results from any code cannot be any better than the data that it uses.* ”
>
> Dermott E. Cullen, *2006*

1.1. Nuclear data and its importance

The results of computer resources in the recent years have achieved a high degree of accuracy, to a capacity where the uncertainty in neutronics simulations can be attributed to the nuclear data. Dermott E. Cullen in his report, “ How Accurately Can We Calculate Neutrons Slowing Down In Water? ” had beautifully emphasized on the importance of nuclear data being as important as the neutron transport simulation codes itself [1]. The reliability of neutronics simulations directly depends on the accuracy of the nuclear cross section data and their associated uncertainties. The nuclear data available to users are in the form of data libraries based on experiments and physics models called as Evaluated Nuclear Data Files (ENDF). The nuclear data library developed and maintained by the United States is referred to as ENDF/B. Likewise, the Joint Evaluated Fission and Fusion (JEFF) nuclear data library is a collaborative project between Nuclear Energy Agency (NEA) data bank participating countries [2]. China has its own nuclear data library called as CENDL [3] and Japanese maintain the JENDL [4] nuclear data library. In these evaluated data libraries, the energy range of the neutron interaction varies from thermal neutron energies (meV range) to higher energies ($\sim$ 20 MeV). It is a common procedure to represent the neutron interaction data in the evaluated data libraries in four major energy regions: thermal, resolved resonance, unresolved resonance (URR) and fast energy regions [5]. Figure 1.1 shows the total cross section for ^{235}U in different neutron energy regions. In the very low energy region the cross section behaves like a $1/v$ distribution where v is the neutron velocity, followed by the resonance region where the cross section has sharp peaks corresponding to the nuclear resonances and subsequently the fast energy region where the cross section behaves smooth as a function of energy. While the entire energy region in Fig. 1.1 is important, proper attention must be given to thermal energy region where thermal nuclear reactors operate.

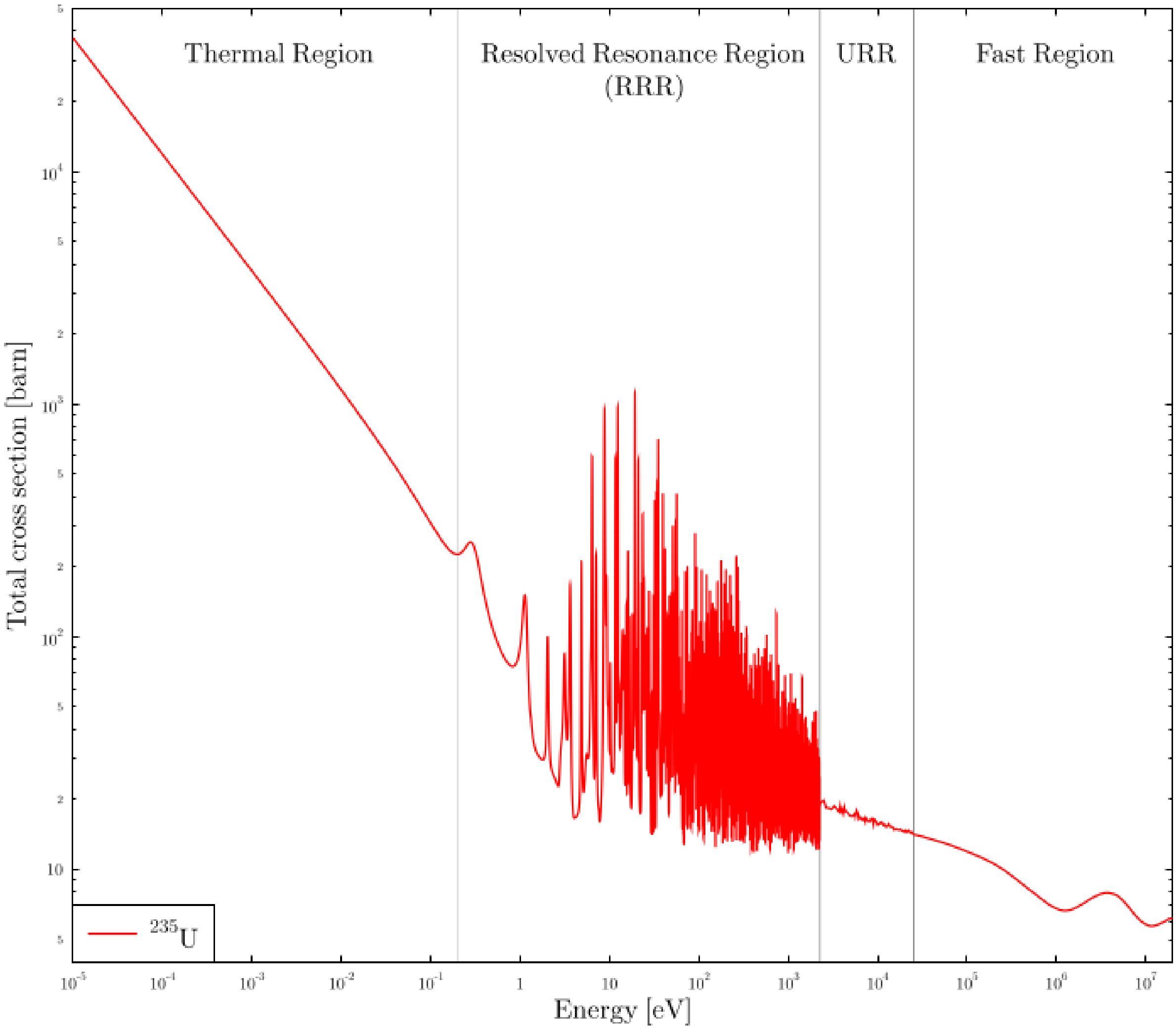

FIGURE 1.1: Total cross section of ^{235}U as a function of incident neutron energy.

However, the neutrons generated in the fission reaction are of fast energies, the fission processes in thermal reactors occur in the thermal energy regions. The slowing down of neutrons from fast energies to thermal energies is dominated by the process of scattering with moderator materials. In the process of moderation, neutrons acquire thermal equilibrium with the moderator temperature, and are called as thermal neutrons and the cross sections are termed as thermal scattering cross sections. Thermal scattering cross section data for several moderator materials are available in standard cross section data libraries. The adequacy of the scattering cross section data has to be investigated, considering its wide applications. In addition to reactor physics applications thermal scattering data find its importance in fields such as design of cold neutron sources, neutron filters and biological materials for dosimetry applications. The existing thermal scattering cross sections are inadequate for many nuclear systems and novel applications [6]. There is a need for accurate thermal scattering cross section data at high temperatures and pressures for thermal reactor applications.

1.2. Motivations and objectives

Generally, elements having low mass number are the preferred choice of moderators in nuclear systems to slow down neutrons to thermal energy range. Also, the absorption cross section should be low to avoid neutrons being absorbed and hinder the process of moderation. Following these reasons, light water is the most widely used moderator in thermal nuclear power reactors, namely the Pressurized Water Reactor (PWR) also known as Light Water Reactor (LWR). A vast majority of nuclear critical benchmark systems are based on light water. A proper understanding of the interaction of neutrons with light water is thus necessary for criticality safety studies and reactor physics applications. The evaluated nuclear cross section data libraries are derived on the basis of physics models [7] describing neutron interaction at low energy governed by the effects of binding atoms/molecules on the system. Neutrons in the thermal energy range not only interact with the interacting atom but also the entire molecule. The cross sections in the thermal scattering region are dependent on the structure and dynamics of the scattering molecule due to the fact that, in the thermal energy region [8]:

- The energy of the incoming neutrons is comparable to the energy of the interacting molecule.
- The de Broglie wavelength of the neutrons is of the order of the inter-atomic distances of the interacting molecule.

The cross section of hydrogen bound in the water molecule is governed by binding effects specific to the molecule, making it different from that of the free atom. This effect can be seen in Fig. 1.2. The solid line in blue is the Doppler broadened hydrogen cross section at 293.6 K, ranging from thermal to fast energy region. This cross

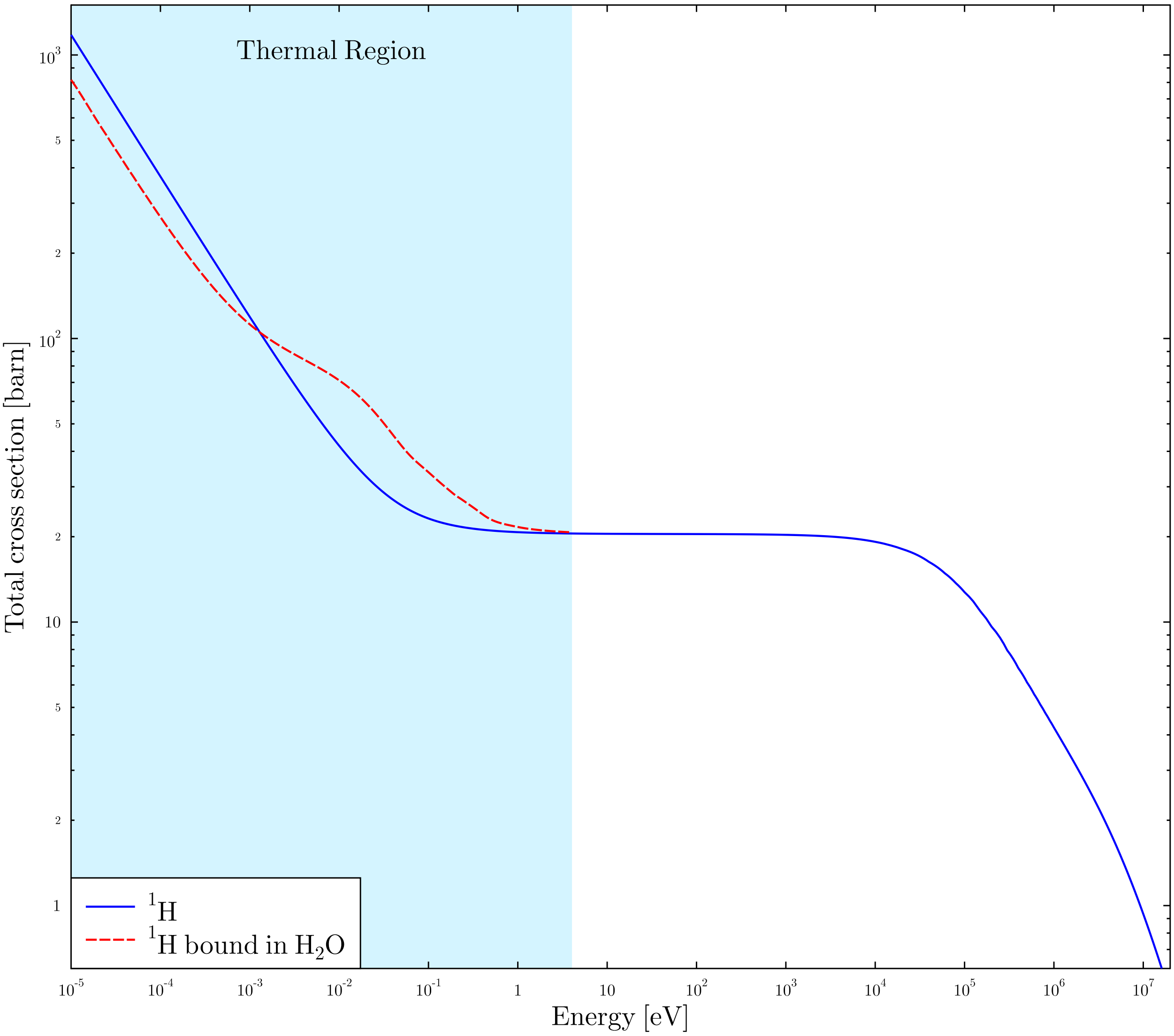

FIGURE 1.2: Total cross section of free hydrogen (solid blue line) and hydrogen bound in light water (dotted red line) at 293.6 K.

section is generated considering hydrogen as a free gas following Maxwell–Boltzmann distribution. The dotted line in red is the cross section of hydrogen bound in the water molecule. It can be seen that in the thermal energy region (blue shaded portion) the cross section of hydrogen changes due to the bound effect of the molecule. Not only for light water, this effect is true for other moderator materials like heavy water, graphite, polyethylene, etc. Along with the energy of the incident neutrons, the thermal scattering cross section depends on the temperature of the moderator materials.

All operating nuclear thermal power reactors in France are PWRs and operate with light water at high temperature and pressure, i.e. 600 K and 150 bar. The present research work deals with the scattering of thermal neutrons with light water at low energies ($<$ 10 eV) and propose an improvement in the thermal scattering cross section data at high temperatures and pressures on the basis of new experimental thermal scattering cross section data. Presently, pressure is not taken into account when generating thermal scattering law for light water. One of the major objectives of this research is to verify the impact of pressure on the thermal scattering data as PWRs operate at high pressures. No attempt has been made in the past to study the impact of pressure on the structure factor of light water and hence the thermal scattering cross section data. This research aims at studying the impact of pressure on the frequency spectrum, double differential and total scattering cross section of light water. The conclusions derived from this study will support designs of future light water reactors and improve the safety of nuclear power reactors.

Although the initial objective of this PhD dissertation was to study the effect of pressure on the thermal scattering data, several other issues also have been investigated. To name a few, the discrepancies observed in the double differential cross section and total cross section of light water in the thermal energy range based on the existing evaluations of light water thermal scattering data and experimental measurements. In Fig. 1.3, the total cross section of light water at 293.6 K based on JEFF-3.1.1 [9] and ENDF/B-VII.1 thermal scattering evaluations are compared with the experimental data [10, 11, 12] and total cross section data of light water available in the Experimental Nuclear Reaction Data (EXFOR) data base [13]. The solid line in blue and the dotted line in red are the total cross section of light water at 293.6 K obtained from the JEFF 3.1.1 [14] and the ENDF/B-VII.1 [15] thermal scattering libraries, respectively. The dotted line in black is the total cross section of light water obtained from the Doppler broadening of hydrogen and oxygen, following Maxwell–Boltzmann distribution of free gas. No significant difference is observed between the total cross sections obtained from the JEFF-3.1.1 and ENDF/B-VII.1 evaluations throughout the entire energy region. Whereas, when both these evaluations are compared with the experimental data, significant differences in the low energy region (< 0.1 meV) and small differences in the thermal energy region (0.025 eV) can be perceived.

A commonly used tool by the reactor physics community, for generating thermal scattering cross section data, is the LEAPR module of the NJOY code [16]. LEAPR calculates the thermal scattering data using several approximations [7, 17, 18] and the entire physics behind the interaction of thermal neutrons and the moderator material is turned into an analytical function of the frequency spectrum of the moderator material [17, 18, 19]. Evaluation of thermal scattering data for light water in ENDF/B-VII.1 and JEFF-3.1.1 are based on the experimental frequency spectrum measured in the 60s with a low accuracy due to the limitations of the experimental and computational capabilities. The discrepancy observed in the total cross section of light water at room temperature might be even larger at high temperatures due to lack of accurate knowledge of

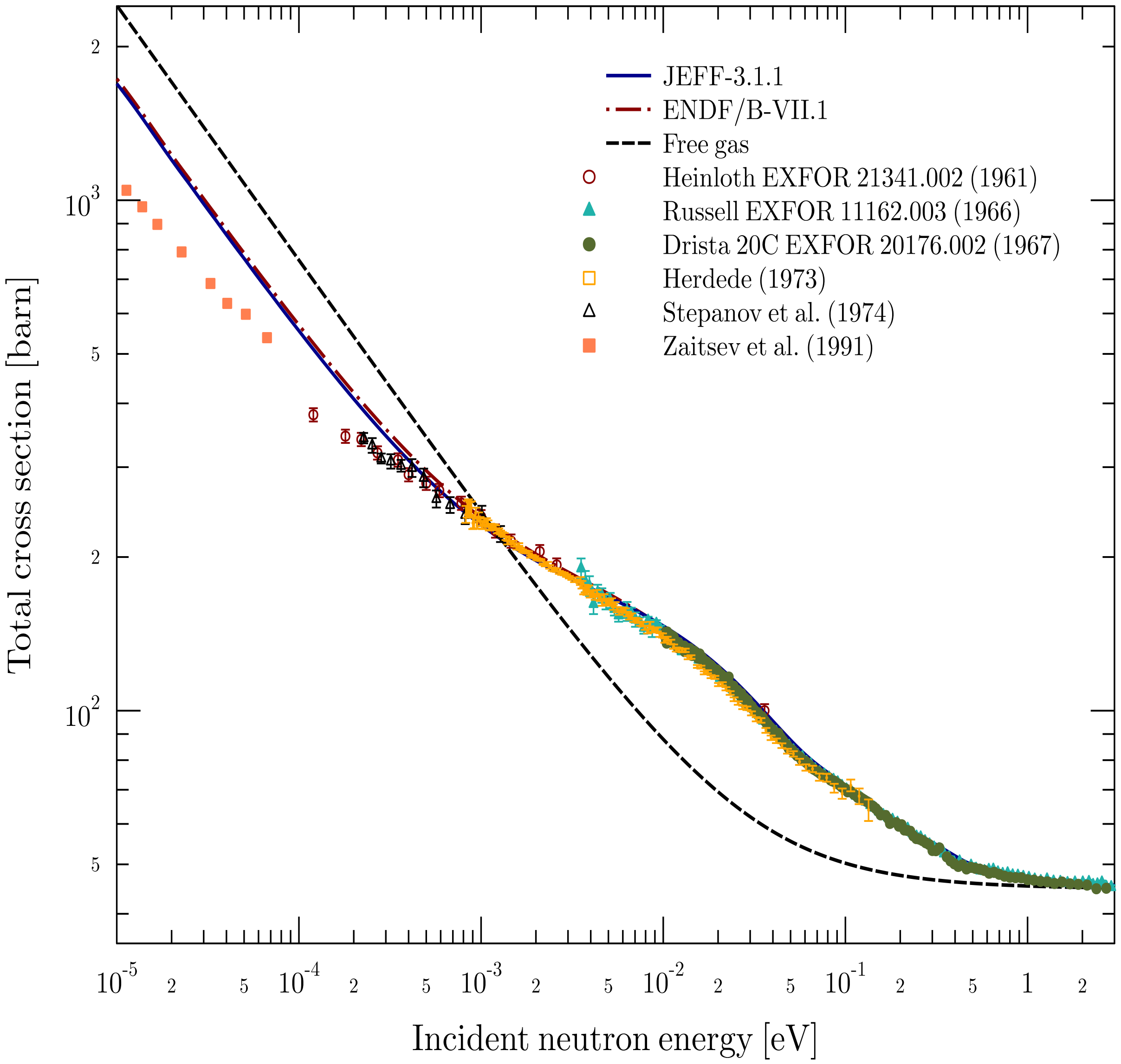

FIGURE 1.3: Total cross section of light water at 293.6 K based on JEFF-3.1.1 and ENDF/B-VII.1 thermal scattering evaluation compared to experimentally measured cross section.

the frequency spectrum of light water at high temperatures. Thermal scattering data for light water in both JEFF-3.1.1 and ENDF/B-VII.1 are based on experimentally measured frequency spectrum at 300 K and 500 K [20, 21]. For the intermediate temperatures and temperatures higher than 500 K, both the libraries interpolate or extrapolate the frequency spectrum to generate the thermal scattering data. Experimentally measured differential and integral cross section data of light water at high temperatures are very limited. It is very difficult to validate thermal scattering cross sections at high temperatures and one has to rely on models to generate cross sections extrapolated to high temperatures.

During the last few years, much progress has been made in re-evaluating the thermal scattering cross section data for light water by incorporating molecular dynamics simulations and available experimental data [22]. Unfortunately, new experimental data for light water, especially at high temperature and pressure, are very scarce and the new evaluations still rely on old experimental data or molecular simulations [21, 23, 24]. There is thus a need for reviewing the existing thermal scattering data evaluations and support new experiments to improve them and expand their applicability. Also, the evaluated thermal scattering data in the nuclear data libraries are tabulated for a set of specific temperatures. For intermediate temperatures, one has to use the closest temperature available in the evaluation as interpolation of the thermal scattering data is not recommended [18]. This choice of using the closest temperature available in the thermal scattering evaluation might lead to misleading results in criticality safety and reactor physics calculations. For instance, thermal scattering data at the appropriate temperature is necessary to study the temperature effects in reactor physics calculations since a slightly different temperature can result in a fundamentally different behavior of the reactor parameters [25]. To address this problem, a methodology has been developed in this work to determine thermal scattering data at desired temperature.

The Institut de Radioprotection et de Surete Nucleaire/ French Institute for Radiological Protection and Nuclear Safety (IRSN) provides technical support for the French nuclear safety authority. IRSN is working on the improvement of existing neutronics simulation tools as well as the nuclear data used by these tools to improve the confidence in the nuclear safety assessments. With this objective, several efforts were initiated to improve the scattering cross section data of light water in the thermal energy region. Improved experiments were performed on light water at ambient temperature and pressure at the Institut Laue-Langevin (ILL), Grenoble, France in 2010 to study the interaction of thermal neutrons with light water [22]. Considering the fact that PWRs operates at high temperature and pressure, i.e., $\sim$ 600 K and 150 bar it was envisioned to perform measurements at high temperature and pressures that was not done in the past with the required accuracy and knowledge of the uncertainty required for reactor applications. IRSN started to develop research in this area by collaborating with University of Lille and ILL, with an aim to improve the existing cross section library for light water thermal scattering data. A sketch in Fig. 1.4 shows the joint effort between the three institutions to develop the thermal scattering law for light water. To fulfill this objective, both the theoretical and experimental aspects of the problem were studied. After a thorough review of the thermal scattering models and existing evaluations of light water, the time-of-flight (TOF) experimental part was carried out at the Institut Laue-Langevin (ILL) in Grenoble. Inelastic neutron scattering (INS) measurements were performed on TOF spectrometers, namely the IN4c and IN6 to measure the thermal scattering data at high temperatures and pressures. The proposed experiments extend the previous measurements beyond room temperature and pressure to more realistic operating

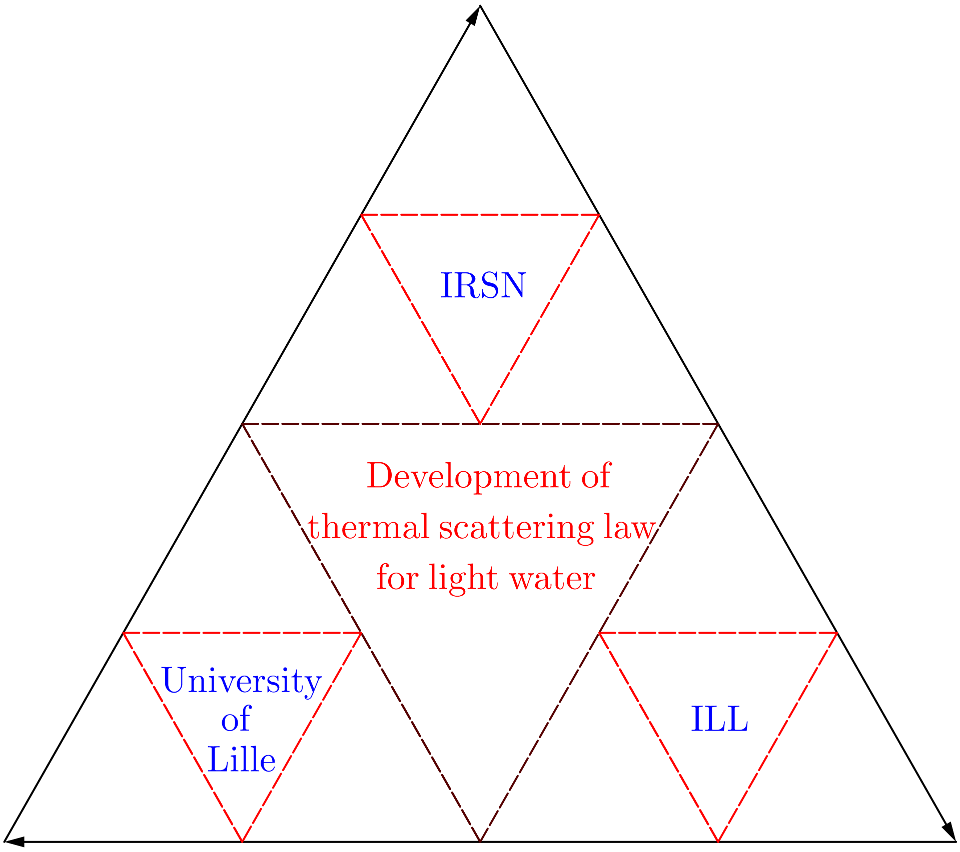

FIGURE 1.4: Joint effort of the three institutions throughout this PhD research.

conditions in connection with nuclear power reactors. The theoretical part concerning the Molecular Dynamics (MD) simulations was carried out at the PhLAM laboratory, University of Lille. The final data analysis and the reduction of the experimental data were carried out at the IRSN leading to the development of a new scattering library for light water especially at high temperatures and pressures. This collaboration helped in trying to explore and understand some of the intricacies behind the complex structure of light water.

1.3. Thesis organization

This PhD work involves both theoretical and experimental approach towards the generation of thermal scattering law for light water at temperatures varying from room temperature up to high temperatures, matching reactor operating conditions. On the experimental side TOF experiments have been performed at the ILL Grenoble, whereas on the theoretical side MD simulations have been performed at the University of Lille.

The thermal scattering law formalism covering the theoretical aspect of the interaction of neutrons at thermal energy region is covered in **Chapter** 2. All the presently existing thermal scattering models and the corresponding thermal scattering cross section data for light water are presented in **Chapter** 3 to have an overview of the present state of the art. The TOF inelastic neutron scattering measurements on light water at the ILL and the data analysis are discussed in **Chapter** 4. Molecular dynamics approach to generate thermal scattering cross section data using the TCPE water model and the obtained results are reported in **Chapter** 5. The evaluation and processing of the thermal scattering cross section data based on the SAB module is explained in **Chapter** 6. The performance of all the newly evaluated thermal scattering data during this research work and its validation on a series of differential, double differential, total cross section measurements as well as a series of ICSBEP critical benchmarks sensitive to thermal energy region is presented in **Chapter** 7. The general conclusion and the future work and perspective is then presented at the end of this manuscript.

Chapter 2

Thermal scattering law formalism

The present chapter provides an overview of the thermal scattering law development. A general description, beginning from the neutron transport equation up to the derivation of double differential scattering cross section from scattering experiments is given, following the references [8, 26, 27, 28]. Generation of thermal scattering law based on the LEAPR module of NJOY is explained in detail in this chapter.

2.1. General description

Accurate understanding of neutron distribution in space, energy and time, $\psi(\vec{r}, E, \Omega, t)$ is necessary to predict the safety parameters of nuclear reactors and critical systems. Nuclear criticality safety calculations of systems containing fissile materials are based on the solution of time-dependent Boltzmann's neutron transport equation. The neutron transport equation is a neutron balance equation (gain or loss) formulated as below:

$$\begin{aligned}\left(\frac{1}{v}\frac{d}{dt} + \Omega \cdot \vec{\nabla} + \Sigma_t\right)\psi(\vec{r}, E, \Omega, t) = &\int_0^\infty dE' \int_{4\pi} d\Omega' \Sigma_s(E', \Omega' \rightarrow E, \Omega)\psi(\vec{r}, E', \Omega', t) \\ &+ \frac{\chi(E)}{4\pi}\int_0^\infty dE' \nu(E')\Sigma_f(E')\phi(\vec{r}, E', t) + Q(\vec{r}, E, \Omega, t)\end{aligned} \tag{2.1}$$

where v is the neutron velocity, ψ is the angular neutron flux, ν is the average number of neutrons produced per fission, χ is the fission spectrum and Q is the source term. The solution of Eq. 2.1 provides the k_{eff} , the effective multiplication factor and the angular neutron flux $\psi(\vec{r}, E, \Omega, t)$. The above equation requires neutron cross section data denoted by Σ, the macroscopic cross section which depends on N, the number density of the material and σ, the microscopic cross section, given by:

$$\Sigma = N\sigma \tag{2.2}$$

Σ_t is the macroscopic total cross section of all the nuclear reactions, Σ_s is the macroscopic scattering cross section and Σ_f is the macroscopic fission cross section. The first term on the left of Eq. 2.1 defines the time rate of change of neutrons, the second term represents the loss of neutron due to leakage, the third term accounts for the loss of neutrons due to all types of nuclear interaction. The first term on the right defines the neutrons with energy E' and solid angle Ω' scattering to energy E and solid angle Ω. The second term on the right takes into account, the number of neutrons created by fission whereas the last term on the right is the gain of neutrons from a source.

In thermal reactors or critical systems, the high energy neutrons are slowed down by the process of scattering governed by the double differential cross section in the first term on the right side of Eq. 2.1, i.e.

$$\int_0^\infty dE' \int_{4\pi} d\Omega' \Sigma_s(E', \Omega' \to E, \Omega)\psi(\vec{r}, E', \Omega', t) \tag{2.3}$$

The scattering cross section can be written as:

$$\Sigma_s(E \to E', \Omega) d\Omega dE' = N \frac{d^2\sigma}{d\Omega dE'} d\Omega dE' \tag{2.4}$$

here Ω is the scattering cosine angle, $\frac{d^2\sigma}{d\Omega dE'}$ is the double differential scattering cross section. Integrating the double differential scattering cross section we obtain the differential scattering cross section and integration again we obtain the total cross section as given in equation below:

$$\frac{d\sigma}{d\Omega} = \int_0^\infty \frac{d^2\sigma}{d\Omega dE'} dE' \ ; \ \ \sigma_s = \int_{4\pi} \frac{d\sigma}{d\Omega} d\Omega \tag{2.5}$$

where $\frac{d\sigma}{d\Omega}$ is the differential scattering cross section and σ_s is the scattering cross section.

When the energy of the neutrons is sufficiently high in comparison to the chemical binding energy of the scattering atom/molecule, the scattering of neutrons can be quantified considering the atoms behaving like a perfect Maxwellian gas. But, when the neutron energy is comparable to the bound energies of the scattering atom/molecule, a special treatment has to be performed in order to correctly characterize the cross sections. In the low energy range ($<$ 10 eV), the exchange of energy and momentum of neutrons with the interacting atom/molecule is governed by a phenomenon often termed as thermal scattering law. In this chapter we will further discuss about the theoretical framework behind the development of thermal scattering law to obtain the double differential scattering cross section.

2.2. Thermal Scattering Law (TSL)

The double differential scattering cross section for thermal neutrons with an incident energy E, scattered to final energy E' in the laboratory system and at temperature T, can be expressed as a function of $S(\alpha,\beta)$, often termed as Thermal Scattering Law (TSL):

$$\frac{d^2\sigma}{d\Omega dE'}\left(E\rightarrow E',\Omega\right)=\frac{\sigma_b}{4\pi k_B T}\sqrt{\frac{E'}{E}}S(\alpha,\beta) \tag{2.6}$$

where α is the change in momentum of the neutron and β, the change in energy, with

$$\alpha=\frac{E+E'-2\mu\sqrt{EE'}}{Ak_B T} \tag{2.7}$$

$$\beta=\frac{E'-E}{k_B T} \tag{2.8}$$

$$\sigma_b=\sigma_f\left(\frac{A+1}{A}\right)^2 \tag{2.9}$$

Here, A is the ratio of the scatterer mass to that of the neutron mass, σ_b is the bound atom scattering cross-section, σ_f is the free atom scattering cross-section, μ is the neutron scattering cosine ($\mu = cos\theta$) in the laboratory system and k_B is the Boltzmann constant.

2.3. Neutron scattering

In a neutron time-of-flight (TOF) experiment, the scattered neutrons after interacting with the scattering medium (sample) are measured as a function of change in their momentum transfer, $\vec{k}$ and energy transfer ω (in terms of $\hbar$). While $\vec{k}$, gives information about the structural properties of the medium, ω provides information about the dynamics of the material. The structure and dynamics of the interacting molecule plays an important role in deciding their interaction mechanism with neutrons. Generally, the output of a neutron scattering experiment is the dynamic structure factor $S(\vec{k},\omega)$, which can be related to the double differential scattering cross section as:

$$\frac{d^2\sigma}{d\Omega dE'}(E \to E',\Omega) = \frac{k'}{k} S(\vec{k},\omega) \tag{2.10}$$

Here k and k' are the incident and the scattered wave of the neutrons, respectively. Often $S(\vec{k},\omega)$ is also denoted as $S(\vec{q},\omega)$ depending on the field. For example, in the time of flight experiments in chapter 4, it will be referred as $S(\vec{q},\omega)$.

The following interactions can occur depending on the fact that the scattered neutron waves from different scattering centers may or may not interfere.

- Elastic scattering: There is no change in energy between the incident and the scattered neutron waves. Hence, there is no information related to the dynamics of the scattering medium and only the the structural information is available.
- Inelastic scattering: There is a change in both the energy and the momentum between the incident and the scattered neutron waves. Hence, both the dynamic and structural information is available.
- Coherent scattering: In this case, the scattered neutron waves from different scattering atoms interfere. Coherent scattering provides information of the relative positions of the atoms, and hence the structure of the material.
- Incoherent scattering: In this case, there is no interference between the scattered neutron waves from different scattering atoms. Incoherent scattering provides no information of the relative positions of the atoms or the structural information of the material.

Thus, while incoherent inelastic scattering provides information about the single atom dynamics, the coherent counterpart gives information on the collective motion of atoms. This is explained in detail in the following section.

2.3.1 Coherent and Incoherent scattering

Scattering of neutrons by a single fixed nucleus can be written as:

$$\sigma_{tot} = 4\pi b^2 \tag{2.11}$$

where b is the scattering length which depends upon the spin of the scattering nucleus and the neutron.

Consider a system of a single element where the scattering length b varies from one nucleus to another. Assuming f_i being the relative frequency of scattering length b_i, the average value of b for the whole system can be defined as:

$$\bar{b} = \sum_i f_i b_i \tag{2.12}$$

and the average of b^2 as:

$$\overline{b^2} = \sum_i f_i b_i^2 \tag{2.13}$$

In the neutron-nucleus system, neutrons having spin $1/2$ along with the spin I of the nucleus can scatter in a state of spin $I + \frac{1}{2}$ and $I - \frac{1}{2}$. Define b^+ as the scattering length of the $I + \frac{1}{2}$ and b^- as $I - \frac{1}{2}$ for the nuclear-neutron system. Let f^+ be the frequency of occurrence for scattering length b^+ given by:

$$f^+ = \frac{2I+2}{(2I+2)+2I} = \frac{I+1}{2I+1} \tag{2.14}$$

and f^- the frequency of occurrence for scattering length b^- given by

$$f^- = \frac{2I}{(2I+2)+2I} = \frac{I}{2I+1} \tag{2.15}$$

Following Eq. 2.12 and 2.13 $\bar{b}$ and $\overline{b^2}$ can be written as:

$$\bar{b} = \frac{I+1}{2I+1} b^+ + \frac{I}{2I+1} b^- \tag{2.16}$$

and

$$\overline{b^2} = \frac{I+1}{2I+1}(b^+)^2 + \frac{I}{2I+1}(b^-)^2 \tag{2.17}$$

If there are several isotopes in the scattering system, where the i^{th} isotope has a relative abundance c_i, nuclear spin I_i, scattering lengths b_i^+ and b_i^-, then Eq. 2.16 and 2.17 can be generalized to

$$\bar{b} = \sum_i c_i \left\{ \frac{I_i+1}{2I_i+1} b_i^+ + \frac{I_i}{2I_i+1} b_i^- \right\} \tag{2.18}$$

and

$$\overline{b^2} = \sum_i c_i \left\{ \frac{I_i+1}{2I_i+1} (b_i^+)^2 + \frac{I_i}{2I_i+1} (b_i^-)^2 \right\} \tag{2.19}$$

Here, $\bar{b}$ is known as the coherent scattering length. Using Eq. 2.11, σ_{coh} and σ_{incoh} can be written as:

$$\begin{aligned} \sigma_{coh} &= 4\pi\bar{b}^2 \\ \sigma_{incoh} &= 4\pi(\overline{b^2} - \bar{b}^2) \end{aligned} \tag{2.20}$$

A complete description of the thermal scattering process can be found in the literature [7, 17, 29]. Using the first Born approximation and Fermi pseudo-potential, as formalized by Van Hove [7], the double differential cross section can be given as

$$\frac{d^2\sigma}{d\Omega dE'} = \frac{k'}{k}\frac{1}{2\pi\hbar}\frac{1}{N}\sum_{jj'}\overline{b_j b_{j'}} \int\limits_{-\infty}^{\infty} \left\langle exp\Big\{-i\vec{k}.\vec{R_{j'}}(0)\Big\} exp\Big\{-i\vec{k}.\vec{R_j}(t)\Big\}\right\rangle e^{-i\omega t} dt \tag{2.21}$$

Here, it is assumed that there is no correlation between scattering lengths b of different nuclei, i.e.:

$$\begin{aligned} \overline{b_{j'} b_j} &= \bar{b}^2, j' \neq j \\ \overline{b_{j'} b_j} &= \overline{b^2}, j' = j \end{aligned} \tag{2.22}$$

Equation 2.21 can be written as a sum of coherent and incoherent part:

$$\begin{aligned} \frac{d^2\sigma}{d\Omega dE'} =& \frac{k'}{k}\frac{1}{2\pi\hbar}\bar{b}^2\frac{1}{N}\sum_{jj'}\left\langle exp\Big\{-i\vec{k}.\vec{R_{j'}}(0)\Big\} exp\Big\{-i\vec{k}.\vec{R_j}(t)\Big\}\right\rangle e^{-i\omega t} dt \\ &+ \frac{k'}{k}\frac{1}{2\pi\hbar}(\overline{b^2} - \bar{b}^2)\frac{1}{N}\sum_{j}\int\limits_{-\infty}^{\infty}\left\langle exp\Big\{-i\vec{k}.\vec{R_j}(0)\Big\} exp\Big\{-i\vec{k}.\vec{R_j}(t)\Big\}\right\rangle e^{-i\omega t} dt \end{aligned} \tag{2.23}$$

From Eq. 2.23 the double differential scattering cross section can be written as a sum of coherent and incoherent double differential cross section as:

$$\frac{d^2\sigma}{d\Omega dE'} = \left(\frac{d^2\sigma}{d\Omega dE'}\right)_{coh} + \left(\frac{d^2\sigma}{d\Omega dE'}\right)_{incoh} \tag{2.24}$$

where

$$\left(\frac{d^2\sigma}{d\Omega dE'}\right)_{coh} = \frac{\sigma_{coh}}{4\pi}\frac{k'}{k}\frac{1}{2\pi\hbar}\frac{1}{N}\sum_{jj'}\int\limits_{-\infty}^{\infty}\Big\langle exp\Big\{-i\vec{k}.\vec{R}_{j'}(0)\Big\}exp\Big\{-i\vec{k}.\vec{R}_j(t)\Big\}\Big\rangle e^{-i\omega t}dt \tag{2.25}$$

and

$$\left(\frac{d^2\sigma}{d\Omega dE'}\right)_{incoh} = \frac{\sigma_{incoh}}{4\pi}\frac{k'}{k}\frac{1}{2\pi\hbar}\frac{1}{N}\sum_{j}\int\limits_{-\infty}^{\infty}\Big\langle exp\Big\{-i\vec{k}.\vec{R}_j(0)\Big\}exp\Big\{-i\vec{k}.\vec{R}_j(t)\Big\}\Big\rangle e^{-i\omega t}dt \tag{2.26}$$

with $\sigma_{coh} = 4\pi\overline{b}^2$ and $\sigma_{inc} = 4\pi(\overline{b^2} - \overline{b}^2)$ from Eq. 2.20.

In Eq. 2.25, $\left(\frac{d^2\sigma}{d\Omega dE'}\right)_{coh}$, the coherent double differential cross section depends on the correlation between the positions of different nuclei at different times as well as on the correlation between the positions of the same nucleus at different times. Whereas the incoherent double differential cross section, $\left(\frac{d^2\sigma}{d\Omega dE'}\right)_{incoh}$ in Eq. 2.26, depends on the correlation between the positions of same nucleus at different times.

The terms in the right hand side of Eq. 2.25 and 2.26 can be represented in terms of the intermediate scattering function as:

$$I_{coh}(\vec{k},t) = \frac{1}{N}\sum_{jj'}\Big\langle exp\Big\{-i\vec{k}.\vec{R}_{j'}(0)\Big\}exp\Big\{-i\vec{k}.\vec{R}_j(t)\Big\}\Big\rangle \tag{2.27}$$

and

$$I_{incoh}(\vec{k},t) = \frac{1}{N}\sum_{j}\Big\langle exp\Big\{-i\vec{k}.\vec{R}_j(0)\Big\}exp\Big\{-i\vec{k}.\vec{R}_j(t)\Big\}\Big\rangle \tag{2.28}$$

Introducing $S(\vec{k},\omega)$, at this point as the dynamic structure factor of materials which can be written as a sum of self and distinct dynamic structure factors as :

$$S(\vec{k},\omega) = S_s(\vec{k},\omega) + S_d(\vec{k},\omega) \tag{2.29}$$

Here, $S_s(\vec{k},\omega)$ is the self structure factor which accounts for the waves that do not interfere with each others after being scattered from each nucleus, i,e, incoherent scattering. $S_d(\vec{k},\omega)$ accounts for the coherent scattering and the scattering waves interfere with each other. Both structure factors can be represented as a Fourier transform in time of the intermediate scattering functions, $I_{coh}(\vec{k},t)$ and $I_{incoh}(\vec{k},t)$ as:

$$S_d(\vec{k},\omega) = \frac{1}{2\pi\hbar}\int\limits_{-\infty}^{\infty} I_{coh}(\vec{k},t)e^{-i\omega t}dt \tag{2.30}$$

and

$$S_s(\vec{k},\omega) = \frac{1}{2\pi\hbar}\int\limits_{-\infty}^{\infty} I_{incoh}(\vec{k},t)e^{-i\omega t}dt \tag{2.31}$$

Using Eq. 2.27 to 2.31, the coherent and incoherent double differential cross sections in Eq. 2.25 and 2.26 can be re-written as:

$$\left(\frac{d^2\sigma}{d\Omega dE'}\right)_{coh} = \frac{\sigma_{coh}}{4\pi}\frac{k'}{k}S_d(\vec{k},\omega) \tag{2.32}$$

$$\left(\frac{d^2\sigma}{d\Omega dE'}\right)_{incoh} = \frac{\sigma_{incoh}}{4\pi}\frac{k'}{k}S_s(\vec{k},\omega) \tag{2.33}$$

The total double differential scattering cross section can then be given as:

$$\frac{d^2\sigma}{d\Omega dE'} = \frac{1}{4\pi}\frac{k'}{k}\left\{\sigma_{coh}S_d(\vec{k},\omega) + \sigma_{incoh}S_s(\vec{k},\omega)\right\} \tag{2.34}$$

In reactor physics, the scattering law $S(\alpha,\beta)$ is written in terms of $S(\vec{k},\omega)$ as:

$$S(\alpha,\beta) = k_B T e^{\frac{\beta}{2}} S(\vec{k},\omega) \tag{2.35}$$

$$\frac{d^2\sigma}{d\Omega dE'} = \frac{1}{4\pi k_B T}\sqrt{\frac{E'}{E}}e^{-\beta/2}\left\{\sigma_{coh}S_d(\alpha,\beta) + \sigma_{incoh}S_s(\alpha,\beta)\right\} \tag{2.36}$$

2.4. Approximations while generating TSL

- Incoherent approximations: Generally TSLs are evaluated based on the incoherent approximation in which $S_d(\alpha,\beta)$ is neglected. Hence Eq. 2.36 takes the form:

$$\frac{d^2\sigma}{d\Omega dE'} = \frac{\sigma_{incoh}}{4\pi k_B T}\sqrt{\frac{E'}{E}}e^{-\frac{\beta}{2}}S_s(\alpha,\beta) \tag{2.37}$$

- Gaussian approximation: An approximation applicable to incoherent part of double differential cross section called as incoherent approximation is often used to calculate the intermediate structure factor $I_{incoh}(\vec{k},t)$ as in Eq. 2.28. The Van Hove space time correlation [7] in the incoherent approximation is approximated as:

$$G(\vec{r},t) = (2\pi\Gamma(t))^{-3/2}e^{(-r^2/2\Gamma(t))} \tag{2.38}$$

  where $\Gamma(t)$ is the width function that can be defined as the mean squared displacement of a particle at time t, from its location at time t=0. The intermediate structure factor can thus be expressed as:

$$I_{incoh}(\vec{k},t) = \int G(\vec{r},t)e^{i\vec{k}\cdot r}dr = \exp\left[-\frac{k^2\Gamma(t)}{2}\right] \tag{2.39}$$

  The width function can be calculated from the frequency spectrum $\rho(\omega)$ as:

$$\Gamma(t) = \frac{\hbar}{M}\int_0^\infty d\omega\frac{g(\omega)}{\omega}\left\{\coth\left(\frac{\hbar\omega}{2k_BT}\right)(1-\cos(\omega t)) - i\sin(\omega t)\right\} \tag{2.40}$$

  NJOY is based on this incoherent approximation to calculate the thermal scattering law.

- Free gas theory: When the energy of the neutrons are sufficiently high as compared to chemical binding energies of the molecules, the scattering of neutrons can be quantified considering the atoms behaving like a perfect Maxwellian gas. In this case the $S(\alpha,\beta)$ is defined as following:

$$S_{FG}(\alpha,\beta) = \frac{1}{\sqrt{4\pi\alpha}}\exp\left[-\frac{(\alpha+\beta)^2}{4\alpha}\right] \tag{2.41}$$

2.5. Evaluation of thermal scattering law using the LEAPR module of NJOY code

NJOY is a nuclear data processing code to generate cross section data libraries in a format to be used by nuclear applications. There are several modules in the NJOY code to treat different neutron interactions in different energy regions of the neutrons based on different physics models. LEAPR module of the NJOY code is used to generate the $S(\alpha,\beta)$ for different moderator materials. In the incoherent and Gaussian approximation LEAPR generates the TSL by a convolution of three functions:

$$S(\alpha,\beta) = S_t(\alpha,\beta) \otimes S_c(\alpha,\beta) \otimes S_v(\alpha,\beta) \tag{2.42}$$

where $\otimes$ represents convolution and

- $S_t(\alpha,\beta)$ is the TSL for the molecular translations.
- $S_c(\alpha,\beta)$ is the TSL that defines the continuous solid type spectrum.
- $S_v(\alpha,\beta)$ models the discrete oscillators and generates the corresponding TSL.

There is an associated weight corresponding to each type of interactions, i.e.,

- w_t Corresponds to the molecular translations.
- w_c Corresponds to the continuous solid type spectrum.
- w_v^i Corresponds to each vibrational oscillator.

These weights should be normalized as:

$$w_t + w_c + \sum_i w_v^i = 1 \tag{2.43}$$

and the analytic frequency spectrum reads:

$$\rho(\beta) = w_t\rho_t(\beta) + w_c\rho_c(\beta) + \sum_{i=1}^{n} w_i\delta(\beta_i) \tag{2.44}$$

2.5.1 Molecular translation

There are two options in LEAPR to generate TSL due to molecular diffusion (translation), i.e. $S_t^{FG}(\alpha, \beta)$ using free gas model or $S_t^{ES}(\alpha, \beta)$ Egelstaff and Schofield molecular translation.

Free gas translation: Free gas model is appropriate for molecules in gaseous phase, but can be used to represent the translational component of water. $S_t^{FG}(\alpha, \beta)$ is calculated using the free gas approximation by [17]:

$$S_t^{FG}(\alpha, \beta) = \frac{1}{\sqrt{4\pi w_t \alpha}} exp\left[-\frac{(w_t\alpha + \beta)^2}{4w_t\alpha}\right] \tag{2.45}$$

Here β is < 0, i.e downscattering. Equation 2.45 follows the detail balance and hence the upscattering part, i.e. $\beta > 0$ is obtained using:

$$S_t^{FG}(\alpha, \beta) = e^{-\beta} S_t^{FG}(\alpha, -\beta) \tag{2.46}$$

Egelstaff and Schofield (ES) molecular translation: $S_t^{ES}(\alpha, \beta)$ is calculated using an analytical diffusion model called "effective width model", developed by Egelstaff and Schofield. The analytical frequency spectrum generated using this model is given by [30]:

$$\rho(\beta) = w_t \frac{4c}{\pi\beta}\sqrt{c^2 + 1/4}\sinh(\beta/2)K_1(\beta\sqrt{c^2 + 1/4}) \tag{2.47}$$

where $K_1(x)$ is the modified Bessel function of the second kind, w_t the translational weight, c is the dimensionless diffusion constant that is defined by:

$$c = \frac{M_{\text{diff}} D}{\hbar} = \frac{M_H D}{w_t \hbar} \tag{2.48}$$

where D is the molecular diffusion coefficient, M_H is the mass of hydrogen and M_{diff} is the diffusive mass of the molecules.

$$\begin{aligned} S_t^{ES}(\alpha, \beta) = & \frac{2cw_t\alpha}{\pi} \exp\left[2c^2 w_t\alpha - \beta/2\right] \times \\ & \frac{\sqrt{c^2 + 1/4}}{\sqrt{\beta^2 + 4c^2 w_t^2 \alpha^2}} K_1\left[\sqrt{c^2 + 1/4}\sqrt{\beta^2 + 4c^2 w_t^2 \alpha^2}\right] \end{aligned} \tag{2.49}$$

LEAPR provides an option to choose between these two models to generate $S_t(\alpha, \beta)$. If the value of c in the LEAPR input is set to 0, LEAPR uses the FG model, else if $c \neq 0$ it uses the ES model for molecular translation.

2.5.2 Continuous solid type spectrum

Under the incoherent and the Gaussian approximation, the TSL can be expressed as a function of the frequency spectrum $\rho(\beta)$ of the excitations in the molecular system by [17]:

$$S_c(\alpha, \beta) = \frac{1}{2\pi} \int_{-\infty}^{+\infty} e^{\iota\beta\hat{t}}\, e^{-\gamma(\hat{t})} d\hat{t} \tag{2.50}$$

where $\hat{t}$ is the time measured in the units of $\hbar/(kT)$ seconds. $\gamma(\hat{t})$ is given by:

$$\gamma(\hat{t}) = \alpha \int_{-\infty}^{+\infty} P(\beta)(1 - \, e^{-\iota\beta\hat{t}})\, e^{-\beta/2} d\beta \tag{2.51}$$

and

$$P_c(\beta) = \frac{\rho(\beta)}{2\beta \sinh(\beta/2)} \tag{2.52}$$

where $\rho(\beta)$ is is the frequency spectrum of excitations in the system expressed as a function of β. Expanding the exponential part in Eq. 2.50 gives the phonon expansion:

$$e^{-\gamma_c(\hat{t})} = e^{-\alpha\lambda_c} \sum_{n=0}^{\infty} \frac{1}{n!} \left[\alpha \int_{-\infty}^{\infty} P_c(\beta) e^{-\beta/2} e^{-i\beta\hat{t}} d\hat{t} \right]^n \tag{2.53}$$

where λ_c is the Debye-Waller factor given by:

$$\lambda_c = \int_{-\infty}^{\infty} P_c(\beta) e^{-\beta/2} d\beta \tag{2.54}$$

The thermal scattering law then becomes:

$$S_c(\alpha, \beta) = e^{-\alpha\gamma_c} \sum_{n=0}^{\infty} \frac{1}{n!} \alpha^n \times \frac{1}{2\pi} \int_{-\infty}^{\infty} e^{i\beta\hat{t}} \left[\int_{-\infty}^{\infty} P_c(\beta') e^{-\beta'/2} e^{-i\beta'\hat{t}} d\beta' \right]^n d\hat{t} \tag{2.55}$$

Equation 2.55 can be represented in terms of $\lambda_c^n T_n(\beta)$ as:

$$S_c(\alpha,\beta) = e^{-\alpha\gamma_c}\sum_{n=0}^{\infty}\frac{1}{n!}\left[\alpha\lambda_c\right]^n \mathcal{T}_n(\beta) \tag{2.56}$$

The zero phonon term, i.e. $n = 0$ is a delta function as seen in equation below:

$$\mathcal{T}_0(\beta) = \frac{1}{2\pi}\int_{-\infty}^{\infty} e^{i\beta\hat{t}}d\hat{t} = \delta(\beta) \tag{2.57}$$

and

$$\mathcal{T}_1(\beta) = \int_{-\infty}^{\infty}\frac{P_c(\beta')e^{-\beta'/2}}{\lambda_c}\left\{\frac{1}{2\pi}\int_{-\infty}^{\infty} e^{i(\beta-\beta')\hat{t}}d\hat{t}\right\}d\beta' = \frac{P_c(\beta)e^{-\beta/2}}{\lambda_c} \tag{2.58}$$

In general $\mathcal{T}_n(\beta)$ takes the form:

$$\mathcal{T}_n(\beta) = \int_{-\infty}^{\infty}\mathcal{T}_1(\beta')\mathcal{T}_{n-1}(\beta-\beta')d\beta' \tag{2.59}$$

Here n is the number of phonons. This value is given as an input to LEAPR.

2.5.3 Discrete vibrational oscillators

In order to model the intra molecular vibration modes present in the frequency spectrum, LEAPR models it as a delta function in energy β. The thermal scattering law $S_v^i(\alpha,\beta)$ for i^{th} discrete oscillator is given as [27]:

$$S_v^i(\alpha,\beta) = e^{-\alpha\lambda_i}\sum_{n=-\infty}^{\infty}\delta(\beta-n\beta_i)I_n\left[\frac{\alpha w_v^i}{\beta_i\sinh(\beta_i/2)}\right]e^{-n\beta_i/2} \tag{2.60}$$

where

$$\lambda_i = w_v^i\frac{\coth(\beta_i/2)}{\beta_i} \tag{2.61}$$

2.5.4 Short Collision Time Approximation (SCTA)

The range of α and β can lie outside the range of tabulated $S(\alpha,\beta)$, for high incident energies. In this case the Short Collision Time Approximation (SCTA) in which LEAPR calculates the solid-type scattering law following the free gas approximation:

$$S^{SCTA}(\alpha,\beta) = \frac{1}{\sqrt{4\pi\omega_c\alpha\frac{T_{eff}}{T}}} exp\left[-\frac{(\omega_c\alpha+\beta)^2}{4\omega_c\alpha\frac{T_{eff}}{T}}\right] \tag{2.62}$$

Here β is < 0, i.e downscattering. Equation 2.62 follows detail balance and hence the upscattering part, i.e. $\beta > 0$ is obtained using:

$$S^{SCTA}(\alpha,\beta) = e^{-\beta}S^{SCTA}(\alpha,-\beta) \tag{2.63}$$

T_{eff} is the effective temperature which is influenced by several vibrational modes present in the frequency spectrum. T^c_{eff} is the effective temperature corresponding to the rotational mode given by:

$$T^c_{eff} = \frac{T}{2}\int_{-\infty}^{\infty}\beta^2 P_s(\beta)e^{-\beta}d\beta \tag{2.64}$$

In the case, where all the vibration modes are present, T_{eff} is obtained by:

$$T_{eff} = \omega_t T + \omega_c T^c_{eff} + \sum_{i=1}^{n}\omega_i\frac{\beta_i}{2}\coth\left(\frac{\beta_i}{2}\right)T, \tag{2.65}$$

where ω_i is the weight and β_i is the energy of each oscillator of the intra molecular mode.

2.6. Generation of TSL for light water using the LEAPR module of NJOY

Certain inputs in specific formats are required by the LEAPR module of NJOY to generate the TSL for light water. First and foremost, T, the temperature of interest and the free atom cross section of hydrogen, i.e, 20.478 barn are required. LEAPR calculates the bound atom cross section using Eq. 2.9 and hence the value of A, the neutron mass of hydrogen, i.e. 0.9991673. Alpha grid, beta grid and the continuous frequency spectrum in a uniform energy grid is then required. Weight of the translation band w_t, weight of the continuous spectrum w_c, energy $\delta(\beta_i)$ and weight of the oscillators ω_i are also required in order to represent the contributions corresponding to the translational, rotational and vibrational motions in the frequency spectrum.

Chapter 3

Presently available TSL evaluations for light water

Evaluations of TSL for light water are available to the users in the form of ENDF nuclear cross section data libraries. This chapter summarizes the present state-of the-art of the most recent TSL evaluations for light water in ENDF/B and JEFF data libraries, i.e. JEFF-3.3 [2] and ENDF/B-VIII.0 [31]. Both these libraries are based on different approaches and hence a comparative study is necessary at this point to understand the physics model incorporated in each evaluation and their validity on reactor physics calculations. As mentioned in **Chapter 1**, the goal of this PhD work is to study the TSL evaluations for light water at high temperatures and pressures, matching reactor operating conditions, hence a special attention will be given to high temperature evaluations. Its worth mentioning that, a comparative study like this is not intended to judge a particular TSL library over the other, but to better understand them and develop a new TSL evaluation with improved applicability. Also, it would be interesting to study the behavior of the present TSL evaluations at temperatures matching reactor operating conditions, since an accurate knowledge of the impact of TSL is important to correctly characterize neutrons slowing down in water.

3.1. TSL generation methodology

Presently, all the TSL evaluations of light water, available in the nuclear data libraries are generated using the LEAPR module of the NJOY code. The most recent release of JEFF is JEFF-3.3 [2] and that of ENDF/B is ENDF/B-VIII.0 [31]. In both these libraries TSL evaluations for light water are generated using LEAPR. The theoretical framework for the generation of TSL based on LEAPR has been covered in **Chapter 2**. As explained before, neutrons in the thermal energy range exchange energy and momentum with light water corresponding to different modes in the frequency spectrum of light water. This frequency spectrum is thus used as an input by LEAPR to generate $S(\alpha, \beta)$ in a format suitable for reactor applications. Hence a proper understanding of the frequency spectrum is necessary to generate TSL for light water.

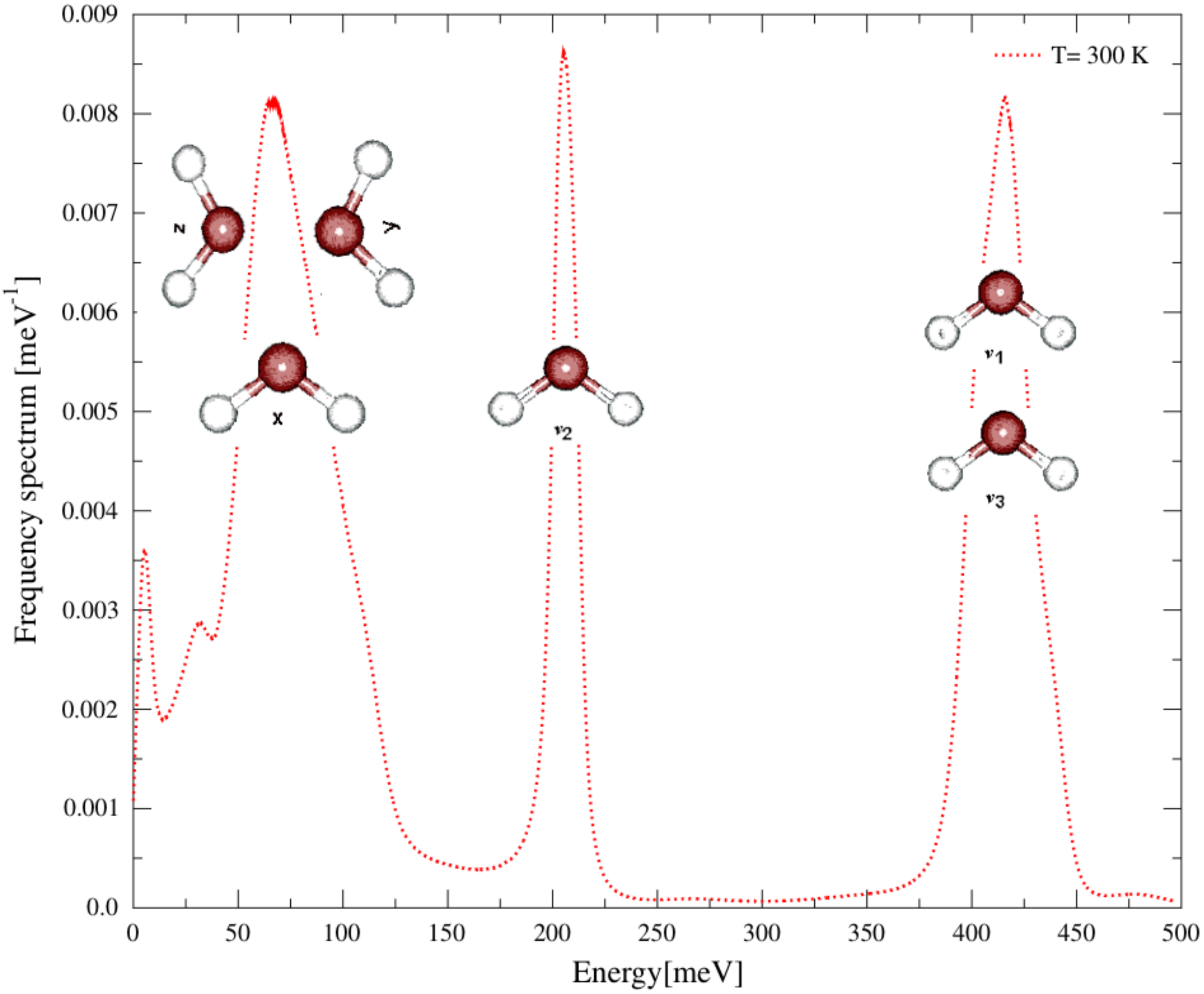

FIGURE 3.1: Pictorial representation of the various energy bands in the frequency spectrum of light water. The data for this particular frequency spectrum has been taken from Ref. [6].

Figure 3.1 shows a pictorial sketch of the different energy bands in the frequency spectrum of light water. Several peaks can be seen in this frequency spectrum corresponding to different vibrational energies available in the light water molecule. The first peak at low energy, i.e. ~ 7 meV corresponds to the molecular translation/diffusion. A broad band of rotation is seen around $60 - 70$ meV which takes into account the rotation of the molecule in X,Y and Z directions. The peak corresponding to the intra molecular bending of the hydrogen bonds (v_2) is observed around 205 meV. Two peaks, v_1 and v_3, that correspond to the intra molecular symmetric and asymmetric stretching modes, respectively are seen around $415 - 436$ meV. The TSL for light water in both JEFF-3.3 and ENDF/B-VIII.0 are based on different methodologies and physics models but both evaluations rely on the frequency spectrum of light water to generate $S(\alpha, \beta)$. There are several ways to obtain the frequency spectrum of light water, for example, Raman spectroscopy, time-of-flight neutron scattering experiments, etc. TSL for light water in JEFF-3.3 and all the other previous evaluations of JEFF have relied on experimentally measured frequency spectrum as shown in Fig. 3.2 [17, 19]. This is also true for the past ENDF/B evaluations for light water, for instance ENDF/B-VII.1 [15], relies on the same experimental data. However, a recent methodology based on generating frequency spectrum of light water using classical molecular dynamics (MD) simulation has been adapted in the ENDF/B-VIII.0 library [24]. In principal, MD simulations based on force fields (inter and intra molecular water potentials) can generate reliable frequency spectrum of light water over a wide range of energy transfer. The benefit of using MD is that, the energy range in the frequency spectrum that cannot be explicitly measured due to experimental limitations, can be effectively generated by MD approach. Recent studies have been done using MD simulations which is found to be of great importance especially at room temperature. As a result, one can say that, on the basis of the type of frequency spectrum used, TSL libraries can be broadly classified into two types: The one obtained from the measurements and the other from MD simulations using classical force fields.

3.1.1 TSL for light water based on experimentally measured frequency spectrum

The very first model developed for the generation of TSL for light water was based on experimentally measured frequency spectrum by Haywood and Thorson [21] as shown in Fig. 3.2. This model was prepared by Koppel and Houston in 1978 [19], often referred as the General Atomics or the **GA model**. The ENDF/B-VI.8 TSL evaluation for light water is based on the GA model, which corresponds to an evaluation modified by Macfarlane in 1994 using LEAPR [17]. Due to limited resolution of the experimental frequency spectrum, the translation band around 7 meV is not present. As a consequence, a function ω^2 was introduced to model solid like

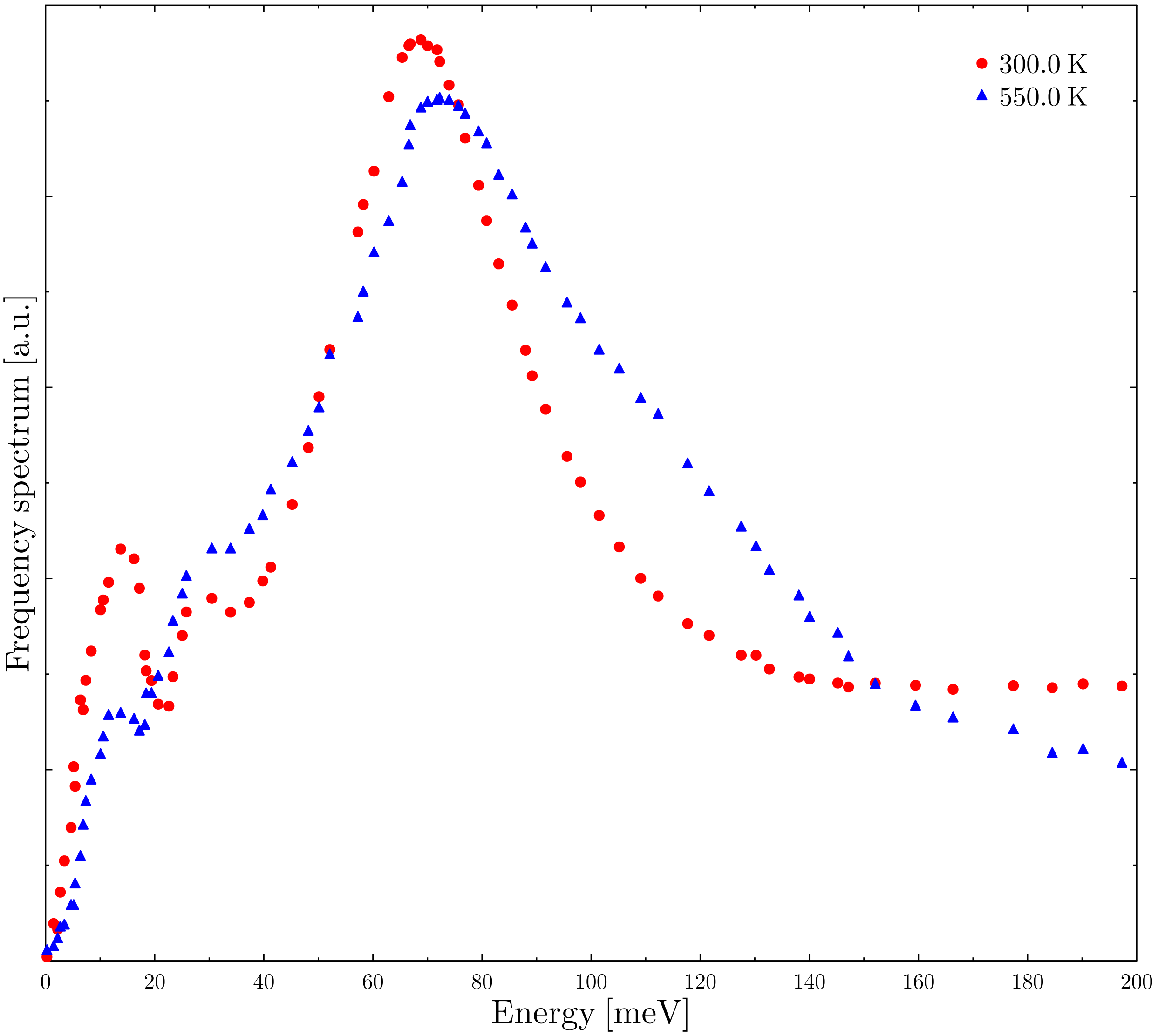

FIGURE 3.2: Frequency spectrum of light water measured at 300 K and 550 K. The data points have been extracted roughly from the conference proceeding [32].

extrapolation for continuous phonon spectrum, the weight of translational mode being deduced by difference. Since the frequency spectra were limited up to the rotation band, the intra molecular interactions were modeled using two discrete oscillators based on Eq. 2.60, one at 205 meV to model the bending mode and the other at 480 meV to model the asymmetric and symmetric stretching modes in the frequency spectrum.

Meanwhile, another model was developed by J. Keinert and M. Mattes in 1984 and then updated in 2005, often referred as **IKE model**. This model is based on experimentally measured temperature dependent frequency spectrum by Haywood and Page at 300 K and 550 K [21]. For the intermediate temperatures between 300 K and 550 K, the frequency spectrum is linearly interpolated. The rotations of the water molecule (around 70 meV) are described as a continuous frequency spectrum and molecular diffusion is modeled as a free gas. The bending mode is modeled using a discrete oscillator at 205 meV, whereas the energy of the stretching mode has been reduced from 480 meV to 436 meV as compared to the GA model. The IKE model was used to develop TSL evaluation for light water in the JEFF-3.1.1 library [18] and it is still in use for the development of TSL for light water in JEFF-3.3. Temperature dependent frequency spectrum of light water based on the IKE model is shown in Fig. 3.3. As can be seen in Fig. 3.3, the energy band corresponding to the hindered rotation of the water molecule is around 70 meV and the energy of the peak of this band is not affected with increasing temperature. However, the intensity of the peak of the rotation band reduces with increasing temperature. Table 3.1 shows the basic input parameters of JEFF-3.3 to generate TSL for light water using LEAPR.

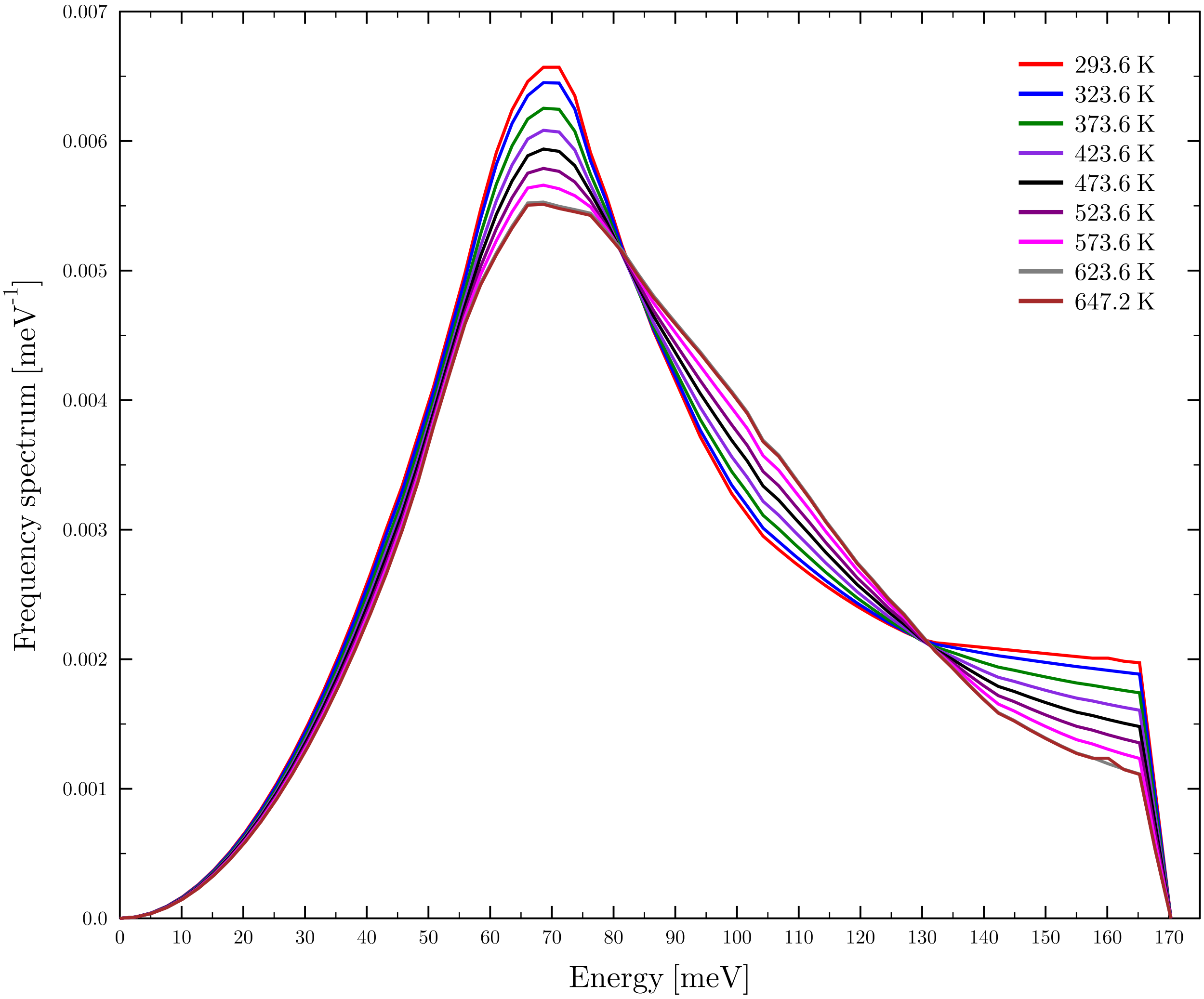

FIGURE 3.3: Frequency spectrum of light water based on the JEFF-3.3 TSL evaluation.

Temperature (K)	Translational weight (ω_t)	Diffusion constant (c)	Continuous spectrum weight (ω_c)	First osc. energy (eV)	First osc. weight	Second osc. energy (eV)	Second osc. weight
293.6	0.021739	0.000	0.4891305	0.205	0.163043500	0.436	0.326087000
323.6	0.025641	0.000	0.4871795	0.205	0.162393167	0.436	0.324786333
373.6	0.032258	0.000	0.4838710	0.205	0.161290333	0.436	0.322580667
423.6	0.037037	0.000	0.4814815	0.205	0.160493833	0.436	0.320987667
473.6	0.040000	0.000	0.4800000	0.205	0.160000000	0.436	0.300000000
523.6	0.043478	0.000	0.4782610	0.205	0.159420333	0.436	0.318840667
573.6	0.045454	0.000	0.4772730	0.205	0.159091000	0.436	0.318180000
623.6	0.047620	0.000	0.4761900	0.205	0.158730000	0.436	0.317460000
647.0	0.049020	0.000	0.4754900	0.205	0.158496667	0.436	0.316993333

TABLE 3.1: LEAPR input parameters for JEFF-3.3 TSL evaluation for light water.

The diffusion constant, c is 0 in Table 3.1, irrespective of the temperature, implies that a free gas model is used in this evaluation. The translation weight increases as a function of temperature. The translational weight is inversely proportional to the effective mass of the water molecule. At high temperatures water tends to have a less collective behavior than at room temperatures, hence the effective mass reduces at higher temperatures.

The IKE model was later adapted by the ENDF/B-VII.1 library for the generation of TSL for light water, by slightly reducing the energy of the hindered rotation band from 70 meV to 60 meV as shown in Fig. 3.4. It should be noted that the TSL for light water in ENDF/B-VII.1 library is based on the same experimental data like JEFF-3.3 but with an adjustment to the frequency spectrum. The idea behind this adjustment was to have better agreement with critical benchmarks in the energy range of 10-100 meV. This energy region is extremely important for thermal reactor applications, any change in the frequency spectrum has a direct impact on criticality calculations. Frequency spectrum of light water based on the ENDF/B-VII.1 TSL library is given in Fig. 3.5 and the corresponding LEAPR input parameters in Table 3.2.

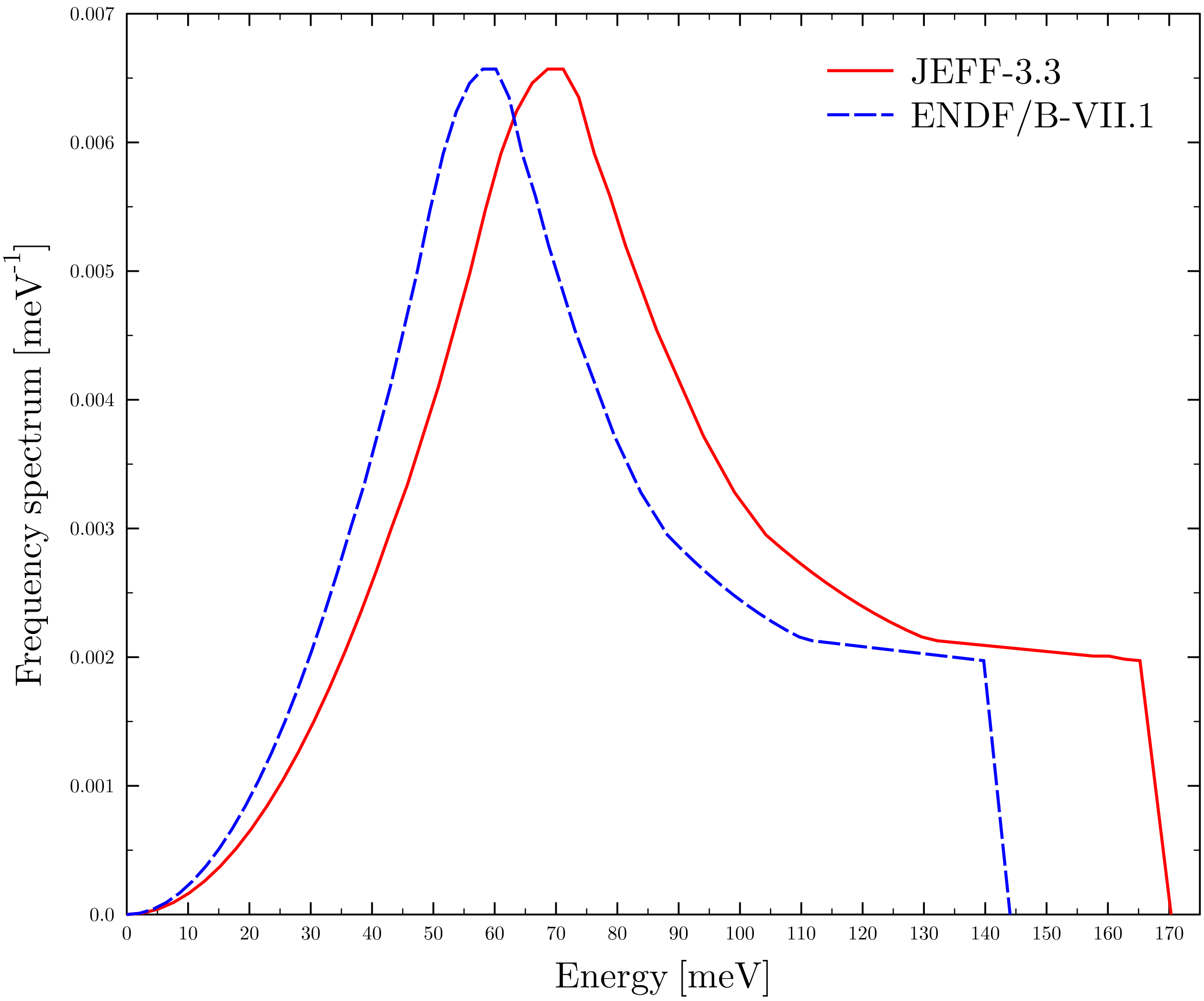

FIGURE 3.4: Frequency spectrum of light water based on the JEFF-3.3 and ENDF/B-VII.1 TSL evaluation.

Temperature (K)	Translational weight (ω_t)	Diffusion constant (c)	Continuous spectrum weight (ω_c)	First osc. energy (eV)	First osc. weight	Second osc. energy (eV)	Second osc. weight
293.6	0.0192000	0.0	0.490400	0.205	0.163467	0.436	0.326933
350.0	0.0291350	0.0	0.485433	0.205	0.161811	0.436	0.323620
400.0	0.0346475	0.0	0.482676	0.205	0.160892	0.436	0.321784
450.0	0.0385185	0.0	0.480741	0.205	0.160247	0.436	0.320494
500.0	0.0417390	0.0	0.479131	0.205	0.159710	0.436	0.319420

Continued on next page

Table 3.2 – continued from previous page

Temperature (K)	Translational weight (ω_t)	Diffusion constant (c)	Continuous spectrum weight (ω_c)	First osc. energy (eV)	First osc. weight	Second osc. energy (eV)	Second osc. weight
550.0	0.0444660	0.0	0.477767	0.205	0.159256	0.436	0.318510
600.0	0.0465370	0.0	0.476730	0.205	0.158911	0.436	0.317821
650.0	0.0490200	0.0	0.475490	0.205	0.158497	0.436	0.316993
800.0	0.0490200	0.0	0.475490	0.205	0.158497	0.436	0.316993

Table 3.2: LEAPR input parameters for ENDF/B-VII.1 TSL evaluation for light water.

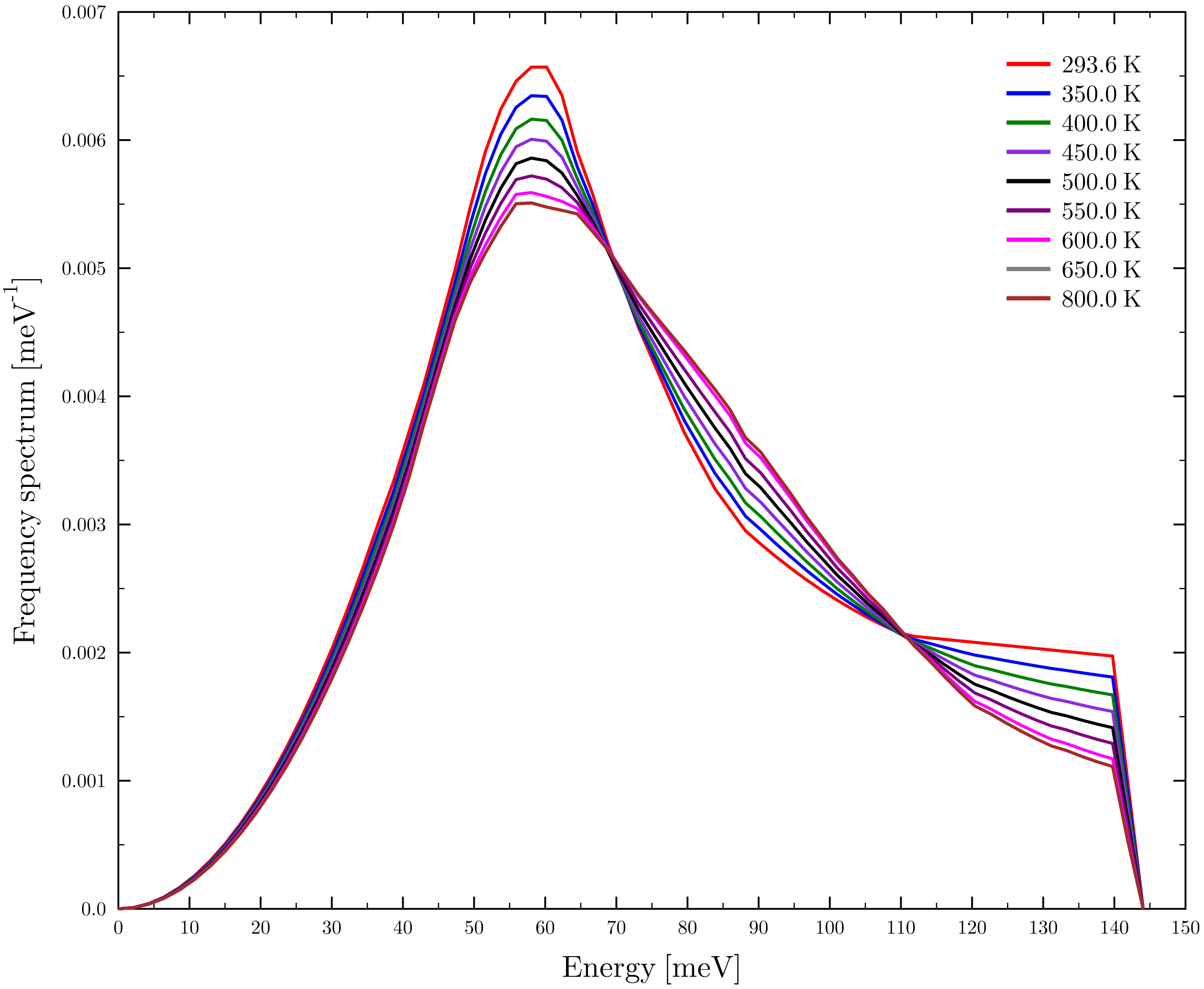

Figure 3.5: Frequency spectrum of light water based on ENDF/B-VII.1 TSL evaluation.

It should be noted that in the evaluation of either JEFF-3.3 or ENDF/B-VII.1, the translation mode that is somewhat visible in the experimental data [21] around 7 meV has been totally removed, while apparently, in practical thermal reactor applications it appears that the impact of this peak is negligible. However, care must be taken when one deals with criticality safety applications, the neutron spectrum can be towards low energy side. For nuclear criticality safety systems operating at temperatures lower than room temperatures, the neutron spectrum may shift to low energy range. New criteria for safety regulations of materials outside nuclear reactors, indicate the need for accurate nuclear data for temperatures as low as 220 K. A recent study, conducted at the IRSN, demonstrates the impact of low temperature nuclear data on practical applications.

The adjustment in the energy band of the frequency spectrum in the TSL evaluation for light water in ENDF/B-VII.1 implies that criticality safety benchmarks are sensitive to the position of the rotation band in the frequency spectrum. Following which, both double differential and total cross section in the thermal energy range could be affected. Thus, a proper study of the frequency spectrum is necessary to obtain reliable TSL for light water at reactor operating conditions. It implies that new high-resolution measurements of the frequency spectrum of light water in a broad energy range are necessary at reactor operating temperatures to properly characterize the position of the molecular vibrations and hindered rotations in the frequency spectrum.

3.1.2 TSL for light water based on molecular dynamics simulations

In the past few years, there has been a renewed interest in reviewing the GA and IKE models. Generation of new thermal scattering libraries is based on recent advancements of light water empirical potentials and improved computational capabilities. Several groups [22, 24, 33] have proposed different methodologies to produce TSL for light water. A promising technique which provides reliable TSL involves MD simulations of light water. This method allows the generation of the temperature-dependent frequency spectrum of light water from the MD trajectories. This methodology is not completely approximation-free, due to the intrinsic limitation of the classical MD simulations at lower and higher energies, which are corrected by applying quantum corrections [33]. Other techniques rely on a combination of MD with available experimental data to calculate the parameters required for the TSL generation. The accuracy of the MD simulations also depends on the intra and inter atomic water potentials used and their accuracy to describe the properties of water at high temperature and pressure. A great deal of water potentials, governed by empirical or semi-empirical inter-molecular potentials exists [34]. A new TSL library for light water has been adapted by ENDF/B-VIII.0 which is referred as the **CAB** model. This new library is based on MD simulations of light water using the non-polarizable TIP4P/2005f [35] flexible light water potential. In this model, simulations are carried out at several temperatures [24] to generate the temperature-dependent frequency spectrum of light water. Fig. 3.6 shows the frequency spectrum of light water available in the ENDF/B-VIII.0 TSL data library and the associated LEAPR parameter file is given in Table 3.3.

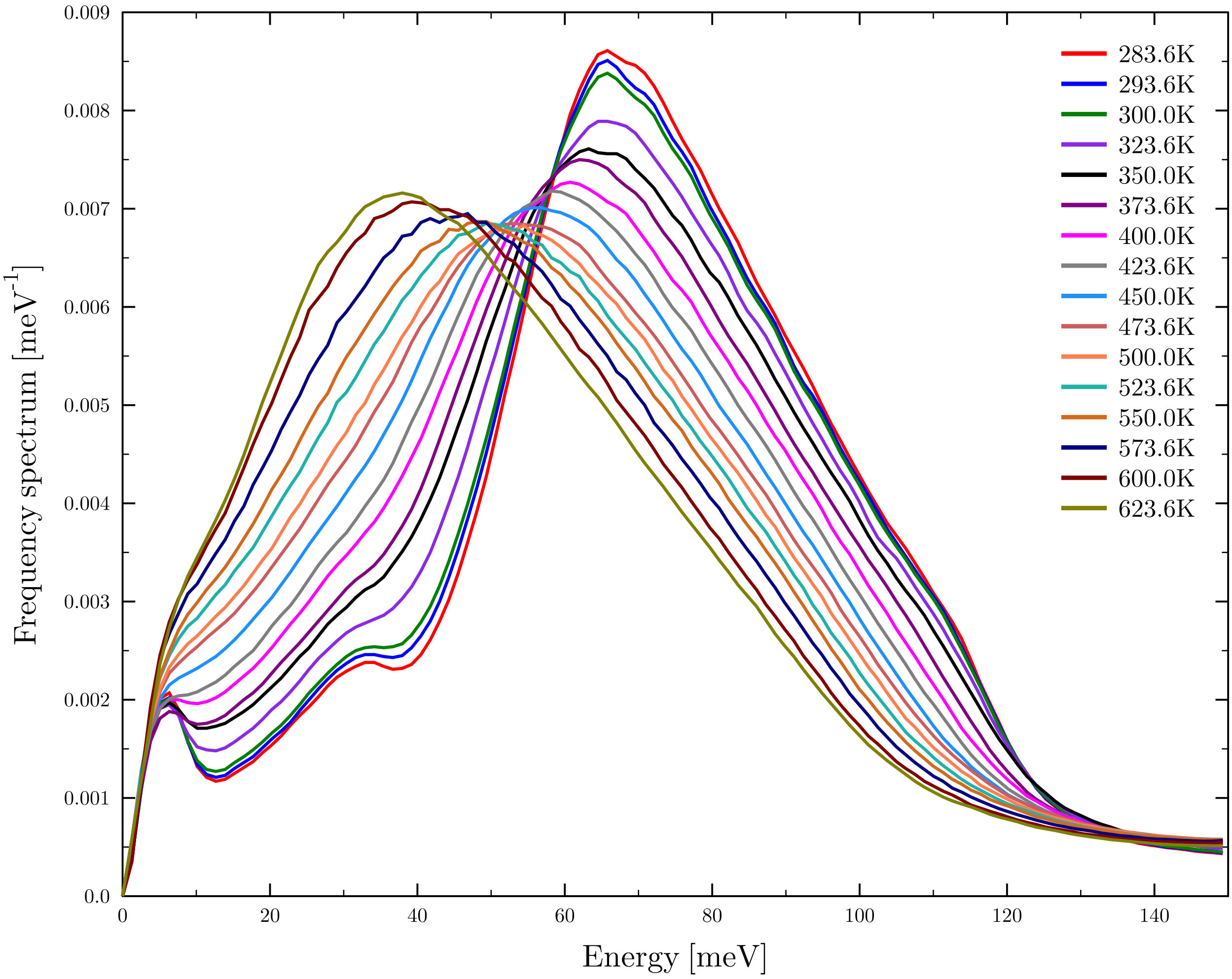

FIGURE 3.6: Frequency spectrum of light water based on the ENDF/B-VIII.0 TSL evaluation.

Temperature (K)	Translational weight (ω_t)	Diffusion constant (c)	Continuous spectrum weight (ω_c)	First osc. energy (eV)	First osc. weight	Second osc. energy (eV)	Second osc. weight
283.6	0.0069210	3.5910	0.52308	0.205	0.15667	0.415	0.31334
293.6	0.0079180	3.9690	0.52208	0.205	0.15667	0.415	0.31334
300.0	0.0084367	4.3487	0.52156	0.205	0.15667	0.415	0.31334
323.6	0.0097580	6.2865	0.52024	0.205	0.15667	0.415	0.31334

Continued on next page

Table 3.3 – continued from previous page

Temperature (K)	Translational weight (ω_t)	Diffusion constant (c)	Continuous spectrum weight (ω_c)	First osc. energy (eV)	First osc. weight	Second osc. energy (eV)	Second osc. weight
350.0	0.0111000	8.1874	0.51890	0.205	0.15667	0.415	0.31334
373.6	0.0123100	9.9389	0.51769	0.205	0.15667	0.415	0.31334
400.0	0.0136500	11.832	0.51635	0.205	0.15667	0.415	0.31334
423.6	0.0148500	13.735	0.51515	0.205	0.15667	0.415	0.31334
450.0	0.0162000	15.677	0.51380	0.205	0.15667	0.415	0.31334
473.6	0.0174000	17.023	0.51260	0.205	0.15667	0.415	0.31334
500.0	0.0187500	19.011	0.51125	0.205	0.15667	0.415	0.31334
523.6	0.0199500	20.578	0.51005	0.205	0.15667	0.415	0.31334
550.0	0.0212900	22.343	0.50871	0.205	0.15667	0.415	0.31334
573.6	0.0224900	24.612	0.50751	0.205	0.15667	0.415	0.31334
600.0	0.0238400	26.832	0.50616	0.205	0.15667	0.415	0.31334
623.6	0.0250470	29.425	0.50495	0.205	0.15667	0.415	0.31334
650.0	0.0262430	31.989	0.50376	0.205	0.15667	0.415	0.31334
800.0	0.0262430	31.989	0.50376	0.205	0.15667	0.415	0.31334

TABLE 3.3: LEAPR input parameters for ENDF/B-VIII.0 TSL evaluation for light water.

The translational weight w_c in this library is adopted by the experimental measurements of the diffusion mass, performed by Novikov [36]. Instead of a free gas molecular translation, as utilized in the IKE model, in the CAB model, the molecular translation are represented using with the Egelstaff and Schofield diffusion model [30, 37] and hence a value of $c \neq 0$ can be seen for all the temperatures. The position of the bending mode is the same as in the IKE model, i.e. 205 meV, whereas the position of the symmetric and asymmetric mode is reduced to 415 meV to have better agreement with the recent measurements performed by Lappi et al. [38].

3.1.3 Comparative study of the frequency spectrum obtained from TOF experiments and MD simulations

Figure 3.7 shows the frequency spectra of light water utilized in the evaluation of ENDF/B-VIII.0 TSL library. This spectrum is obtained from MD simulations with the GROMACS code using the TIP4P/2005f flexible water potential. These spectra are specifically plotted within the energy range of 10 meV - 100 meV to emphasize the thermal energy region sensitive to reactor physics applications. An interesting observation that can be made from this figure is that, the energy of the rotational band, centered around 65 meV at room temperature, shifts towards lower energies with increasing temperature. This shift is strong for higher temperatures, i.e., the peak of the rotation band which is observed at 65 meV at 293.6 K, shifts to around 35 meV at 623.6 K. The latter temperature is close to reactor operating temperature. Such a strong down shift in energy of the rotation band with increasing temperature, draws our attention to investigate this behavior, in order to correctly generate

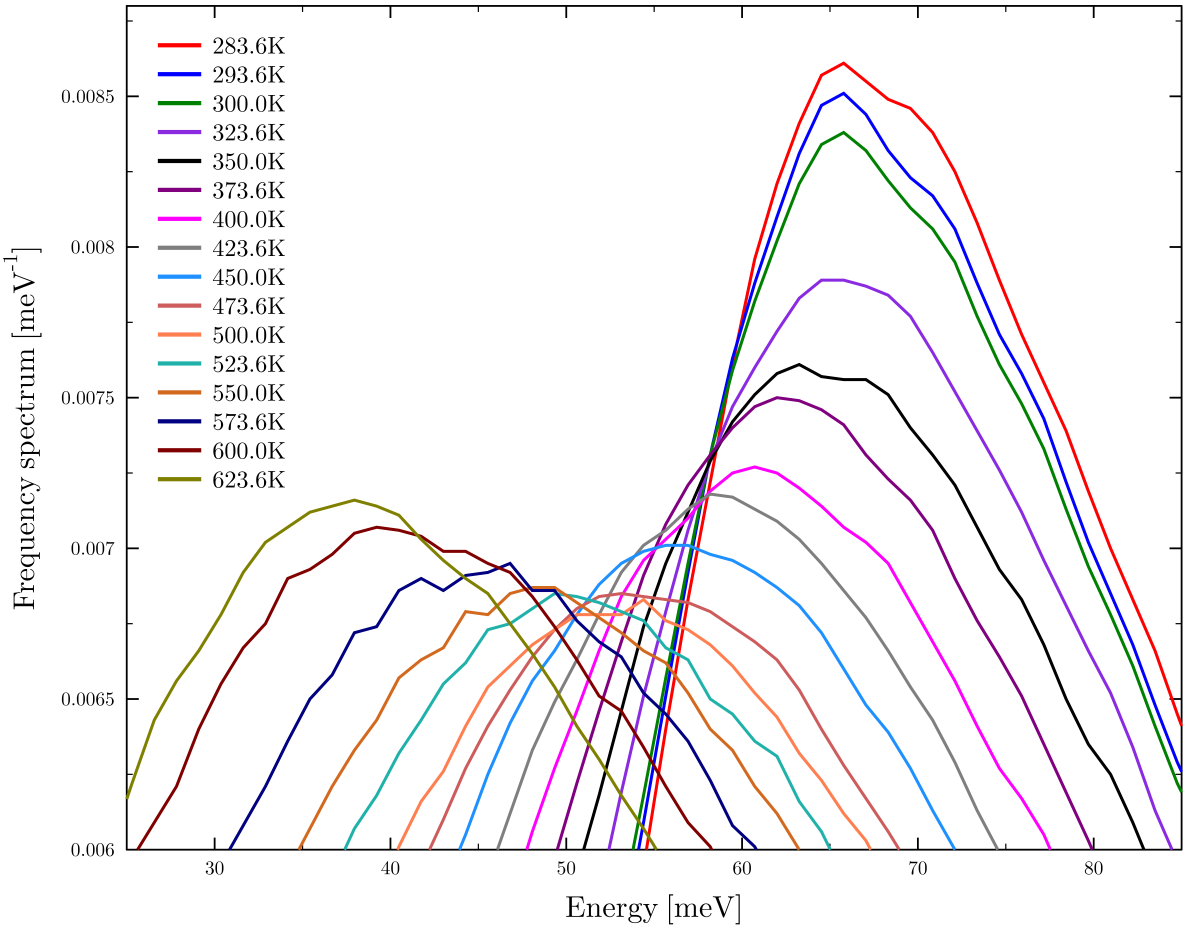

FIGURE 3.7: Variation in the energy of rotation band in the frequency spectrum of light water based on the ENDF/B-VIII.0 TSL evaluation.

the TSL at high temperatures. This shift is not in agreement with the existing experimental data of frequency spectrum of light water [20, 21], used to generate the present JEFF-3.3 TSL library.

A literature review of the existing experimental TOF data for light water was carried out. It was found out that among the available data in the literature most of them are for room temperatures. Very few data at high temperature exist, like the one in Ref. [21, 39, 40, 41, 42]. Significant work was done in 1971 by Esch et al. to develop thermal scattering models for light water based on double differential cross section measurements at the RPI linear electron accelerator [39]. Figure 3.8 represents the frequency spectrum of light water based on several

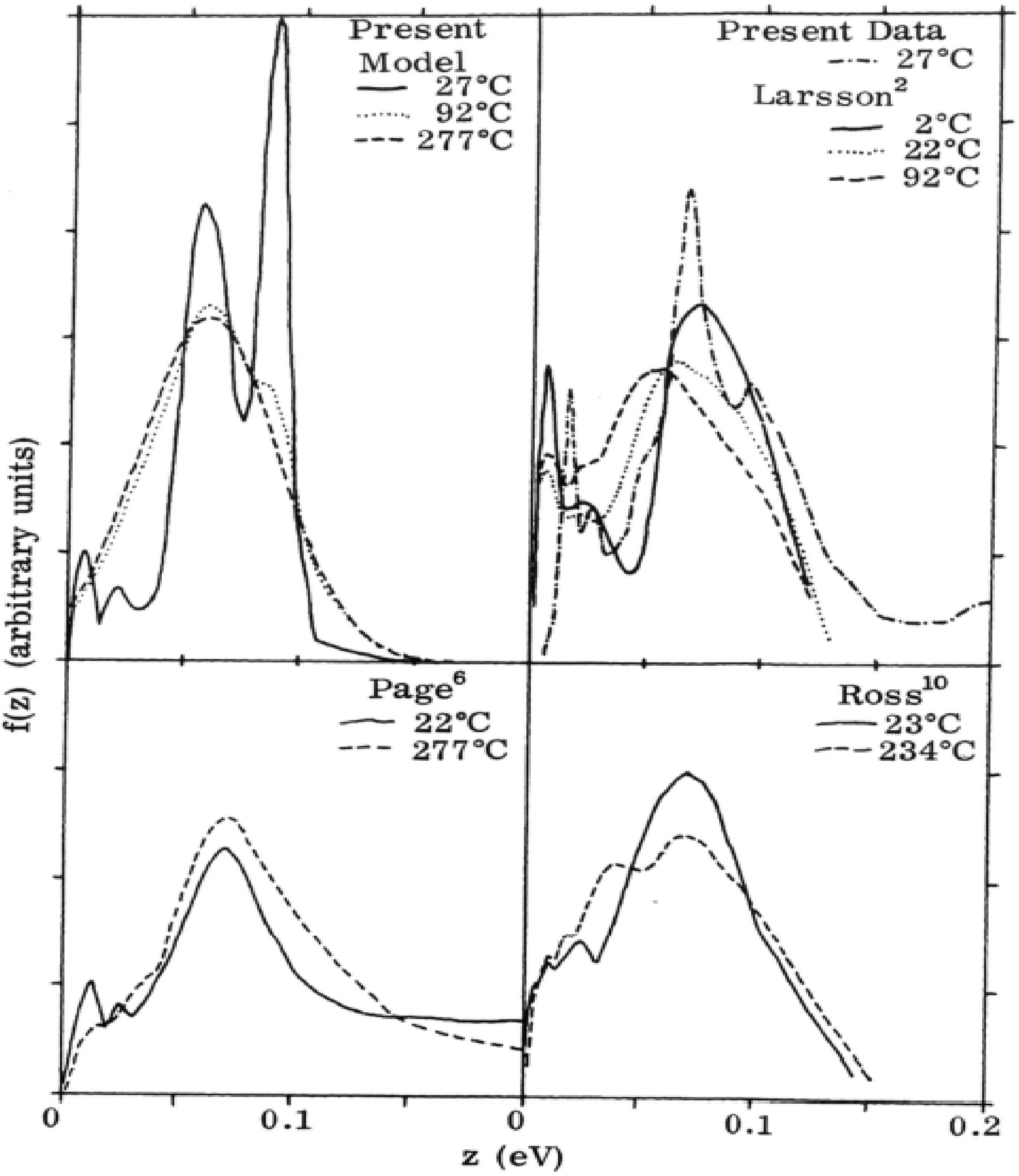

FIGURE 3.8: Frequency spectrum of light water at room and high temperature obtained from several experiments and physical models. This curve has been taken from Ref. [39].

experiments and models developed in the past. The x-axis (z(eV)) corresponds to the energy transfer in eV, whereas y-axis (f(z)), is the frequency spectrum in arbitrary units. In the top left part of the figure, a slight down shift in energy of the rotation band is observed with increasing temperature. The top right part in this figure shows the measurements carried out by Larsson and Dahlborg and the frequency spectrum is shown for 275.15 K, 295.15 K and 365.15 K [40]. The bottom right part in this figure is the experimental frequency spectrum derived by Ross et al. for 296.15 K and 507.15 K [42]. In all these experiments, the position of the rotation band lies around 60 meV - 75 meV, even at high temperatures.

To our knowledge the most recent TOF experimental data for light water at high temperature, available in the literature is the one by Novikov et al. [36]. In this work, TOF experiments for light water were performed at 300, 400, 500 and 600 K. The frequency spectrum derived from this measurement is shown in Fig. 3.9. As seen

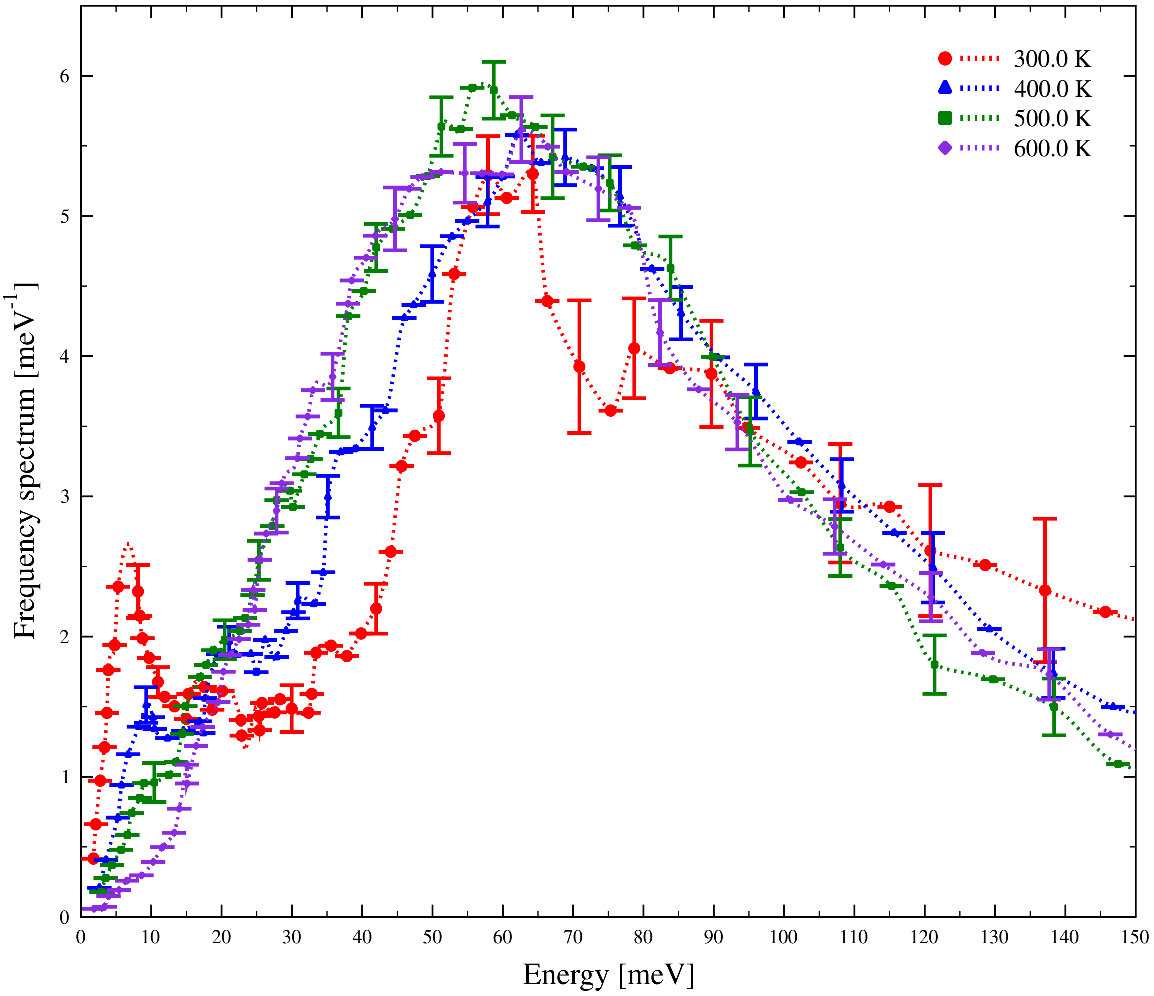

FIGURE 3.9: Frequency spectrum of light water measured by the TOF experiments of Novikov *et al.* [36].

before, even this experimental data is in agreement with all the previous measurements of the frequency spectra of light water in terms of the shape of the spectrum and position of the rotation band.

All the experiments mentioned so far in this work are in clear opposition with the CAB model prediction capability at higher temperature than 300 K. Hence, in an overall comparison between the frequency spectrum obtained from the experiments and MD simulations, it can be concluded that there is a need to investigate the behavior of MD simulations especially at high temperatures. It can be linked to the fact that MD simulations are based on interaction potentials [35] that are parametrized to simulate bulk water properties at room temperature. A flexible water potential, like the one used in ENDF/B-VIII.0, partially accounts for the polarization of the water. Though, it might provide convincing results at room temperature and pressure but fails to mimic the properties of water at high temperatures and pressure in agreement with the experiments [34]. Figure 3.10 demonstrates the effectiveness of MD simulations at room temperature. The translation band is visible in the

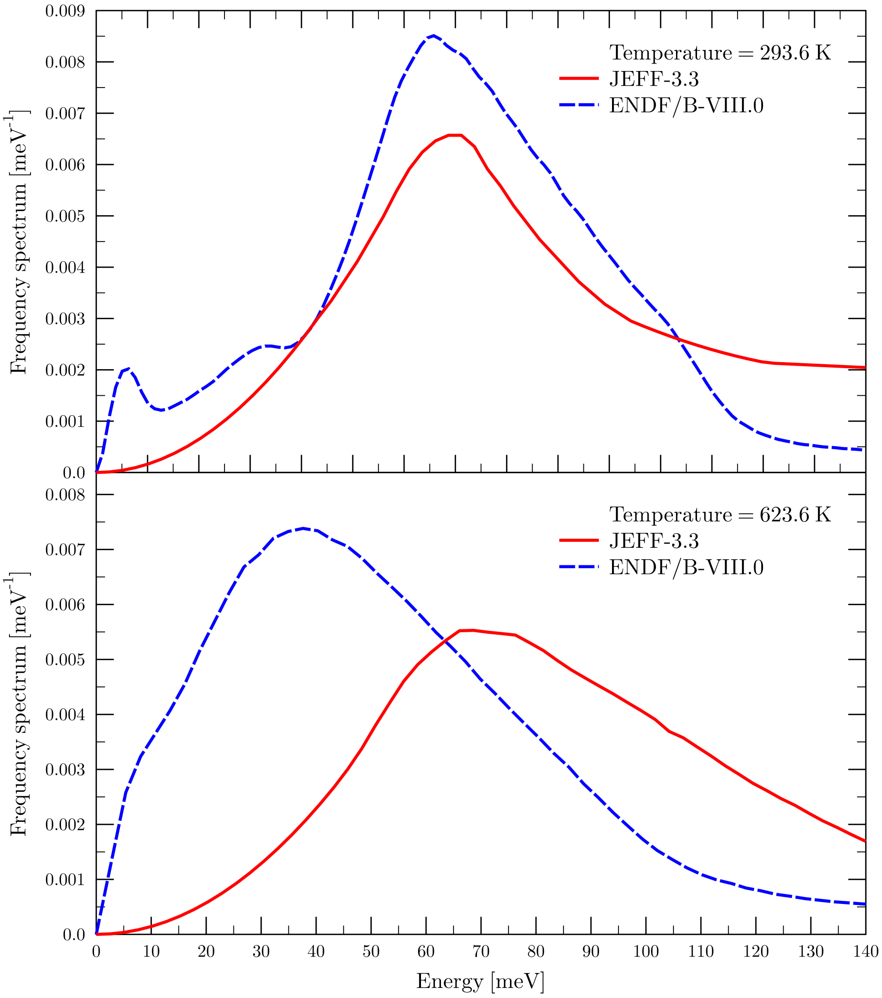

FIGURE 3.10: Frequency spectrum of light water based on the JEFF-3.3 and ENDF/B-VIII.0 at 293.6 K (top) and 623.6 K (bottom).

293.6 K frequency spectrum of ENDF/B-VIII.0 which is missing in the JEFF-3.3 spectrum. Also, the energy of the rotation band lies roughly around same peak position at 293.6 K. However, when one observes the frequency spectrum at 623.6 K utilized by both ENDF/B-VIII.0 and JEFF-3.3, the translation band is not visible in both the evaluations and the rotation band of the ENDF/B-VIII.0 shifts to lower energies. A direct comparison of the MD result with the experimental data at high temperatures and pressures is important for the validation of these observations and thus MD simulations and the water model/potential used.

3.2. TSL evaluations for light water in the JEFF-3.3 and ENDF/B-VIII.0 library

The previous section describes the different methodology adapted for generating TSL evaluations for light water. In this section, attention will be focused on the latest TSL evaluations for light water in JEFF-3.3 and ENDF/B-VIII.0 of ENDF/B. A comparative study of the frequency spectrum utilized by both these evaluations have been discussed in the previous section. Also, it is worth mentioning again that ENDF/B-VIII.0 uses Egelstaff and Schofield diffusion model and JEFF-3.3 relies on the free gas model to model the molecular diffusion at low energy transfers. However, both these evaluations utilizes harmonic oscillators to model the bending and the stretching mode of the frequency spectrum at somewhat similar energies. The impact of TSL data on nuclear systems at thermal energies do not have significant impact at higher energy transfers and both these TSL evaluations do not differ much in this energy region. But, at thermal and cold neutron energy region both these model differ significantly. It is worth observing the shape of the TSL data to observe the differences in these two evaluations. TSL data, i.e. $S(\alpha, \beta)$ is generally a matrix that defines the scattering process as a function of momentum transfer α and energy transfer β. A comparison of the $S(\alpha, \beta)$ at 293.6 K as a function of α for both JEFF-3.3 and ENDF/B-VIII.0 TSL evaluation is presented in Fig. 3.11. Several β values are chosen to demonstrate the difference, especially low beta values (<7.5 meV) corresponding to an energy transfer of around 190 meV below which the two models differ significantly. At high energy transfers (high β) both the evaluations rely on the same model, i.e. discrete oscillators at nearly same energies and hence the shape of the $S(\alpha, \beta)$ do not differ much. Figure 3.11 clearly indicates that both the JEFF-3.3 and ENDF/B-VIII.0 differ significantly at low energy transfers (β < 0.1) since ENDF/B-VIII.0 uses Egelstaff and Schofield diffusion model and JEFF-3.3 relies on the free gas model to define molecular diffusion at low energies. However, this difference reduces at high energy transfers (β >2.5). For instance, β around 2.5, corresponds to an energy transfer associated to the

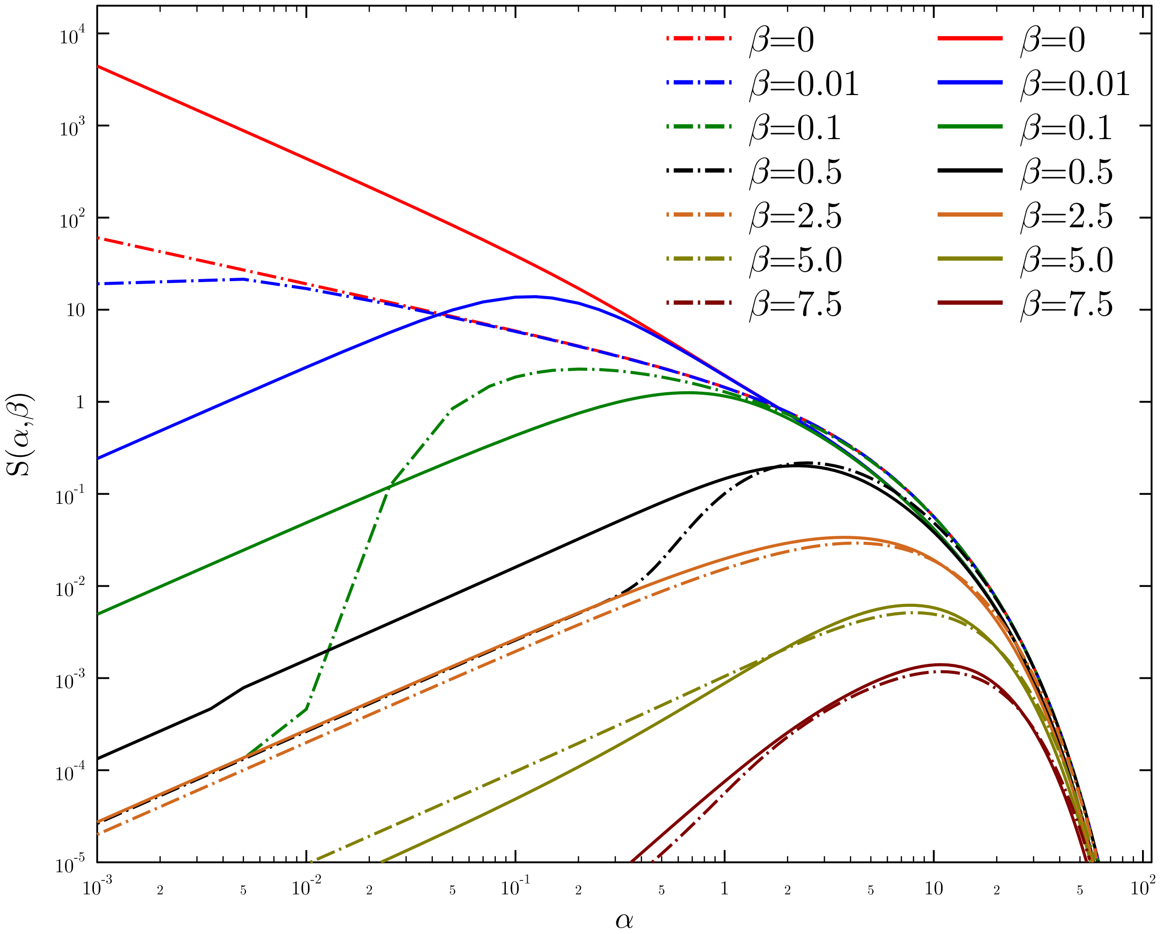

FIGURE 3.11: $S(\alpha, \beta)$ at 293.6 K as a function of α for different β values. The solid lines represent the ENDF/B-VIII.0 TSL evaluation whereas the dotted lines represent the JEFF-3.3 TSL evaluation for light water.

rotational motion of the water molecule. A small difference in this energy region is due to the peak position of the energy of the rotation band in the frequency spectrum utilized by JEFF-3.3 and ENDF/B-VIII.0 at 293.6 K as discussed in the previous section.

To see the impact of the $S(\alpha, \beta)$ at high temperature (close to reactor operating temperature), a comparison of the $S(\alpha, \beta)$ at 573.6 K as a function of α for both JEFF-3.3 and ENDF/B-VIII.0 TSL evaluation is presented in Fig. 3.12. As compared to Fig. 3.11 the differences in the $S(\alpha, \beta)$ at low β value (β <0.1) between JEFF-3.3 and ENDF/B-VIII.0 reduces as the impact of molecular diffusion on the TSL at high energies are low. However, for β>0.1 the overall differences in the shape of the $S(\alpha, \beta)$ increases due to the difference in the position of the rotation band in the frequency spectrum between both the evaluations at 573.6 K. A thorough investigation is further necessary to observe the impact of these evaluations by comparing it with double differential and total scattering cross sections that will be discussed in the following sections.

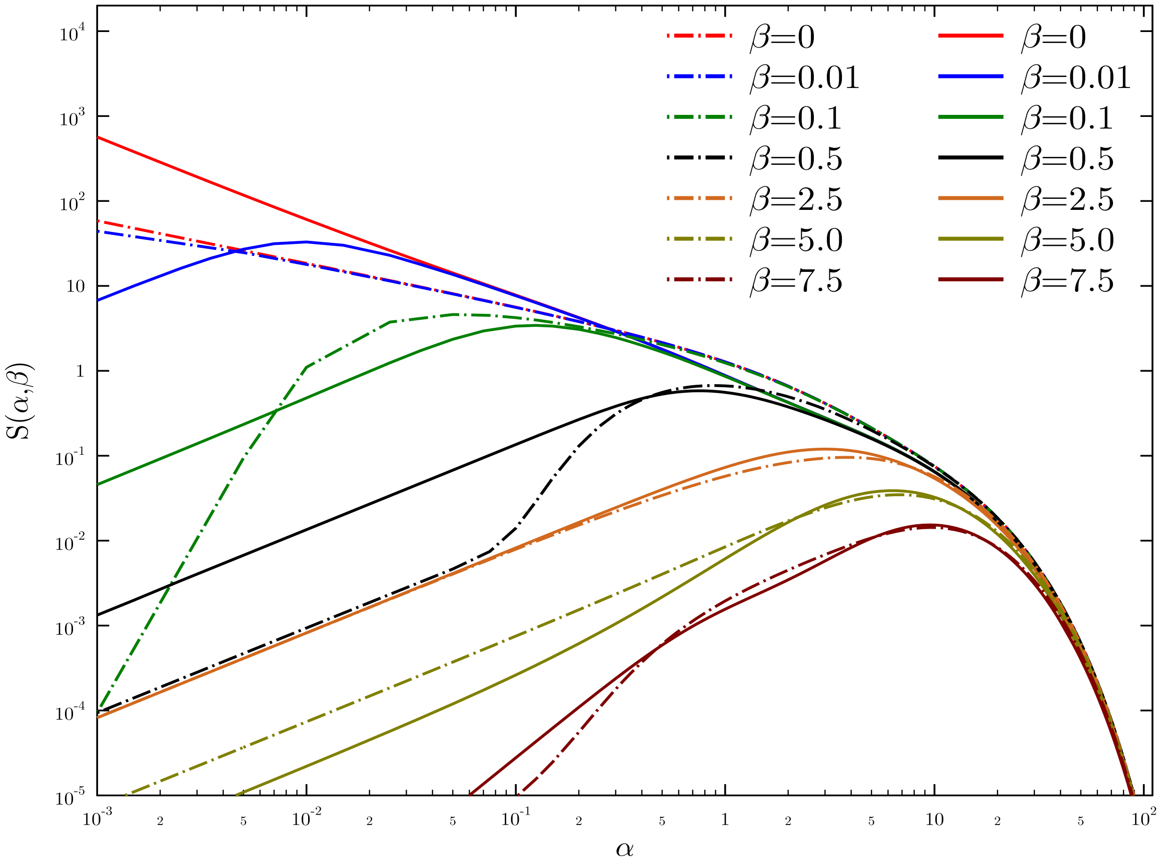

FIGURE 3.12: $S(\alpha,\beta)$ at 573.6 K as a function of α for different β values. The solid lines represent the ENDF/B-VIII.0 TSL evaluation whereas the dotted lines represent the JEFF-3.3 TSL evaluation for light water.

3.3. Impact of TSL evaluations on the double differential cross section of light water

The double differential cross section is calculated based on Eq. 3.1 using $S(\alpha,\beta)$ from JEFF-3.3 and ENDF/B-VIII.0 TSL evaluations at room temperature and compared with a series of experimental data.

$$\frac{d^2\sigma}{d\Omega dE'} = \frac{\sigma_b}{4\pi k_B T}\sqrt{\frac{E'}{E}}S(\alpha,\beta) \tag{3.1}$$

The double differential cross sections obtained using TSL evaluations are free from resolution effects. A direct comparison of the experimental data with the derived double differential cross section from the TSLs cannot be achieved unless the experimental resolution effects are convoluted on the calculations as the experimental data are limited by the experimental resolution. For instance, the quasi-elastic peak in the experimental double differential data is broadened due to the resolution of the experiment. The appropriate resolution function of the TOF spectrometer is approximated by a Gaussian function. The standard deviation of the Gaussian function was estimated from the knowledge of the experimental resolution available in the literature.

As a matter of explanation, it should be emphasized that the double differential cross section is a function of the secondary energy of the neutrons in the laboratory system after scattering with the target. It should not be confused with the energy exchange between the neutron and the scattering target as is the case with some authors to represent the double differential experimental data [33]. In the case where the double differential cross section is represented as a function of the energy transfer $\hbar\omega$, the final energy E' must be obtained as a subtraction of the incident energy E from $\hbar\omega$. The comparison of double differential data with the experimental data presented in this work is expressed as a function of scattered neutron energy E'.

Double differential data were calculated for an incident neutron energy of 154 meV and 231 meV, using $S(\alpha, \beta)$ from JEFF-3.3 and ENDF/B-VIII.0 TSL evaluations at room temperature. Two scattering angles were chosen in each case, i.e. θ = 14 $^\circ$ and θ = 25 $^\circ$. The results are displayed in Fig. 3.13, 3.14, 3.15 and 3.16, compared with measurements carried out by Bischoff et al. in 1967 [43]. The resolution of this experimental data were approximated to be around 5%.

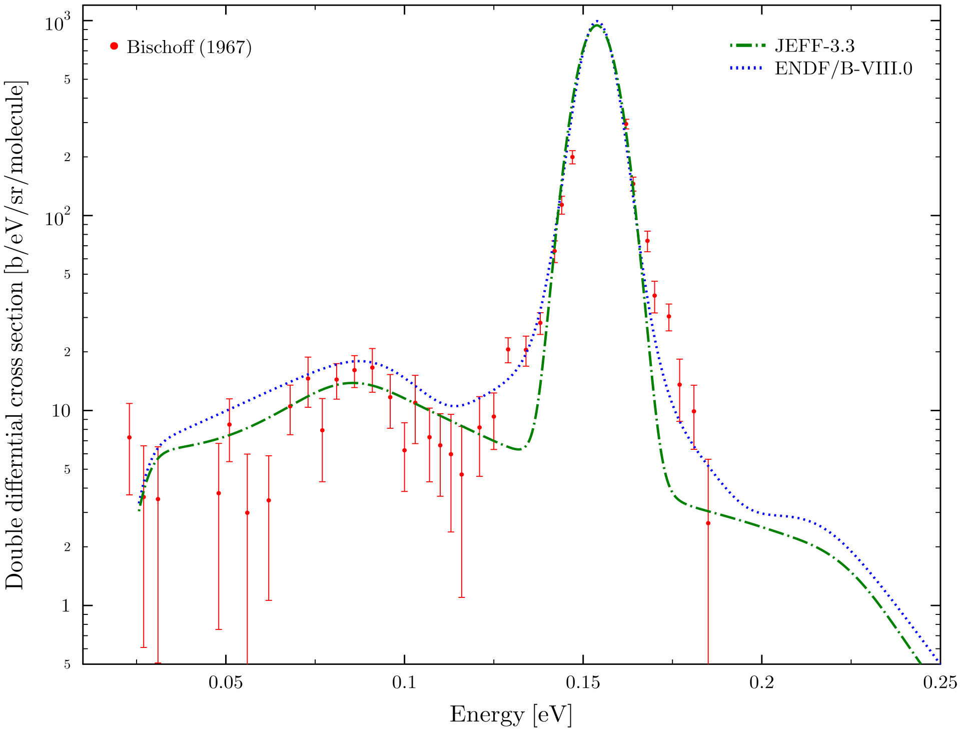

FIGURE 3.13: Double differential scattering cross section of light water at incident energy $E = 154$ meV and scattering angle θ=14°.

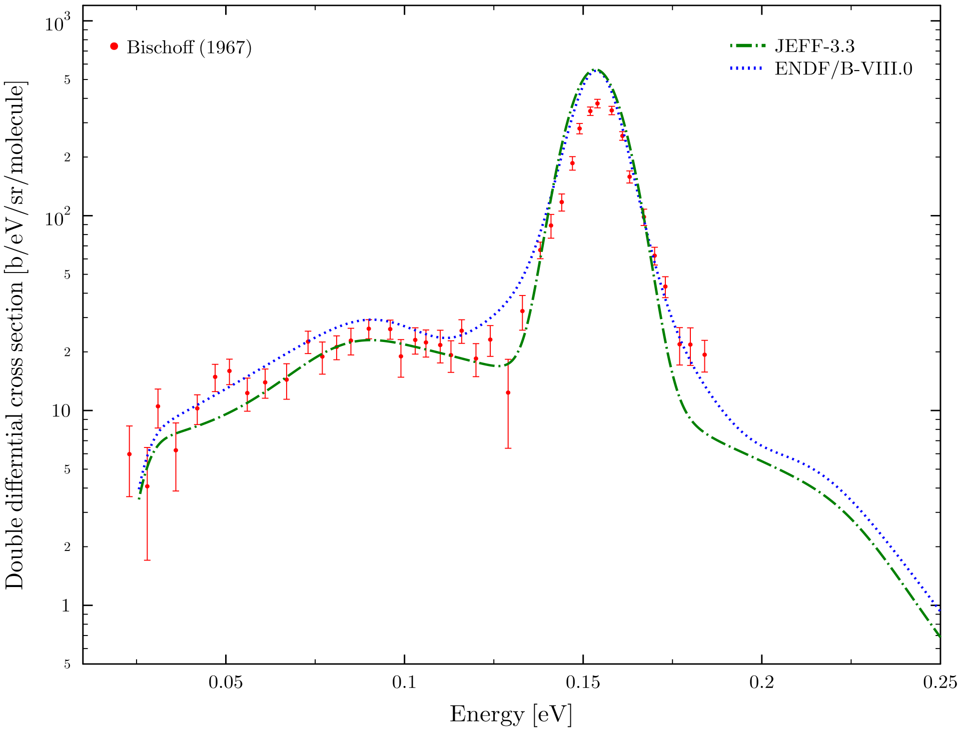

FIGURE 3.14: Double differential scattering cross section of light water at incident energy $E = 154$ meV and scattering angle θ=25°.

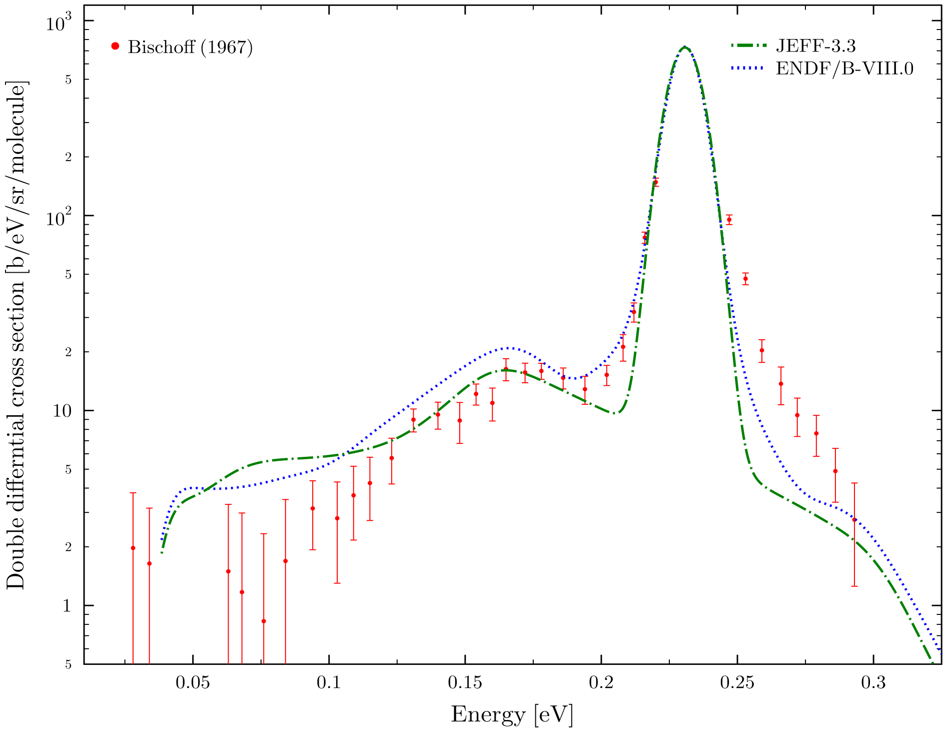

FIGURE 3.15: Double differential scattering cross section of light water at incident energy $E = 231$ meV and scattering angle θ=14°.

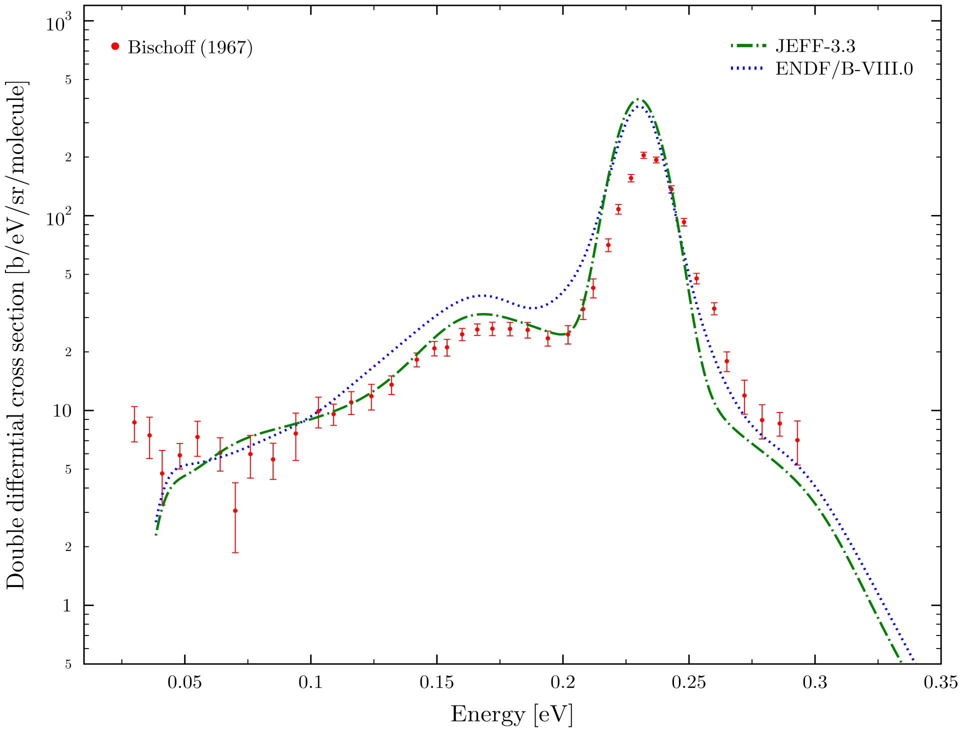

FIGURE 3.16: Double differential scattering cross section of light water at incident energy $E = 231$ meV and scattering angle θ=25°.

Another measurement carried out by Harling [44] are used to compare the double differential cross section obtained using JEFF-3.3 and ENDF/B-VIII.0 TSL evaluations. Double differential data were calculated for an incident neutron energy of 151 meV and two scattering angle θ = 15 ° and θ = 32 °. The results are displayed in Fig. 3.17 and 3.18, for θ = 15 ° and θ = 32 °, respectively and compared with measurements by Harling. Another calculation was carried out with incident neutron energy of 305 meV and and two scattering angle θ = 15 ° and θ = 30 °. The results are shown in Fig. 3.19 and 3.20, for θ = 15 ° and θ = 30 °, respectively.

The evaluations describe the experimental data reasonably well in all the comparisons. Due to lack of experimental double differential data of light water a comparison with high temperature TSL was not carried out. All the comparisons performed in this section show that both the evaluations perform reasonably well for the chosen incident energies and scattering angle. However, in some cases the ENDF/B-VIII.0 TSL evaluation showed improved results. The next step is to compare the total scattering cross section obtained using TSL evaluations with available experimental data. Also, a detailed review of both these evaluations is necessary at both room temperature and high temperature, that will be discussed in the next section.

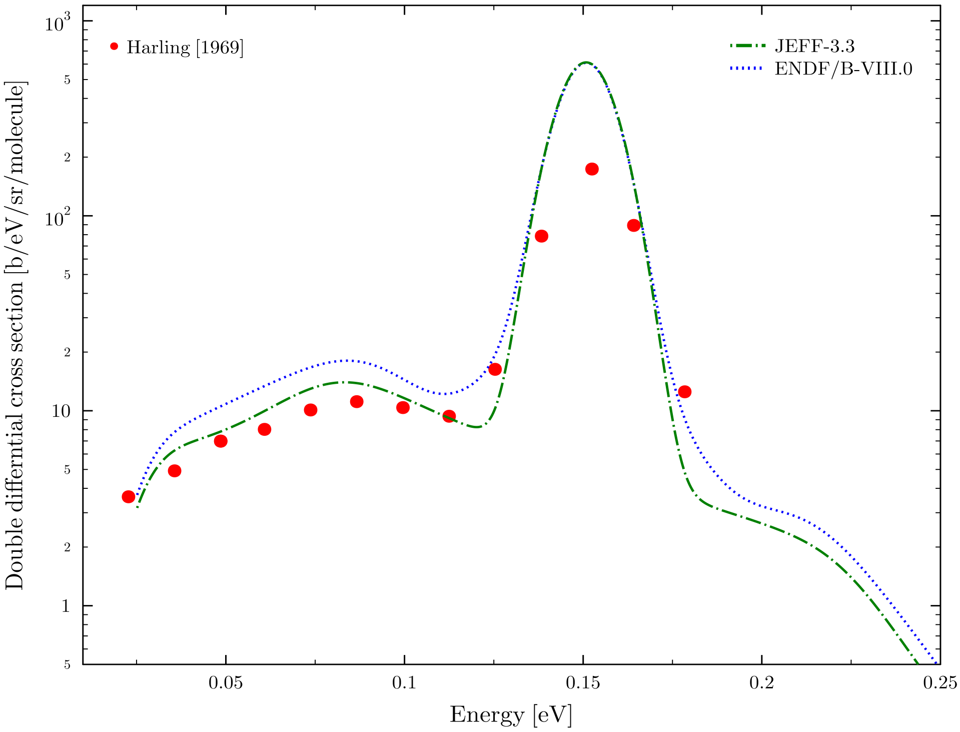

FIGURE 3.17: Double differential scattering cross section of light water at incident energy $E = 151$ meV and scattering angle θ=15°.

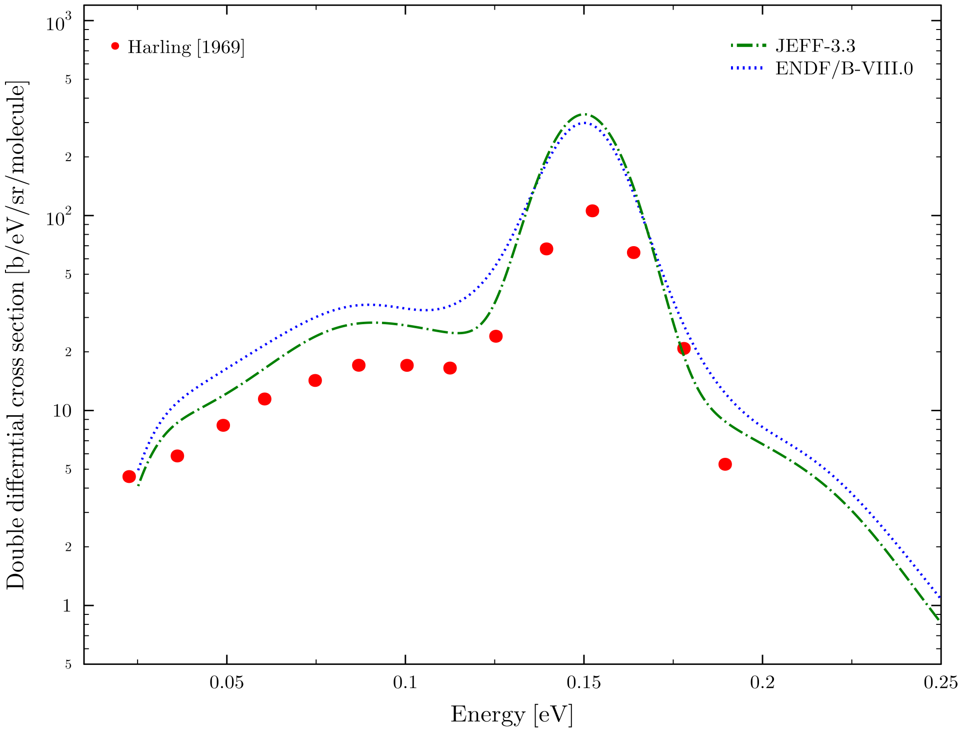

FIGURE 3.18: Double differential scattering cross section of light water at incident energy $E = 151$ meV and scattering angle θ=32°.

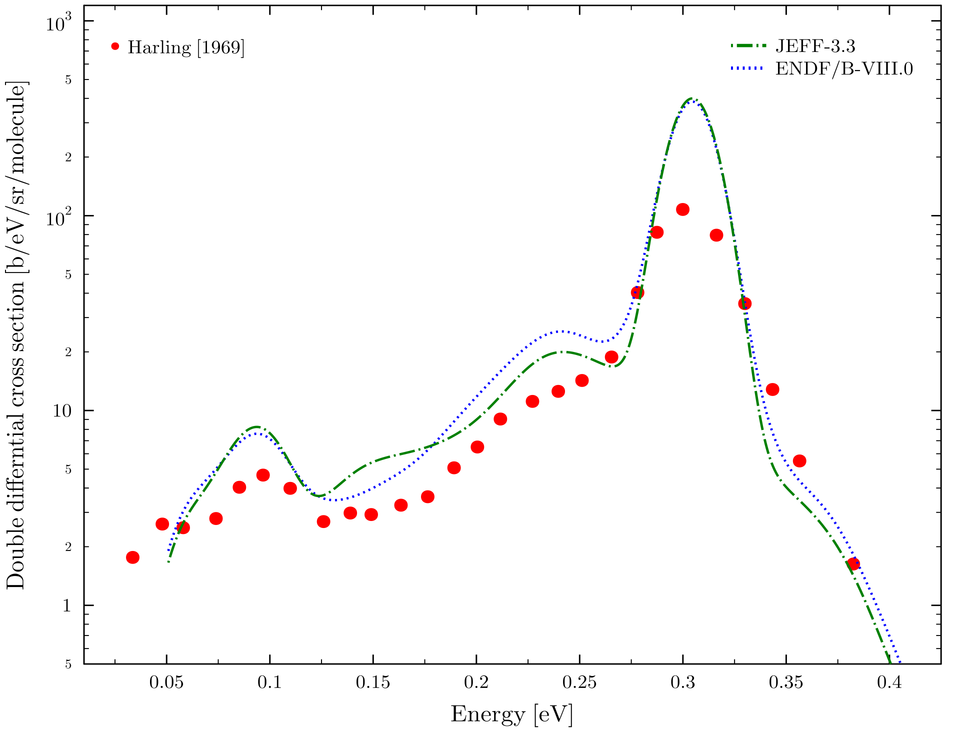

FIGURE 3.19: Double differential scattering cross section of light water at incident energy $E = 305$ meV and scattering angle θ=15°.

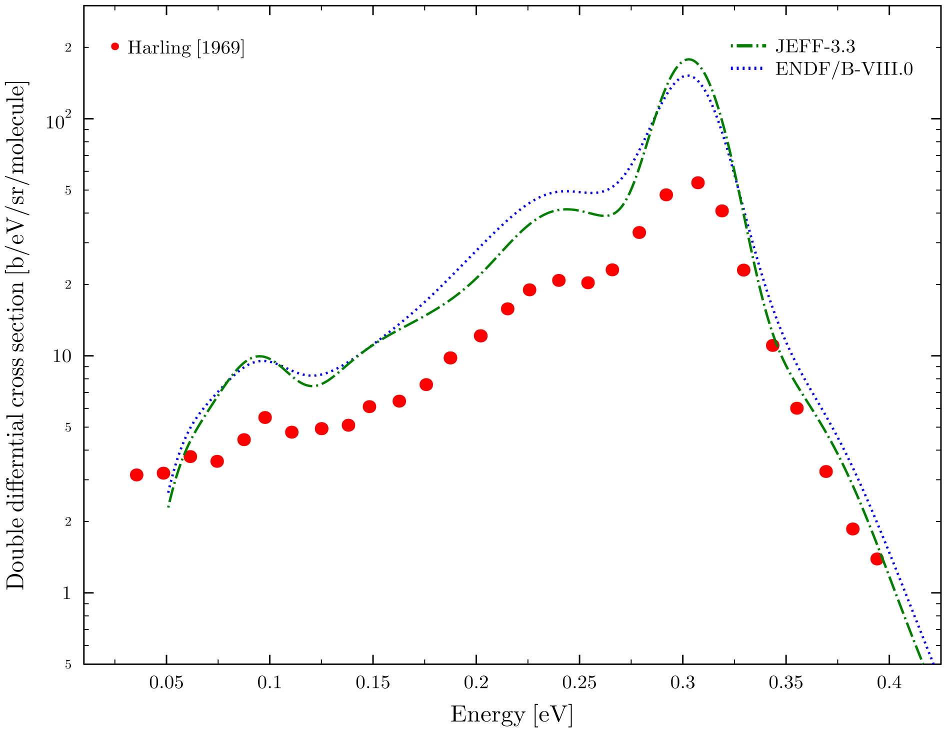

FIGURE 3.20: Double differential scattering cross section of light water at incident energy $E = 305$ meV and scattering angle θ=30°.

3.4. Impact of TSL evaluations on the total cross section of light water

Several TSL evaluations for light water are chosen to demonstrate the impact of TSL on total scattering cross sections. Special attention is given on the high temperature data so as to investigate the behavior of existing TSLs for light water at high temperatures. The impact of the shape of the frequency spectrum particularly at high temperatures is addressed.

The total scattering cross-section for light water has been computed using the TSL and the THERMR module of the NJOY code. The oxygen cross section is treated as a free gas. The total scattering cross-section is obtained in the following manner:

$$\begin{aligned}\sigma_{(H_2O),t} = 2 \times \Big(\sigma_{H,s} + \sigma_{H,\gamma}\Big) \\ + \Big(\sigma_{O,t}\Big)\end{aligned} \tag{3.2}$$

Here, $\sigma_{(H_2O),t}$ is the total scattering cross section of light water. $\sigma_{H,s}$ and $\sigma_{H,\gamma}$ are the inelastic scattering cross section and capture cross section of hydrogen, respectively. $\sigma_{O,t}$ is the total cross section of oxygen.

3.4.1 Total cross section based on free gas TSL model

The effect of the atoms bound in the molecules on the cross section is governed by $S(\alpha, \beta)$. Light water in the liquid state, can also be approximated by a scattering law assuming it to be free gas. The free gas TSL, $S_{FG}(\alpha, \beta)$ can be given by Eq. 2.41. The total cross section of light water in the thermal energy range can be approximated using $S_{FG}(\alpha, \beta)$ for hydrogen bound in water molecule. The free gas total cross section for light water at room temperature is given in Fig. 3.21. Figure 3.21 shows the total cross section of light water based on free gas model at high temperatures, i.e. between 323.6 K and 623.6 K in steps of 50 K. The bottom part in this figure, is the ratio of the cross section w.r.t. 323.3 K data. One can see that the ratio of the cross sections increases with increasing temperature in the thermal region and converges to the free gas scattering cross section of light water. This observation is in agreement with the fact that cross sections in the thermal energy range increase with increasing temperatures due to an increase in the probability of up scattering.

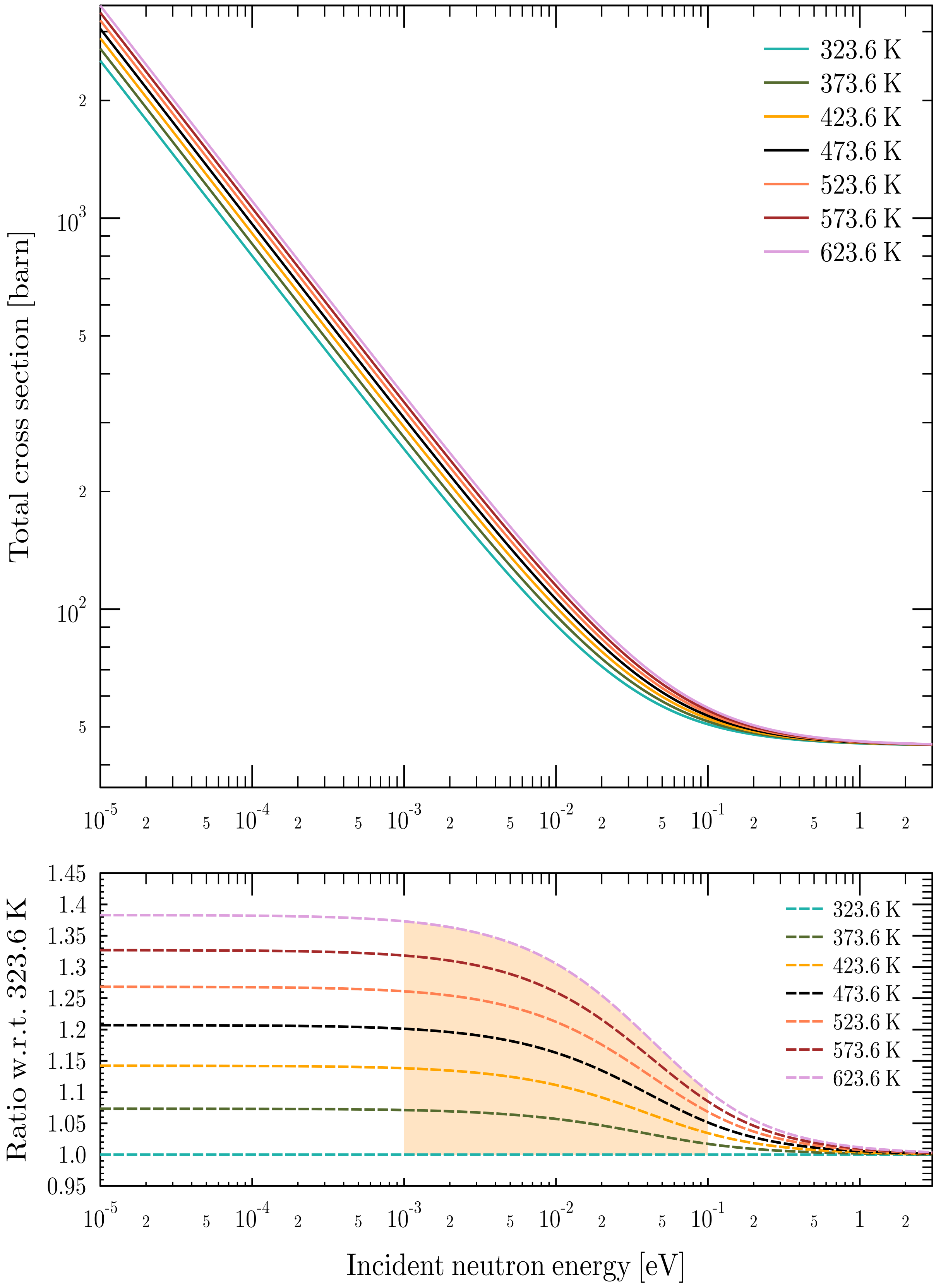

FIGURE 3.21: Temperature dependence of the free gas model on the total cross section of light water.

3.4.2 Total cross section based on JEFF-3.1.1 and ENDF/B-VII.1 TSL evaluation

In this section the total cross section of light water obtained from JEFF-3.1.1 and ENDF/B-VII.1 TSL evaluations are compared. This type of comparison served an initial hint about the impact of the position of the rotation band in the frequency spectrum on the total cross section.

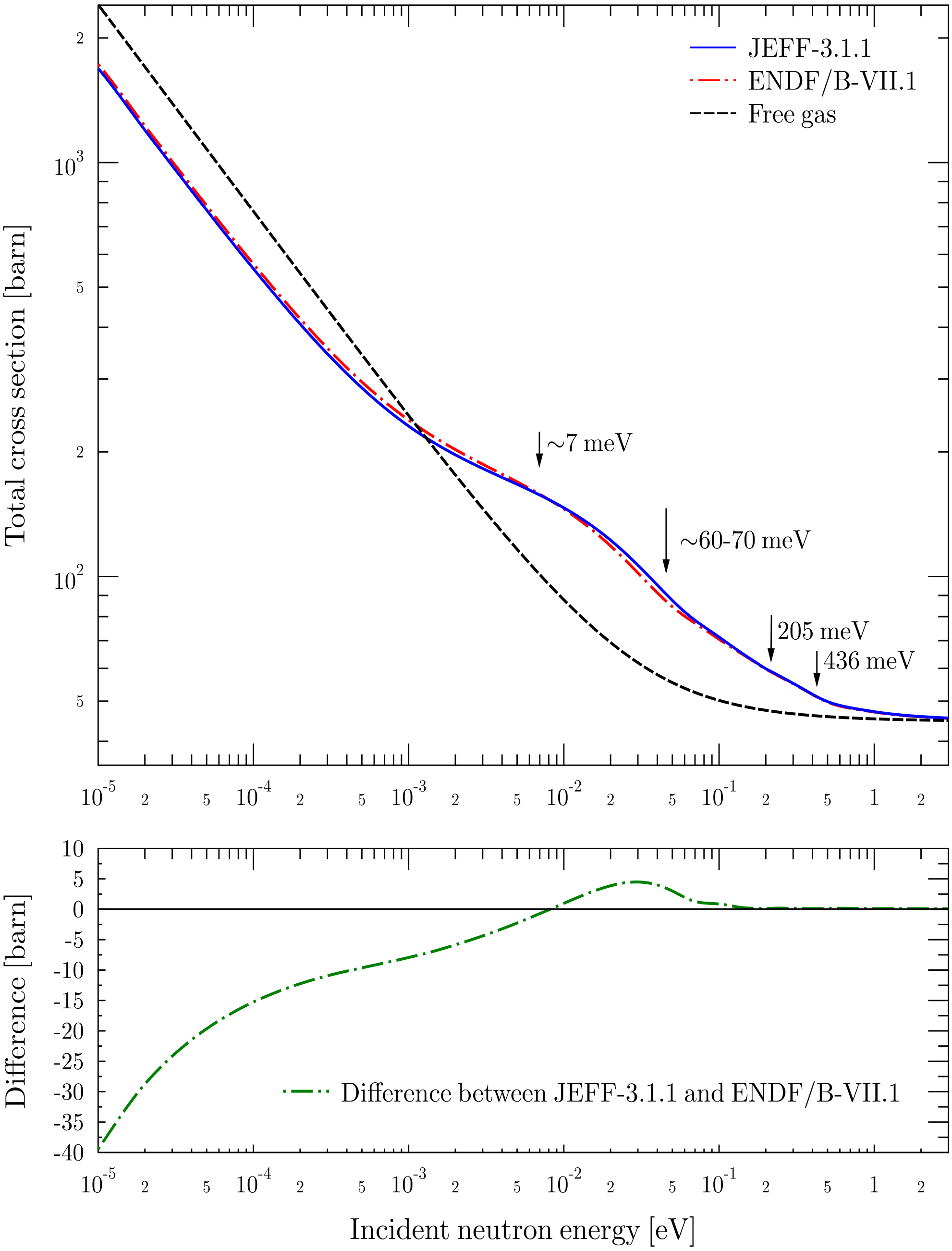

FIGURE 3.22: Comparison of the total cross section of light water based on JEFF-3.1.1 and ENDF/B-VII.1 TSL evaluations.

As seen in Fig. 3.4, the rotation band in the frequency spectrum of ENDF/B-VII.1 was shifted to lower energy. This shift affects the total cross section as can be seen in the top part of Fig. 3.22 marked by arrow pointing towards 60-70 meV. Both evaluations perform somewhat similar in the thermal energy range (with a difference of around 5 barn) whereas this difference is larger in the very low neutron energy range (around 40 barn).

3.4.3 Comparative study of the total cross section based on JEFF-3.3 and ENDF/B-VIII.0 TSL evaluation at room temperature

Figures 3.23 and 3.24 represent the total cross section of light water obtained from JEFF-3.3 and ENDF/B-VIII.0 TSL evaluation at 293.6 K. The solid line in red is based on JEFF-3.3 whereas the dotted line in blue is based on ENDF/B-VIII.0. The plots at the bottom of both these figures show the relative difference (barn) in the total cross section obtained from both these TSL evaluations. These two evaluations differ significantly (around 600 barn) in the low energy range where the molecular diffusion effect is dominant, while the difference is small in the thermal energy range at room temperature. When these evaluations are compared with the EXFOR experimental data in Fig. 3.23, one observes that the ENDF/B-VIII.0 TSL evaluation performs better in the low neutron energy range and has an excellent agreement with the EXFOR experimental total cross section data. This highlights the impact of using the Egelstaff and Schofield diffusion model to describe molecular diffusion.

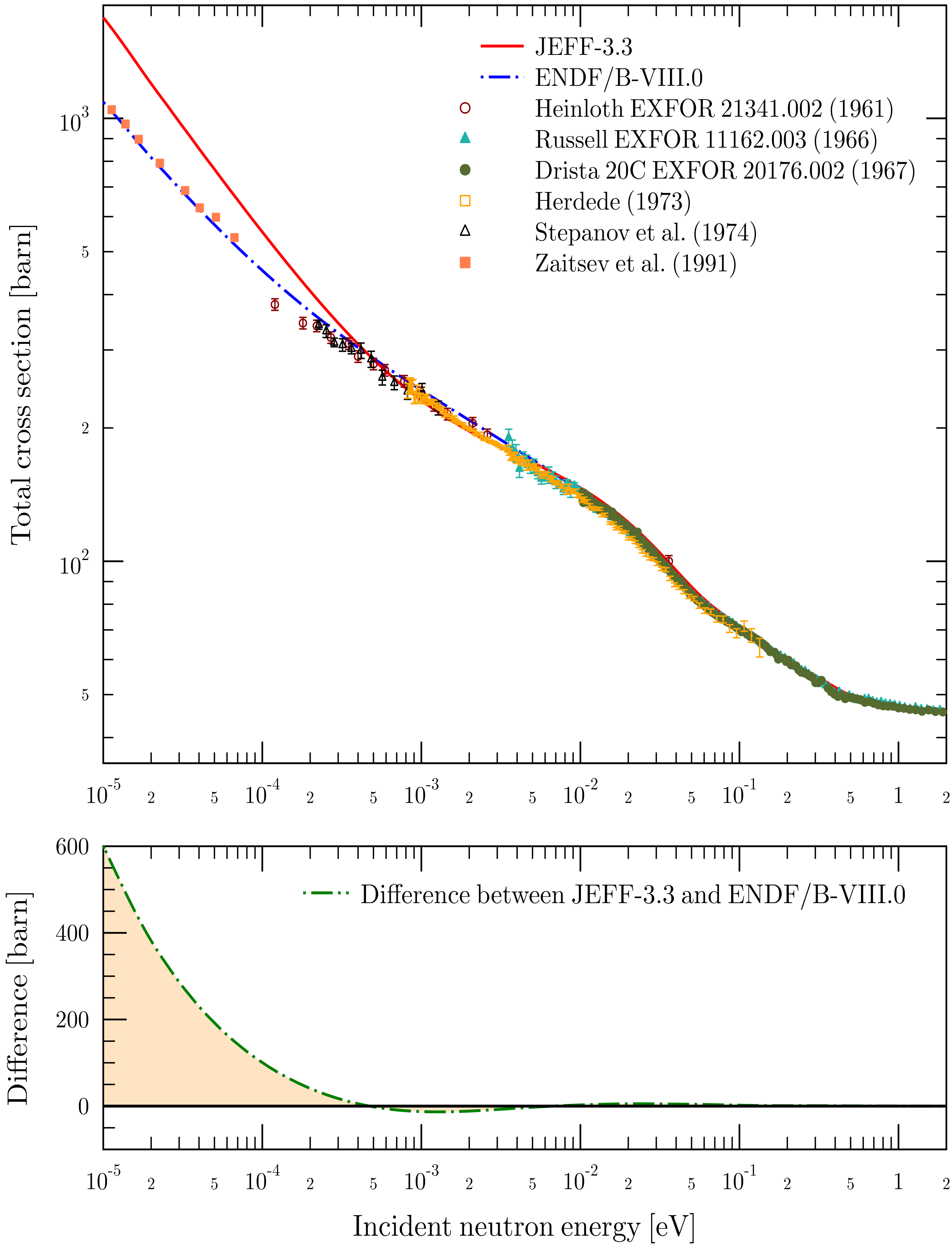

FIGURE 3.23: Comparison of the total cross section of light water at 293.6 K based on JEFF-3.3 and ENDF/B-VIII.0 TSL evaluations along with EXFOR experimental data.

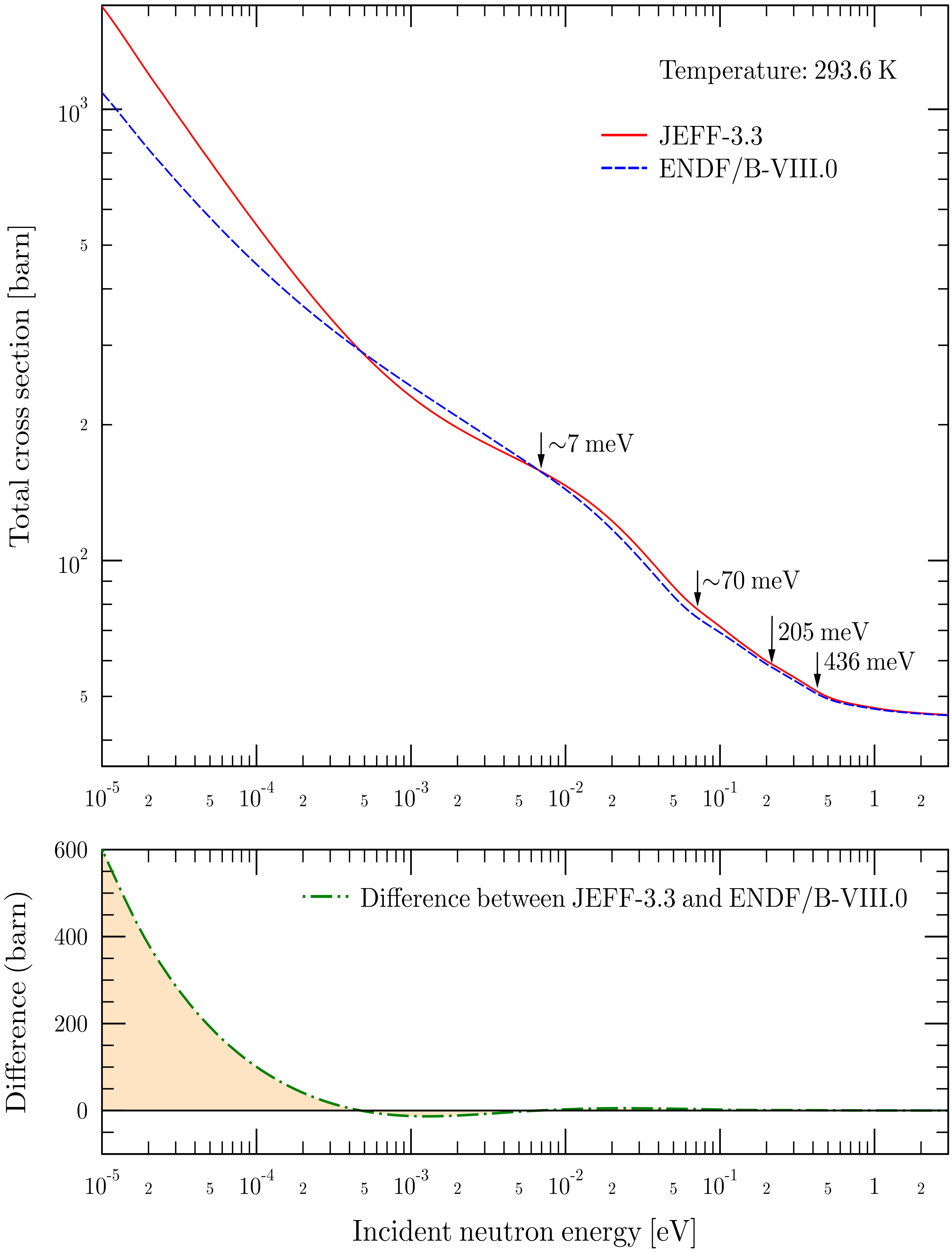

FIGURE 3.24: Comparison of the total cross section of light water at 293.6 K based on JEFF-3.3 and ENDF/B-VIII.0 TSL evaluations.

3.4.4 Total cross section based on JEFF-3.3 TSL evaluation at high temperatures

The total cross section for light water based on the JEFF-3.3 TSL evaluation is given in Fig. 3.25. The cross sections are plotted for a series of temperatures starting from room temperature, i.e. 293.6 K up to 623.6 K.

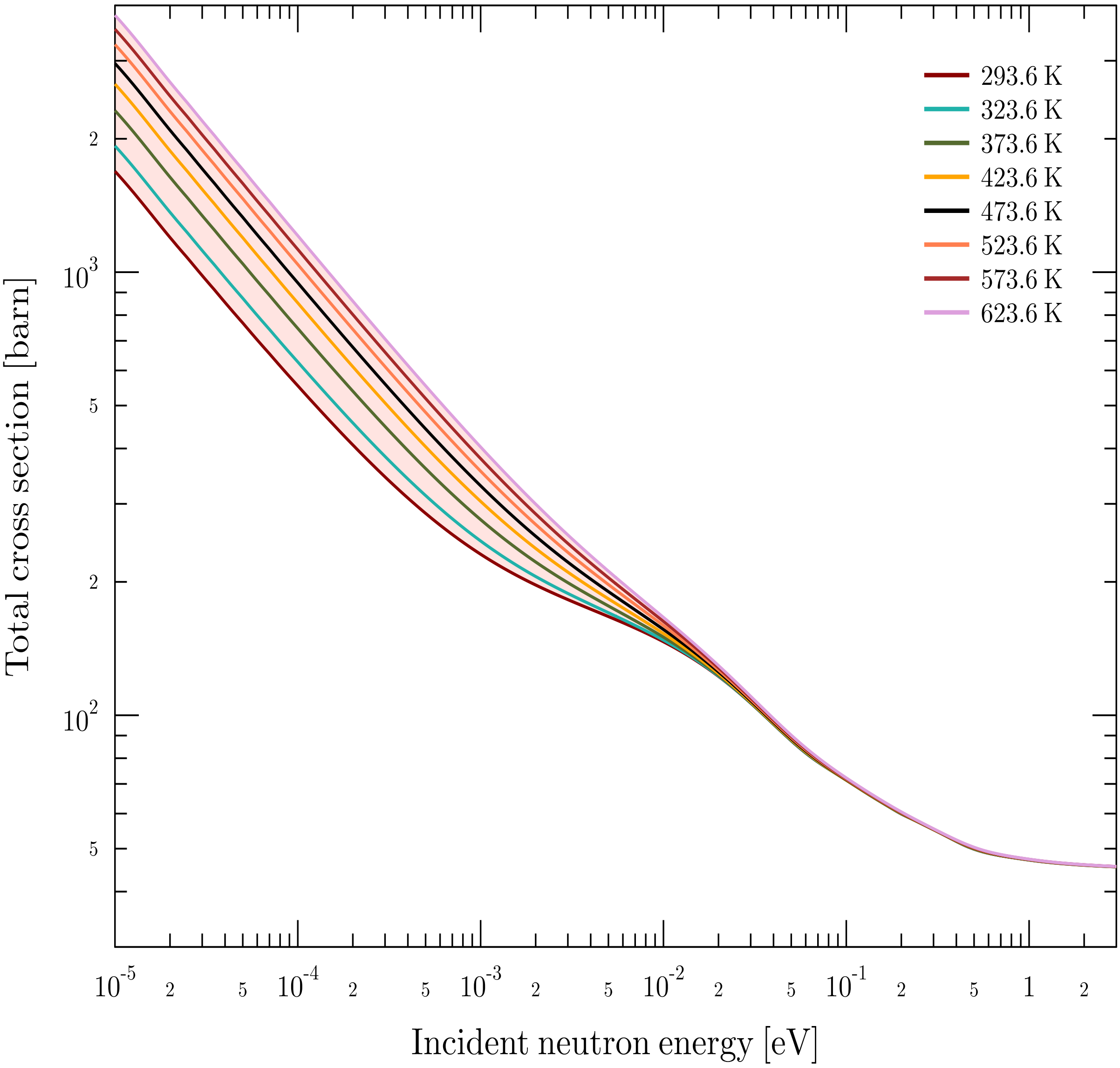

FIGURE 3.25: Total cross section of light water based on JEFF-3.3 TSL evaluation.

Figure 3.26 shows the behavior of cross sections as a function for different temperature in the energy range of 10-100 meV. The bottom part of Fig. 3.26 validates that the ratio of the total cross section increases with increasing temperature.

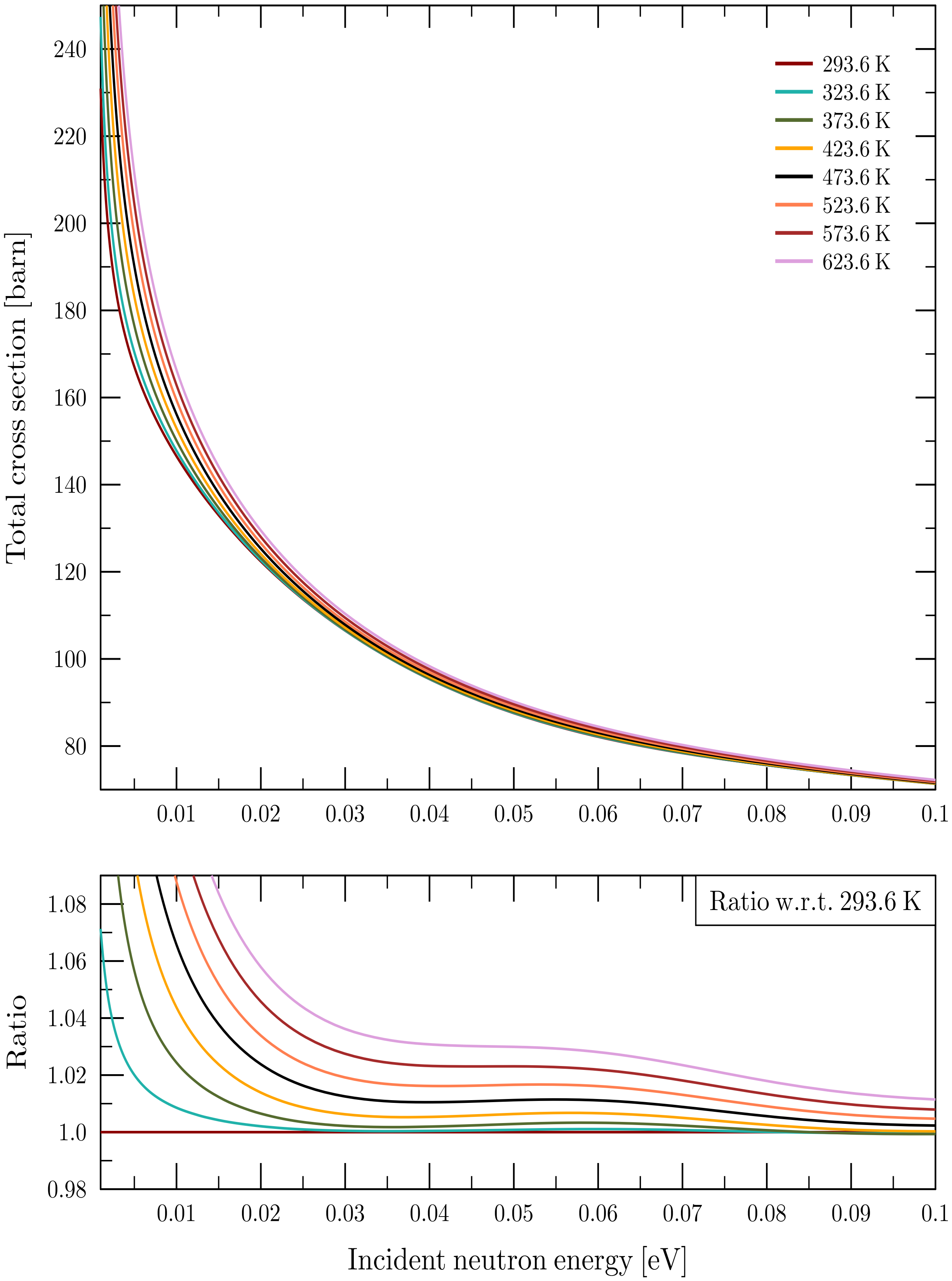

FIGURE 3.26: Ratio of the total cross section of light water at different temperatures w.r.t. 293.6 K based on JEFF-3.3 TSL evaluation.

3.4.5 Total cross section based on ENDF/B-VIII.0 TSL evaluation at high temperatures

The total cross section for light water based on the ENDF/B-VIII.0 TSL evaluation is given in Fig. 3.27. The cross sections are plotted for a series of temperatures starting from room temperature, i.e. 293.6 K up to 623.6 K.

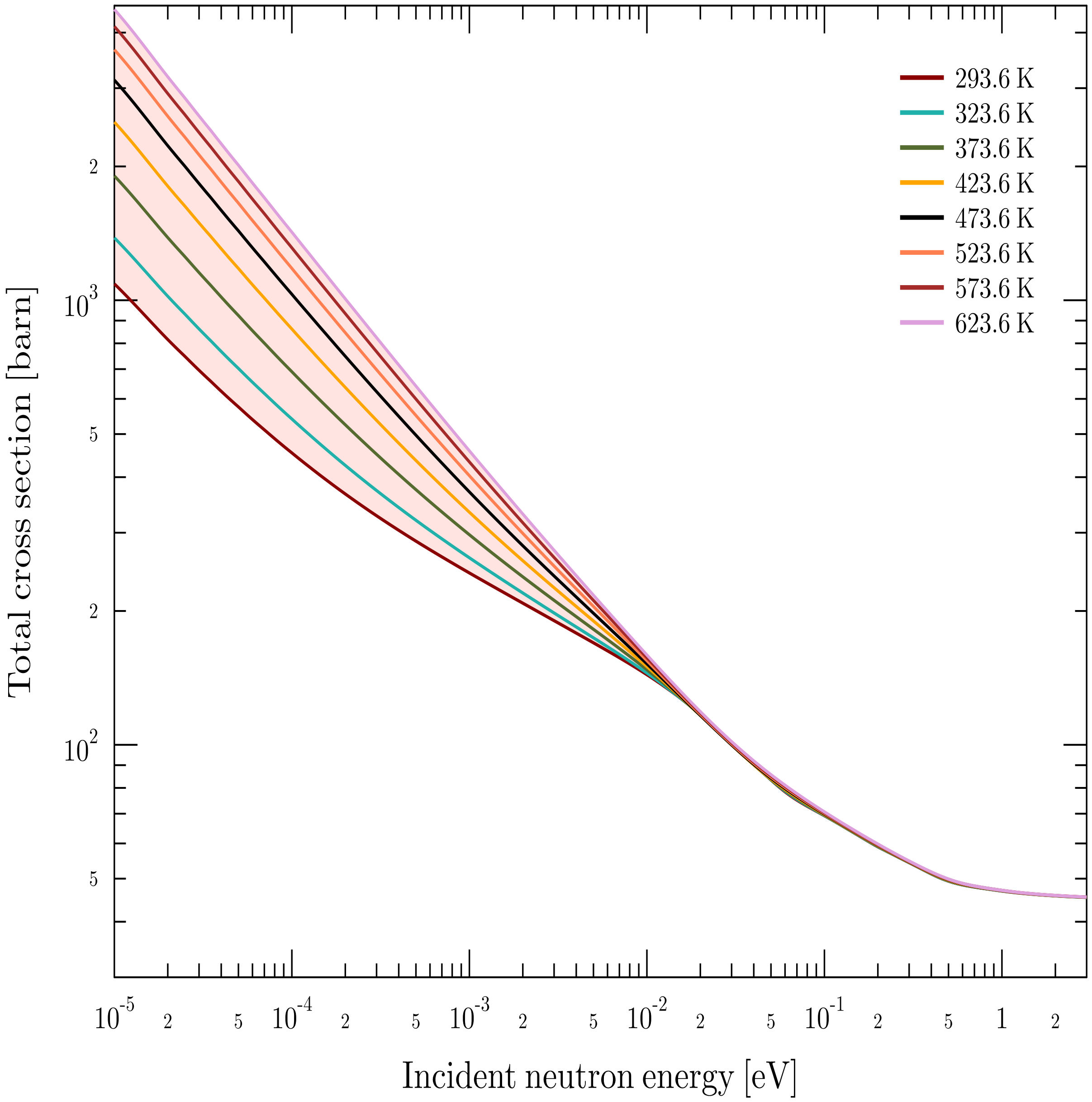

FIGURE 3.27: Total cross section of light water based on ENDF/B-VIII.0 TSL evaluation.

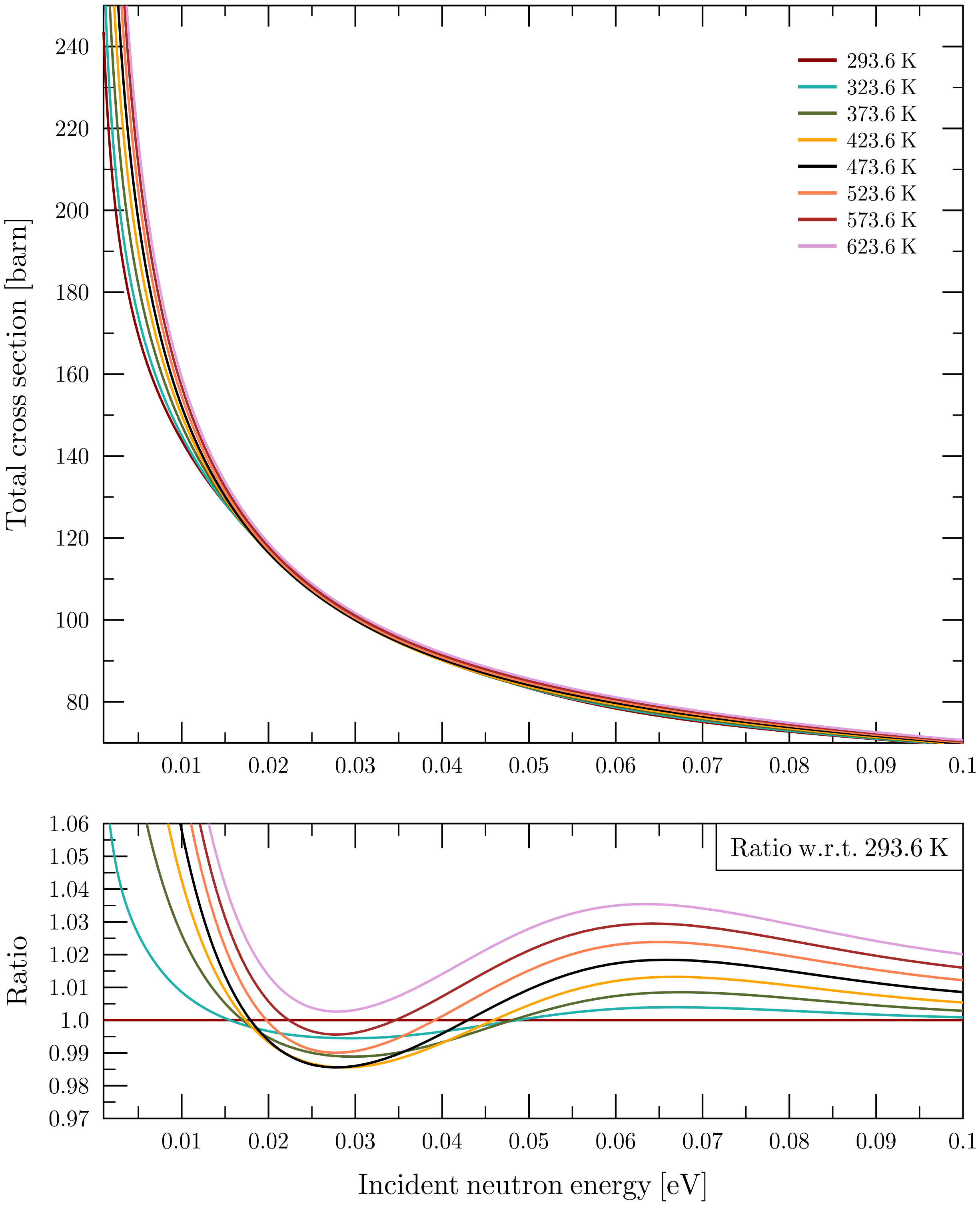

FIGURE 3.28: Ratio of the total cross section of light water at different temperatures w.r.t. 293.6 K based on ENDF/B-V111.0 TSL evaluation.

Figure 3.28 shows the behavior of cross sections as a function for different temperature in the energy range of

10 meV - 100 meV. The bottom part of Fig. 3.28 is not in agreement with the previous observation to that of JEFF-3.3. Here the cross sections at high temperature decrease with increasing temperature. This effect can have serious impacts on reactor applications as this energy is sensitive to thermal nuclear systems operating at higher temperatures. The decrease of cross section in this energy range can be related to the fact that the frequency spectrum in the ENDF/B-VIII.0 TSL library shifts to lower energies with increasing temperatures. Hence, new TOF experiments especially at high temperatures and pressures are important to thoroughly investigate this behavior which will be seen in the next chapter.

3.4.6 Comparative study of the total cross section based on JEFF-3.3 and ENDF/B-VIII.0 TSL evaluation at high temperatures

Figure 3.29 shows a comparative study of the ENDF/B-VIII.0 and JEFF-3.3 TSL evaluation for light water specifically at high temperatures. The top part shows the total cross section of light water as a function of incident neutron energies at different temperatures, whereas the bottom part shows the relative difference in the total cross section obtained using the two evaluations. It can be observed that the relative difference between the two libraries in the total cross sections at low incident neutron energies is positive until 423.6 K, whereas the difference beyond 423.6 K is negative. The reason behind this change in the cross section in the low incident neutron energy region is the the choice of diffusion model used between the two TSL evaluations. However, one would expect to see the relative difference only on a particular side (either positive or negative). Further investigation is necessary to study this observation.

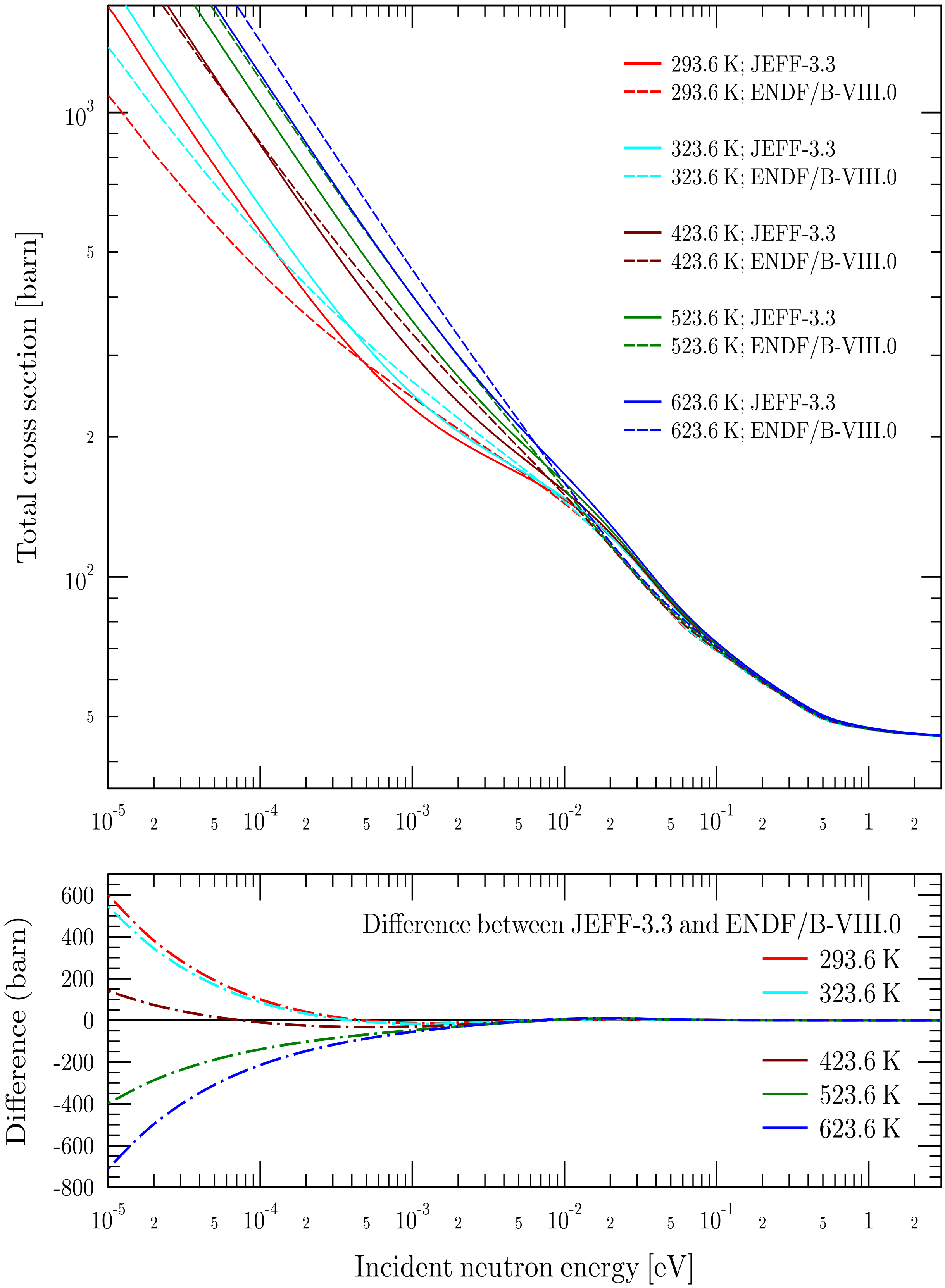

FIGURE 3.29: Comparison of the total cross section of light water based on JEFF-3.3 and ENDF/B-VIII.0 TSL evaluation at high temperatures.

3.4.7 Development of a new evaluation based on ENDF/B-VIII.0 and JEFF-3.3 TSL library

After observing the differences between the JEFF-3.3 and ENDF/B-VIII.0 TSL evaluations for light water, it it clear that both these libraries have their own limitations. While comparing with the room temperature experimental total cross section measured by Zaitsev et al., ENDF/B-VIII.0 performs better at low incident neutron energies as compared to JEFF-3.3. This is due to the fact that ENDF/B-VIII.0 describes the diffusion of the water molecules using the Egelstaff and Schofield model whereas JEFF-3.3 is based on free gas diffusion model. However, at high temperatures, ENDF/B-VIII.0 provides a disagreement with the ratio of the total cross section with increasing temperatures. This effect may be associated to the down shift in energy of the position of the rotation band in the frequency spectrum obtained using molecular dynamics simulations. However, JEFF-3.3 does not show any such shift in the position of the rotation band in the frequency spectrum at high temperatures. Hence, it was a favorable option to use the frequency spectrum of JEFF-3.3 for any further development of the light water TSL evaluation until new experiments or molecular dynamics simulations are carried out to verify the shift.

As a further step, a comparative study between a modified JEFF-3.3 and ENDF/B-VIII.0 TSL evaluation was carried out where the diffusion models used in these two evaluations were switched to observe the impact on the evaluations. Egelstaff and Schofield model was imposed on the JEFF-3.3 evaluation and a free gas model was imposed on the ENDF/B-VIII.0 evaluation. Figure 3.30 represents the total cross section of light water obtained with JEFF-3.3, ENDF/B-VIII.0 and modified JEFF-3.3 evaluation using the Egelstaff and Schofield diffusion model. It was observed that with the addition of Egelstaff and Schofield diffusion model, JEFF-3.3 evaluation behaved closer to ENDF/B-VIII.0 as can be clearly seen in the bottom part of Fig. 3.30 where the difference in the low energy cross sections decreases from 600 barn to around 50 barn. Figure 3.31 represents the total cross section of light water obtained with JEFF-3.3, ENDF/B-VIII.0 and modified ENDF/B-VIII.0 evaluation using free gas diffusion model. Using free gas diffusion model in the ENDF/B-VIII.0 evaluation brings the total cross section closer to the JEFF-3.3 evaluation, as can be clearly seen in the bottom part of Fig. 3.31 where the difference in the low energy cross sections decreases from 600 barn to around 120 barn. Learning from this comparison, a new TSL evaluation for light water was prepared where the JEFF-3.3 library was modified keeping the same frequency spectrum and using the Egelstaff and Schofield model instead of free gas model. Since the frequency spectrum utilized in JEFF-3.3 is limited to the rotation band, two discrete oscillators were used to replace the bending mode and the stretching mode at 205 meV and 436 meV, respectively. This new library is named as $S(\alpha,\beta)_{\text{JEFF-3.3-MOD}}$ and its performance is presented in **Chapter 7**.

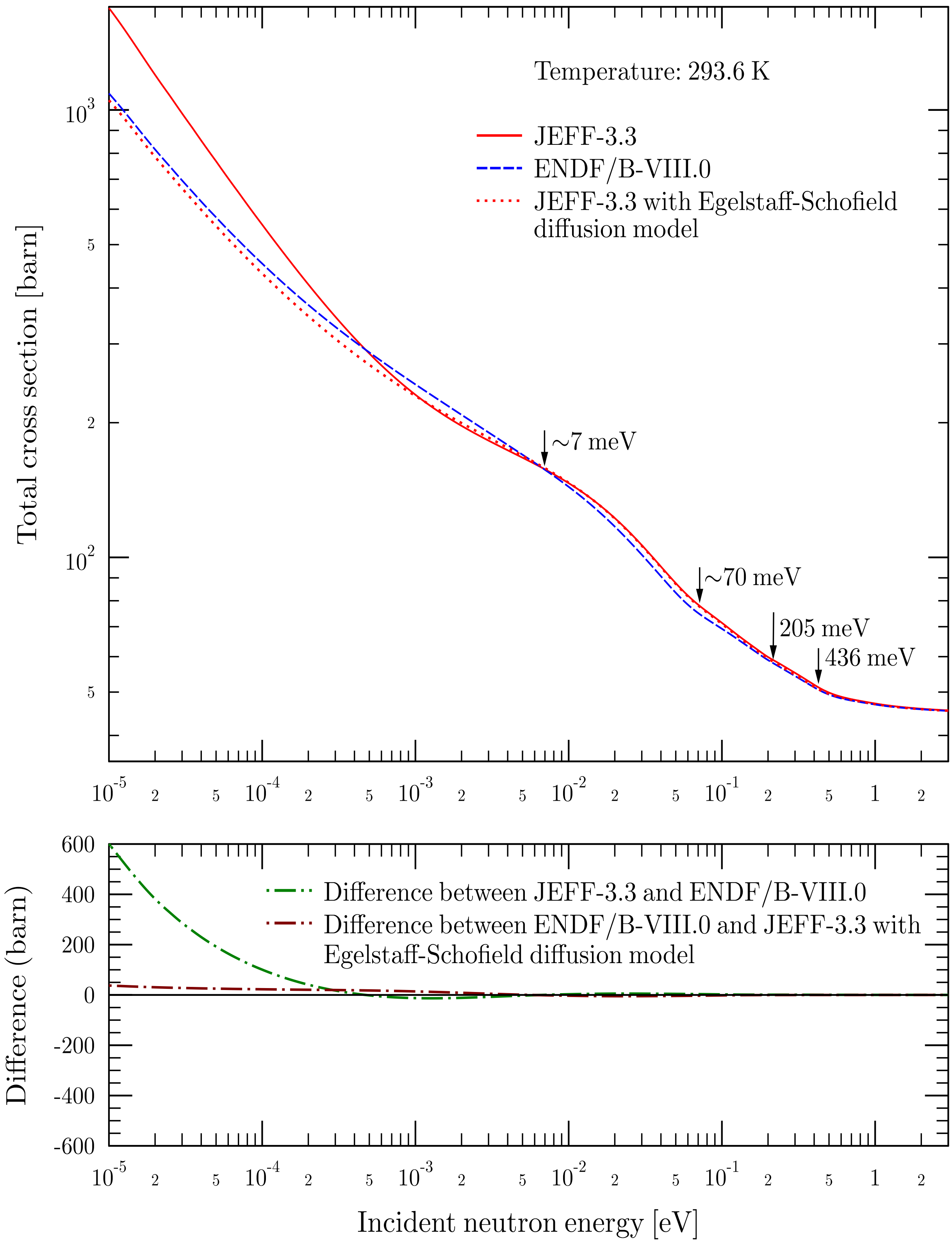

FIGURE 3.30: Comparison between the total cross section of light water at 293.6 K based on JEFF-3.3, ENDF/B-VIII.0 and modified JEFF-3.3 with Egelstaff and Schofield model for molecular diffusion.

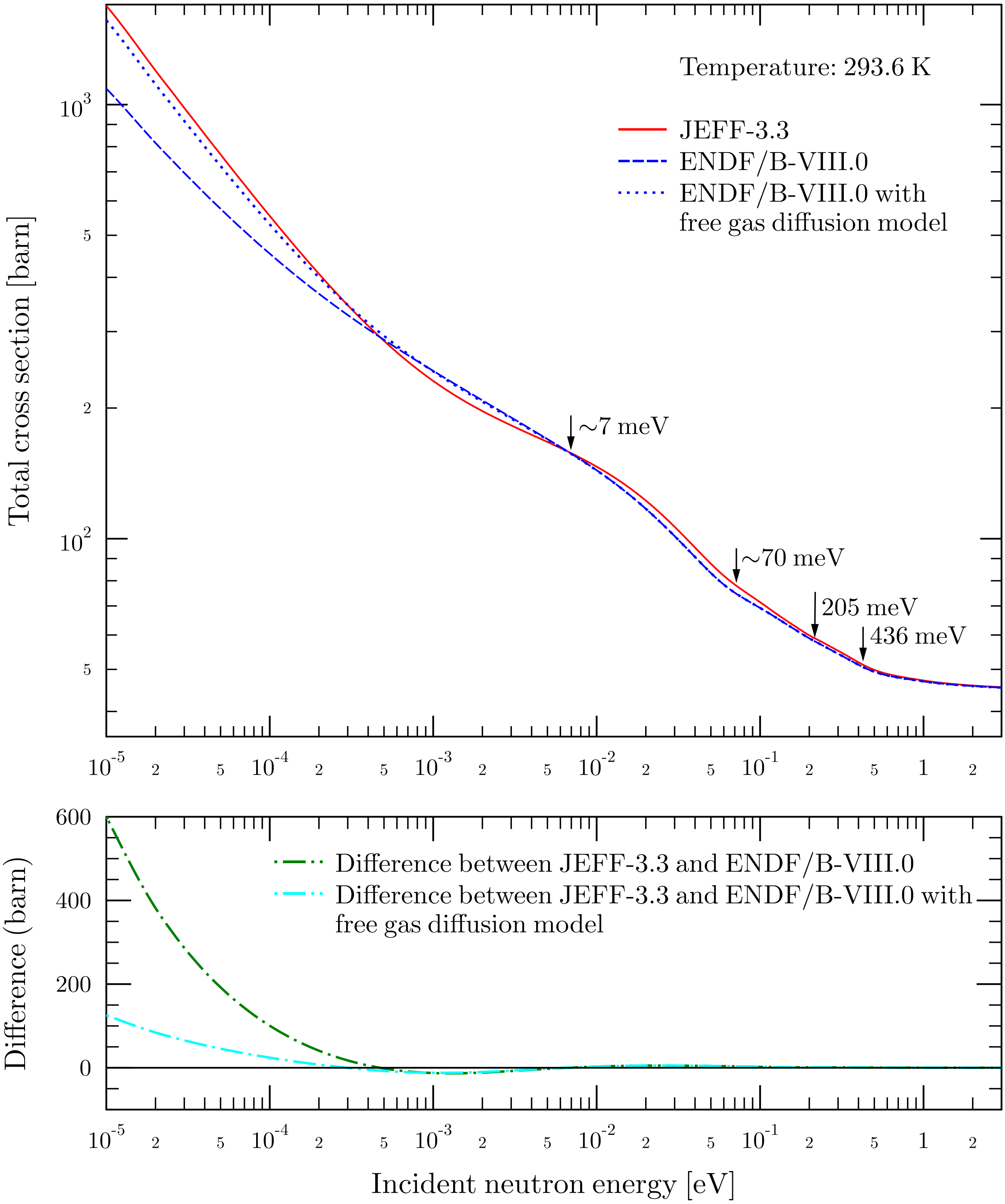

FIGURE 3.31: Comparison between the total cross section of light water at 293.6 K based on JEFF-3.3, ENDF/B-VIII.0 TSL and modified ENDF/B-VIII.0 with free gas diffusion model for molecular diffusion.

Chapter 4

TOF inelastic neutron scattering experiment for light water

The TOF methodology used in this research work to carry out neutron scattering experiments will be discussed in this Chapter. A brief introduction of the TOF spectrometers used at Institut Laue-Langevin (ILL), Grenoble and the data analysis will be presented, followed by the obtained results.

4.1. TOF neutron scattering

Due to the wave–particle dual nature of the neutrons, it is an excellent choice in spectroscopy to study material properties. For so, the most frequently used technique are that based on Inelastic Neutron Scattering (INS). In an INS experiment, the energy of the incident neutron is transferred to the scattering atoms/molecules. This process of energy exchange excites the vibrational and rotational modes of the scattering material. As mentioned before in Chapter 1, the energies and wavelengths of thermal neutrons are comparable to the inter atomic and inter molecular distances of the scatterer. It is also known that hydrogenous material can easily be studied using INS experiment as hydrogen has very high thermal scattering cross section (82.03 barn) and low absorption cross section (0.3326 barn) at thermal energy and thus offering favorable conditions of scatter in INS measurements.

INS experiments with thermal neutrons can thus reveal information about the structure and dynamics of light water. One can then determine the frequency spectrum of light water up to a wide range of energy transfer using the experimentally measured dynamic structure factor. The methodology of obtaining the frequency spectrum from TOF INS will be described in the next sections.

Generally, neutrons from a nuclear reactor or those generated by means of spallation reaction, are used for neutron spectroscopy. High energy reactor neutrons are generated by fission reaction using a fissile material. Whereas, spallation neutrons are generated by impinging high energy proton beams on a metal target, thus emitting high energy neutrons. These high energy neutrons are then thermalized with the help of moderators, to slow down their energies to the thermal range, to be used for the purpose of neutron spectroscopy. Some of the major spallation facilities available to users are ISIS in the United Kingdom, SNS in the United states of America and JPARC in Japan. The European Spallation Source (ESS) in Lund, Sweden is under construction. Facilities operating with reactor sources are the ones like the ILL in France.

In an INS, the knowledge of the incident and the scattered neutron energies are important to estimate the energy transfer to the sample. Before moving further it is worth explaining the principle behind the TOF. In the TOF method, the number of scattered neutrons at a particular angle are measured as a function of time. The neutron detector placed at certain angles cannot measure the energy of the scattered neutron, can only measure the time the neutron takes to reach the detectors which provides the final energy of the neutrons with the known sample to detector distance. One can then derive the energy transfer between the neutron and the sample, with the previous knowledge of the incident energy of the neutron chosen for the experiment. However, there are different ways of performing a TOF experiment by fixing the incident/final neutron energy which are introduced in the following section.

4.1.1 Types of TOF spectrometer

TOF spectrometers can be broadly classified in two types based on the following criteria:

- **Direct geometry spectrometer**: In the direct geometry TOF spectrometer, the incident energy of the neutron is fixed using Fermi choppers and the scattered neutron is measured as a function of several final energies. For example, MARI, MAPS, MERLIN at ISIS in the UK, ARCS, SEQUOIA and CNCS at SNS in the US, 4SEASONS, HRC and AMATERAS at JPARC in Japan, IN46, IN5 and IN6 at ILL in France are direct geometry TOF spectrometers.

- **Indirect geometry spectrometer**: In the indirect geometry TOF spectrometer, a white beam of neutrons (neutrons having a broad range of energies) is utilized and the scattered neutrons are collected as a function of a fixed final energy. For example, TOSCA at ISIS and VISION at SNS are indirect geometry TOF spectrometers.

4.1.2 Accessible regions of $(\vec{q}, \omega)$ in a TOF experiment

In a TOF experiment, the dynamic range of the energy and momentum transfer that one can access depends on the incident neutron energy and momentum selection rules. The accessible q and ω range of $S(\vec{q}, \omega)$ measured experimentally can be understood with the help of the scattering triangles as shown in Fig. 4.1. Here $\vec{k}$ is the wave vector of the incident neutron with energy E, $\vec{k'}$ is the wave vector of the scattered neutron with energy E' and $\vec{q}$ denotes the wave vector transfer. For direct geometry spectrometers $\vec{k}$ is fixed and $\vec{k'}$ varies as a function of time whereas for indirect geometry spectrometers $\vec{k}$ varies as a function of time while $\vec{k'}$ is fixed.

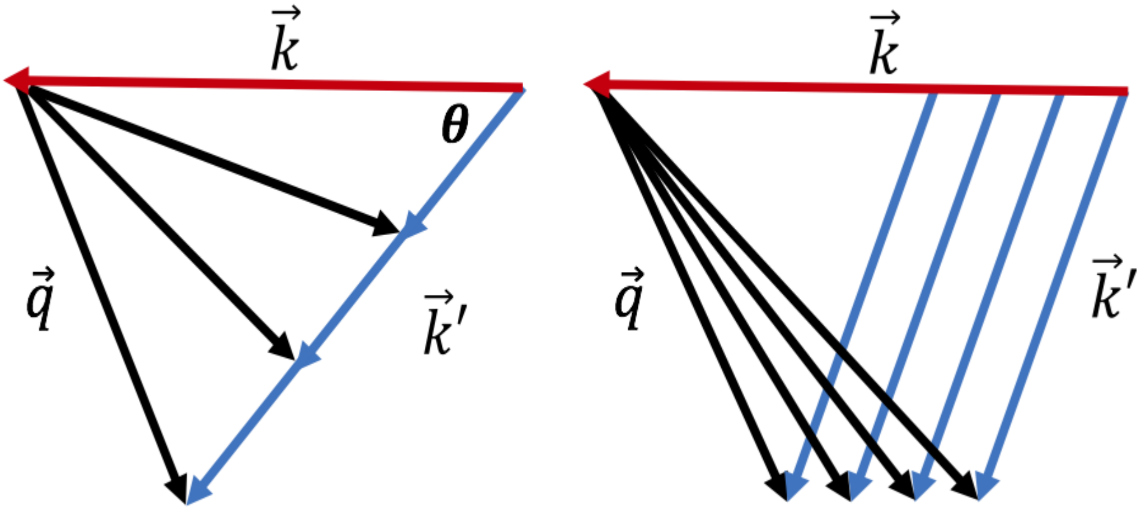

FIGURE 4.1: Momentum transfer $\vec{q}$ in the case of direct (left) and indirect (right) geometry TOF neutron scattering.

According to the cosine rule,

$$|\vec{q}|^2 = |\vec{k}|^2 + |\vec{k'}|^2 - 2|\vec{k}||\vec{k'}|cos\theta \tag{4.1}$$

implying that

$$\frac{\hbar^2|\vec{q}|^2}{2m} = E + E' - 2\sqrt{EE'}cos\theta \tag{4.2}$$

For direct geometries E' can be replaced as $E - \hbar\omega$ and hence the trajectory, that a neutron at an angle θ will cover in the $\vec{q}$ and ω space is given by:

$$\frac{\hbar^2|\vec{q}|^2}{2m} = 2E - \hbar\omega - 2\sqrt{E(E-\hbar\omega)}cos\theta \tag{4.3}$$

Equation 4.3 indicates that the neutrons are measured by the detectors in parabolic path of the $S(q,\omega)$ space.

For an example, Fig. 4.2 shows the $(\vec{q},\omega)$ space accessible by a neutron of incident energy 100 meV after being scattered to different scattering angles (3° - 120°). Due to this limitation one can not experimentally obtain $S(q,\omega)$ and hence $S(\alpha,\beta)$ on a rectangular grid, which is necessary for reactor applications. To solve this issue one relies on doing several measurements with different incident energies and later combining the measurements to access a broad range of $\vec{q}$ and ω

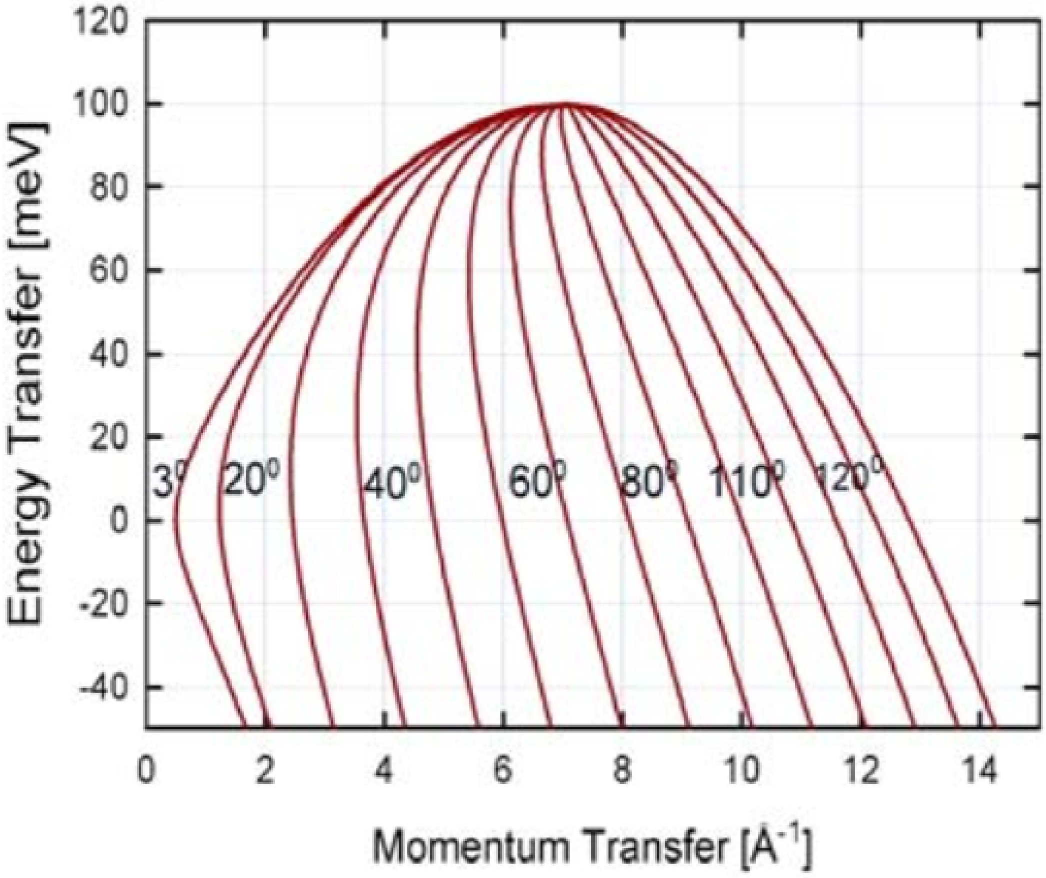

FIGURE 4.2: Accessible $S(\vec{q},\omega)$ range in a neutron TOF experiment [45].

4.2. TOF experiment at ILL

In order to obtain the dynamic structure factor $S(\vec{q}, \omega)$, TOF experiments were carried out at the ILL in December 2015. ILL is an international research center that provides a powerful source of neutrons produced by a high flux reactor (HFR) and a matching suite of experimental facilities (some 40 instruments) which acts as a valuable tool for investigating many important features of matter, particularly condensed matter. The HFR produces the most intense neutron flux in the world, i.e. 1.5×10^{15} n/cm^2/s. As a matter of identification, the instruments available at the ILL are labeled based on the experimental techniques used, for example, **IN** refers to instruments carrying out **IN**elastic neutron scattering, **D** for instruments carrying out **D**iffraction measurements.

For this research work, two direct geometry TOF spectrometers, namely the IN4c and the IN6 were chosen. The reason behind choosing two different spectrometers was to cover a wide range of momentum and energy transfer ranges possible, within the experimental limitations of each instrument. These two spectrometers have different resolutions and cover different regions in the $\vec{q}$ and ω space by choosing different energies of the incident neutrons. A picture of the experimental facility for both the IN4c and IN6 is given in the Fig. 4.3. The two spectrometers will be described in detail in the next section, along with the description of the preparation of the light water samples.

FIGURE 4.3: The IN4c (left) and IN6 (right) TOF facilities at the ILL.

4.2.1 Sample preparation

In order to perform the experiment at high temperature and pressure, the cryogenics team at the ILL developed a special cylindrical pressure cell (sample holder) of CuBe (ϕ= 0.6 cm interior, 0.8 cm exterior; height = 7 cm) as shown in Fig. 4.4. This sample holder can withstand high temperature and pressure and can easily fit in a cryo-furnace. The pressure cell was designed in such a way that it can allow performing measurements with light water up to 600 K and 150 bar. Though there were certain limitations on the cryo-furnace (heating system) which limited the measurements up to 500 K. High-purity water sample was inserted in this pressure cell for the TOF measurements with both the spectrometers. Figure 4.5 pictorially illustrates the interaction of neutrons with

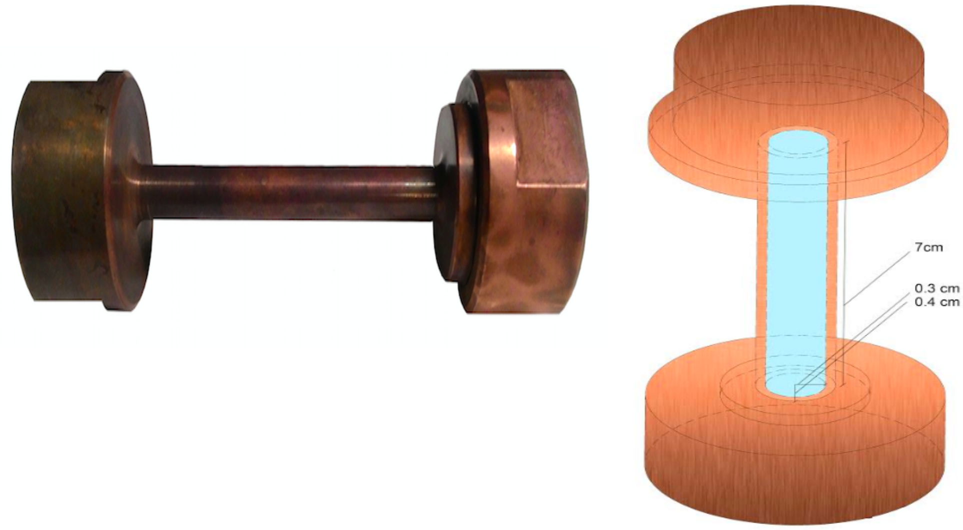

FIGURE 4.4: CuBe pressure cell (sample holder).

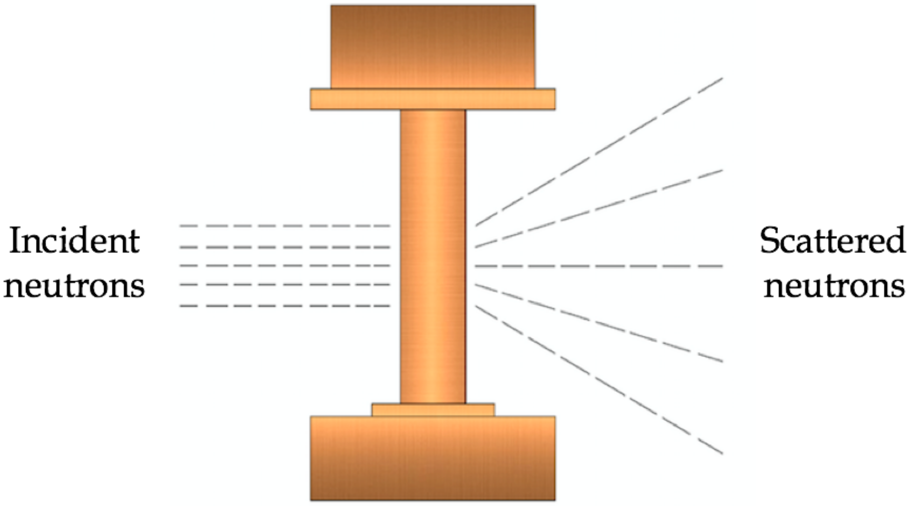

FIGURE 4.5: Schematics of the TOF measurements.

light water contained in the sample holder. The incident neutrons after interacting with the sample (in this case light water) are scattered to a certain angle, thereby, reaching the detector placed at that angle.

4.2.2 IN4c TOF spectrometer

The IN4c is a direct geometry TOF spectrometer which works in the thermal neutron energy range between 10 to 100 meV, offering a high flux $\sim 5 \times 10^5$ n/cm^2/s at the sample position [46]. A schematic representation of the instrument is given in Fig. 4.6. The main components of the incident beam side of the instrument are the two background choppers, the double curvature monochromator with four faces and the Fermi chopper. The background choppers are rapidly pulsating beam shutters which efficiently eliminate background noise coming from fast neutrons and gamma rays in the spectra [47]. These background choppers are placed in different compartments so as to remove the undesired neutrons in the early stage itself. The suitable incident energy is selected from the thermal neutron spectrum with a Cu (III) crystal monochromator. The Fermi chopper rotates at speeds of up to 32000 rpm. It transmits short neutron pulses to the sample. The sample environment is designed to accommodate standard cryo-furnace which can maintain high pressure and temperature. A radial collimator around the sample position is used to reduce the scattering from the sample environment. The secondary flight-path of 300 cm is in vacuum to avoid parasitic scattering of the transmitted neutrons. Good counting rate is ensured by a large detector bank with ^{3}He tubes (length 300 mm, width 30 mm, elliptical section, pressure 6 bar)

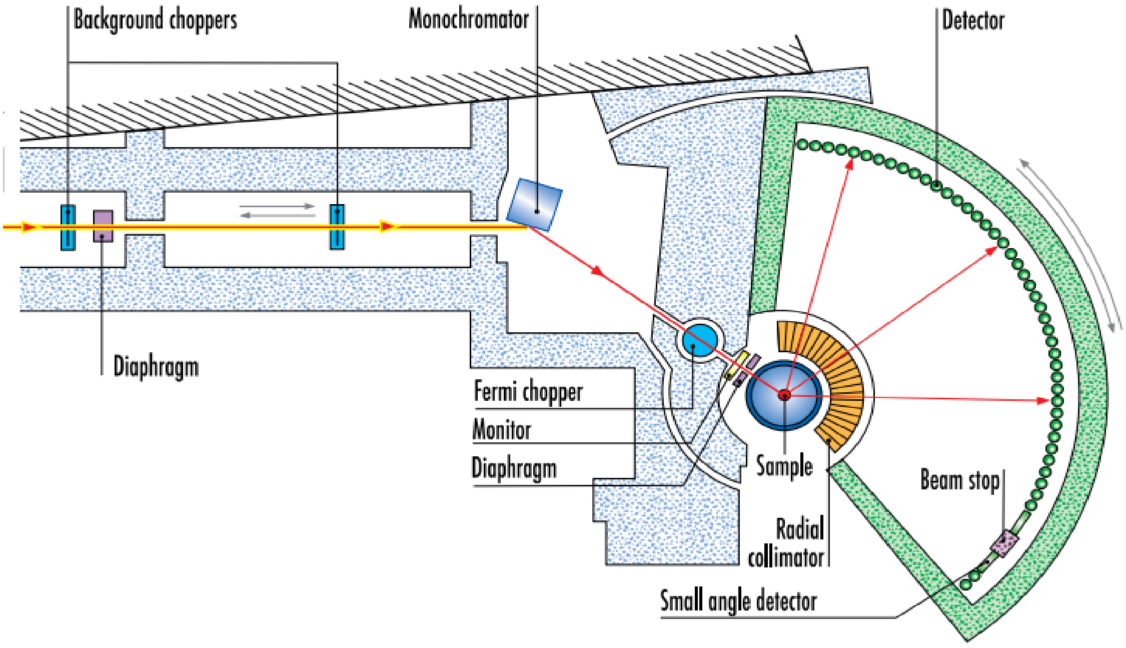

FIGURE 4.6: Experimental setup of the IN4c TOF spectrometer [46].

covering scattering angles up to 120 degree. In addition to the ^{3}He detector tubes, a ^{3}He filled multi detector (eight sectors with 12 radial cells each; outer diameter 60 cm) will allow to observe forward scattering. The time-of-flight of neutrons between the chopper and the sample can be measured by using precise electronic circuitry. For our measurements with the IN4c, wavelength of the incident neutron was chosen as 2.41 Å . This wavelength corresponds to a neutron energy of 14.2 meV. The speed ratio of background/ Fermi chopper was chosen as 1:2 to minimize frame overlap and to extend the time range for data acquisition.

As mentioned before the objective of this PhD work is to study the thermal scattering cross section data for light water at high temperature and pressure. Especially, it is interesting to study the impact of pressure on the dynamic structure factor for light water. Table 4.1 shows the temperature and pressure conditions at which the measurements were performed at the IN4c.

Specifications	Temperature (K)	Pressure (bar)	Data acquisition time (hours)
λ=2.4 Å E=14.2 meV	300	1	2.5
	300	88-100 (94)	2
	350	115	2
	392-466 (430)	128-165 (147)	~ 1
	479-485 (482)	172-180 (176)	~ 1
	490-497 (494)	185	10.5
	517	42	3

TABLE 4.1: Experimental conditions for the measurements with light water at the IN4c. The brackets indicate the average value.

4.2.3 IN6 TOF spectrometer

IN6 is a time-focusing time-of-flight spectrometer designed for quasi-elastic and inelastic scattering experiments [46]. A schematic diagram of the IN6 TOF spectrometer is given in Fig. 4.7.

This instrument consists of three vertically focusing pyrolytic graphite monochromatic crystals, which can provide incident wavelengths in the range of 4 to 6 Å . Fermi chopper is used for the time focusing and the distance between Fermi chopper and the sample is 38 cm while the sample to detector distance is 248 cm. The flux that can be achieved at the sample position is $\sim 8.9 \times 10^4$ n/cm^2/s [46]. There are 337 elliptical ^{3}He

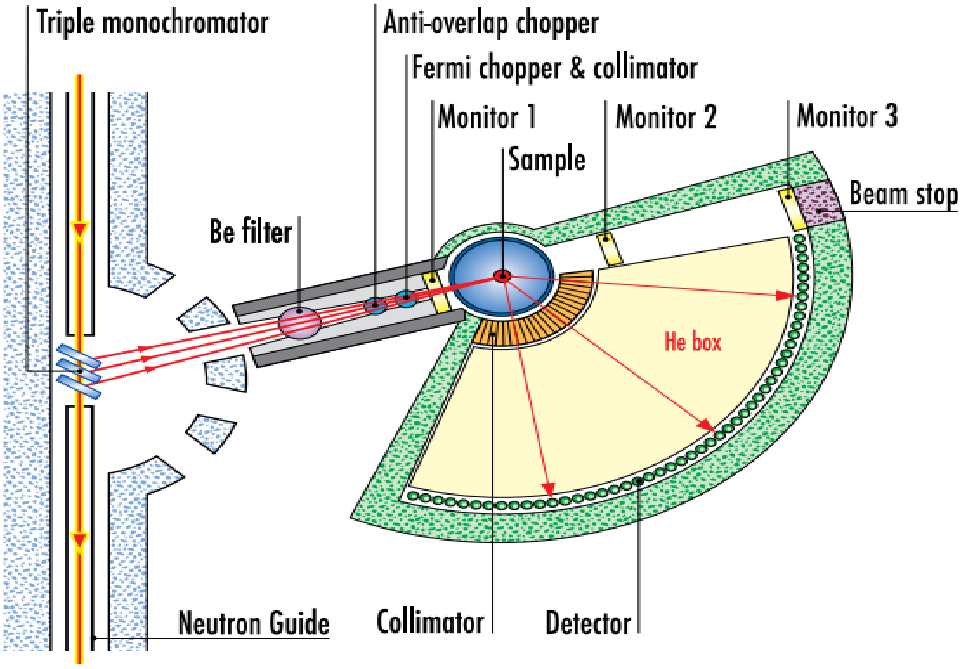

FIGURE 4.7: Experimental setup of the IN6 TOF spectrometer.

detectors that cover an angular range of 10–115 °. The wavelength of the incident neutron for measurements with the IN6 spectrometer was chosen as 5.1 Å for a neutron energy of 3.15 meV. The speed ratio of background/ Fermi chopper was chosen as 1:1 with extended time range for data acquisition and to minimize the overlap. Elastic energy resolution obtained by choosing this incident neutron wavelength is about 2.2 %.

Like with the IN4c spectrometer, TOF experiments at IN6 were also carried at different temperatures and pressures. Measurements were made at two different temperatures i.e. 350 K and 494 K. The measurements at 494 K were carried out at two different pressures, one at 70 bar and the other at 470 bar. Table 4.2 shows the temperature and pressure conditions at which the experiments were carried out at IN6.

Specifications	Temperature (K)	Pressure (bar)	Data acquisition time (hours)
	350	1	4
λ=2.4 Å	494	70	9
E = 3.15 meV	494	340-600(470)	4

TABLE 4.2: Experimental conditions for the measurements with light water at the IN6.

4.3. TOF data reduction

In order to utilize the maximum of the beam time allotted at the ILL facility for both the IN4c and IN6 spectrometers, we chose several thermodynamic states of light water (pressure and temperature combinations) as shown in Fig. 4.8, covering the liquid phase of light water respecting the constraints imposed by the cryostat and the pressure cell specification (maximum temperature and pressure).

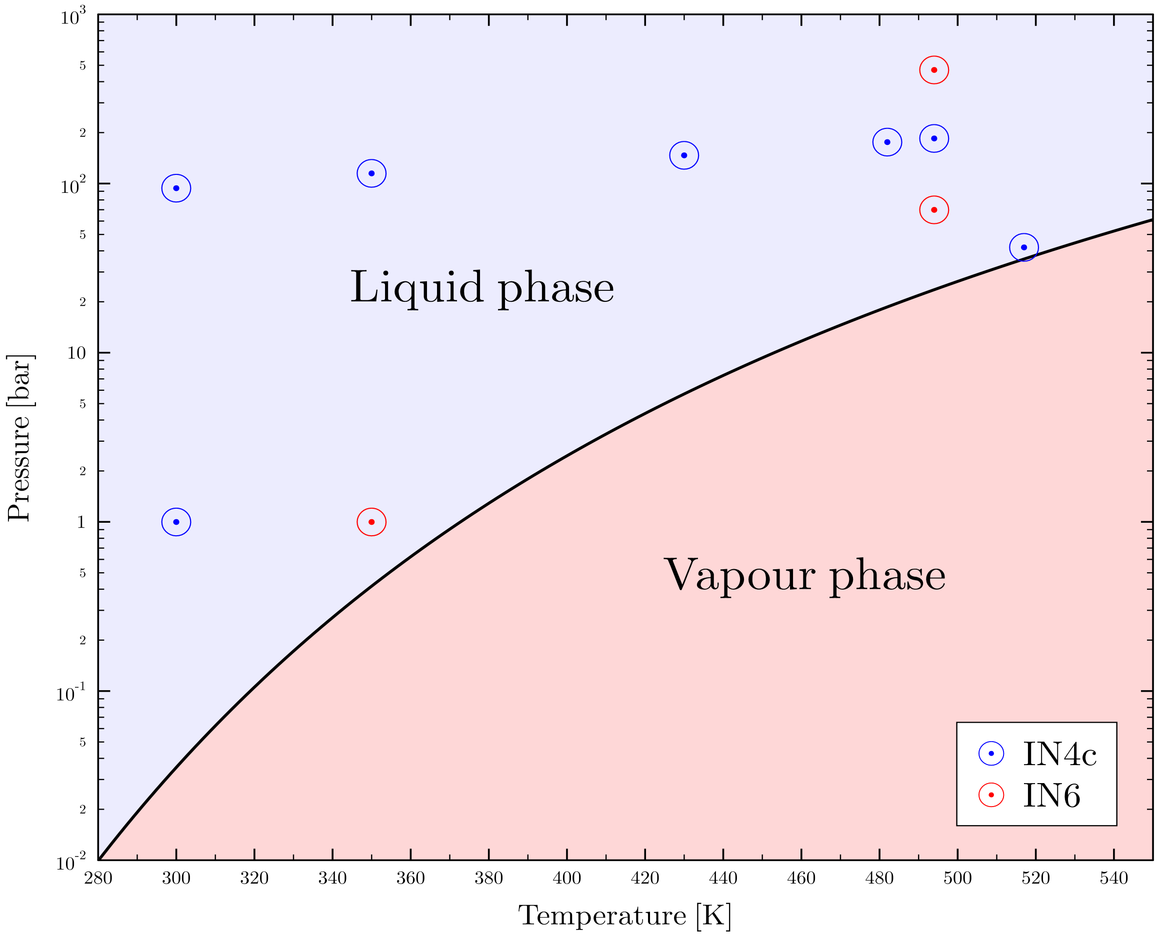

FIGURE 4.8: Thermodynamic conditions of the INS measurements for light water at the ILL.

The incident neutron energy for the IN4c and IN6 were 14.2 meV and 3.15 meV, respectively. These two spectrometers provide high resolution spectroscopy, allowing a flexible energy and momentum transfer range. Measurements were carried out in the temperature range of 300-517 K and pressure range of 1-470 bar matching the normal operating conditions of nuclear power reactors as shown in Fig. 4.8. We saw some fluctuations in the temperature and pressure during the measurements for different experimental runs. The numbers in bracket in Tables 4.1 and 4.2 represent the average temperature and pressure for which the data analysis is carried out.

4.3.1 Data reduction procedure

The data collected in the TOF experiments can be reduced to a format suitable to generate $S(\vec{q},\omega)$. There are several softwares to perform the data reduction of the ILL data. We have used the LAMP platform, an in-house code developed by the computer science group at the ILL. A sketch of the LAMP interface is given in Fig. 4.9 The treatment parameters have been fed as an input and the output is obtained in a standard format. The input

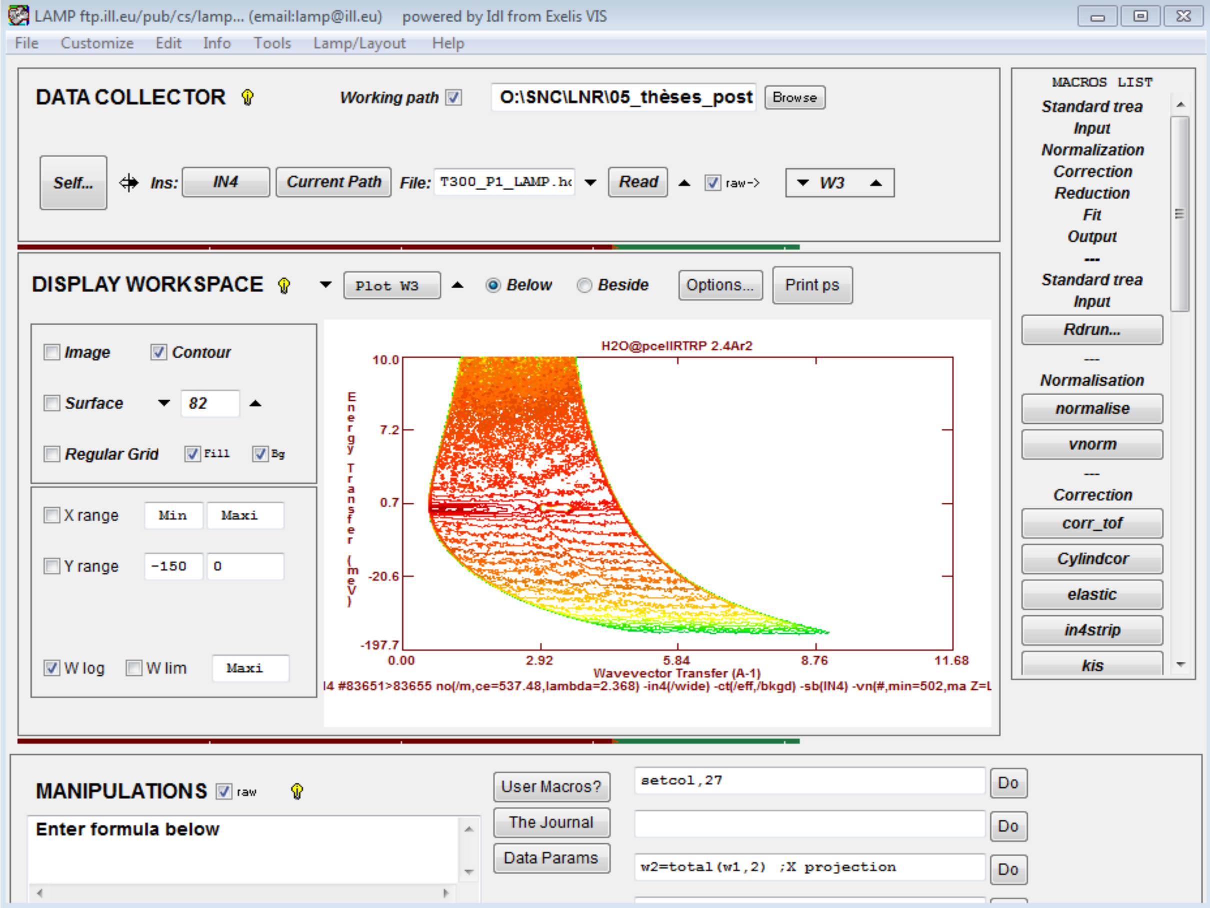

Working path ☑ O:\SNC\LNR\05_thèses_post

Ins: IN4

File: T300_P1_LAMP.hc

☑ raw-> W3

Plot W3

● Below ○ Beside

☐ Image ☑ Contour

☐ Surface 82

☐ Regular Grid ☑ Fill ☑ Bg

☐ X range Min Maxi

☐ Y range -150 0

☑ W log ☐ W lim Maxi

I4 #83651>83655 no(/m,ce=537.48,lambda=2.368) -in4(/wide) -ct(/eff,/bkgd) -sb(IN4) -vn(#,min=502,ma Z=L

☑ raw

Enter formula below

setcol,27

w2=total(w1,2) ;X projection

FIGURE 4.9: Block diagram of the LAMP data analysis tool.

files (.prox files) for the data reduction of both the IN4c and IN6 are provided in the Appendix A. For clarity, a brief explanation of the data reduction procedure is give hereby:

- The instrument for which the data correction is to be done is selected in order to import the spectrometer parameters.
- The directory of the raw time of flight data is specified. TOF raw data (input parameters) can be read-in from individual files (Run number) of a particular experiment stored in a local directory.
- The measured data is then normalized to the number of incident neutrons via the monitor counts.

- In order to obtain the contribution of the sample, the empty sample holder measurement is subtracted from the data with sample plus sample holder. While performing the subtraction, the sample transmission is taken care of by subtracting only a percentage of the empty sample holder.
- The data is then normalized to a vanadium measurement. Vanadium is used as a standard to calibrate the relative efficiencies of all detectors because of its purely isotropic scattering nature. The geometrical shape of the vanadium sample also affects the angular distribution of the scattering neutrons. One can correct for this effect for slab or cylindrical vanadium samples.
- The normalized data is then corrected for the efficiency of the detectors, as well as the not working detectors are removed, etc.
- The detectors are then grouped to improve the statistics of the measured signal, the average scattering angles are now represented by $\bar{\theta}$.
- The time of flight is converted to energy, thus providing $S(\bar{\theta}, \omega)$.
- The $S(\vec{q}, \omega)$ is finally obtained by interpolating $S(\bar{\theta}, \omega)$.
- Finally the $S(\vec{q}, \omega)$ can be transformed to the frequency spectrum $g(\omega)$ by:

$$\rho(\omega) \simeq \lim_{q \to 0} S(\vec{q}, \omega) \frac{\omega^2}{q^2} \tag{4.4}$$

The experimental data are not corrected for multiple scattering. However, all other necessary corrections have been performed following the above procedure to provide qualitative results. The measurements are reliable only for an energy transfer less than the chosen incident energy of the neutrons. The chosen incident neutron energy in our case for the IN4c and IN6 is 14.2 meV and 3.15 meV, respectively. This limits our measurement of the dynamic structure factor of light water to 14.2 mev for the IN4c and 3.15 meV for the IN6 measurements.

4.4. Analysis of the TOF experimental data

As can be seen from the block diagram of the data analysis procedure in Fig. 4.10, the experimental double differential data can be translated to both $S(\vec{q}, \omega)$ and the frequency spectrum. To proceed with the analysis of the TOF data it is first important to characterize the resolution function of the spectrometer.

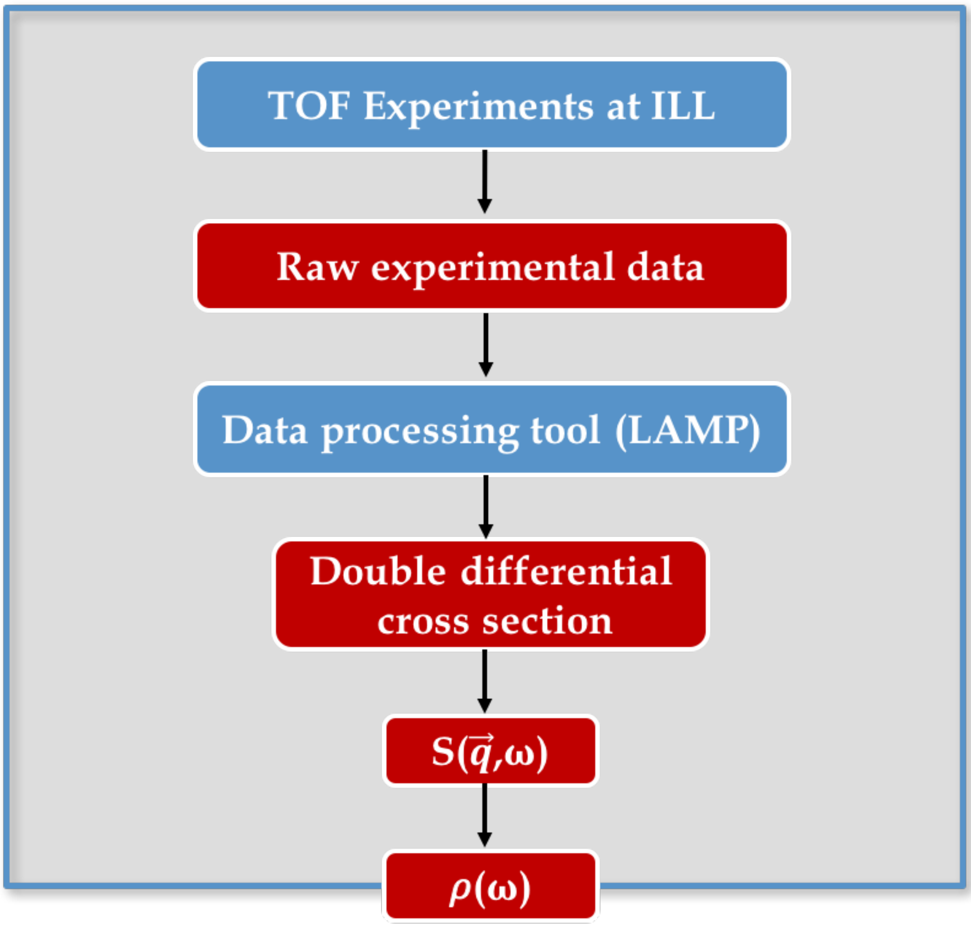

FIGURE 4.10: Block diagram of the experimental data analysis.

4.4.1 Resolution of the IN4c and IN6 spectrometers

The experimental resolution of both the spectrometers were derived by performing a TOF measurement of a Vanadium sample. A cylindrical Vanadium sample was used in this case. The data analysis was performed using the LAMP [48] data analysis tool to obtain the elastic peak of Vanadium. Figure 4.11 shows the elastic peak of the Vanadium measurement obtained at the IN4c spectrometer. The x-axis corresponds to energy transfer, y-axis the angle of scattering and z-axis is the scattering intensity. Vanadium has mostly only incoherent neutron scattering cross section. Hence, it is generally used to normalize INS measurements. The elastic peak ($\hbar\omega = 0$) of Vanadium can be observed in the measured spectra. This peak also provides the resolution function of the spectrometer for the chosen incident energy of the neutron. Hence with the IN4c, the Vanadium measurements were performed at an incident neutron energy of 14.2 meV, whereas for IN6 the measurements were carried out at 3.15 meV. Likewise, Fig. 4.12 shows the measured spectra of Vanadium from the IN6 spectrometer.

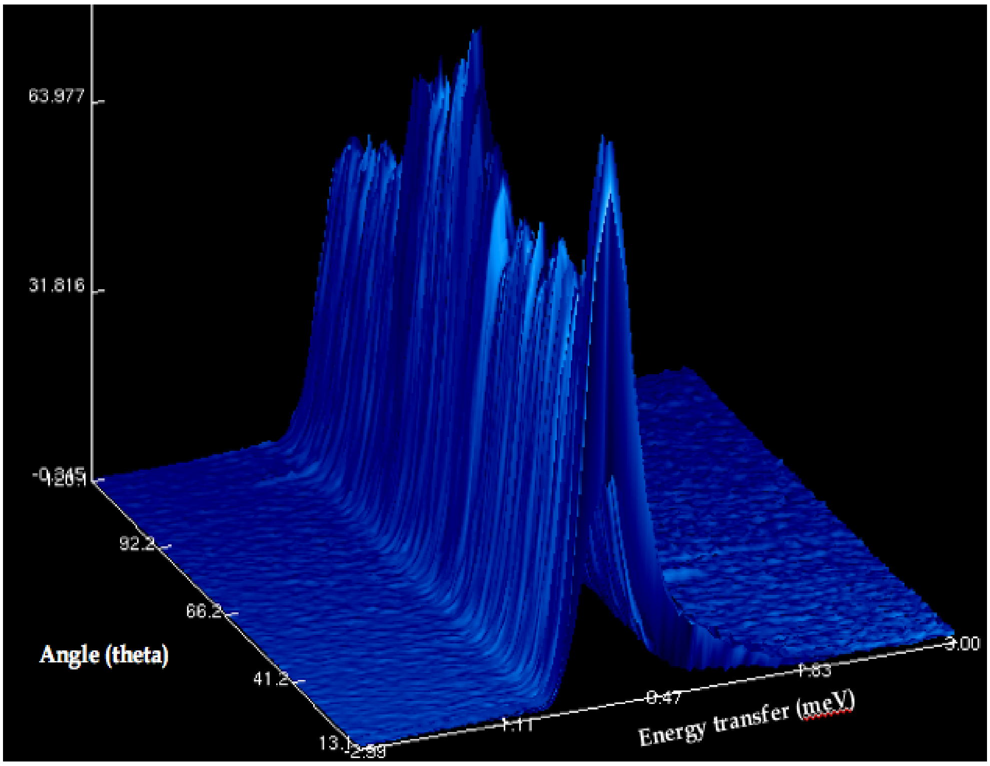

FIGURE 4.11: Vanadium spectra obtained from the IN4c at incident neutron energy of 14.2 meV.

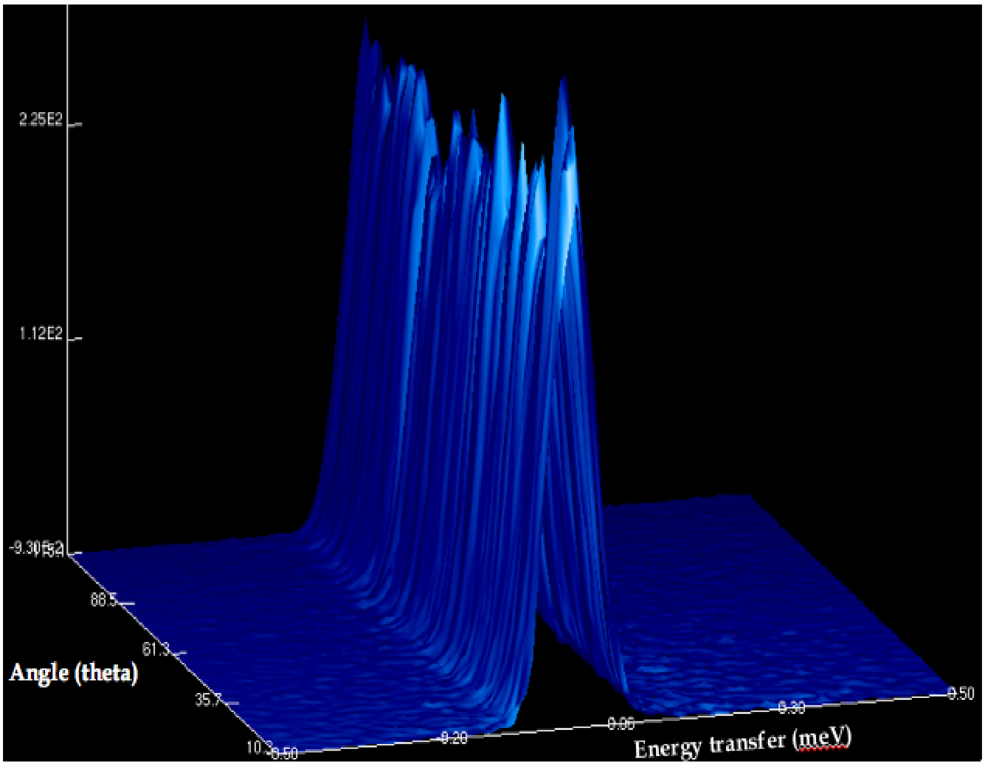

FIGURE 4.12: Vanadium spectra obtained from the IN6 at incident neutron energy of 3.15 meV.

The resolution of the TOF spectrometers also changes with respect to the angle of scattering. Curve fitting of the Vanadium spectra at different angles were obtained using the Str_Fit module of the LAMP code. The

Str_Fit module is a powerful tool that allows simultaneous fitting of the spectra with several fitting functions. As a matter of choice a Gaussian function was chosen to fit the Vanadium spectra to obtain the spectrometer resolution. The choice of a Gaussian fitting for the Vanadium arises from the fact that it provided a better fitting and residual parameters. A Gaussian fitting of the Vanadium spectra obtained from IN6 is presented in Fig. 4.13. The x-axis corresponds to energy transfer, y-axis the angle of scattering and z-axis is the scattering intensity. A plot of FWHM of the Gaussian fit of the elastic peak of Vanadium w.r.t. angle of scattering $\bar{\theta}$ is given in Fig. 4.14 and 4.15 for the IN4c and IN6, respectively. Both the Figures indicate that the resolution of the spectrometers does not change much with the scattering angle. For the IN4c the resolution is close to 4 $\%$ whereas for the IN6 it is around 2.5 $\%$. The resolution did not change as a function of temperature and pressure.

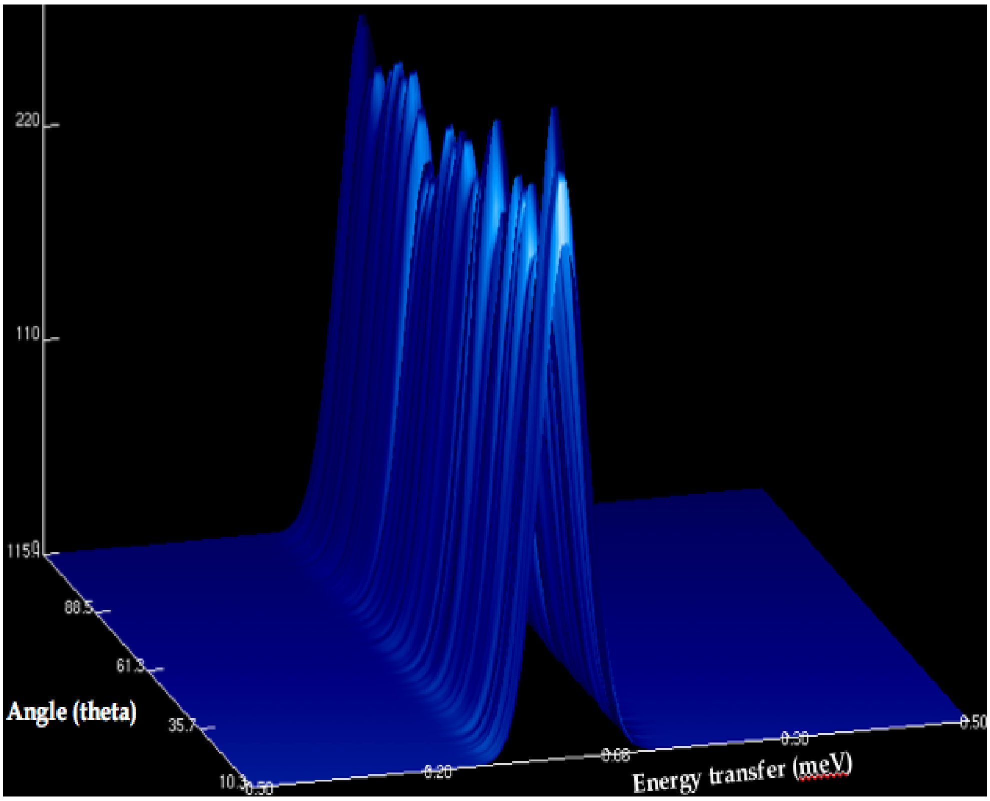

FIGURE 4.13: Gaussian fitting of the vanadium spectra obtained from the IN6.

4.4.2 $S(\vec{q},\omega)$ derived from TOF measurements

Figure 4.16 shows the shape of the $S(\vec{q},\omega)$, the structure factor obtained from the IN6 TOF spectrometer with light water at 350 K. The experimental $S(\vec{q},\omega)$ is a tabulated function (2-D matrix) over a $\vec{q}$ and ω grids. One can see a sharp peak around zero energy transfer. This peak is the elastic peak which is followed by a quasi-elastic peak and a tail. The $S(\vec{q},\omega)$ is first symmetrized to $S_{sym}(\vec{q},\omega)$ which is generally utilized in generating $S(\alpha,\beta)$

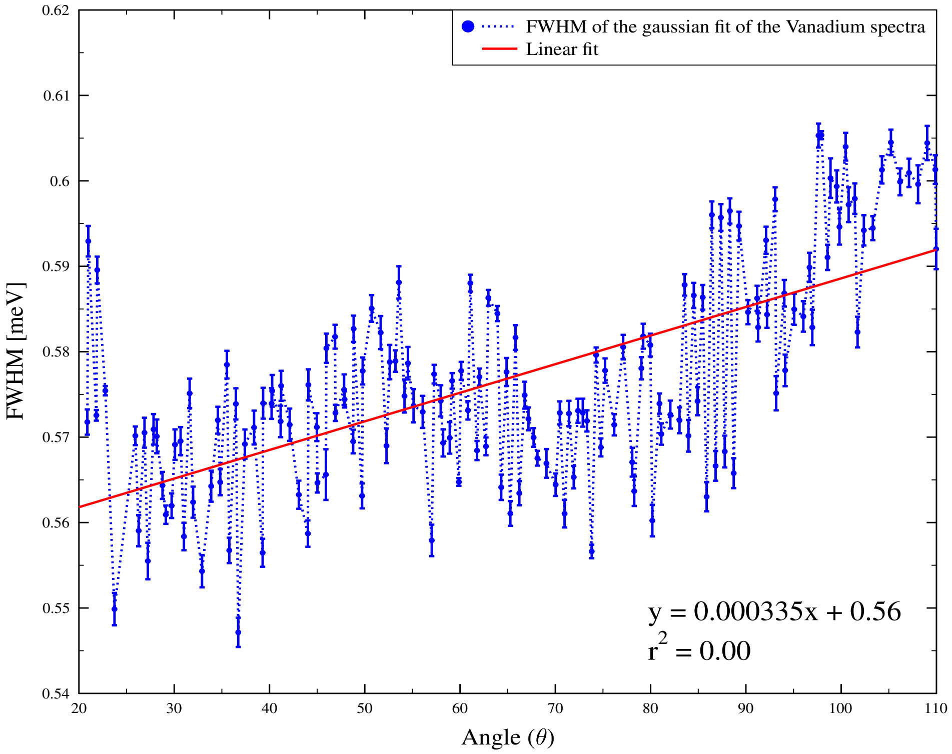

FIGURE 4.14: FWHM of the Gaussian fit of the Vanadium spectra obtained from the IN4c.

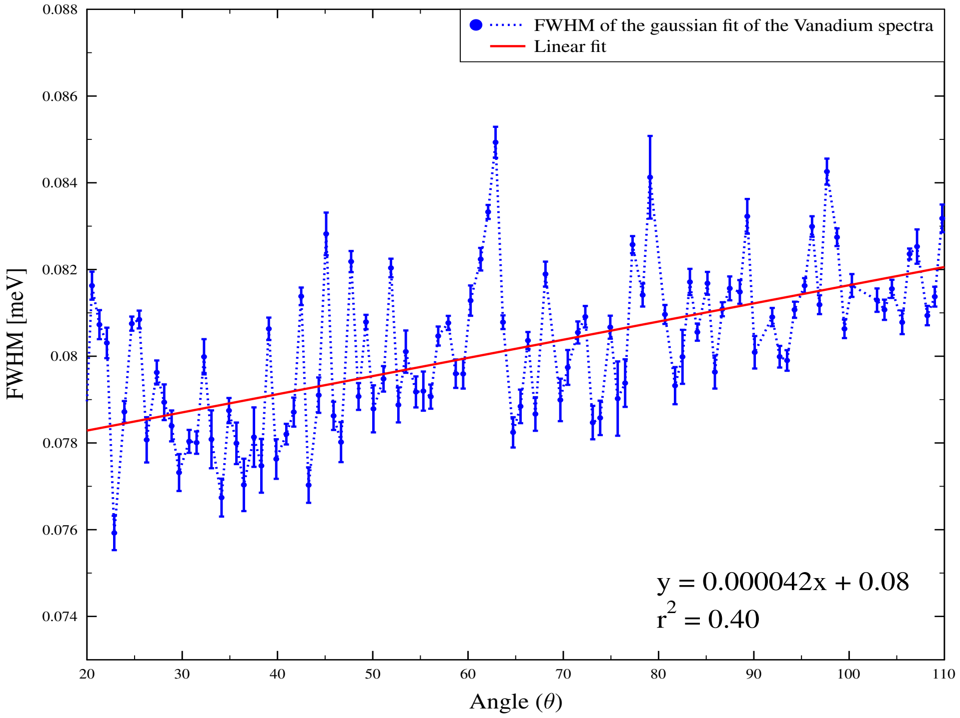

FIGURE 4.15: FWHM of the Gaussian fit of the Vanadium spectra obtained from the IN6.

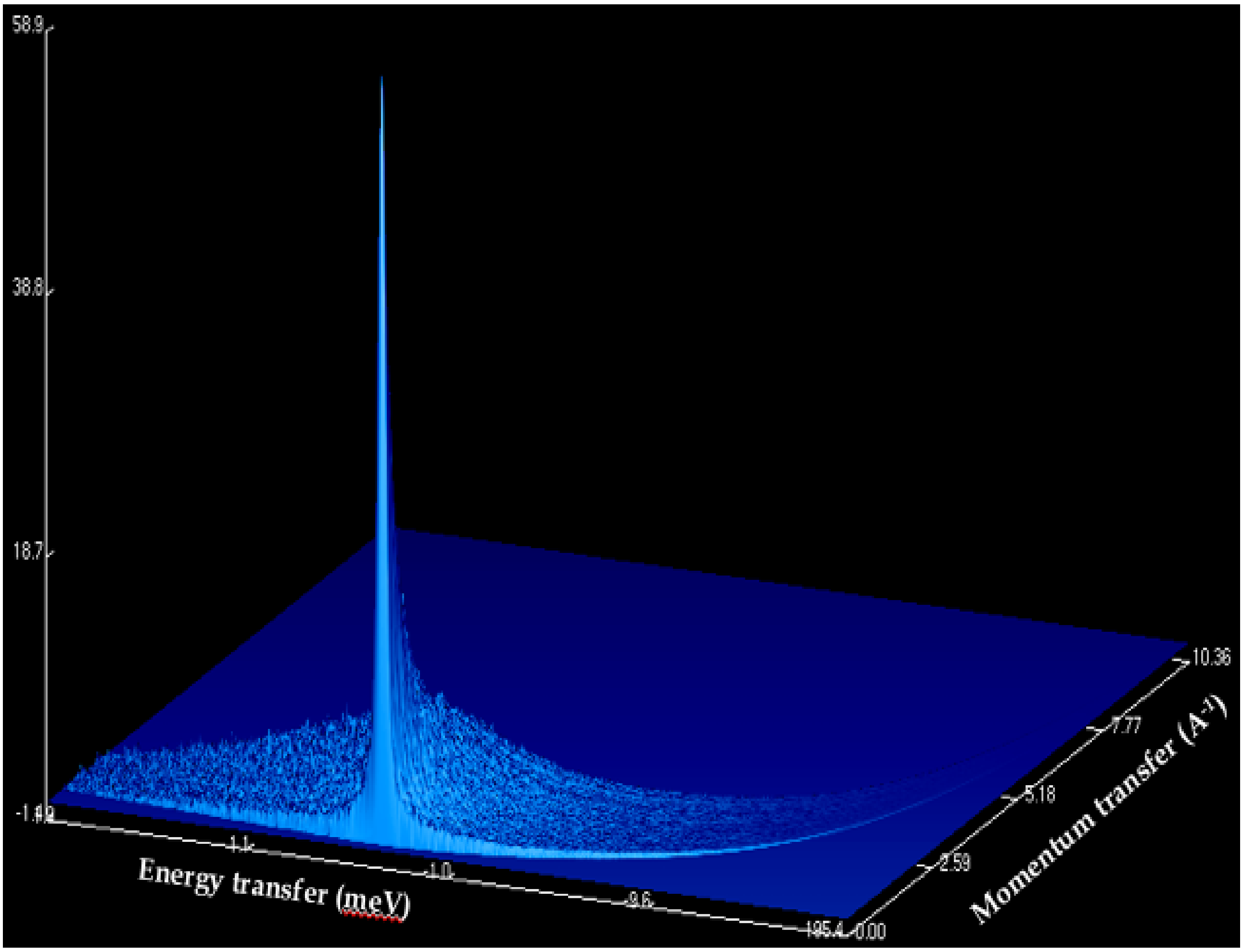

FIGURE 4.16: $S(\vec{q},\omega)$ obtained from the IN6.

for reactor applications following Eq. 4.5.

$$S_{sym}(\vec{q},\omega) = \frac{S(\vec{q},\omega)}{Q} \tag{4.5}$$

where Q is the correction factor applied to the $S(\vec{q},\omega)$ to transform it to the $S_{sym}(\vec{q},\omega)$. Generally when one transforms the $S(\vec{q},\omega)$ measured experimentally to a symmetric form, care must be taken to take into account the detail balance correction in the $S_{sym}(\vec{q},\omega)$. Several options for Q can be found in the literature [49] and the most widely used is the one developed by Schofield given by [37]:

$$Q = \exp\left[\frac{\hbar\omega}{2k_BT}\right] \tag{4.6}$$

Another correction factor referred to as harmonic correction, performs even better at high energy transfers and is given by [50]:

$$Q = \frac{\frac{\hbar\omega}{K_B T}}{1 - \exp\left[\frac{-\hbar\omega}{k_B T}\right]} \tag{4.7}$$

In both the above corrections factors, i.e. Schofield and harmonic, the Q value increases with energies due to the $\hbar\omega$ term in the numerator. The standard approximation [51] developed by Frommhold is another correction factor that performs well in higher energy transfer region due to fact that there is no $\hbar\omega$ in the numerator. In this case, Q is given as:

$$Q = \frac{2}{1 + \exp\left[\frac{-\hbar\omega}{k_B T}\right]} \tag{4.8}$$

The correction factors given in Eq. 4.6, 4.7 and 4.8 have their own limitations depending on the system and one has to make a choice based on the application [52]. However, LAMP uses Eq. 4.7 for Q to symmetrize the experimental $S(\vec{q}, \omega)$ considering its applicability on high energy transfers.

Generally a fitting of $S(\vec{q}, \omega)$ can provide a great deal of information about the properties of the sample. As opposed to the Vanadium fitting where a Gaussian shape was chosen, the $S(\vec{q}, \omega)$ is defined more adequately by a Lorentzian [24]. The fitting of the experimental $S(\vec{q}, \omega)$ has been done using the STR_Fit module of the LAMP. STR_Fit takes the vanadium resolution as an input and fits the $S(\vec{q}, \omega)$ with a Lorentzian. The STR_Fit then provides the fitted data, residuals and the fitting parameters. A Lorentzian fitting using the Vanadium spectra as resolution function obtained from IN6 is presented in Fig. 4.17 .

One of the major point of this study is to investigate the impact of temperature and pressure on the double differential, frequency spectrum and the total cross section of light water. A detailed discussion of this issue is presented in the following sections.

4.5. Double differential scattering cross section

The double differential cross section was calculated from the $S(\vec{q}, \omega)$ obtained experimentally from both the IN4c and IN6 spectrometers. As mentioned before it is interesting to observe the impact of temperature and pressure on the double differential cross section of light water.

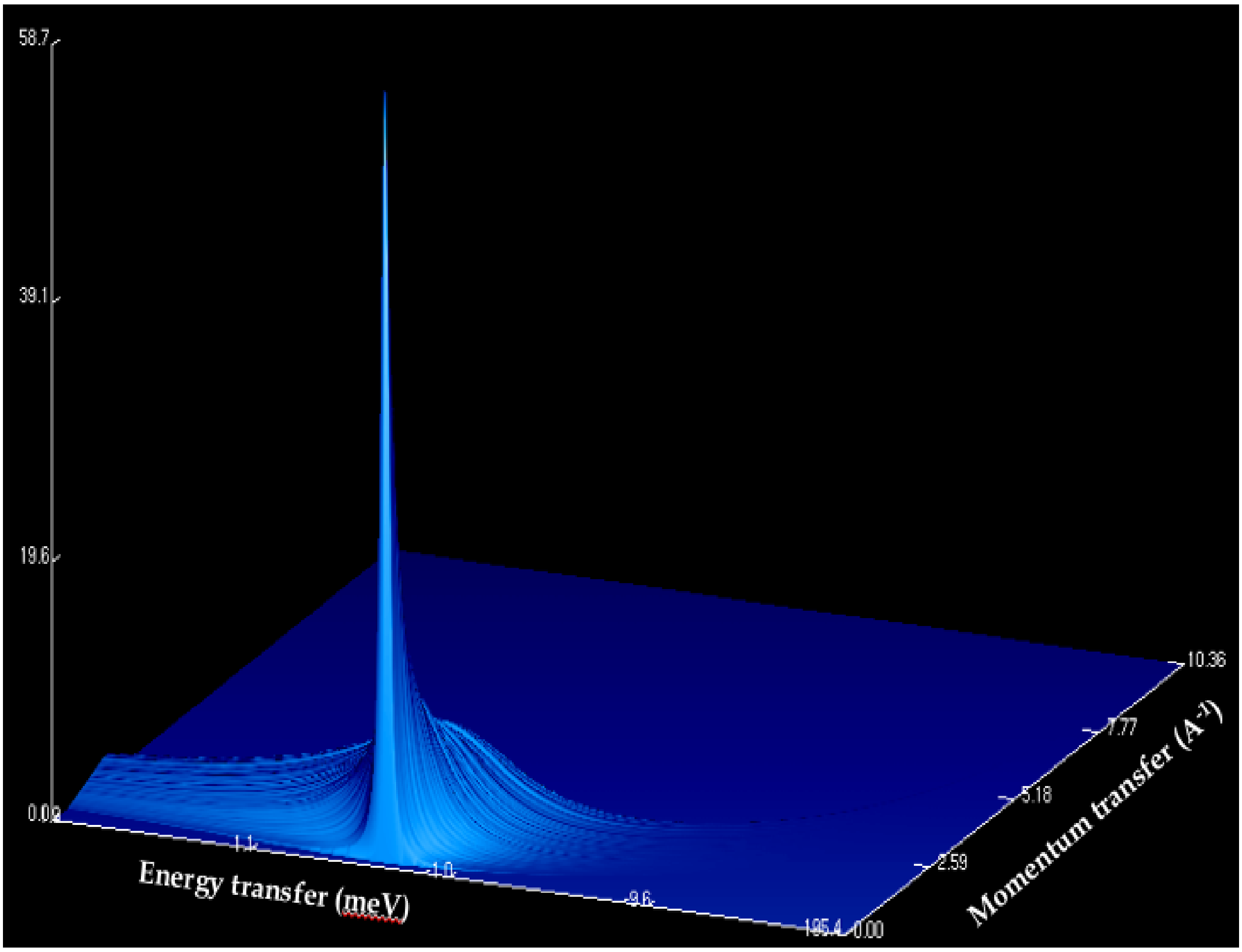

FIGURE 4.17: Lorentzian fitting of the $S(\vec{q},\omega)$ obtained from the IN6.

4.5.1 Pressure dependence on the double differential scattering cross section

Figure 4.18 represents the experimental double differential cross section of light water measured at the IN4c for an incident energy of 14.20 meV and scattering angle θ, 15°. Both the data are at the same temperature but at different pressures to see the pressure effect. The solid line in red is at 300 K and 1 bar, whereas the dotted line in blue is at 300 K and 94 bar. Figure 4.19 represents the experimental double differential scattering cross section of light water measured at the IN6 for an incident energy of 3.15 meV and scattering angle θ, 15° for pressures of 70 and 470 bars.

Observing Fig. 4.18 and 4.19, it was found out that pressure has a negligible impact on the double differential cross section of light water. It is the first time that a study like this has been carried out which directly verifies the impact of pressure on the double differential data.

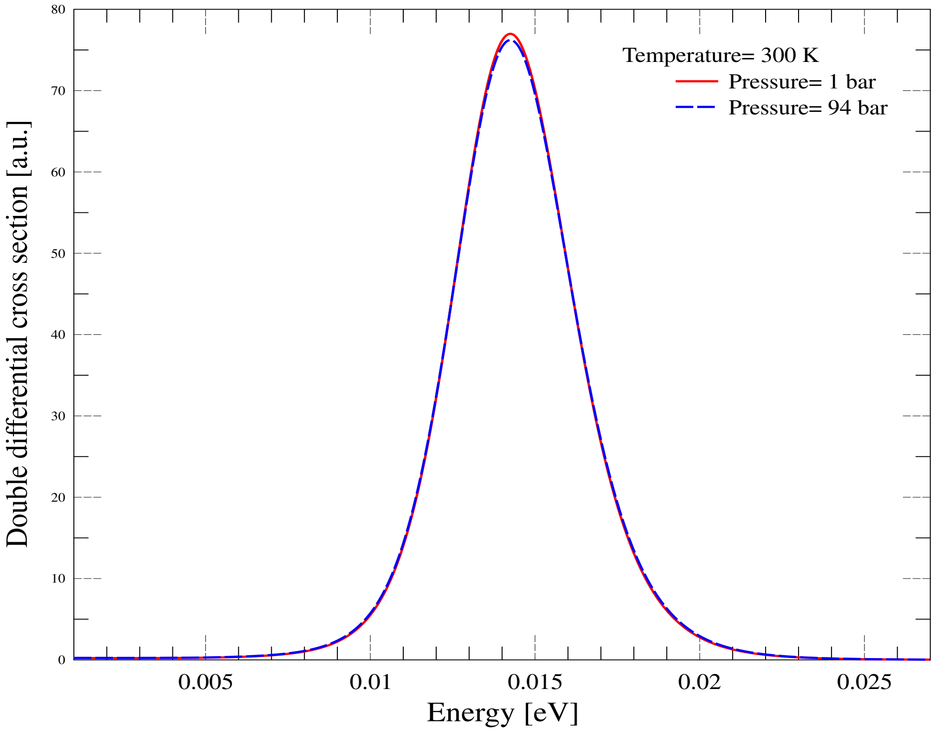

FIGURE 4.18: Double differential cross section for light water measured at the IN4c at different pressures.

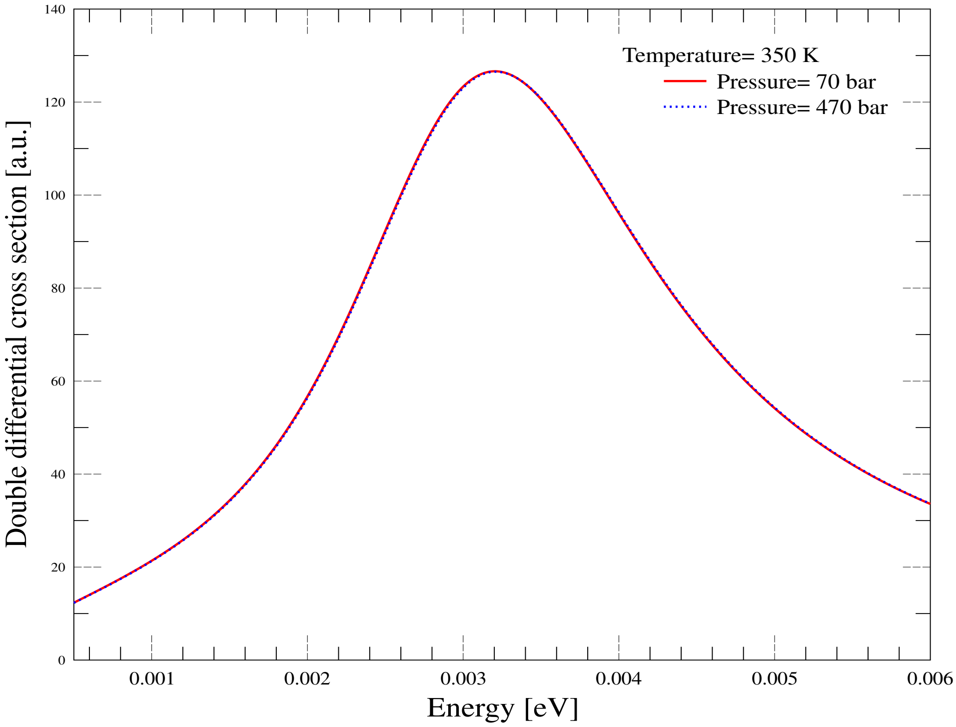

FIGURE 4.19: Double differential cross section for light water measured at the IN6 at different pressures.

4.5.2 Temperature dependence on the double differential scattering cross section

Figure 4.20 shows the experimental double differential scattering cross section of light water measured at the IN4c for an incident energy of 14.20 meV and scattering angle θ, 15° for temperatures ranging from 300 K to 517 K.

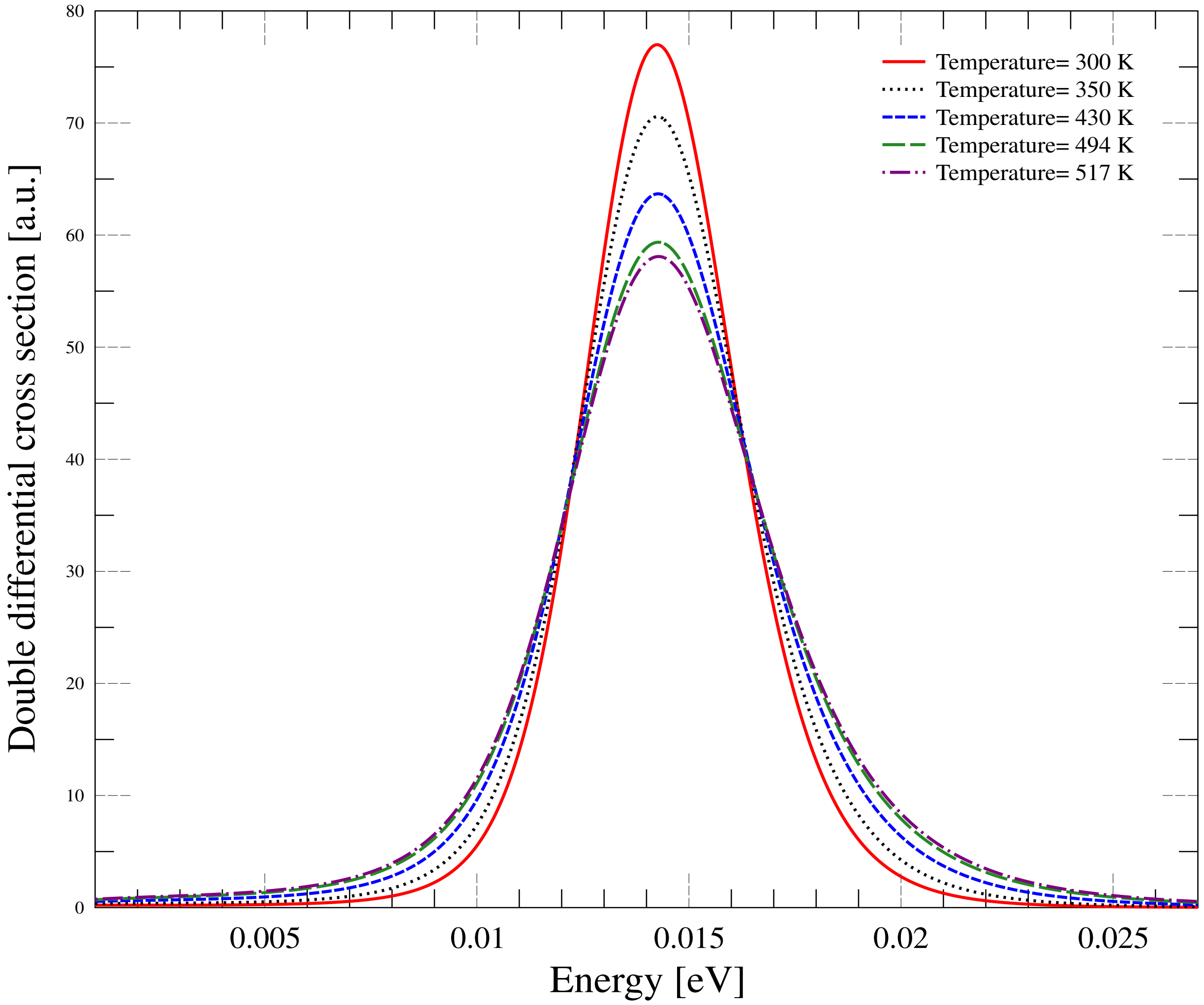

FIGURE 4.20: Double differential cross section for light water measured at the IN4c at different temperatures.

Figure 4.21 shows the experimental double differential scattering cross section of light water measured at the IN6 for an incident energy 3.15 meV and scattering angle θ, 15° at 350 and 494 K. These results are extremely important due to the fact that a majority of nuclear reactor operating in France are pressurized water reactors.

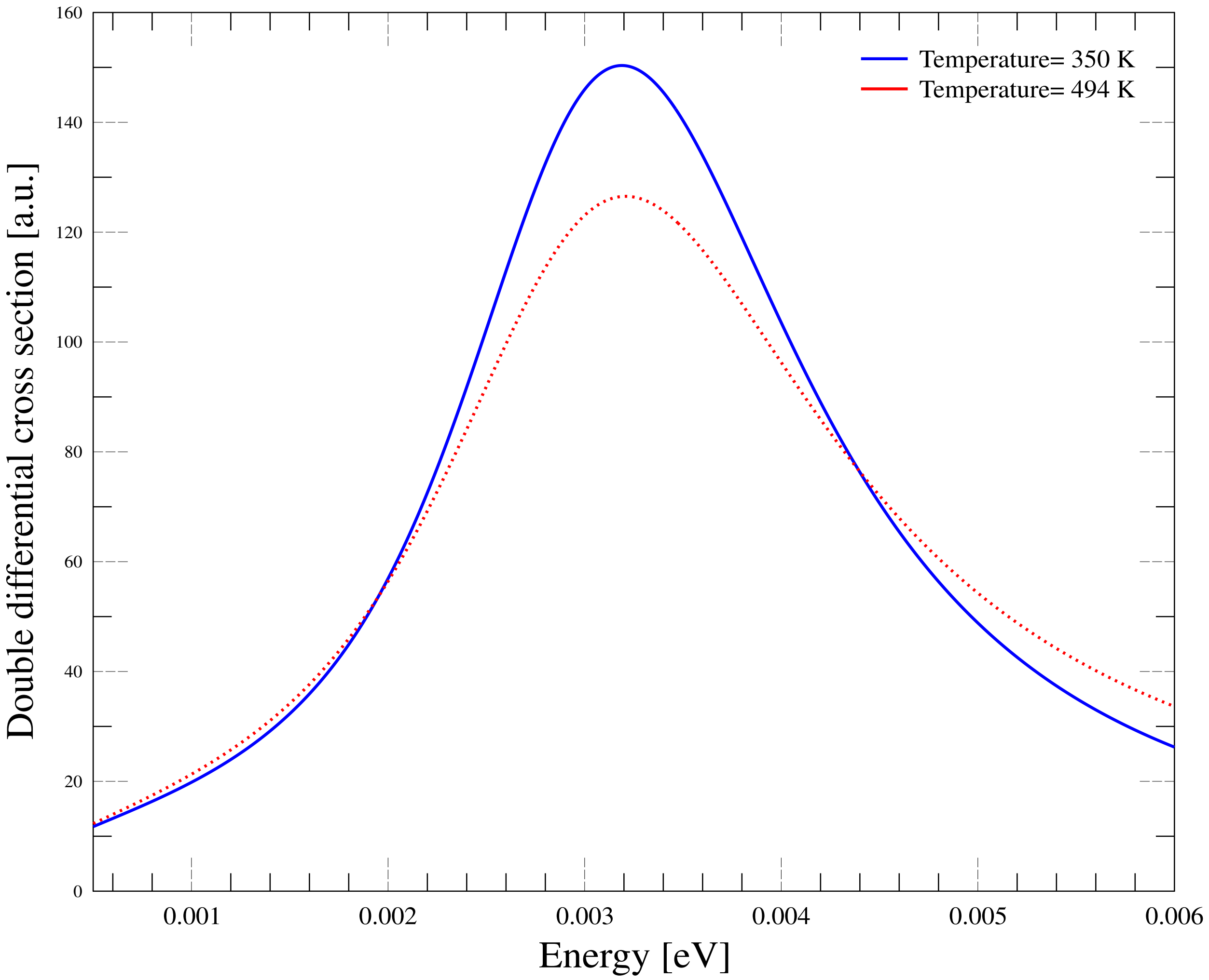

FIGURE 4.21: Double differential cross section for light water measured at the IN6 at different temperatures.

4.6. Frequency spectrum

The frequency spectrum defines the density function of available atomic vibrational energy states for energy exchange between a neutron and a water molecule. These energy states correspond to the intra molecular and intermolecular vibrations, rotations and molecular diffusion of the water molecule. The translational (diffusive properties) and rotational modes describe the motion of the water molecule as a whole whereas the vibrational modes (bending and stretching) describe the motions of the atoms within the molecule. The frequency spectrum is derived from the INS spectra obtained from both the IN4c and IN6 spectrometers following Eq. 4.4. In the next sections the effect of pressure and temperature on the frequency spectrum measured at the IN4c and IN6 are studied.

4.6.1 Pressure Dependence on the Frequency Spectrum

Two measurements at the same temperature but at different pressures have been carried out to study the impact of pressure on the TSL and also to validate our previous study of the impact of pressure on the experimental double differential cross section. The results obtained from the INS spectra measured at the IN4c at 300 K and two different pressures, i.e., 1 and 94 bar are shown in Fig. 4.22. The results from the IN6 measurements at 494 K and two different pressures, i.e, 70 and 600 bar, respectively are shown in Fig. 4.23. The results obtained from both the spectrometers indicate that there is a negligible change in the frequency spectrum of water with the change in pressure.

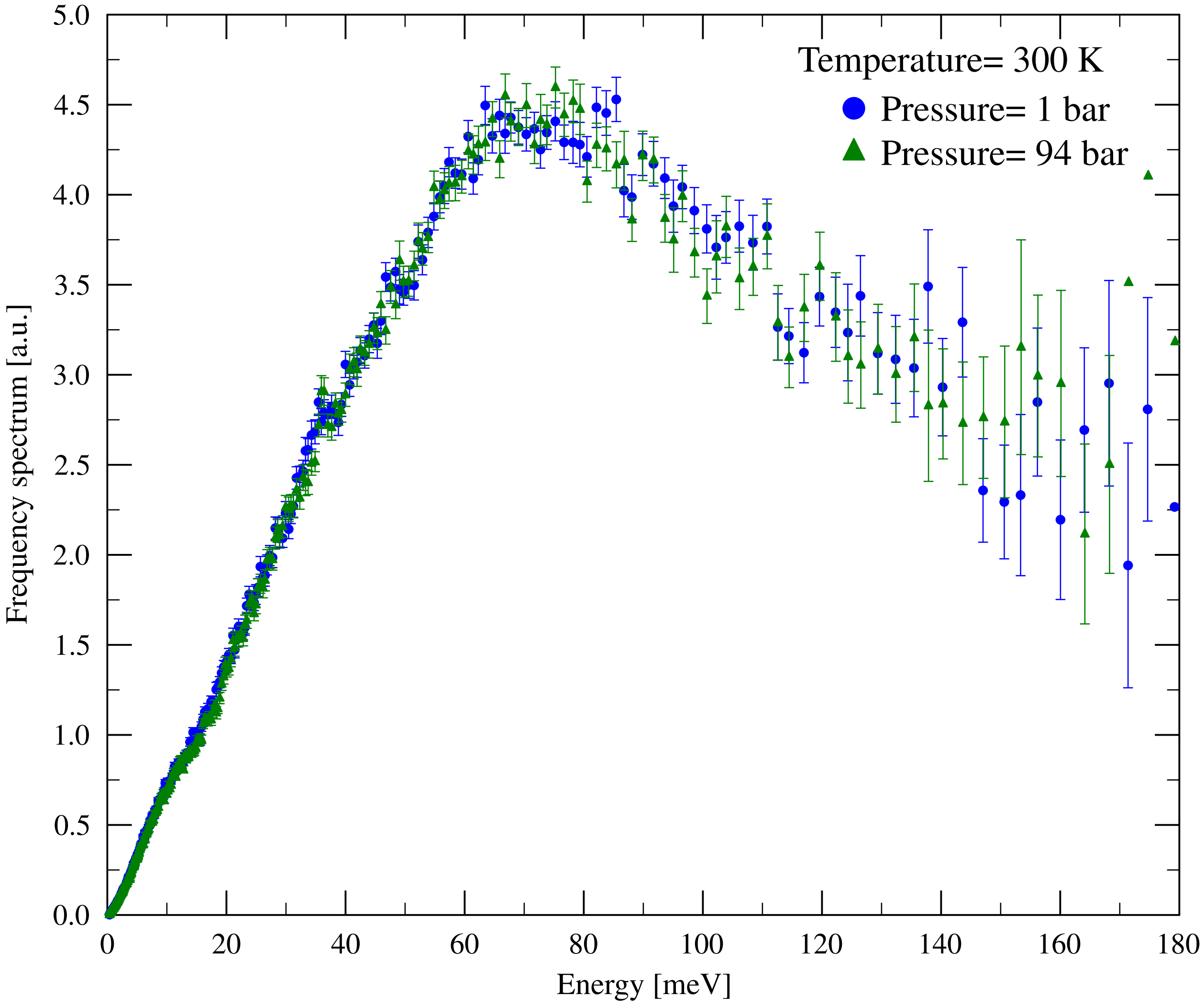

FIGURE 4.22: Frequency spectrum of light water measured at the IN4c for different pressures at 300 K.

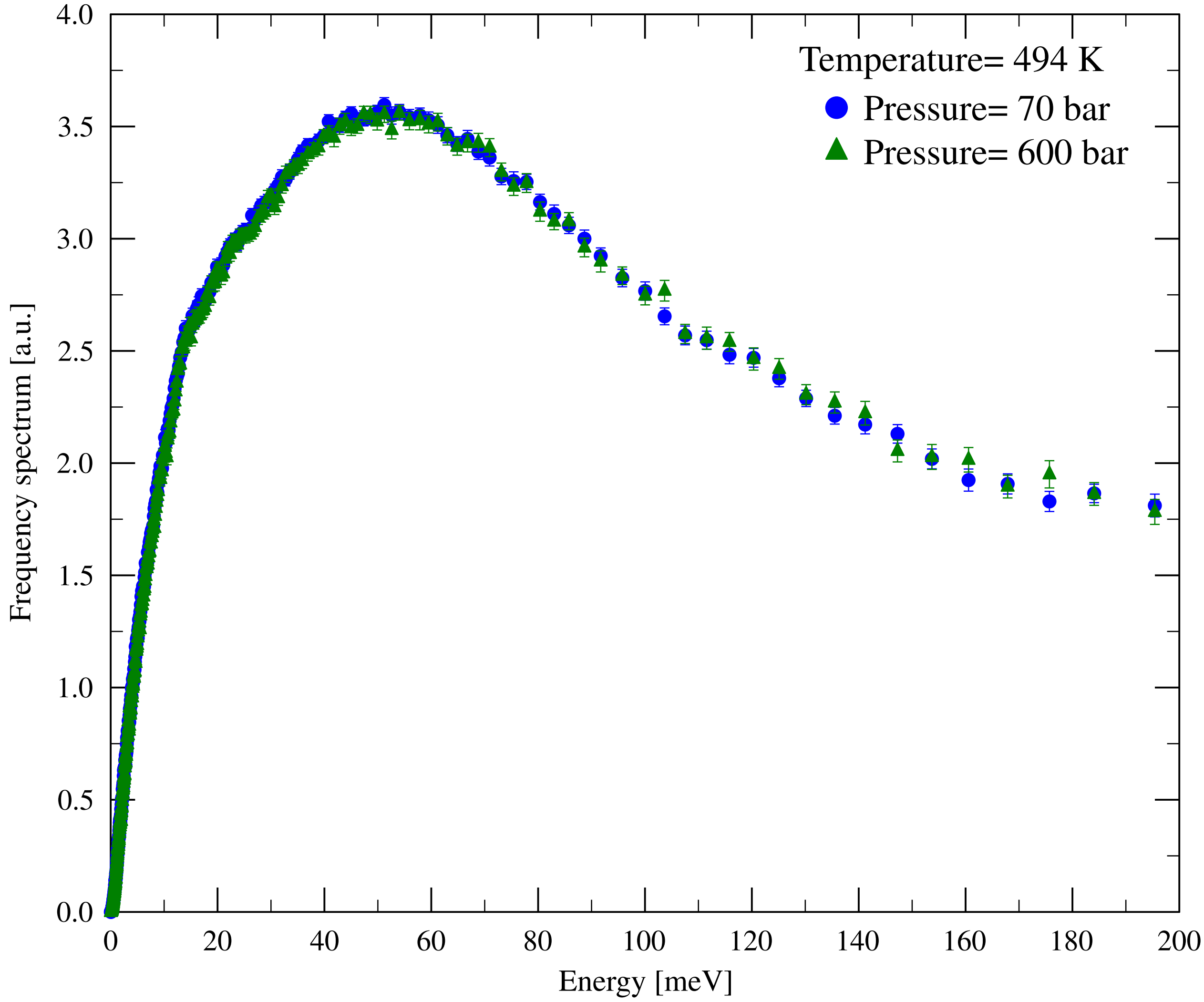

FIGURE 4.23: Frequency spectrum of light water measured at the IN6 at different pressures at 494 K.

4.6.2 Temperature Dependence on the Frequency Spectrum

Figures 4.24 and 4.25 show the variations of the frequency spectrum of water with respect to temperature for the IN4c and IN6, respectively. In Fig. 4.24, the energy corresponding to the rotation band around 75 meV, observed in the IN4c measurement at 300 K is in good agreement with the measurements by Haywood and Thorson [21]. There is a slight shift in the rotational band towards lower energy with increasing temperatures. A possible reason for this shift might be the weakening of hydrogen bonds at higher temperatures. But, within the experimental limitations of the instrument resolution at higher energies it can be concluded that the rotational band lies close to 75 meV. Due to the limitation in the experimental resolution, the translational band is missing in the IN4c spectra at all temperatures. In the IN6 spectra shown in Fig. 4.25, the rotational band is slightly shifted towards lower energy side, i.e., around 60 meV at 350 K and around 55 meV at 494 K. For both these

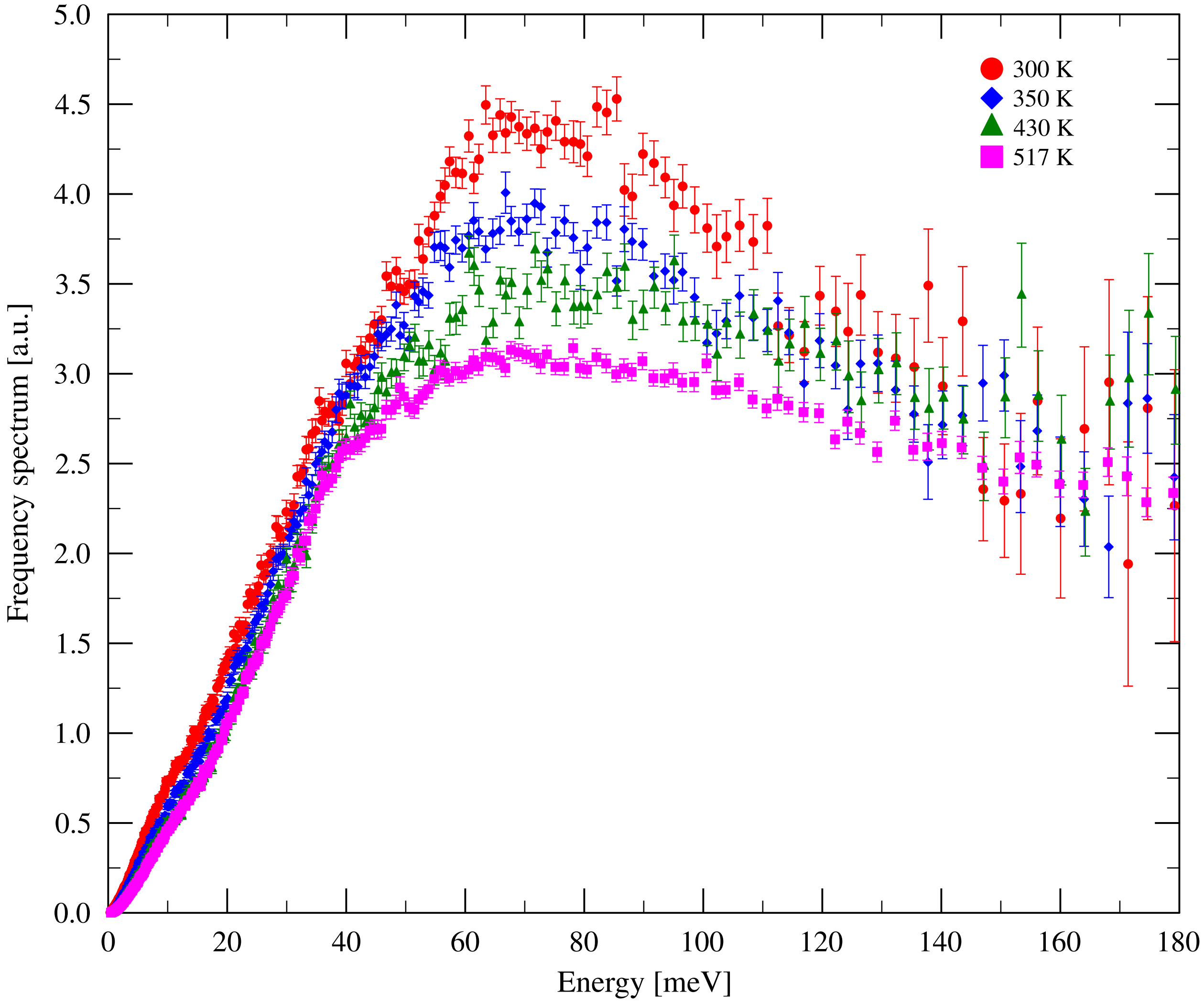

FIGURE 4.24: Frequency spectrum of light water measured at the IN4c at different temperatures.

temperatures, a peak around 12 meV is observed which might possibly correspond to the translation band of light water. A similar peak at this energy is observed in the frequency spectrum of Haywood and Thorson [21].

The present results of the frequency spectrum from both the IN4c and IN6 spectra can only reveal information on the rotational band due to the limitation in the energy transfer range. This limited range of energy transfer from both the spectrometers makes it insufficient to be fully used as an input frequency spectrum to the LEAPR module of the NJOY code. In order to overcome this deficiency, new experiments have been performed in the last week of July 2018 at the Spallation Neutron Source (SNS), Oak Ridge National Laboratory (ORNL) to extend the present measurements at high incident neutron energies. Given the large amount of time needed to carry out a thorough analysis, they will be very preliminarily discussed in the perspectives and future work.

The frequency spectrum obtained from the IN4c were used to generate TSL libraries for the temperatures

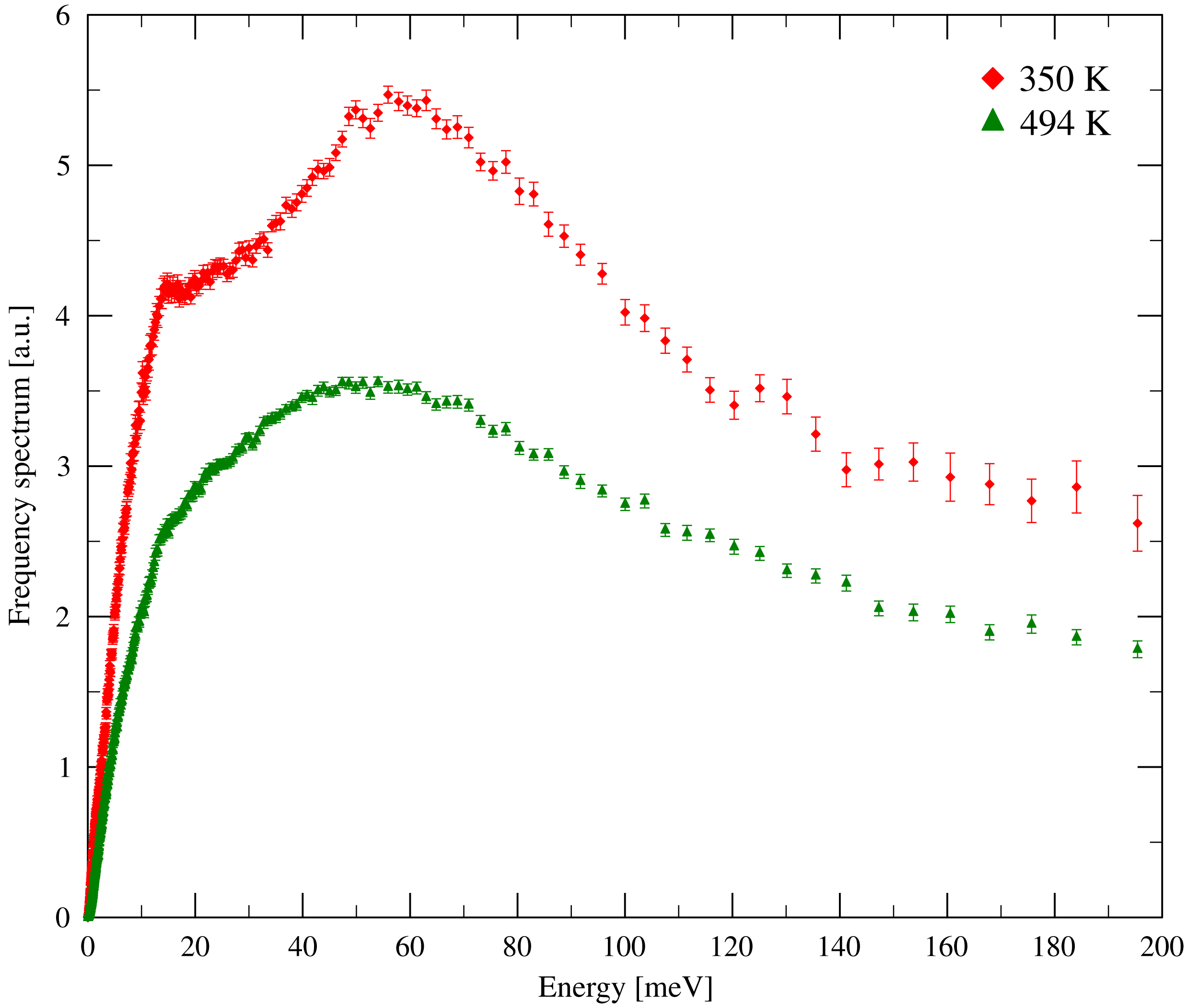

FIGURE 4.25: Frequency spectrum of light water measured at the IN6 at different temperatures.

mentioned in Table 4.1. Due to the energy and momentum transfer limitations governed by Eq. 4.3 (see also Fig. 4.2) at this chosen energy, i.e. 3.15 meV, one cannot rely on higher energy momentum and energy transfers from the measurements at the IN6. Consequently, the rotation band observed from the measurements at IN6 was not be taken into account while preparing thermal scattering cross section data using the LEAPR module of the NJOY code.

A block diagram of the procedure to generate TSL evaluation from experimental data is shown in Fig. 4.26. Two harmonic oscillators were used to represent the bending and the stretching mode of the frequency spectrum. The bending mode was described by an oscillator of energy 205 meV and the stretching mode was described by another oscillator at 436 meV. The choice of these energy for the intra molecular vibrations were adopted from the JEFF-3.3 TSL evaluation. This library is named as $S(\alpha,\beta)_{\mathrm{ILL}}$ and its performance will be evaluated in

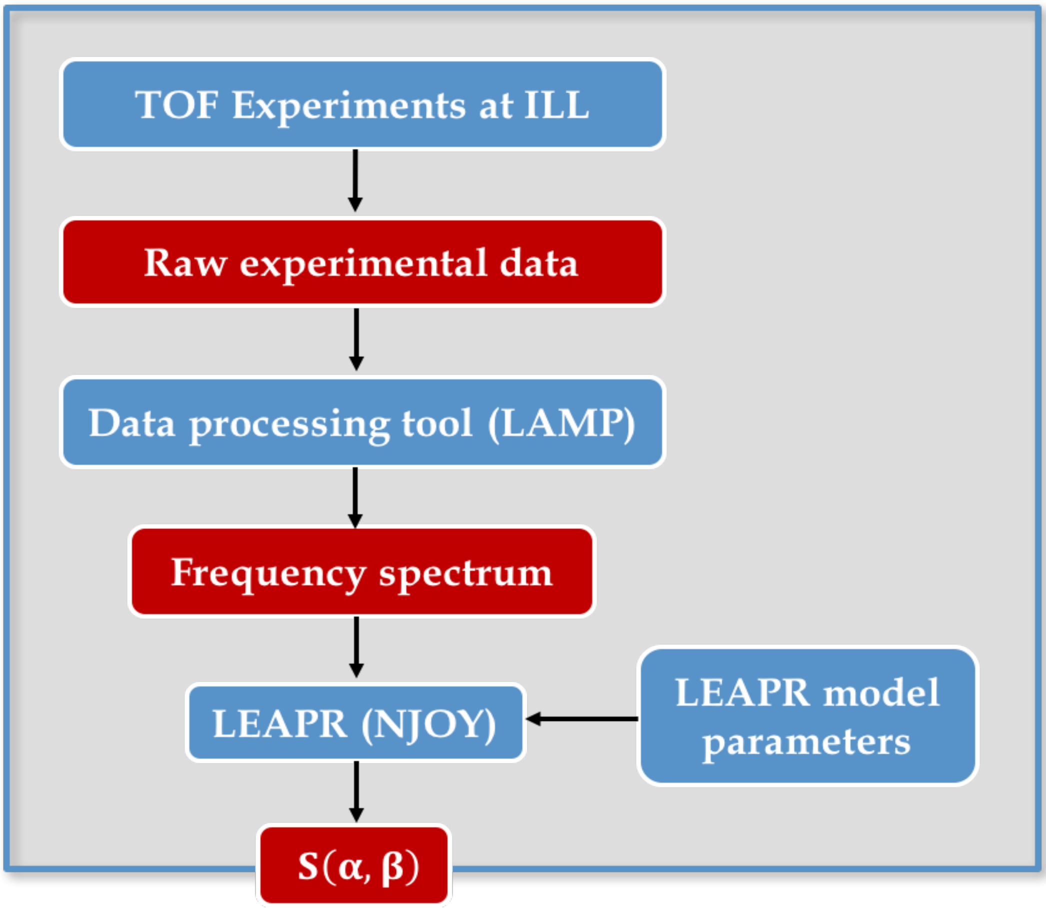

FIGURE 4.26: Block diagram of the procedure to generate TSL evaluations from TOF experiments.

Chapter 7. However, the impact of pressure and temperature on the total scattering cross section of light water is discussed in the following section.

4.7. Total scattering cross section

$S(\alpha,\beta)_{\mathrm{ILL}}$ developed using the frequency spectrum obtained at the IN4c was used to generate the total cross section of light water and compared with experimental data. Its worth mentioning that $S(\alpha,\beta)_{\mathrm{ILL}}$ was generated only at the temperatures at which the measurements were carried out at ILL. The impact of pressure and temperature on the total cross section was studies using the $S(\alpha,\beta)_{\mathrm{ILL}}$.

4.7.1 Pressure dependence on the total scattering cross section of light water

It has been shown in the previous sections that pressure has no impact on the double differential cross section and the frequency spectrum of light water measured experimentally. Figure 4.27 presents the total cross section of light water at 300 K and at two different pressures, i.e. 1 bar and 94 bar. Observing Fig. 4.27, it can be

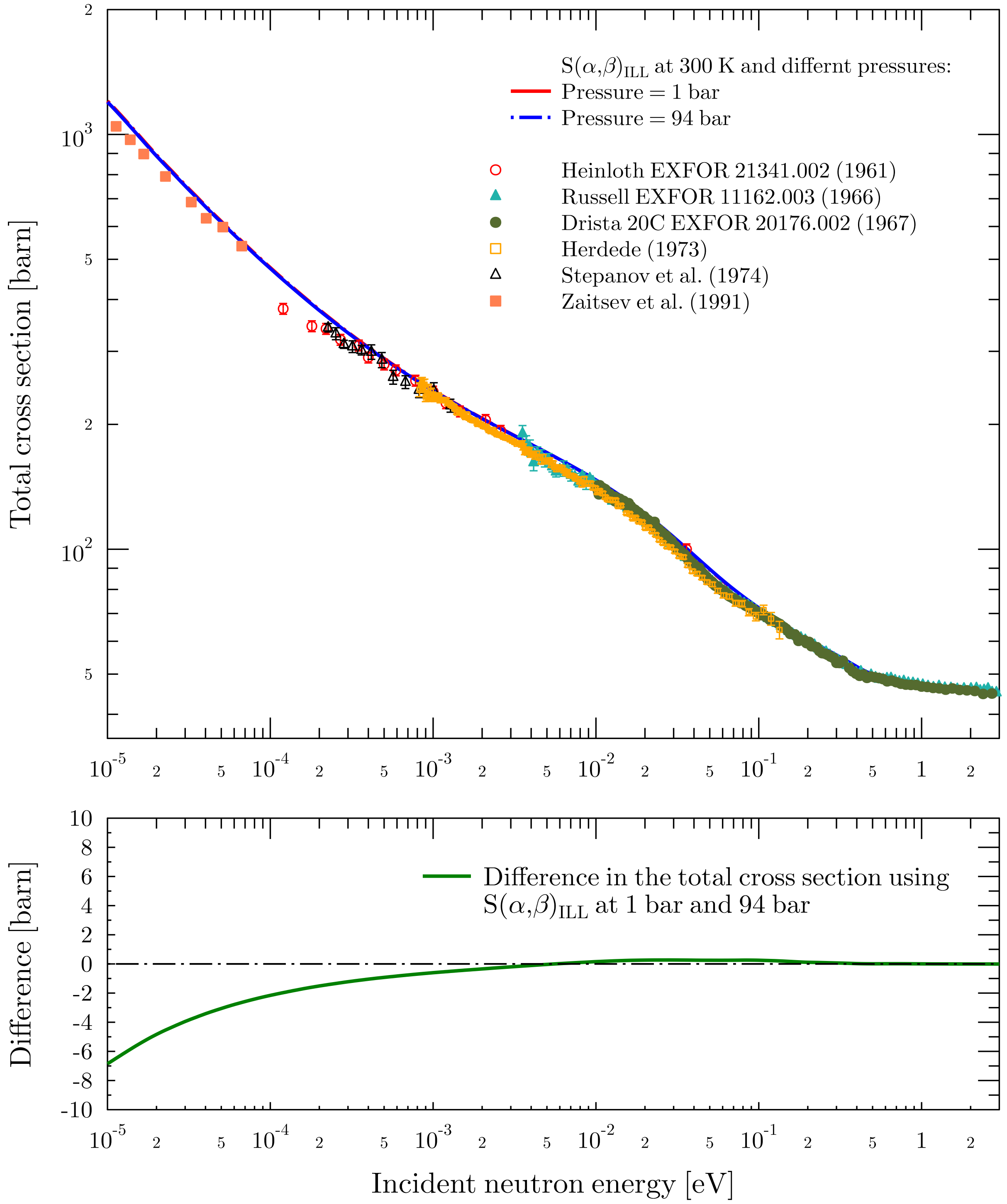

FIGURE 4.27: Comparison of the total cross section of light water at 300.0 K based on $S(\alpha,\beta)_{\text{ILL}}$ at 1 bar and 94 bar, along with the EXFOR experimental data.

concluded that pressure has negligible impact on the total cross section of light water.

4.7.2 Temperature dependence on the total scattering cross section of light water

A ratio of the total cross section of light water at high temperatures w.r.t. to room temperature data was again investigated like the one discussed in the previous chapter. Figure 4.28 shows the total cross section at the experimental temperatures generated using $S(\alpha, \beta)_{\mathrm{ILL}}$ (top curve). The ratio of total cross section (bottom curve) at the experimental temperatures generated using $S(\alpha, \beta)_{\mathrm{ILL}}$ with respect to the room temperature data showed agreement with the JEFF-3.3, i.e. the ratio increases with increasing temperatures. This is in contrast with the observation that was made with the total cross section obtained using the ENDF/B-VIII.0 TSL evaluation where this ratio decreases with increasing temperature in the range of 20 meV to 50 meV.

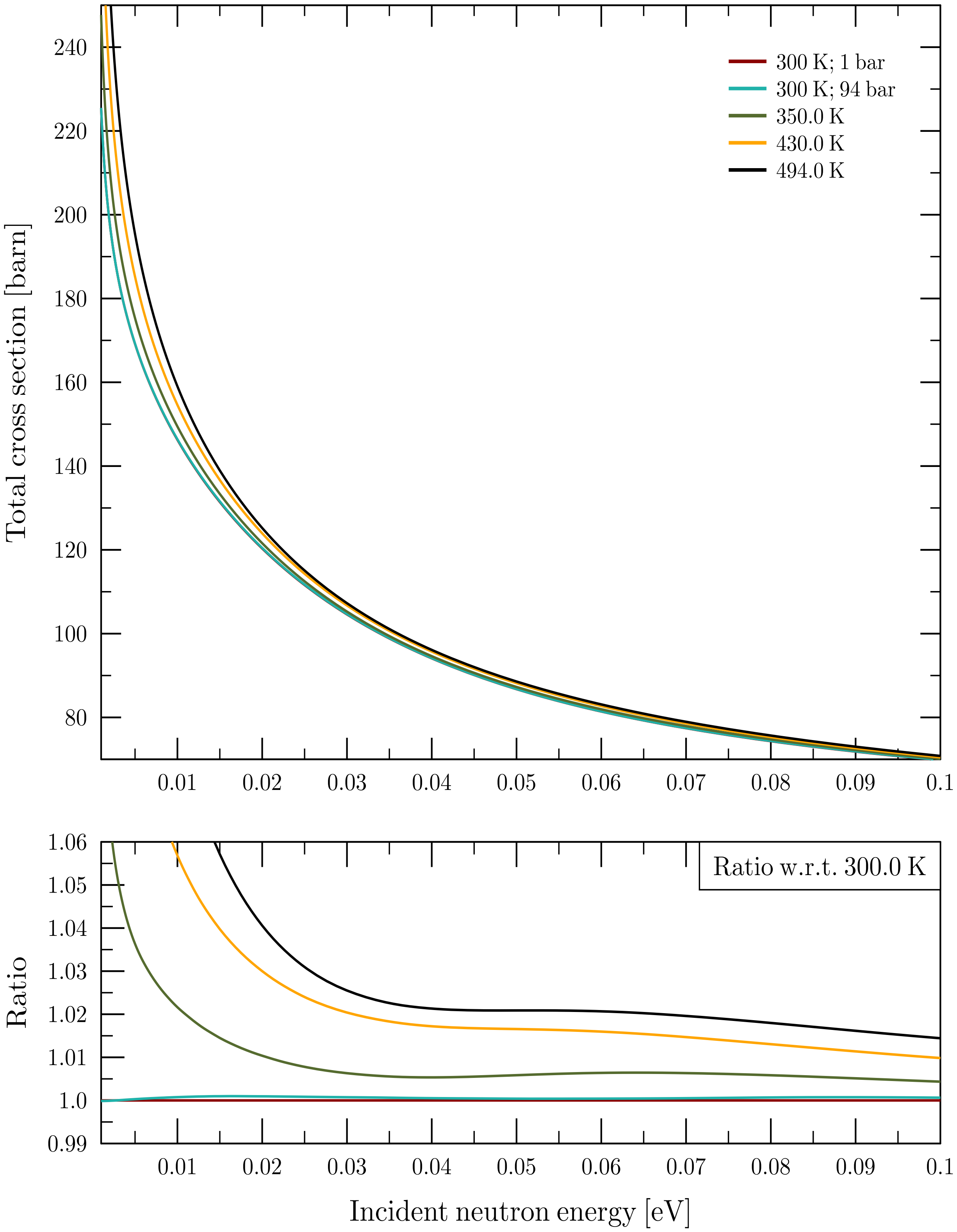

FIGURE 4.28: Ratio of the total cross section of light water at different temperatures w.r.t. 300.0 K based on $S(\alpha, \beta)_{\mathbf{ILL}}$.

Chapter 5

Molecular Dynamics simulations for light water

Inelastic neutron scattering measurements are ideal to determine the dynamical properties of a molecular system at the atomic level. Inelastic neutron scattering, discussed in the previous chapter holds its own limitations. For instance, due to kinematics restrictions and limited angular range of the detectors utilized in a typical TOF experiment one cannot measure the structure factor of light water beyond a certain energy and momentum transfer range. These limitations can be overcome by performing molecular dynamics simulations. With the rise in the computational capacities, it is possible to simulate these systems with great precision. The aim behind this chapter is to introduce the basics of molecular dynamics (MD) simulations and how one can use these simulations to predict the properties of the molecular system and can generate thermal scattering cross sections.

5.1. General overview

Light water is one of the most complex liquids and much work still needs to be done to develop a molecular model that would be able to reproduce all the properties adequately. Molecular dynamics simulations of light water rely on water models to better understand the behavior of light water at certain temperatures and pressure conditions. Molecular Dynamics (MD) simulations are based on the solution of classical equations of motion for a system composed of atoms and molecules to obtain the time evolution of the system. MD simulations differ from Monte Carlo simulations to a sense that in these simulations the time evolution of the system leads to a true dynamic process rather than through a stochastic or random walk process. While the quantum mechanical effects are supposedly important in the atomic scale, the de Broglie wavelengths of the atoms are sufficiently small for the atoms to be considered as classical. MD simulations are computationally intensive because of the involvement of solution of the equations of motions of many interacting particles. The knowledge of the atomic positions, velocities and forces are recorded as a function of time, out so as to obtain the positions and velocities at a time t and $t + \Delta$t. From the new positions, atomic forces are re-calculated and the simulation continues for another instance of time. The time steps chosen in a typical MD simulation is of the order of 1-10 femto seconds (fs), reflecting the time scale on which atomistic dynamics takes place. The overall simulation is carried out for several million time steps and the averaged properties of the system are thus obtained statistically (by time averaging the data from a single simulation over a long period of time). Several MD codes like NAMD [53], LAMMPS [54], DL_POLY [55], GROMACS [56] and PolarisMD [57] exist and all these codes provide a flexibility to choose different water models as per the user specific purpose. The output of the MD simulations is influenced by the choice of the water model used and the code itself merely acts as an engine to perform these calculations. When these models are able to predict some of the properties of the system at desired thermodynamic conditions one can utilize this model to generate other physical properties and rely on the results. To better understand the behavior of light water at various temperature and pressure conditions, the extracted properties from the MD simulations rely on the description of the water molecule itself (charge, dipole, intramolecular potential) $U^{\text{intramolecular}}$ but even more on the description of the water-water interactions, $U^{\text{intermolecular}}$. A force-field model (in our specific water model) is the total interaction potential U_{int}, sum of $U^{\text{intramolecular}}$ and $U^{\text{intermolecular}}$:

$$U_{int} = U^{\text{intramolecular}} + U^{\text{intermolecular}} \tag{5.1}$$

In the following section, the two types of water models that were explored along this study, the so-called TIP4P/2005f flexible non-polarizable model (used in the CAB model and ENDF/B-VIII.0), and TCPE rigid polarizable model are presented.

5.2. Water models and force fields

The structure of the water molecule appears to be simple. It has two hydrogen atoms and one oxygen atom having a charge of $+q$ on each hydrogen atom and $-2q$ on the oxygen atom. The water molecule is held together by electron pairing and formation of covalent bonds. Two bonding pairs and two lone pairs are formed on the oxygen atom with four unpaired electrons, thereby acquires a tetrahedron shape to form the water molecule. Intermolecular forces acting between water molecules also play an efficient role in describing the model behavior. The two lone pairs on the oxygen interact with an electron deficient hydrogen atom of the neighboring molecule. Also, the electronegative oxygen of a water molecule is attracted towards the electropositive hydrogen of the neighboring molecules. This is the hydrogen bond interaction. Depending on the temperature and pressure of the system, these intermolecular forces define the state of the system, i.e., solid, liquid or a gas.

Several informations are required to build a water model which is based on the positions of the charge, the arrangements of the charge, the distance between the hydrogen and the oxygen atoms, the H-O-H angle and the interactions between different molecules, etc. Generally, the O-H bond length varies between 0.957 Å and 1.00 Å and the H-O-H bond angles between 104.52° and 113.24° [34] due to the intramolecular vibrations of the water molecules, i.e. the bending of the H-O-H bond angles and the symmetric and asymmetric stretching of the O-H bonds.

A variety of classical water models have been developed in the past that can successfully reproduce the molecular properties of light water. They differ in several ways:

- Based on the treatment of covalent bonds. For instance, some models are termed as flexible which can allow for the bond length or angle between oxygen and hydrogen atom to change whereas rigid ones are those where these terms are fixed.
- Some models account or not for polarization effects explicitly (even higher-order terms), and few treat explicitly hydrogen bonding.

The parametrization of these models are determined to maximize the agreement of the model to thermodynamic properties. However, it should be noted that no single model can completely reproduce all the properties of water. In the next section, two water models are discussed in brief to provide a general idea of what are the basis behind construction of water models and how these models can effectively reproduce the properties of water using MD simulations especially at high temperature and pressure conditions.

5.2.1 TIP4P/2005f water potential

The water models developed in the past are mostly rigid, i.e., the intramolecular degrees of freedom are fixed. The TIP4P/2005f [35] model is a flexible water model based on the rigid TIP4P/2005 model [58]. Re-parametrization of the original TIP4P/2005 model was performed to better represent the intramolecular properties of the water molecules. One of the computational challenges arises with the use of a flexible model is that, due to the high frequency modes involved in modeling the bending and stretching modes of water one has to take a very small time step (0.1 fs) in the MD simulation. This drastically increases the simulation time. This model is described by four point charges out of which two are distributed on the hydrogen atom, one on the oxygen and one on a dummy atom placed at the angle bisector between H-O-H and hence the name 4P. A pictorial diagram of this four point interaction is given in Fig.5.1.

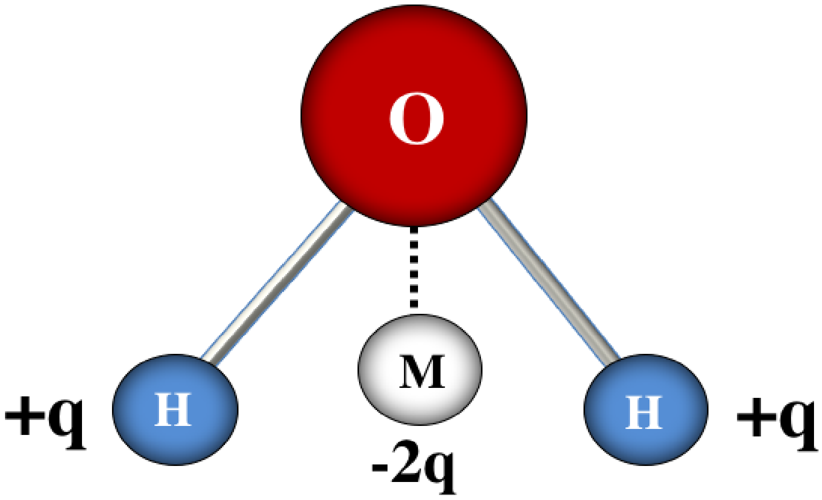

FIGURE 5.1: TIP4P/2005f water model.

In the TIP4P/2005f model, the intramolecular terms $U^{\text{intramolecular}}$ in Eq. 5.1 makes this model flexible. $U^{\text{intramolecular}}$ is described by using a Morse potential U_{OH_i} to account for the symmetric and asymmetric stretching of the OH bond and a harmonic potential $U_{HOH}(\theta)$. The functional form of U_{OH_i} and $U_{HOH}(\theta)$ are:

$$\begin{aligned} U_{OH_i} &= D_r\left[1 - e^{-\beta((r_{OH_i} - r_{eq})}\right]^2 \\ U_{HOH}(\theta) &= \frac{1}{2}k_\theta\left[\theta - \theta_{eq}\right]^2 \end{aligned} \tag{5.2}$$

Here, θ_{eq} is the equilibrium angle between the hydrogen and oxygen atom, r_{eq} is the equilibrium OH bond length and r_{OH_i} is the instantaneous OH bond lengths. The Morse potential parameters, i.e. D_r and β, define the strength and width of the bonds.

The intermolecular terms $U^{\text{intermolecular}}$ in Eq. 5.1 is described using using an electrostatic interaction and a Lennard-Jones potential U_{LJ} between oxygen atoms. The electrostatic interactions between the two hydrogen atom and the dummy atoms are described using a Coulomb potential $U_{qq'}$. The functional form of the $U_{qq'}$ is given as:

$$U_{qq'} = \frac{1}{4\pi\varepsilon_0} \sum_{i<j} \frac{q_i q_j}{r_{ij}} \tag{5.3}$$

where ε_0 is the permittivity of free space, q_i and q_j are charges of particles i and j, respectively and r_{ij} is the distance between these particles. The functional form of U_{LJ} acting between oxygen atoms is represented as:

$$U_{LJ} = 4\epsilon \left[\left(\frac{\sigma_{ij}}{r_{ij}} \right)^{12} - \left(\frac{\sigma_{ij}}{r_{ij}} \right)^{6} \right] \tag{5.4}$$

Here, ε is depth of the potential well and σ_{ij} is the finite distance between particles i and j at which the potential is zero.

5.2.2 TCPE water potential

Polarization can be defined as redistribution of charge due to electric field. A more realistic model to describe water properties can be the one which takes into account the polarization of the molecules. Polarization effect should be included in the model to expect it to behave satisfactorily at high temperatures. TCPE is one of those models which is based on three static charge sites and a polarizable site which effectively models the electrostatic properties of water molecules. A pictorial diagram of the model is shown in Fig. 5.2.

Moreover, to account for long-range interactions, a specific hydrogen bonding interaction is modeled by an isotropic short-range many-body energy term. The model successfully reproduces many light water properties at ambient conditions as well as over a wide range of temperatures and pressures [57]. This led to a favorable choice of water model for reactors operating at high temperature and pressure conditions. A detailed description about the water model can be found in Ref. [57, 59]. A brief explanation about the interaction mechanism of the TCPE potential is explained below.

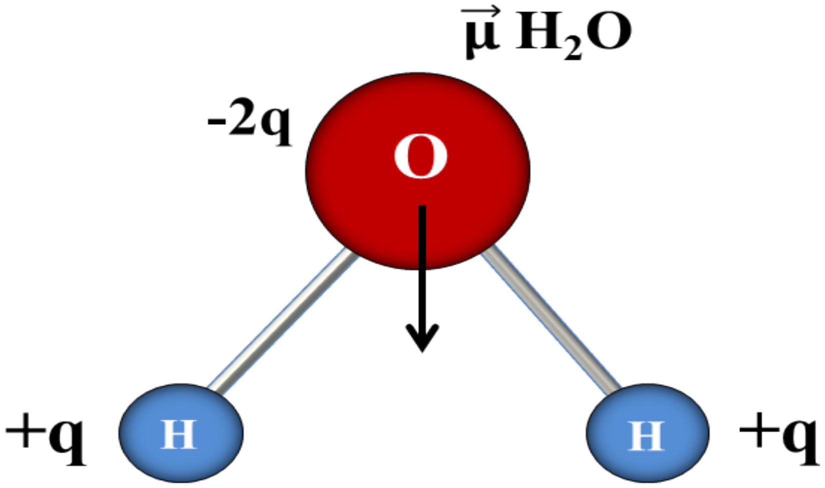

FIGURE 5.2: TCPE water model.

The TCPE water model is based on the decomposition of the potential energy U_{int} as follows:

$$U_{int} = U_{rep} + U_{qq'} + U_{pol} + U_{hb} \tag{5.5}$$

The individual terms in Eq. 5.5, corresponds to the repulsive term, the Coulombic term, the polarization term, the intramolecular relaxation term and the hydrogen bonded term.

The intermolecular repulsive term is given by a radial pairwise energy form. For a system of N atoms, U_{rep} is given as:

$$U_{rep} = \sum_{i,j}^{N} A_{ij} exp(B_{ij} r_{ij}) \tag{5.6}$$

where A_{ij} and B_{ij} are parameters that depends on the chemical nature of the atoms i and j, and r_{ij} is the distance between the atoms.

The standard additive potential is used to define the Coulombic term $U_{qq'}$ follows,

$$U_{qq'} = \frac{1}{4\pi\varepsilon_0} \sum_{i<j} \frac{q_i q_j}{r_{ij}} \tag{5.7}$$

where q_i and q_j are static point charges at the centers of the atom.

U_{pol} taken into account the polarization effects,

$$U_{pol} = \sum_{i=1}^{N_{pol}} \frac{\vec{\mu}_i^2}{2\alpha_i} - \sum_{i=1}^{N_{pol}} \vec{\mu}_i \vec{E}_i^o - \sum_{ij,i\neq j}^{N_{pol}} \vec{\mu}_i \hat{\mathbf{T}}(|\vec{r}_i - \vec{r}_j|)\vec{\mu}_j \tag{5.8}$$

where $\vec{\mu}_i$ is a set of induced dipole moments, the isotropic polarizability of the polarizable atom i is given by α_i, $\vec{E}_i^o$ is the static electric field and T_{ij} is the dipolar tensor.

And finally, U_{hb} is the many-body hydrogen bond term to model the interactions between water molecules [59]. Since TCPE is a rigid model for water, the bond length of OH is fixed to be 0.97 Å and the angle between H-O-H is set to 106.0°. All the parameters can be found in Ref. [57]. The parameters of the TCPE model were parametrized to reproduce the interaction energy of water clusters using ab initio quantum chemical methods. No parameters were fitted to reproduce the experimental data as is generally the case with the development of water models where the models are fitted to reproduce some specific properties of water measured experimentally. This makes the TCPE model different, i.e. unbiased to reproduce some specific water properties.

5.2.3 Preferred choice between TIP4P/2005f and TCPE water potential for reactor physics applications

Shvab and Sadus have compared a bunch of water models both rigid/flexible and polarized for both ambient and supercritical conditions [34]. The paper draws the attention that adding flexibility to a water model might not necessarily improve its overall performance. It was found that the flexible TIP4P/2005f model fails to reproduce some of the properties of light water like supercritical heat capacities and thermal expansion coefficient as compared to its rigid counterpart TIP4P/2005. It can also be argued that intramolecular vibrations are quantum mechanical phenomena and hence using classical molecular dynamics simulations to study this behavior should be taken with care as one might need to apply quantum corrections. Temperatures and pressures outside the ambient temperatures where these models were parametrizes, start seeing disagreements with experimental data. Hydrogen bonding and shell structures plays an important role in developing a water model valid at high temperatures [34]. As compared to rigid non-polarizable models, polarizable models respond to fluctuations in the electric field due to molecular motion.

Since nuclear reactors operate at high temperatures and pressures the choice of a water model depends on its performance, i.e. its ability to reproduce water properties at high temperatures and pressures. It appears that a polarizable model is a promising solution for reactor physics applications where the reactors operate at high temperatures and pressure. Also, since the purpose of our study is to generate frequency spectrum of light water to be later utilized by the LEAPR module of the NJOY code, where the high energy intramolecular modes are generally replaced by discrete oscillators, choosing a flexible model will not be of much help. This can also be validated with the fact that even though flexible TIP4P/2005f water model was utilized for generating TSLs in the

ENDF/B-VIII.0, the intramolecular modes were still modeled using discrete oscillators. Though TIP4P/2005f model has been validated on a number of thermodynamic, dynamic and structural properties of light water but its application is still limited for water molecules at high temperatures and pressures. Whereas, TCPE water model though being a rigid model accurately reproduces the experimental self-diffusion coefficient of water for a series of high temperatures, a property that is important for reactor applications, in particular generating TSLs. Due to these reasons the TCPE water model was used throughout the entire MD simulations carried out in this work.

5.3. Light water simulations using TCPE model

The calculation of the frequency spectrum from MD simulations has been successfully carried out in the past and the results at ambient conditions are promising [24]. This has also been shown in the **Chapter 3** where the TSL in the ENDF/B-VIII.0 library performs very good at ambient temperatures. Out of the two models presented before, the non-polarizable, flexible model, i.e. TIP4P/2005f is utilized in the ENDF/B-VIII.0. Tremendous work has already been done using the TIP4P/2005f water model by Centro Atomico Bariloche (CAB) team in Argentina. Hence, as an initial approach, this model was chosen as a base for developing our knowledge to generate frequency spectra using GROMACS (Groningen Machine for Chemical Simulations) MD package [56]. After understanding the methodology needed to generate frequency spectra using MD codes and potentials like TIP4P/2005f, the final simulations for light water was performed with TCPE polarizable water potential using the PolarisMD code. The simulations were carried out on the PhLAM cluster of the University of Lille for a series of temperature and pressures. Periodic boundary conditions and standard Ewald summation techniques were utilized, considering a cubic box of size 30 $Å^3$ with 997 water molecules (2991 atoms). The equations of motion were solved with a time step of 1 fs to take into account the short range inter-molecular interactions between the light water molecules. The generalized Gaussian moment thermostat for NVT ensembles whereas, Nosé-Hoover barostat was used for NPT ensembles. Both O-H bonds and the H-O-H angles were fixed irrespective of the thermodynamic ensemble. For each condition, equilibration simulation is performed for 1 ns, and further pursued for 100 ps, saving the positions and velocities each 5 fs. The temperatures and pressures at which the simulations were performed are mentioned in Table. 5.1.

Temperature	Pressure
(K)	(bar)
283.6	1
293.6	1
295.0	1
323.6	1
350.0	1
373.6	3
400.0	8
423.6	10
450.0	20
473.6	20
500.0	30
523.6	50
550.0	75
573.6	100
600.0	150

TABLE 5.1: Simulation with TCPE potential at different temperatures and pressures.

For the calculation of the frequency spectrum of light water, the trajectory file containing the positions and velocities of the atoms in the simulations were analyzed. A block diagram of the procedure to obtain the frequency from MD simulations is summarized in Fig. 5.3. A code was written in python to do the transformation of the trajectories (velocities of the atoms at different instance of time) to the velocity auto correlation function (VACF) following Eq. 5.9.

$$\mathit{VACF(t)} = \frac{\sum_{i=1}^{N}\langle \mathbf{v}_i(t)\cdot\mathbf{v}_i(0)\rangle}{\sum_{i=1}^{N}\langle \mathbf{v}_i(0)\cdot\mathbf{v}_i(0)\rangle} \tag{5.9}$$

The denominator in Eq. 5.9 is the normalization factor which can be replaced with $3Nk_BT$ to take the form:

$$\mathit{VACF(t)} = \frac{1}{3Nk_BT}\sum_{i=1}^{N}\langle \mathbf{v}_i(t)\cdot\mathbf{v}_i(0)\rangle \tag{5.10}$$

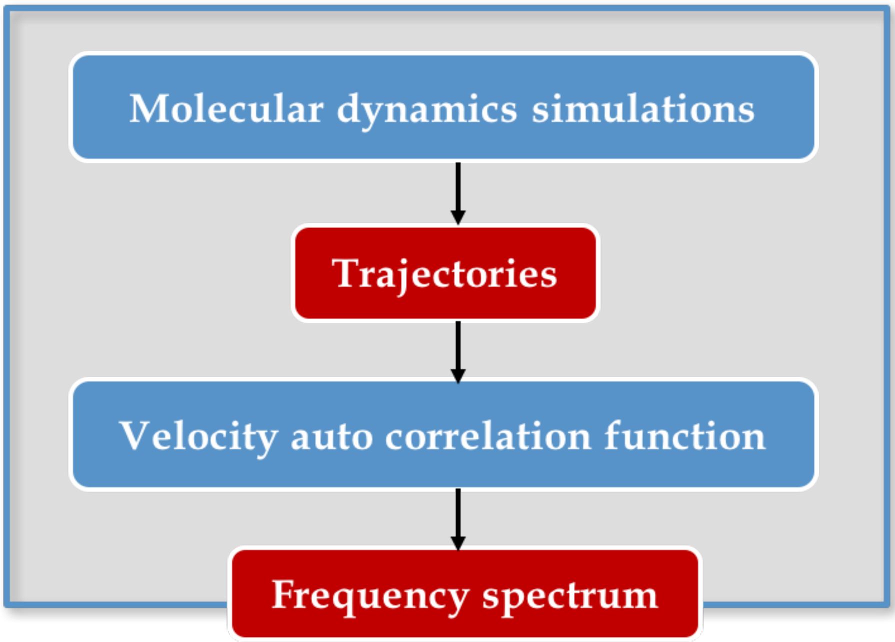

FIGURE 5.3: Block diagram of the MD data analysis.

VACF, has the complete information about the time evolution of the system. The frequency spectrum is then computed as the cosine Fourier transform of the VACF as below:

$$\rho(\omega) = \frac{1}{3NTk_B} \int_{-\infty}^{\infty} \sum_{i=1}^{N} \langle \mathbf{v}_i(t) \cdot \mathbf{v}_i(0) \rangle \, e^{i\omega t} dt \tag{5.11}$$

5.3.1 Analysis of the MD simulation data

The procedure mentioned in Fig. 5.3 is applied individually on both hydrogen and oxygen to obtain the frequency spectrum of hydrogen bound in light water $\rho(\omega)_H$, and oxygen bound in light water $\rho(\omega)_O$. However, for the case of light water the frequency spectrum of the light water molecule $\rho(\omega)_{H_2O}$ can be well approximated with the frequency spectrum of hydrogen $\rho(\omega)_H$. This is due to the fact that in a vibrating system each specie vibrates at the same frequency but the amplitude of motion of each specie is roughly proportional to the inverse of the mass of the specie. Hence, for light water molecule, with the mass of Oxygen being 16 and that of Hydrogen being 1, $\rho(\omega)_{H_2O}$ is close to $\rho(\omega)_H$. Hence, the frequency spectrum of light water was approximated by the frequency spectrum of hydrogen bound in light water for all the simulations carried out during this study. A series of temperatures were simulated ranging from 283.6 K up to 600.0 K as presented in Table. 5.1.

Figure 5.4 shows the frequency spectra of light water obtained using the TCPE water potential at several thermodynamic conditions. One can clearly observe both the translation and the rotation bands in the frequency

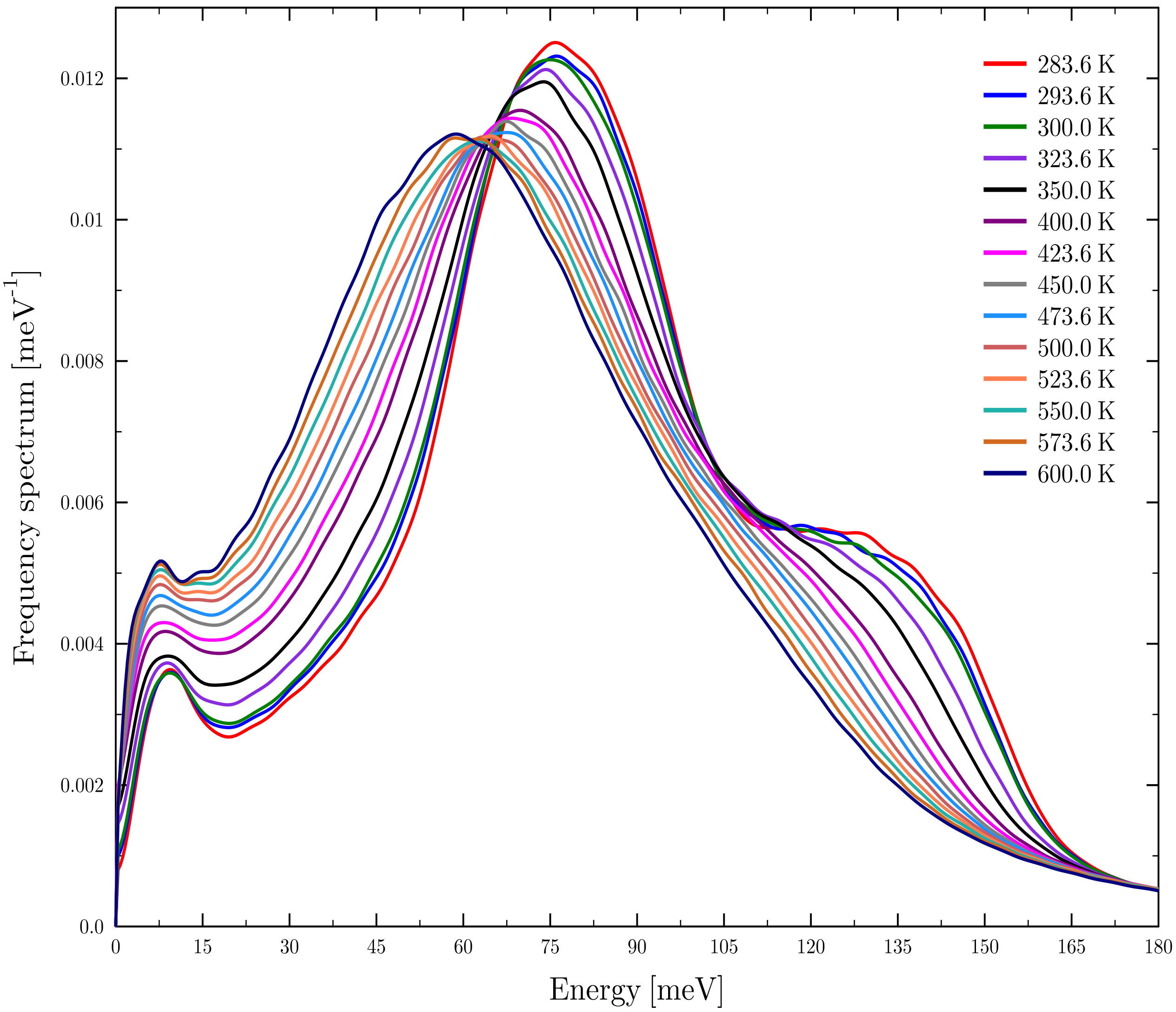

FIGURE 5.4: Frequency spectrum of light water obtained using TCPE water potential.

spectra for the entire range of temperatures. The bending and the stretching modes are not visible in the frequency spectra as TCPE, being a rigid potential, does not reflects the intramolecular bands of the frequency spectrum. However, this does not pose any limitation to our simulations as the bending and stretching modes are generally replaced using harmonic oscillators while preparing the thermal scattering data using the LEAPR module of NJOY.

On investigating the shape of the frequency spectrum, it was observed that the position of the rotation band at 293.6 K is around 75 meV, slightly higher than the one observed in the ENDF/B-VIII.0 where it is peaked at around 65 meV. The peak around 75 meV obtained using TCPE potential is in agreement with the ILL measurements at the IN4c where the rotation band was observed around 75 meV. Hence, the shape of the frequency spectra obtained using ILL measurements were validated with better confidence using these TCPE MD simulations. The position of the rotation band which lies around thermal energy range is important in reactor applications. A down shift in the energy of the rotation band of around 15 meV was observed with increasing temperatures between 293.6 K and 600.0 K. However, the shift is not as significant as compared to the frequency spectrum of the ENDF/B-VIII.0 generated using the TIP4P/2005 potential which is around 25 meV.

From the frequency spectra obtained using TCPE water model, TSL evaluations at different temperatures were prepared and was named as $S(\alpha,\beta)_{\text{TCPE}}$. A block diagram of the procedure to generate TSL evaluations using MD simulations is given in Fig. 5.5. The LEAPR model parameters in Fig. 5.5 is similar to the one used in the ENDF/B-VIII.0 TSL for light water where an Egelstaff and Schofield model was used to describe molecular diffusion after subtracting the diffusion component from the frequency spectrum. Verification and validation of this new $S(\alpha,\beta)_{\text{TCPE}}$ on differential, double differential and total cross section are discussed in **Chapter 7**. $S(\alpha,\beta)_{\text{TCPE}}$ is also tested on a set of ICSBEP benchmarks sensitive to thermal scattering energy region and the results are presented in **Chapter 7**.

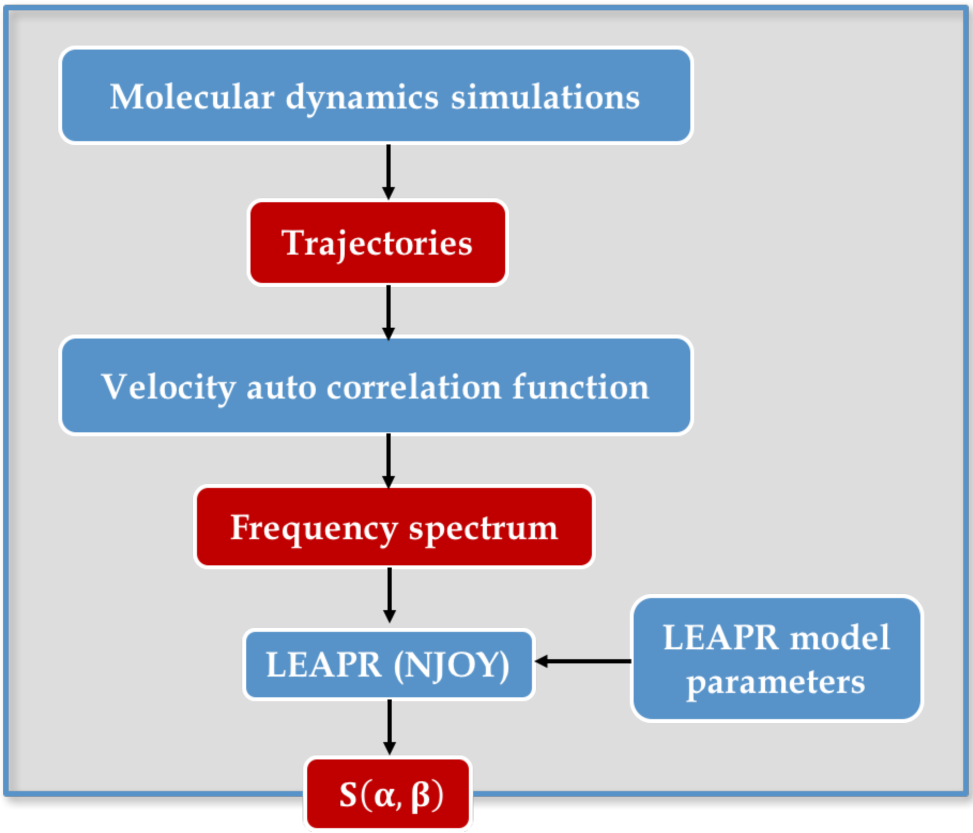

FIGURE 5.5: Block diagram of the procedure to generate TSL evaluations from MD simulations.

Chapter 6

Evaluation and processing of TSL for light water

Neutronics codes require processed cross section data in a specific format to carry out simulations. These cross section data are computed using evaluated nuclear data files available in the nuclear data libraries. Presently, a variety of nuclear data processing codes like NJOY, AMPX [60], PREPRO [61], etc. exist which consist of several modules that perform operations on the evaluations and compute the cross sections to be used by the neutronics tools. This chapter deals with the evaluation and processing of thermal scattering cross section data of light water using IRSN in-house code, GAIA which is under development as a part of the INSIDER (**I**nvestigations in **N**eutronics for **S**afety margin assessment based on data assimilation from **I**ntegral and **D**ifferential **E**xperimental **R**esearches) project.

6.1. Nuclear data evaluation and processing at IRSN

6.1.1 GAIA project

IRSN utilizes Monte Carlo codes like MORET, MCNP, VESTA, SCALE 6 and DRAGON/DONJON suites for reactor and criticality safety studies and verification of designs given by the nuclear utilities. These simulation codes require either multi-group or continuous energy cross section libraries in specific format, such as for instance, ACE files for MCNP, XML files for MORET, etc,.

IRSN follows three major steps to check the validity of the nuclear data library for internal use:

- Firstly, the library processing methodology is verified and documented.
- Secondly, the output printed by the processing codes is examined.
- Thirdly and finally, the processed data library is validated for use after testing it on a preselected critical benchmarks sensitive to different neutron energy regions, i.e. thermal, intermediate and fast energy region.

The GAIA project is under development at the IRSN, to process nuclear cross section data libraries with innovative features and processing capabilities. The project is taking shape in the form of two different codes:

- GAIA 1: In the initial phase of the GAIA project, an NJOY wrapper called as GAIA 1 was developed to minimize the effort for the generation of nuclear data libraries using the NJOY code. It reads the ENDF file, generates the corresponding NJOY input file and processes the cross section data using the NJOY data processing code. The latest version of the GAIA 1 code is GAIA 1.1.1 which is based on NJOY 2016.35, not only generates cross section data libraries, but also performs additional tasks to verify these cross sections and adds any missing data. As an example, verification of the unresolved probability tables is carried out where it checks if there are any negative cross-section values. In the case of negative cross section values, it reruns NJOY without the probability tables. It produces standard neutron cross sections and thermal scattering cross section data in the ACE format to be used by the MCNP and MORET codes. In addition, it also has the capability to generate PENDF files to be used by the VESTA code, XML files for the MORET code. Covariance files are also generated in the BOXER format.
- GAIA 2: GAIA 2 is an advanced version over its predecessor GAIA 1 and is on a developmental stage. It is a nuclear data manipulation software framework based on C++ modular programming. The main idea of the GAIA 2 project is to process nuclear data libraries not only independent of the NJOY code as far as possible but also involving new processing methodologies. Multiple ways of using the software have been planned, i.e. as a standalone application or as an integrated component in other applications. A block diagram of the nuclear data processing under the GAIA project is shown in Fig. 6.1. The main objectives of GAIA 2 are summarized below:
  - Implement the knowledge acquired on processing methodologies at IRSN to a nuclear data processing code.

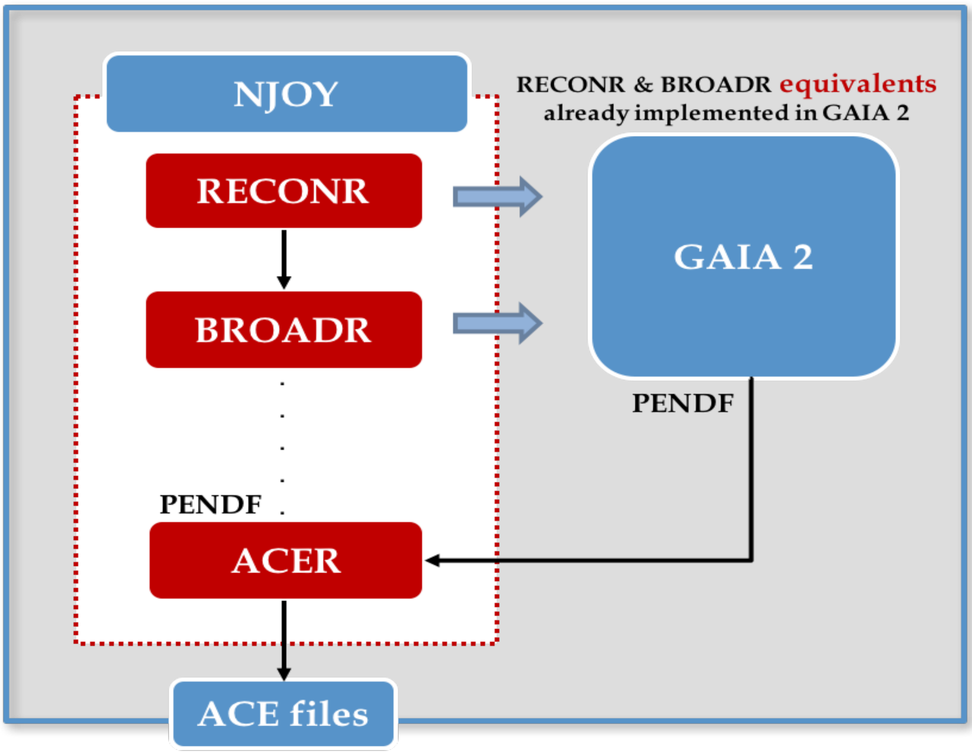

FIGURE 6.1: Nuclear data processing in the GAIA project.

- Generate nuclear cross section data libraries in specific formats for present and future neutronics tools.
- Provide the capability to read and write from various cross section data formats, i.e. ENDF, GND or any new future format.
- Manipulate cross section data outside the scope of existing cross section processing tools.
- Generalized R-matrix formalism for resonance reconstruction.
- Doppler broadening based on innovative methodologies like Fourier transformation [62].
- Improved formalism in the unresolved resonance region (Ongoing PhD subject at IRSN)
- Implementation of the developments carried out during this PhD thesis, to generate TSL evaluations as a new module named as "SAB module".

The next section introduces the SAB module that was developed as a part of this PhD work, which facilitates the generation of TSL libraries.

6.2. SAB Module

As part of the present research work thermal scattering developments made throughout this PhD were embedded in the form of a new module called as SAB module to generate thermal scattering cross section data in the ACE format. Presently, only light water developments have been taken into account but other moderators will be added in the near future. The motivation for developing a new module in the GAIA 2 code was related to ease the generation of TSL. The TSL in the SAB module can be generated following distinct paths such as from TOF experiments, MD simulations as well as from the existing evaluations. A block diagram of the SAB module is given in Fig. 6.2. TSL in the ACE format is in general required in order to be used by a majority of the neutronics codes, for instance MCNP, MORET, etc. Keeping this in mind, the aim of the SAB module is to prepare TSL in the ACE format.

As can be seen in Fig. 6.2, the user has to first select the moderator material for which TSL evaluations has to be generated, followed by the desired temperature. As mentioned before only TSL for light water developments have been included in the code but other moderator materials can be easily added to this module to enhance its functionality. There are two major blocks in generating TSL in the SAB module. Firstly, new TSLs at desired temperature can be generated using preexisting TSL evaluation in the nuclear data libraries or new libraries can be generated based on MD simulations and TOF experimental data.

First, a general methodology of generating TSLs from preexisting TSL evaluations is explained. A set of LEAPR input parameters from different TSL evaluations, for instance, JEFF-3.3, ENDF/B-VII.1, ENDF/B-VIII.0, etc, are stored for different temperatures. User then has to make a choice between the evaluations which is to be used to further generate the TSL evaluation. If the temperature requested by the user exists in these LEAPR model parameter files, it is straightforward passed to the THERMR and ACER block to generate TSL libraries in the ACE format. However, if the requested temperature is not one of those existing in the LEAPR model parameter files, the SAB module will interpolate the frequency spectrum and other LEAPR model parameters and run LEAPR to generate TSL at the desired temperature, followed by THERMR and ACER modules to generate TSL in ACE formats.

Another interesting feature of the SAB module is the capability to read experimentally measured frequency spectrum (as discussed in **Chapter 4**) or frequency spectrum generated using MD simulations (as discussed in **Chapter 5**) and generate TSL evaluations accordingly. A set of frequency spectrum are stored in the SAB modules at different temperatures generated using MD simulations (TCPE water model) as well as the

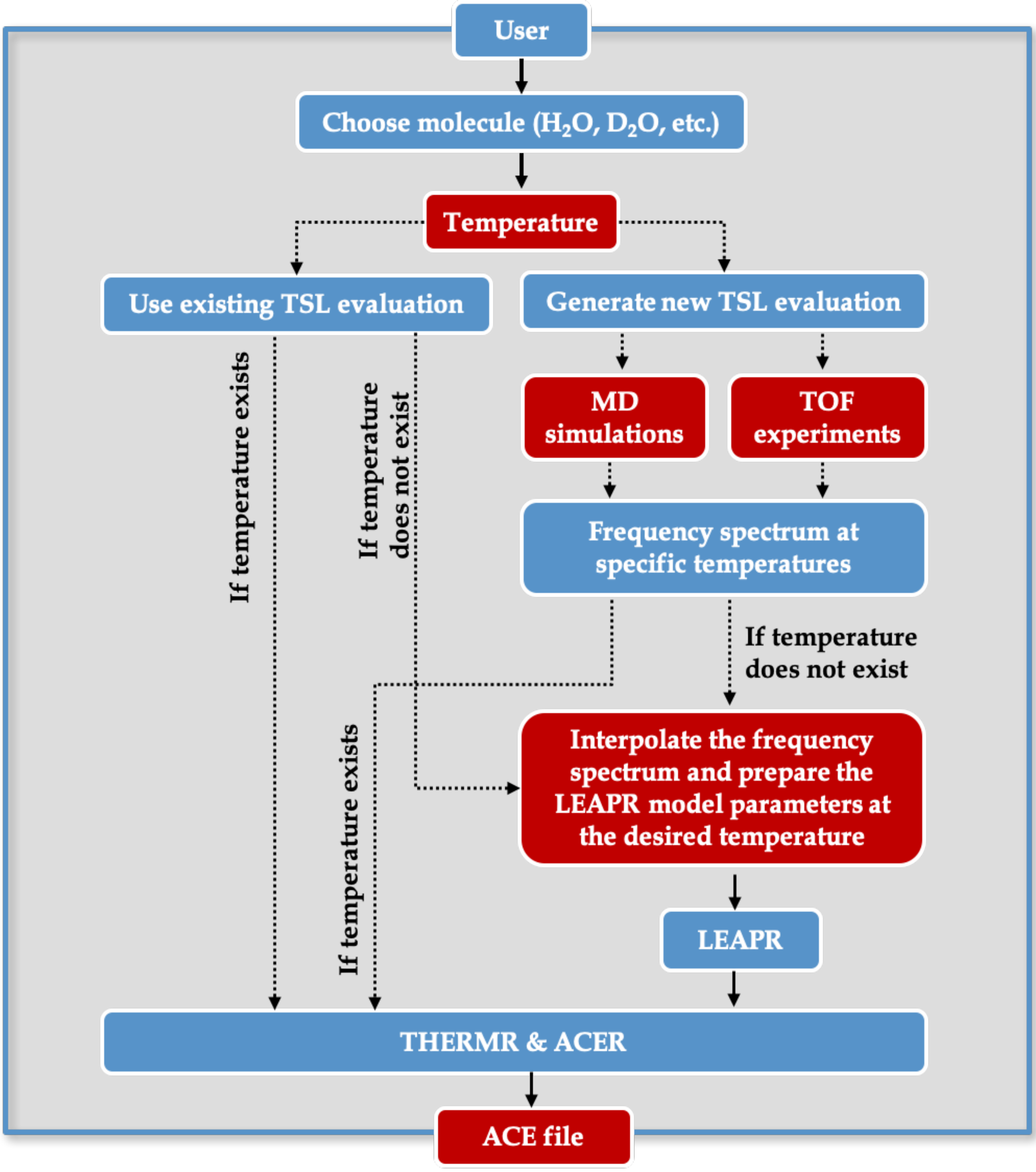

FIGURE 6.2: Block diagram of the SAB module of the GAIA 2 code.

experimental frequency spectrum at specific temperatures for which the TOF experiments at the ILL were carried out. Again, if the temperature requested by the user matches with the temperature available under the option of MD simulations or TOF experiments, the SAB module will run the THERMR and ACER block to deliver the final TSL library. On the other hand if the temperature is not available, it will interpolate the frequency spectrum at the desired temperature and prepare the LEAPR input file accordingly. Additionally, in all the cases, where new evaluations are prepared using MD simulations and TOF experimental data, molecular diffusion has been modeled using Egelstaff and Schofield model for low energy transfers, as described in **Chapter 2**. The new TSL evaluations discussed in the **Chapter 4** and **Chapter 5**, i.e. $S(\alpha,\beta)_{\text{ILL}}$ and $S(\alpha,\beta)_{\text{TCPE}}$, respectively have been developed using the SAB module. The impact of this new TSL will be discussed in the next chapter.

There can be cases where the LEAPR input parameters are not available for a particular TSL evaluation and one still needs to generate TSL data at certain temperature not available in the evaluation. In this case the SAB module can transform the $S(\alpha,\beta)$ matrix provided in the evaluation to the frequency spectrum and then interpolate the frequency spectrum at the required temperature. Other LEAPR parameters can then be directly calculated to prepare the evaluation. The $S(\alpha,\beta)$ available in the evaluations are generally symmetric, i.e. $S^{eval}_{sym}(\alpha,\beta)$. Frequency spectrum is then obtained from the $S^{eval}_{sym}(\alpha,\beta)$ following Eq. 6.1:

$$\rho(\omega) = \beta^2 \lim_{\alpha\to 0}\left[\frac{S^{eval}_{sym}(\alpha,\beta)}{\alpha}\right] \tag{6.1}$$

However, the transformation of the experimental $S^{exp}(\alpha,\beta)$ (the one obtained from direct transformation of experimental $S(\vec{q},\omega)$ to $S^{exp}(\alpha,\beta)$) to the frequency spectrum is done by first transforming the $S^{exp}(\alpha,\beta)$ to $S^{exp}_{sym}(\alpha,\beta)$ using Eq. 4.5, as discussed in **Chapter 4** and then following:

$$\rho(\omega) = 2\beta \sinh\left(\frac{\beta}{2}\right) \lim_{\alpha\to 0}\left[\frac{S^{exp}_{sym}(\alpha,\beta)}{\alpha}\right] \tag{6.2}$$

Equations 6.1 and 6.2 differ due to the fact that the $S(\alpha,\beta)$ matrix available in the TSL evaluations are classical scattering law, i.e. symmetric in β, whereas the $S(\alpha,\beta)$ measured experimentally are quantum scattering law and asymmetric in β. A brief derivation of Eq. 6.1 and 6.2 is given in Appendix B following [49].

As it has been shown in Fig. 6.2, the SAB module has a capability to generate TSL at the requested temperature by the user which makes it a convenient tool to generate TSL for reactor physics or criticality safety applications. This feature of the SAB module was tested on the "French plutonium temperature effect experimental program" where TSL data at exact temperatures were necessary to correctly obtain criticality safety parameters which will be discussed in the next section. The existing TSL evaluations in the JEFF-3.3 and ENDF/B-VIII.0 were reevaluated at specific temperatures using the SAB module by interpolation of the LEAPR model parameters.

6.3. Impact of TSL for light water on the French plutonium temperature effect experimental program

Generally, an increase in the operating temperature of nuclear power reactors leads to a decrease in the reactivity. This trend is known as negative reactivity effect which favors the safety of power reactors in case of temperature rise due to reactor transients or accidental scenarios. But, in the case of highly diluted plutonium solutions a theoretical study suggests that with the rise in temperature, the reactivity may increase [63]. IRSN being a criticality safety regulator aims to verify this effect, since the rise in reactivity with increasing temperature can lead to a criticality safety accident.

6.3.1 Experimental setup

A series of experiments were conducted by the IRSN at the ‘Apparatus B’ facility of CEA VALDUC to study the positive temperature effect for diluted plutonium solutions [64, 65]. The experimental setup is shown in Fig. 6.3. A great deal of information about the details of the experimental setup is available in Ref. [25].

FIGURE 6.3: Setup of the plutonium nitrate temperature effect experimental program [66].

The experiment at 22 °C (295.15 K) corresponds to the 3007A test in the ’PU-SOL-THERM-038’ critical benchmark available in the ICSBEP handbook [66]. Likewise, the experiment at 28 °C (301.15 K) corresponds to the 3007B test in the ’PU-SOL-THERM-039’ critical benchmark. The experiments were carried out with a plutonium concentration of 14.3 g/l, following a sub-critical approach. First, the measurements were performed at 22 °C and then the plutonium solution was drained out and heated to 28 °C . Criticality was obtained for a solution height of 133.254 cm for the experiment at 22 °C , whereas for 28 °C it was obtained for a solution height of 131.997 cm. With a rise in temperature by 6 °C , the solution height decreased by 1.257 cm. This decrease in height of the plutonium solution to maintain criticality, was an evidence that a positive temperature effect exists. The estimated positive reactivity effect was around 2 pcm/°C (between 22 °C and 28 °C). These experiments demonstrated a positive temperature effect within the temperature range of 22 °C to 28 °C whereas Monte Carlo transport simulations carried out on these benchmarks in the past showed negative temperature effect between these two temperatures. However, it was found out that the observed positive effect was not due to various physical effects like expansion of the plutonium solution, thermalization of neutron spectrum and Doppler effect. Haeck et al. suggested that TSL for light water at appropriate temperature were necessary to observe such a positive temperature effect [**wim_plutonium_nodate**, 67]. Apart from the unavailability of TSL data in the existing evaluations at the temperatures where experiments were performed, a possible reason to observe the negative effect can be the model of TSL data itself. For instance, using a free gas model to define the molecular diffusion or the shape of the frequency spectrum utilized in the past libraries might be one of the possible reasons that a negative effect was observed.

6.3.2 Benchmark Specifications

A benchmark model was prepared in order to simulate the experimental setup shown in Fig. 6.3. Figure 6.4 shows the geometry used in the benchmark specifications (R-Z representation). Five different materials were considered in this benchmark:

- Water reflector (shown in blue)
- Plutonium solution (shown in yellow)
- Air above the water reflector and the plutonium solution (in white)
- Stainless steel: Z2 CN 18–10 for the reflector vessel and cover (in dark green)
- Stainless steel: Z2 CN 17–12 for the plutonium vessel and cover (in light green)

The compositions of elements in the water reflector and the plutonium solution at 22 °C and 28 °C are shown in Tables 6.1 and 6.2, respectively.

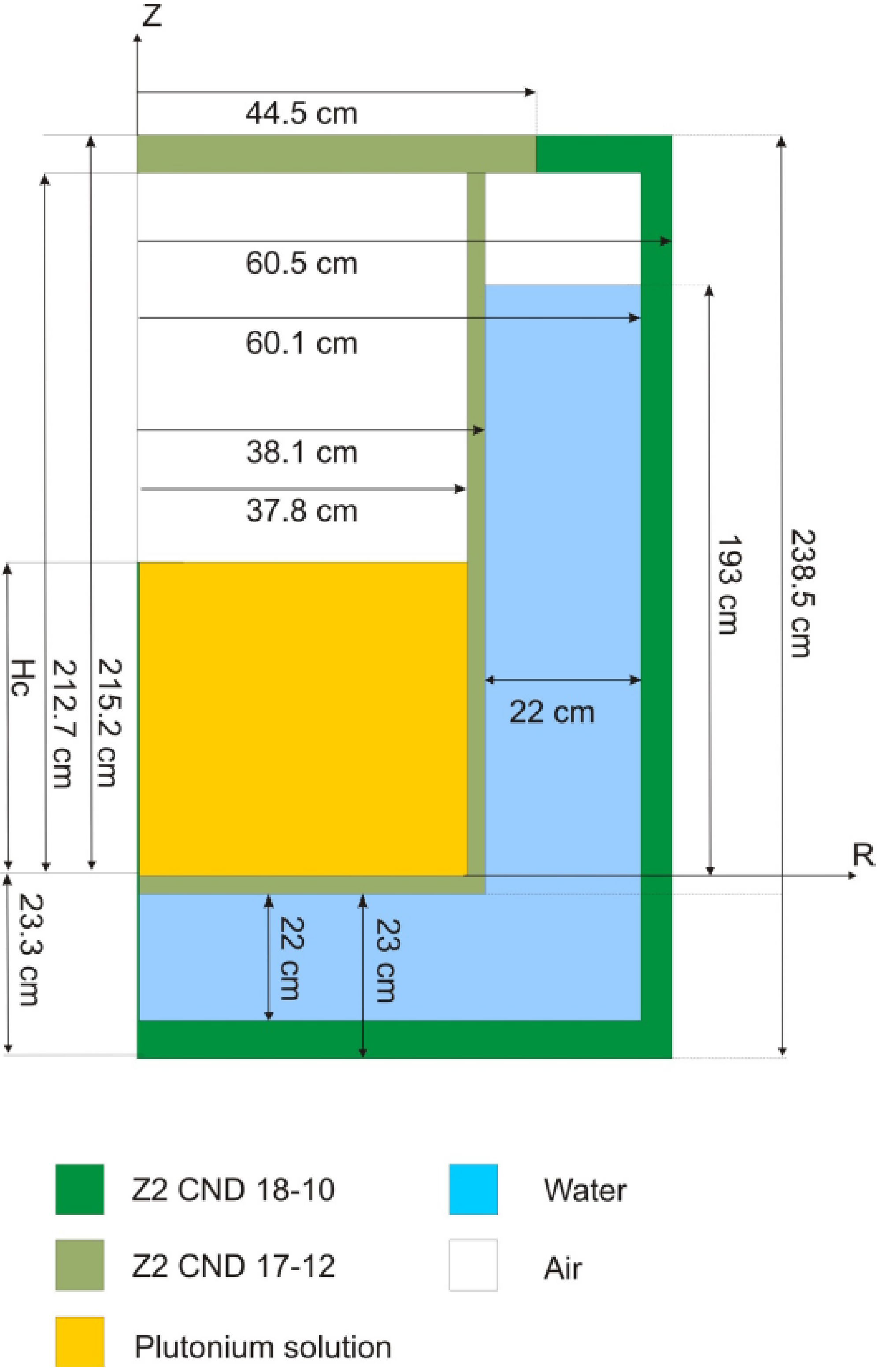

FIGURE 6.4: Benchmark model for the plutonium nitrate temperature effect experimental program [65].

Temperature	22 °C	28 °C
Element	Atom Density (atoms/barns/cm)	Atom Density (atoms/barns/cm)
H	6.6707E-02	6.6604E-02
O	3.3353E-02	3.3302E-02

TABLE 6.1: Composition of the water reflector at 22 °C and 28 °C.

Temperature	22 °C	28 °C
Element	Atom Density (atoms/barns/cm)	Atom Density (atoms/barns/cm)
^{238}Pu	6.9540E-08	6.9393E-08
^{239}Pu	2.7667E-05	2.7608E-05
^{240}Pu	7.4424E-06	7.4267E-06
^{241}Pu	3.8092E-07	3.8011E-07
^{242}Pu	3.9087E-07	3.9005E-07
H	6.4938E-02	6.4802E-02
O	3.4455E-02	3.4382E-02
N	7.6555E-04	7.6393E-04
^{241}Am	3.9950E-08	2.8977E-08
B	1.2248E-07	8.8841E-08
Ba	6.5743E-09	4.7686E-09
Ca	7.2086E-08	5.2287E-08
Cr	7.7556E-08	5.6255E-08
Fe	3.6643E-07	2.6579E-07
Mg	5.6957E-08	4.1313E-08
Ni	2.0100E-07	1.4580E-07
Pb	1.0457E-09	8.4280E-10
^{232}Th	5.1878E-09	3.7629E-09
Zn	3.2216E-08	2.3368E-08

Continued on next page

Table 6.2 – continued from previous page

Temperature	22 °C	28 °C
Element	Atom Density (atoms/barns/cm)	Atom Density (atoms/barns/cm)

TABLE 6.2: Composition of the plutonium solution at 22 °C and 28 °C

The compositions of air, stainless steel Z2 CN 18-10 and stainless steel Z2 CN 17-12 are considered independent of the experiment temperature and are given in Tables 6.3, 6.4 and 6.5, respectively.

Temperature	22 °C	28 °C
Element	Atom Density (atoms/barns/cm)	Atom Density (atoms/barns/cm)
N	4.1985E-05	4.1985E-05
O	1.1263E-05	1.1263E-05

TABLE 6.3: Composition of Air at 22 °C and 28 °C.

Temperature	22 °C	28 °C
Element	Atom Density (atoms/barns/cm)	Atom Density (atoms/barns/cm)
Cr	1.6470E-02	1.6470E-02
Ni	8.1061E-03	8.1061E-03
Mo	8.6597E-04	8.6597E-04
Mn	8.7145E-04	8.7145E-04
Si	1.6939E-03	1.6939E-03
P	6.1439E-05	6.1439E-05
S	4.4512E-05	4.4512E-05
C	1.1883E-04	1.1883E-04
Fe	5.9546E-02	5.9546E-02

TABLE 6.4: Composition of Stainless Steel Z2 CN 18-10 at 22 °C and 28 °C.

Temperature	22 °C	28 °C
Element	Atom Density (atoms/barns/cm)	Atom Density (atoms/barns/cm)
Cr	1.5653E-02	1.5653E-02
Ni	9.7889E-03	9.7889E-03
Mo	1.1228E-03	1.1228E-03
Mn	8.7145E-04	8.7145E-04
Si	1.7046E-03	1.7046E-03
P	6.1827E-05	6.1827E-05
S	4.4786E-05	4.4786E-05
C	1.1958E-04	1.1958E-04
Fe	5.7137E-02	5.7137E-02

TABLE 6.5: Composition of Stainless Steel Z2 CN 17-12 at 22 °C and 28 °C.

6.3.3 MORET Monte Carlo simulations

In order to quantify the temperature effect, IRSN simulated the benchmark model with its own codes and processed libraries. The benchmark calculations were carried out using the Monte Carlo continuous energy transport code, MORET which is a tool developed and maintained by IRSN. In particular, the latest version of MORET, i.e., MORET 5.D.1 was utilized in this study, together with the most recent TSL evaluations of light water JEFF-3.3 and ENDF/B-VIII.0. As can be seen from Tables 3.1 and 3.3, the closest temperature to this particular experiment in JEFF-3.3 data library are 293.6 K and 350 K, whereas in ENDF/B-VIII.0 it is 293.6 K and 300 K. In case of unavailability of the required temperature in the tabulated TSL data libraries one generally make a choice between the closest available temperature in the evaluations. In the present study new TSL files were generated at exact temperatures (295.15 K and 301.15 K) using the SAB module as described in the previous section by interpolating ENDF/B-VIII.0 LEAPR model parameters. This could serve a way to validate the SAB module and its capability to generate TSL data at the desired temperatures. The study was conducted by using the JEFF-3.3 nuclear data library as the base for all the calculations. Nevertheless, the TSL evaluations (existing/newly generated) were replaced in the JEFF 3.3 evaluation for each specific calculation. A total of 2200 batches of 1500 neutrons per batch were run to reach a Monte Carlo standard deviation of 0.00005

(5 pcm). The first 150 batches were skipped. Calculation results of the benchmark model k_{eff} with different TSL evaluations are given in Table. 6.6

TSL evaluation for light water	Effective multiplication factor k_{eff} at T		Reactivity difference
	22 °C	28 °C	Δ k_{eff} (pcm)
JEFF-3.3	0.99730 (293.6 K)	0.99696 (293.6 K)	-34
ENDF/B-VIII.0	0.99553 (293.6 K)	0.99586 (300.0 K)	+33
Interpolating ENDF/B-VIII.0 LEAPR model parameters using the SAB module	0.99570 (295.15 K)	0.99600 (301.15 K)	+30

TABLE 6.6: Impact of the TSL evaluation for light water on the French plutonium temperature effect experimental program. The temperature of the TSL evaluation is given in parentheses.

As can be seen in the Table 6.6, the change in reactivity is negative (-34 pcm) when using the 293.6 K TSL data available in the JEFF-3.3 data library for both the experiments at 22 °C and 28 °C , respectively. Whereas, when using the TSL evaluation at 293.6 K for the experiment at 22 °C and 300.0 K for 28 °C , respectively, available in the ENDF/B-VIII.0 data library a positive reactivity difference was observed (+33 pcm). Finally, when the new TSL evaluations at 295.15 K and 301.15 K, generated using the SAB module for the experiment at 22 °C and 28 °C were tested, a positive reactivity was observed (+30 pcm). This positive reactivity observed when using both the TSL evaluation in the ENDF/B-VIII.0 and the newly evaluated one from the SAB module, confirms the necessity of TSL data of light water at desired temperatures, lack of which leads to very different effect than expected. This experimental benchmark verifies the ability of the SAB module, in generating TSL evaluations for light water at desired temperatures requested by the user. The SAB module will play an important role in criticality safety, where accurate TSL data at required temperature can play significant roles.

Chapter 7

Verification and validation of new TSL evaluations for light water

The impact of the new TSL evaluations for light water was verified by comparisons with experimentally measured double differential cross sections, angular differential cross sections and the total scattering cross sections. A set of critical benchmarks available in the ICSBEP (International Criticality Safety Benchmark Evaluation Project) handbook, sensitive to the thermal scattering region were retrieved from the DICE database (Database for the International Criticality Safety Benchmark Evaluation Project) and used in this study. The results obtained from using the new evaluations are presented. In addition, calculations done using existing TSL evaluations for light water from JEFF-3.3 and ENDF/B-VIII.0 are also compared.

7.1. Double differential scattering cross section

The double differential cross section were calculated to validate new TSL evaluations and compared with a series of available experimental data. The standard deviation of the Gaussian function was estimated from the knowledge of the experimental resolution available in the literature. Double differential data were calculated by different TSL evaluations for an incident neutron energy of 154 meV and 231 meV. Two scattering angle were chosen in each case, i.e. θ = 14 ° and θ = 25 °. The results are displayed in Fig. 7.1, 7.2, 7.3 and 7.4, compared with measurements carried out by Bischoff et al. in 1967 [43]. The resolution of this experimental data were approximated to be around 5 %.

Another measurement carried out by Harling [44] are used to validate the new TSL evaluations developed in this work. Double differential data were calculated by different TSL evaluations for an incident neutron energy of 151 meV and two scattering angle θ = 15 ° and θ = 32 °. The results are displayed in Fig. 7.5 and 7.6, for θ = 15 ° and θ = 32 °, respectively and compared with measurements by Harling. Another calculation was carried out with incident neutron energy of 305 meV and and two scattering angle θ = 15 ° and θ = 30 °. The results are shown in Fig. 7.7 and 7.8 for θ = 15 ° and θ = 30 °, respectively and compared with the measurements.

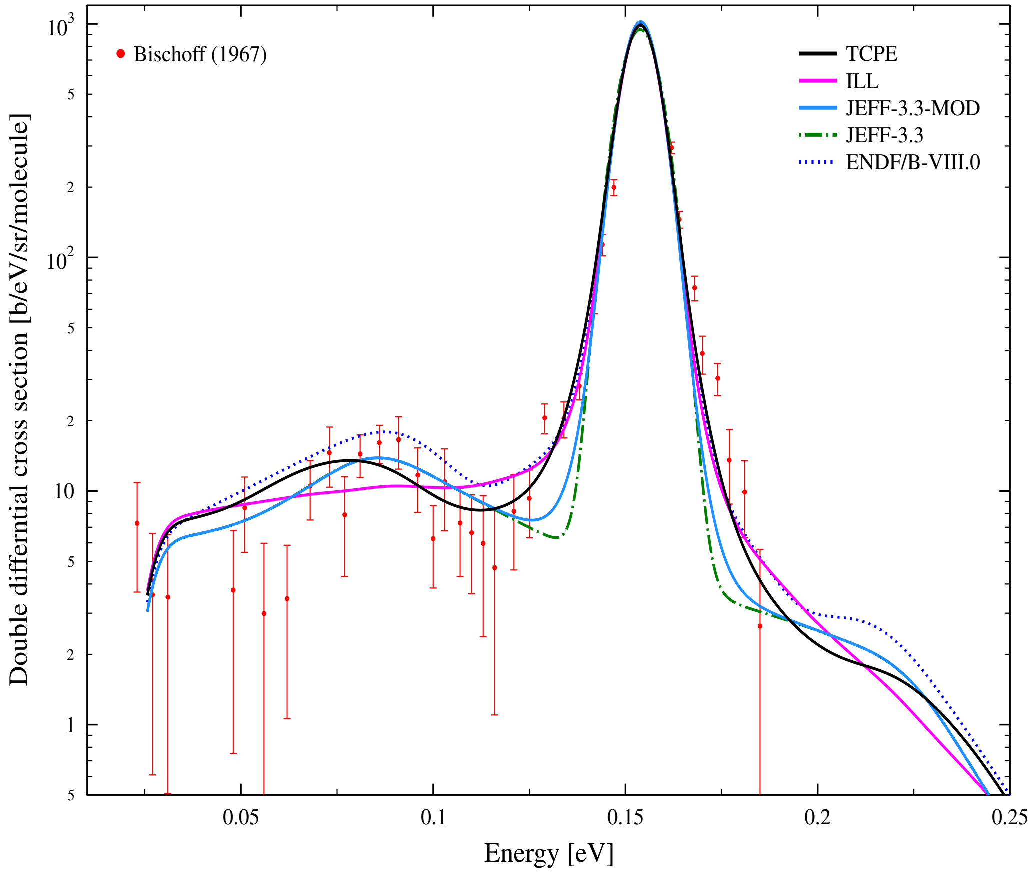

FIGURE 7.1: Double differential scattering cross section of light water at incident energy $E = 154$ meV and scattering angle θ=14°.

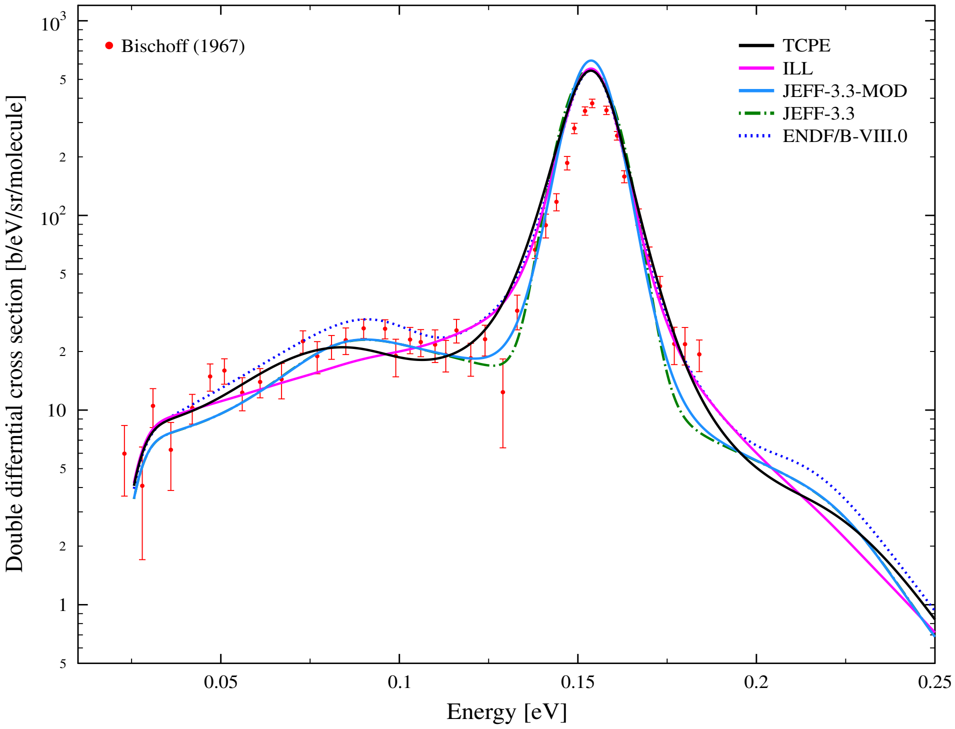

FIGURE 7.2: Double differential scattering cross section of light water at incident energy $E = 154$ meV and scattering angle θ=25°.

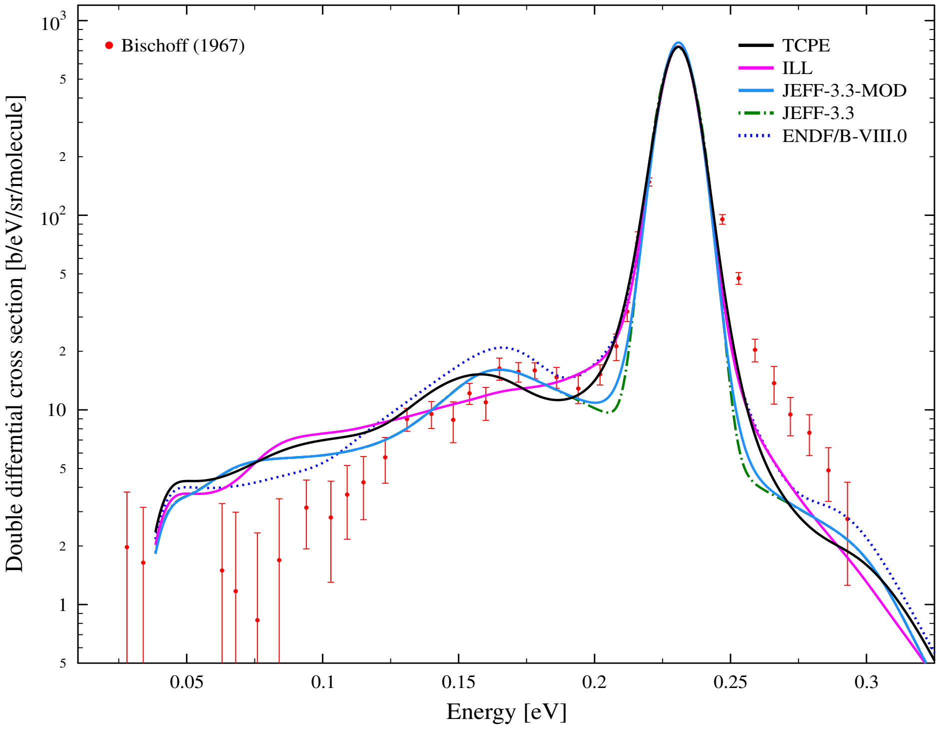

FIGURE 7.3: Double differential scattering cross section of light water at incident energy $E = 231$ meV and scattering angle θ=14°.

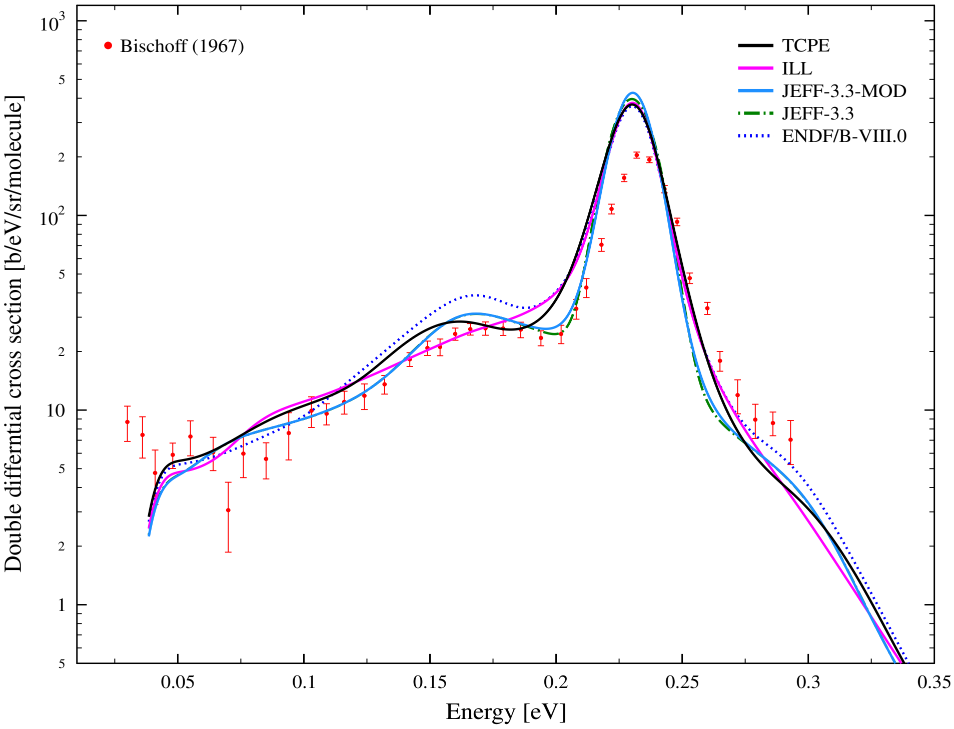

FIGURE 7.4: Double differential scattering cross section of light water at incident energy $E = 231$ meV and scattering angle θ=25°.

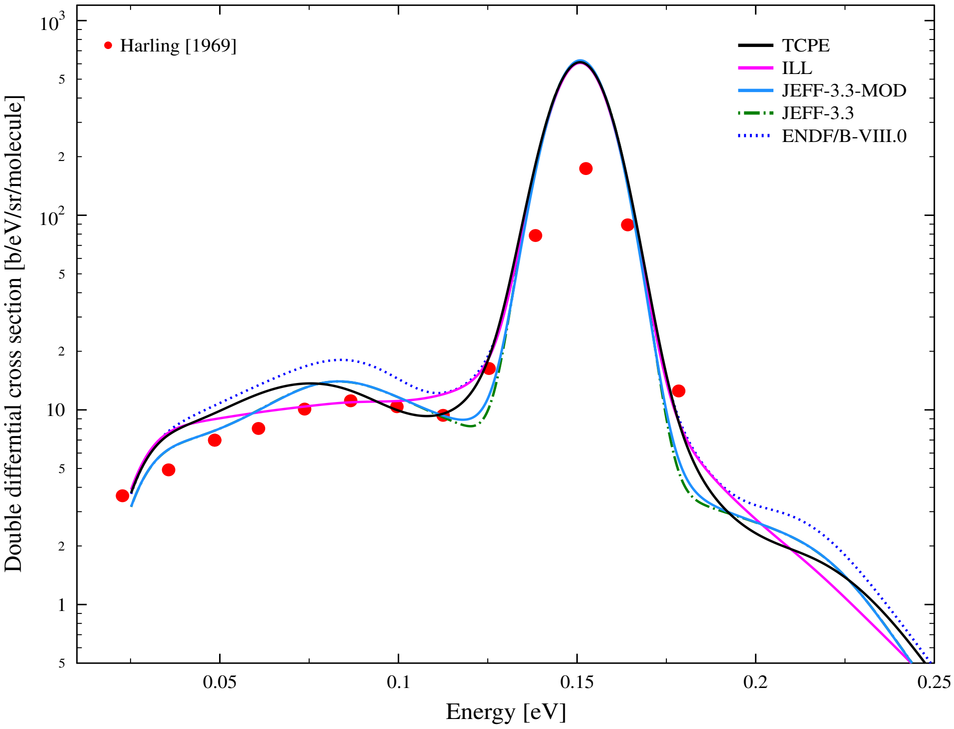

FIGURE 7.5: Double differential scattering cross section of light water at incident energy $E = 151$ meV and scattering angle θ=15°.

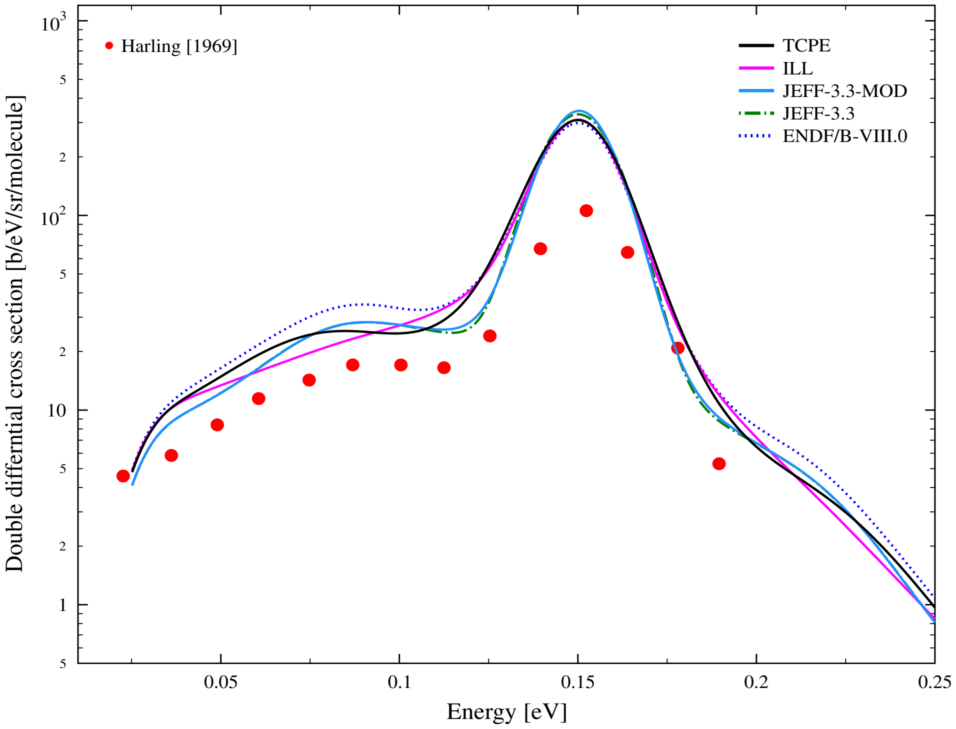

FIGURE 7.6: Double differential scattering cross section of light water at incident energy $E = 151$ meV and scattering angle θ=32°.

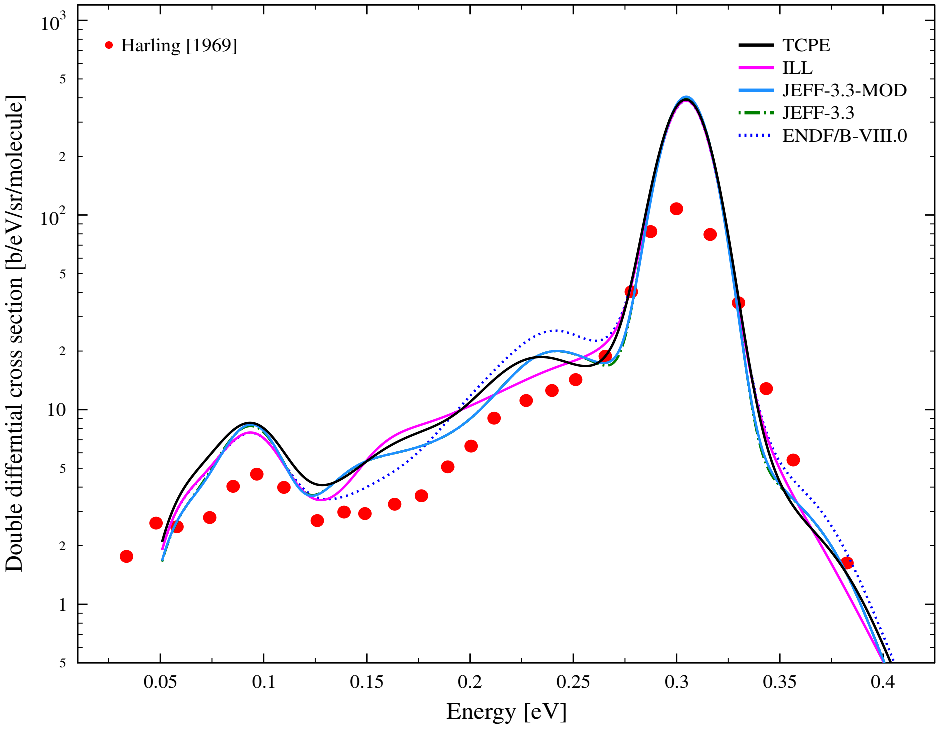

FIGURE 7.7: Double differential scattering cross section of light water at incident energy $E = 305$ meV and scattering angle θ=15°.

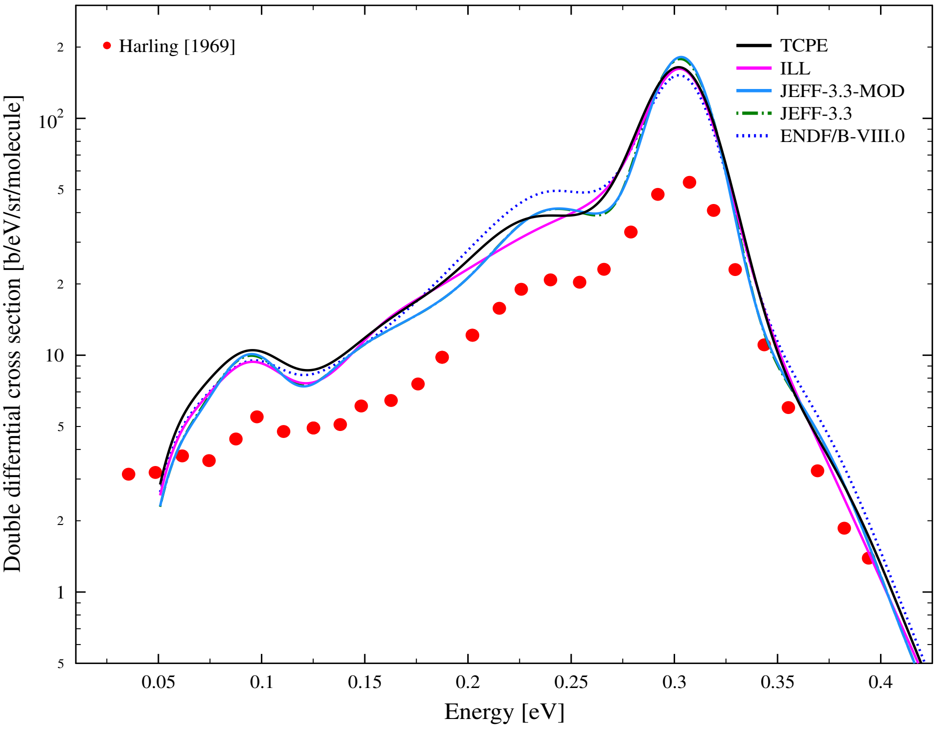

FIGURE 7.8: Double differential scattering cross section of light water at incident energy $E = 305$ meV and scattering angle θ=30°.

Comparing the results obtained using new TSL evaluations with the experimental data, one can observe that the shape of the elastic and the quasi elastic elastic peak is well represented by the new evaluations.

7.2. Differential scattering cross section

The angular differential scattering cross section was computed using new TSL evaluations, existing TSL evaluations in JEFF-3.3, ENDF/B-VIII.0 and compared with the experimental result by Beyster [68]. Differential scattering cross section for incident energy $E = 0.0569$ and $E = 0.179$ are given in Fig. 7.9 and 7.10, respectively.

The results at both these incident energies are reasonable and TSL from TCPE and ENDF/B-VIII.0 are quite similar as compared to other libraries.

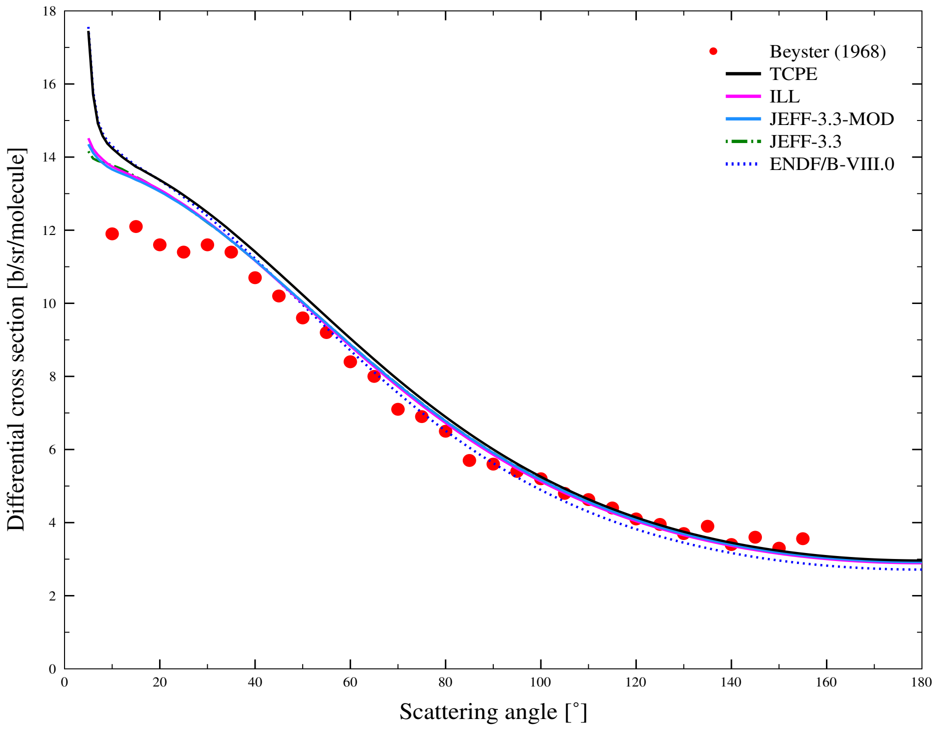

Figure 7.9: Differential cross section for light water at $E = 56.9$ meV.

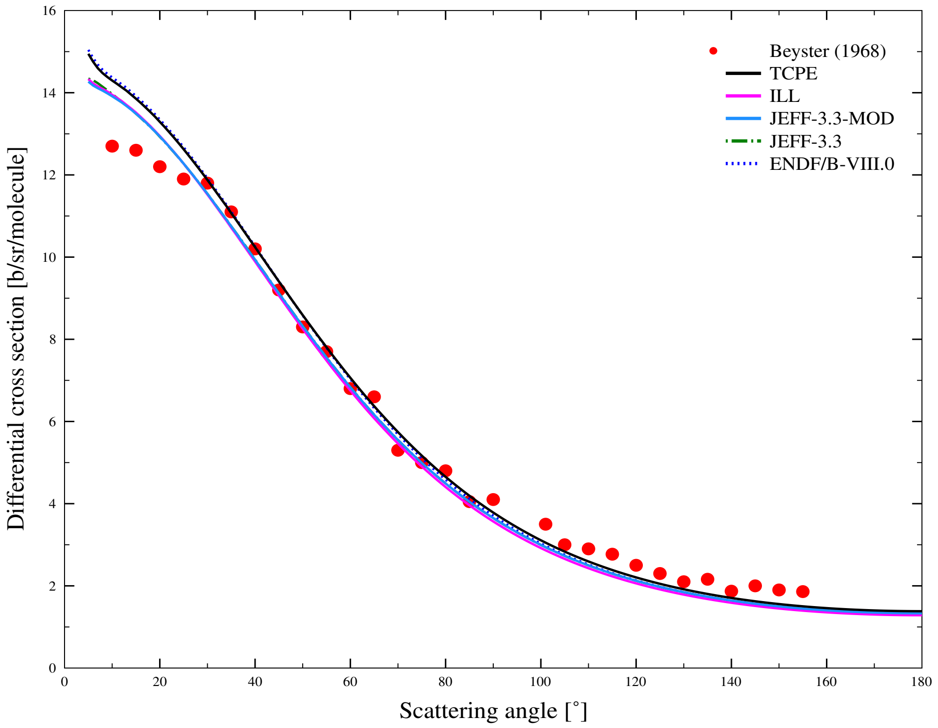

Figure 7.10: Differential cross section for light water at $E = 179$ meV.

7.3. Total scattering cross section

The total scattering cross sections for light water were calculated using different TSL evaluations and compared with the experimental data. The results displayed in Fig. 7.11 show a comparison of the total cross section obtained by using new TSL evaluations developed during this work and existing evaluations in the JEFF-3.3 and ENDF/B-VIII.0 with the available experimental and EXFOR data as described in **Chapter 1**. Again the results obtained using new TSL evaluations are promising and in good agreement with the ENDF-B/VIII.0 evaluations. It can be seen that both the evaluation obtained from PolarisMD simulations, i.e. TCPE and the ILL TOF experimental data are able to reproduce the total cross section in good agreement.

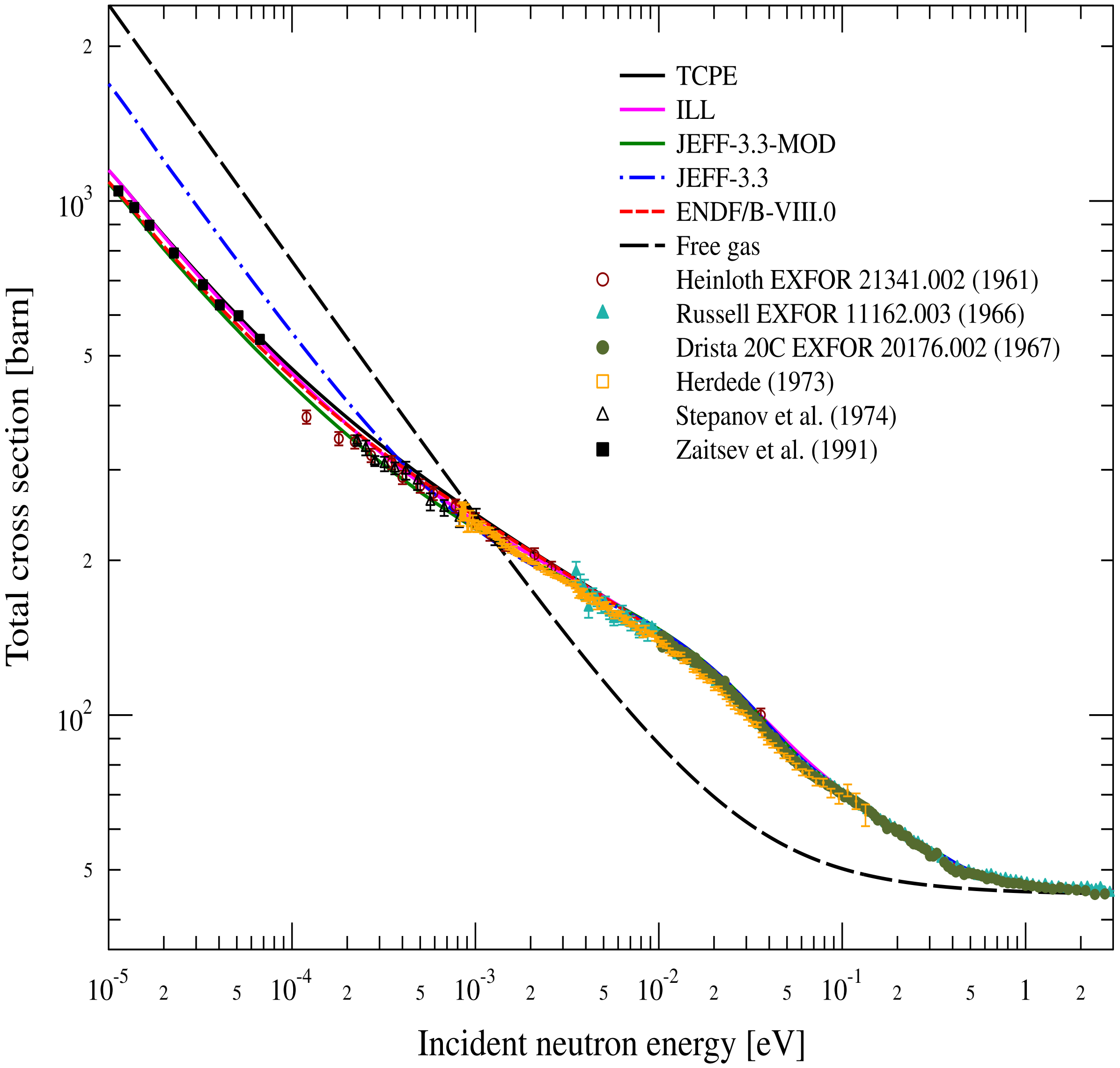

FIGURE 7.11: Total cross section of light water based on newly evaluated TSLs for light water.

7.4. Testing new TSL evaluations on ICSBEP critical benchmarks

ICSBEP includes a series of critical and sub-critical experiments referred as benchmarks. These benchmarks serve as a tool to validate neutronics simulation codes and cross-section data libraries. In the ICSBEP Handbook the experiments are categorized based on:

- Type of fissile material used: Low, intermediate, mixed and highly enrichment uranium, Uranium-233, Plutonium, etc.
- Form of the fissile material used: Metal, compound, solution, etc.
- Neutron energy range: Thermal, intermediate, fast, and mixed energy spectrum.

A series of critical benchmarks were chosen to test the newly evaluated TSL developed during the course of this PhD thesis. The chosen benchmarks are sensitive to the thermal scattering cross sections of light water in the thermal and epithermal energy range. The evaluation ID and the title of the chosen benchmarks are given in the list below:

- **HEU-SOL-THERM-001.c01**: Minimally reflected cylinders of highly enriched solutions of uranyl nitrate.
- **LEU-COMP-THERM-007.c01**: Water-reflected 4.738-wt.%-enriched uranium dioxide fuel-rod arrays arranged in a 1.26 cm square pitch.
- **LEU-COMP-THERM-007.c02**: Water-reflected 4.738-wt.%-enriched uranium dioxide fuel-rod arrays arranged in a 1.60 cm square pitch.
- **LEU-COMP-THERM-007.c03**: Water-reflected 4.738-wt.%-enriched uranium dioxide fuel-rod arrays arranged in a 2.10 cm square pitch.
- **LEU-COMP-THERM-007.c04**: Water-reflected 4.738-wt.%-enriched uranium dioxide fuel-rod arrays arranged in a 2.52 cm square pitch.
- **LEU-COMP-THERM-049.c01**: Maracas Programme: Polythene-reflected critical configurations with low-enriched and low-moderated uranium dioxide powder, U(235)O_2 - H/U = 2 – critical distance = 2.60 cm.

- **LEU-COMP-THERM-049.c02**: Maracas Programme: Polythene-reflected critical configurations with low-enriched and low-moderated uranium dioxide powder, U(235)O_2 - H/U = 2 – critical distance = 3.30 cm.
- **LEU-COMP-THERM-049.c03**: Maracas Programme: Polythene-reflected critical configurations with low-enriched and low-moderated uranium dioxide powder, U(235)O_2 - H/U = 2 – critical distance = 9.83 cm.
- **LEU-COMP-THERM-071.c01**: Low moderated 4.738-wt.%-enriched uranium dioxide fuel rod arrays (36×35) arranged in a 1.1 cm square pitch.
- **LEU-COMP-THERM-071.c02**: Low moderated 4.738-wt.%-enriched uranium dioxide fuel rod arrays (33×33) arranged in a 1.1 cm square pitch.
- **LEU-COMP-THERM-071.c03**: Low moderated 4.738-wt.%-enriched uranium dioxide fuel rod arrays (32×32) arranged in a 1.1 cm square pitch.
- **LEU-COMP-THERM-071.c04**: Low moderated 4.738-wt.%-enriched uranium dioxide fuel rod arrays (35×35) arranged in a 1.075 cm square pitch.
- **LEU-COMP-THERM-MIRTE1.c13**: Two lattices of low moderated 4.738-wt.%-enriched uranium dioxide fuel rods separated by 50 mm of water (French MIRTE experiments).
- **LEU-COMP-THERM-MIRTE1.c14**: Two lattices of low moderated 4.738-wt.%-enriched uranium dioxide fuel rods separated by 100 mm of water (French MIRTE experiments).
- **PU-SOL-THERM-039.c06**: Plutonium temperature effect program - low concentrated (14.3 g/l) plutonium nitrate solutions at 28 °C .

7.4.1 Testing of new TSL evaluations

The benchmark calculations were carried out using MORET 5.D.1 Monte Carlo continuous energy transport code. The study was conducted by using the JEFF-3.3 nuclear data library as the base for all the calculations. Nevertheless, the TSL evaluations from different sources were replaced in the JEFF 3.3 evaluation for each specific calculation. Tables 7.1 shows the multiplication factor k_{eff} for the chosen benchmarks using different TSL evaluations. Columns 1 and 2 show the benchmark ID and the k_{eff} of the chosen benchmarks. Columns 3, 4 and 5 show the k_{eff} obtained using the $S(\alpha,\beta)_{\text{ILL}}$, $S(\alpha,\beta)_{\text{JEFF-3.3-MOD}}$ and $S(\alpha,\beta)_{\text{JEFF-3.3}}$, respectively.

Benchmark ID & k_{eff}		k_{eff} using different TSLs		
		ILL	JEFF-3.3-MOD	JEFF-3.3
HEU-SOL-THERM-001.c01	1.00040 (0.00600)	0.99917	0.99926	0.99973
LEU-COMP-THERM-007.c01	1.00000 (0.00140)	0.99800	0.99865	0.99873
LEU-COMP-THERM-007.c02	1.00000 (0.00080)	0.99956	0.99954	0.99979
LEU-COMP-THERM-007.c03	1.00000 (0.00070)	0.99766	0.99772	0.99811
LEU-COMP-THERM-007.c04	1.00000 (0.00080)	0.99793	0.99707	0.99730
LEU-COMP-THERM-049.c01	1.00000 (0.00340)	1.00380	1.00372	1.00459
LEU-COMP-THERM-049.c02	1.00000 (0.00340)	1.00443	1.00452	1.00513
LEU-COMP-THERM-049.c03	1.00000 (0.00340)	1.00393	1.00388	1.00433
LEU-COMP-THERM-071.c01	1.00000 (0.00070)	0.99747	0.99746	0.99802
LEU-COMP-THERM-071.c02	1.00000 (0.00070)	0.99717	0.99756	0.99808
LEU-COMP-THERM-071.c03	1.00000 (0.00070)	0.99715	0.99779	0.99761
LEU-COMP-THERM-071.c04	1.00000 (0.00060)	0.99724	0.99788	0.99822
LEU-COMP-THERM-mirte1.c13	1.00000 (0.00106)	0.99778	0.99824	0.99784
LEU-COMP-THERM-mirte1.c14	1.00000 (0.00105)	0.99711	0.99758	0.99793
PU-SOL-THERM-039.c06	1.00050 (0.00133)	0.99721	0.99682	0.99700

TABLE 7.1: Benchmark and calculated multiplication factor k_{eff} using different TSL evaluations. Benchmark and the statistical uncertainty in the k_{eff} are given in parentheses.

A better interpretation of the results displayed in Table 7.1 is shown in Fig. 7.12. Here C-E (Calculated - Experimental) value of k_{eff} is presented for the chosen benchmarks. A (C-E) value close to zero indicates that the evaluation (Calculation) is close to the benchmark results and hence one can relate this to an improved evaluation of nuclear data library used. In Fig. 7.12 C-E value of the LEU-COMP-THERM-049 benchmark for all the three cases shows improvement with the new TSL evaluations. A possible reason for this could be that this benchmark is in the epithermal energy range and the new evaluations perform better in this energy region. Whereas, it is difficult to conclude the impact of new TSL evaluations on other benchmarks as the k_{eff} vales are within the statistical uncertainty of the Monte Carlo simulations.

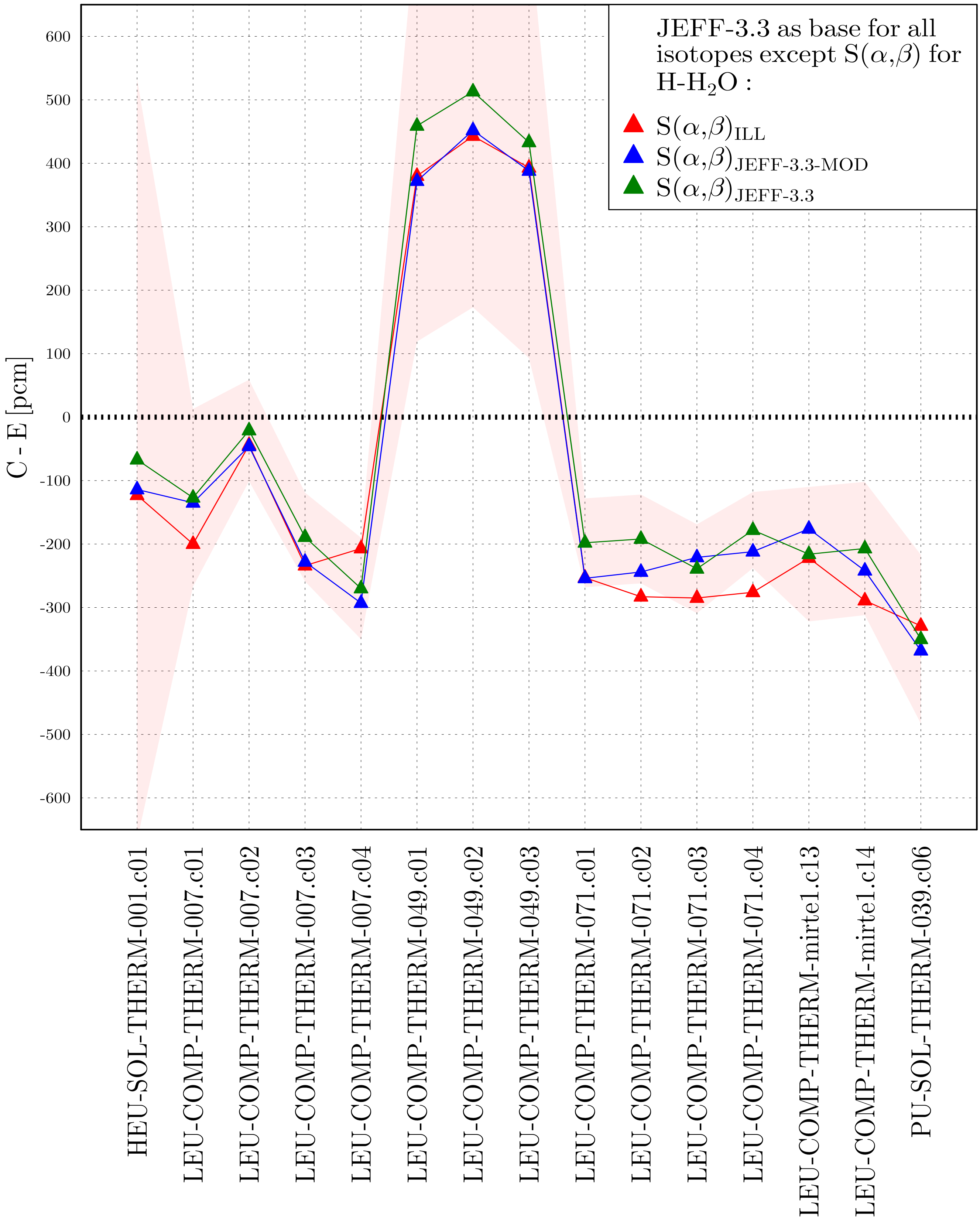

FIGURE 7.12: Calculated - Experimental (C-E) results for the selected ICSBEP benchmark using different TSL evaluations.

The results presented in Table 7.1 and Fig. 7.12 do not indicate any significant conclusion between the used TSL evaluations. However, it should be pointed out that in the TSL evaluations presented in this work, a great deal of physics inherent in the TSL generation was included. It appears that the particular set of benchmark chosen in this study are primarily impacted by the rotational energy of the water molecule. Apparently, the diffusion and the intra molecular modes in the frequency spectrum of the light water have minimal impact on the k_{eff} calculation of these benchmarks.

7.4.2 Additional tests with new TSL evaluations

In addition to the calculations performed previously, the TSL impact on critical benchmark calculation were also tested together with new evaluations performed at IRSN, in particular, ^{16}O and ^{235}U evaluations.

New TSL evaluations along with the new IRSN ^{16}O evaluation

Since the chosen benchmarks are sensitive to light water TSL in both thermal and epithermal range. Oxygen cross section can also impact the k_{eff} values. An effort has been carried out by Leal et al. [69] at the IRSN to improve the oxygen cross section . Benchmark calculations were done using the new TSLs and the new IRSN ^{16}O evaluation. The results obtained from these benchmarks are given in Table 7.2.

Benchmark ID & k_{eff}		k_{eff} using different TSLs		
		ILL	JEFF-3.3-MOD	JEFF-3.3
HEU-SOL-THERM-001.c01	1.00040 (0.00600)	0.99665	0.99631	0.99676
LEU-COMP-THERM-007.c01	1.00000 (0.00140)	0.99598	0.99648	0.99675
LEU-COMP-THERM-007.c02	1.00000 (0.00080)	0.99763	0.99713	0.99773
LEU-COMP-THERM-007.c03	1.00000 (0.00070)	0.99684	0.99600	0.99609
LEU-COMP-THERM-007.c04	1.00000 (0.00080)	0.99597	0.99621	0.99638
LEU-COMP-THERM-049.c01	1.00000 (0.00340)	1.00283	1.00297	1.00351
LEU-COMP-THERM-049.c02	1.00000 (0.00340)	1.00293	1.00301	1.00372
LEU-COMP-THERM-049.c03	1.00000 (0.00340)	1.00258	1.00259	1.00340
LEU-COMP-THERM-071.c01	1.00000 (0.00070)	0.99536	0.99545	0.99580

Continued on next page

Table 7.2 – continued from previous page

Benchmark ID & k_{eff}		k_{eff} using different TSLs		
		ILL	JEFF-3.3-MOD	JEFF-3.3
LEU-COMP-THERM-071.c02	1.00000 (0.00070)	0.99568	0.99525	0.99553
LEU-COMP-THERM-071.c03	1.00000 (0.00070)	0.99513	0.99505	0.99538
LEU-COMP-THERM-071.c04	1.00000 (0.00060)	0.99466	0.99567	0.99600
LEU-COMP-THERM-mirte1.c13	1.00000 (0.00106)	0.99606	0.99614	0.99631
LEU-COMP-THERM-mirte1.c14	1.00000 (0.00105)	0.99593	0.99603	0.99631
PU-SOL-THERM-039.c06	1.00050 (0.00133)	0.99619	0.99587	0.99610

TABLE 7.2: Benchmark and Calculate multiplication factor k_{eff} using different TSL evaluations and new IRSN ^{16}O evaluation. Benchmark and the statistical uncertainty in the k_{eff} is given in parentheses.

Compared with the previously presented k_{eff} result, the replacement of 16O with the new evaluation appears to deteriorate the C-E results as can be seen in Fig. 7.13. This is due to a lower value of the scattering cross section for ^{16}O in the new evaluation. The following section will study the impact of the addition of ^{235}U developed by Leal et al. at IRSN which will mitigate the k_{eff} results.

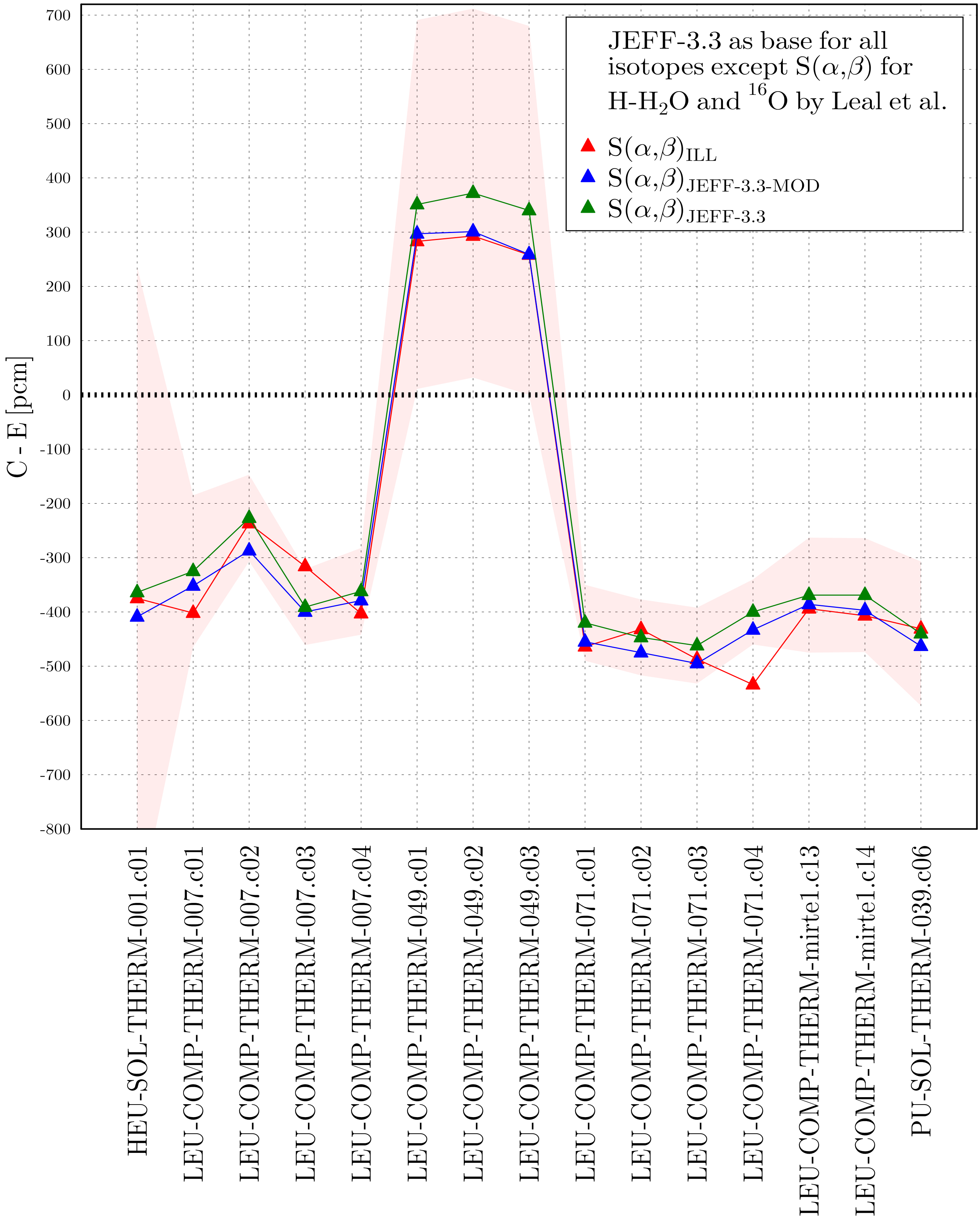

FIGURE 7.13: Calculated - Experimental (C-E) results for the selected ICSBEP benchmark using different TSL evaluations and the IRSN new ^{16}O evaluation.

New TSL evaluations along with the new IRSN ^{16}O and ^{235}U evaluations

Benchmark calculation were also done using the new TSLs and the new IRSN ^{16}O and ^{235}U evaluations. The results obtained from these benchmarks are given in Table. 7.3 and the corresponding C-E plot in Fig. 7.14.

Benchmark ID & k_{eff}		k_{eff} using different TSLs		
		ILL	JEFF-3.3-MOD	JEFF-3.3
HEU-SOL-THERM-001.c01	1.00040 (0.00600)	0.99775	0.99794	0.99793
LEU-COMP-THERM-007.c01	1.00000 (0.00140)	0.99712	0.99681	0.99828
LEU-COMP-THERM-007.c02	1.00000 (0.00080)	0.99871	0.99904	0.99934
LEU-COMP-THERM-007.c03	1.00000 (0.00070)	0.99799	0.99783	0.99819
LEU-COMP-THERM-007.c04	1.00000 (0.00080)	0.99797	0.99768	0.99783
LEU-COMP-THERM-049.c01	1.00000 (0.00340)	1.00331	1.00382	1.00398
LEU-COMP-THERM-049.c02	1.00000 (0.00340)	1.00409	1.00419	1.00463
LEU-COMP-THERM-049.c03	1.00000 (0.00340)	1.00335	1.00400	1.00418
LEU-COMP-THERM-071.c01	1.00000 (0.00070)	0.99536	0.99532	0.99580
LEU-COMP-THERM-071.c02	1.00000 (0.00070)	0.99568	0.99535	0.99553
LEU-COMP-THERM-071.c03	1.00000 (0.00070)	0.99596	0.99599	0.99680
LEU-COMP-THERM-071.c04	1.00000 (0.00060)	0.99466	0.99567	0.99600
LEU-COMP-THERM-mirte1.c13	1.00000 (0.00106)	0.99736	0.99780	0.99772
LEU-COMP-THERM-mirte1.c14	1.00000 (0.00105)	0.99700	0.99753	0.99792
PU-SOL-THERM-039.c06	1.00050 (0.00133)	0.99625	0.99593	0.99599

TABLE 7.3: Benchmark and Calculate multiplication factor k_{eff} using different TSL evaluations along with new IRSN ^{16}O and ^{235}U evaluation. Benchmark and the statistical uncertainty in the k_{eff} is given in parentheses.

It seems to be that addition of both ^{16}O and ^{235}U show great improvement in the k_{eff} results and improves the C-E value for a majority of benchmarks. In the ^{235}U evaluation presently in the JEFF-3.3 library, the thermal fission cross section is low by around 0.4% compared to the standard value [2]. In the new IRSN ^{235}U evaluation, the thermal fission cross section has been corrected close to the new standard value [70]. This explains why the value of k_{eff} increases.

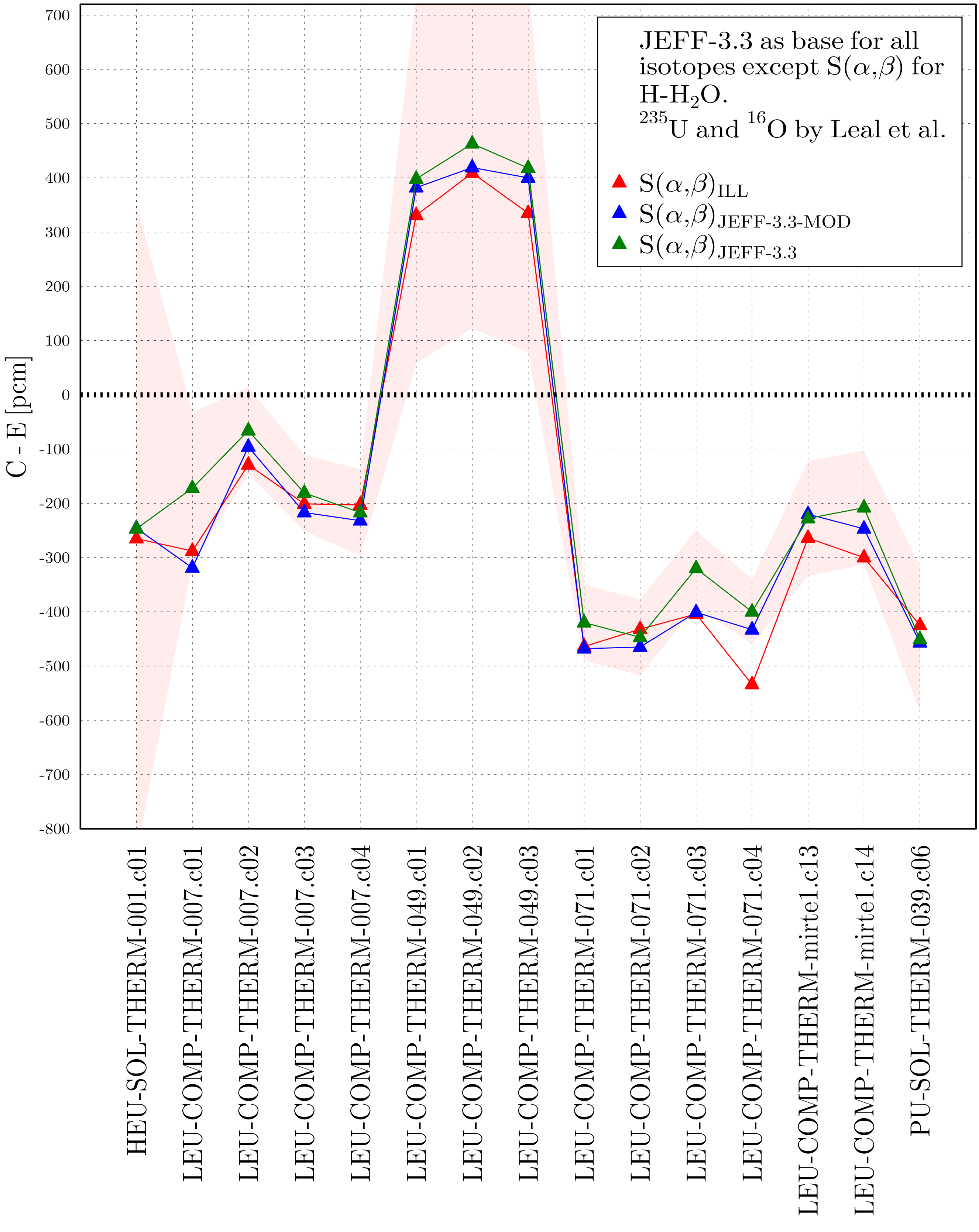

FIGURE 7.14: Calculated - Experimental (C-E) results for the selected ICSBEP benchmark using different TSL evaluations and the new IRSN ^{16}O and ^{235}U evaluations.

New TSL evaluations along with the new IRSN ^{16}O, ^{235}U evaluation and ^{235}U prompt fission neutron spectra (PFNS) from ENDF/B-VIII.0

New TSL evaluations were tested with ^{235}U prompt fission neutron spectra (PFNS) from ENDF/B-VIII.0 along with the new evaluations of ^{16}O and ^{235} by Leal et al. The use of this PFNS indicates an improvement in the benchmark calculation as can be seen in Table. 7.4 and Fig. 7.15.

Benchmark ID & k_{eff}		k_{eff} using different TSLs		
		ILL	JEFF-3.3-MOD	JEFF-3.3
HEU-SOL-THERM-001.c01	1.00040 (0.00600)	0.99882	0.99909	0.99914
LEU-COMP-THERM-007.c01	1.00000 (0.00140)	0.99792	0.99797	0.99860
LEU-COMP-THERM-007.c02	1.00000 (0.00080)	0.99940	0.9993	0.99956
LEU-COMP-THERM-007.c03	1.00000 (0.00070)	0.99809	0.99819	0.99824
LEU-COMP-THERM-007.c04	1.00000 (0.00080)	0.99819	0.99832	0.99783
LEU-COMP-THERM-049.c01	1.00000 (0.00340)	1.00037	1.00021	1.00037
LEU-COMP-THERM-049.c02	1.00000 (0.00340)	1.00390	1.00402	1.00422
LEU-COMP-THERM-049.c03	1.00000 (0.00340)	1.00415	1.00427	1.00461
LEU-COMP-THERM-071.c01	1.00000 (0.00070)	1.00353	1.00368	1.00467
LEU-COMP-THERM-071.c02	1.00000 (0.00070)	0.99676	0.99715	0.99734
LEU-COMP-THERM-071.c03	1.00000 (0.00070)	0.99671	0.99647	0.99685
LEU-COMP-THERM-071.c04	1.00000 (0.00060)	0.99758	0.99673	0.99758
LEU-COMP-THERM-mirte1.c13	1.00000 (0.00106)	0.99659	0.99892	0.99709
LEU-COMP-THERM-mirte1.c14	1.00000 (0.00105)	0.99769	0.99791	0.99790
PU-SOL-THERM-039.c06	1.00050 (0.00133	0.99744	0.99803	0.99744

TABLE 7.4: Benchmark and Calculate multiplication factor k_{eff} using different TSL evaluations along with new IRSN ^{16}O and ^{235}U evaluation. In addition, the new ^{235}U prompt fission neutron spectrum from ENDF/B-VIII.0 has been used in this study. Benchmark and the statistical uncertainty in the k_{eff} are given in parentheses.

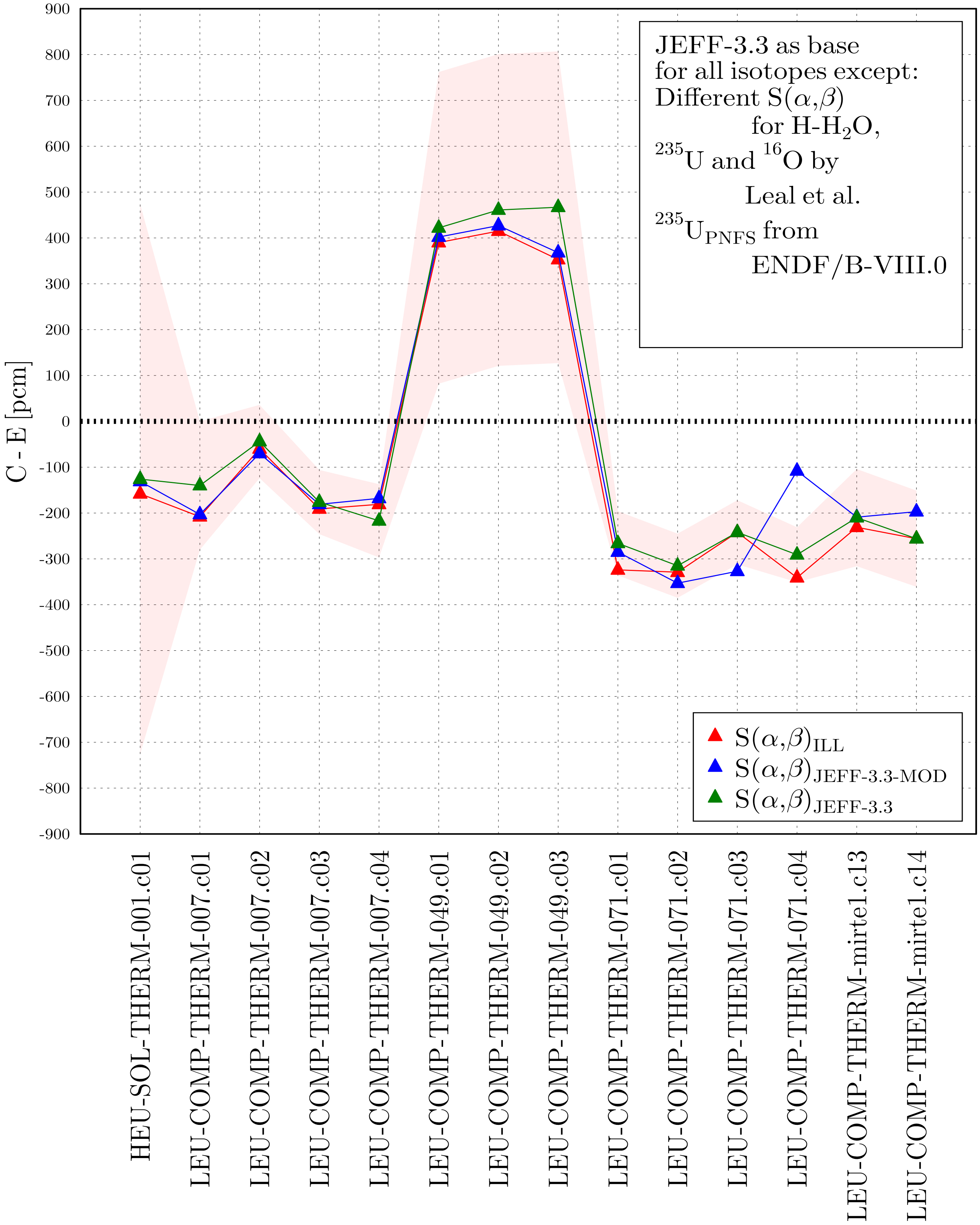

FIGURE 7.15: Calculated - Experimental (C-E) results for the selected ICSBEP benchmark using different TSL evaluations, new IRSN ^{16}O and ^{235}U evaluations. In addition, the new ^{235}U prompt fission neutron cross section from ENDF/B-VIII.0 has been used in this study.

The effort to improve the evaluation on the basis of differential data is crucial so as to include the best physics available (first principle). However, for practical applications such as criticality safety benchmark calculations, one must take into the account the contributions from each isotopes present in the benchmark contributing to the k_{eff} . This can be clearly seen in the calculations before where the new TSL, ^{16}O, ^{235}U and $^{235}U_{PFNS}$ evaluations were used in conjunction. One might dispute whether the benchmark result presented by using new TSL evaluations in combination with other new IRSN evaluations has improved the results. However, the observed results as a whole do not deteriorate the existing result.

Conclusions

The research work developed in this PhD is in connection to reactor physics applications, where accurate determinations of thermal scattering cross sections for light water are important to model nuclear systems that utilize light water as a moderator or coolant. Special attention was given to the TSL behavior at high temperatures and pressures at which nuclear reactors operate, i.e. temperature around 550 K and pressure around 150 bar. One of the major objectives of this thesis was to investigate the impact of pressure on the TSL for light water as no information exists in the literature on the impact of pressure in TSL for practical applications.

Several thermal scattering models used in the TSL evaluations available in the major nuclear data libraries were reviewed. In particular, the latest TSL evaluation for light water in the JEFF-3.3 and ENDF/B-VIII.0 were investigated in terms of the methodologies incorporated in generating thermal scattering cross section data based on the LEAPR module of the NJOY code. The TSL for light water in JEFF-3.3 is based on experimentally measured frequency spectrum whereas, ENDF/B-VIII.0 is based on molecular dynamics simulations using the TIP4P/2005f flexible water potential. Molecular diffusion is also modeled differently in these two libraries. A free gas model is used in the JEFF-3.3 whereas the Egelstaff and Schofield diffusion model is used in the ENDF/B-VIII.0 TSL library.

Both JEFF-3.3 and ENDF/B-VIII.0 TSL evaluations were further investigated on the basis of comparing the double differential cross sections and total cross sections with the available experimental data at room temperatures. It was found that both the libraries perform equally good at room temperatures and the comparison of the double differential cross section shows acceptable results. In particular, ENDF/B-VIII.0 showed better agreement with the quasi-elastic peak (< 10 meV) of the double differential cross section when compared with measurements performed at low incident neutron energies. This can be linked to the fact that ENDF/B-VIII.0 uses Egelstaff and Schofield model to describe molecular diffusion and a great deal of physics is involved in the low energy region where the diffusion process occurs. The advantage of using the Egelstaff and Schofield model was also observed when the comparison of the total cross section was made with the experimental data. ENDF/B-VIII.0 showed better agreement with experimental total cross section at low neutrons energies (< 1 meV) whereas the cross sections are high in JEFF-3.3 in this energy region.

Some differences in the shape of the frequency spectrum used in JEFF-3.3 and ENDF/B-VIII.0 were observed. The frequency spectrum utilized in the ENDF/B-VIII.0 at room temperature is able to represent correctly the energy bands corresponding to the molecular translation and rotation, whereas the translation band is missing in the frequency spectrum used in JEFF-3.3. However, at high temperatures, the shapes of the frequency spectrum in both libraries differ significantly in terms of the rotation band position. It was found that the rotation band in the frequency spectrum used in JEFF-3.3 does not changes with increasing temperature whereas a down shift in energy was observed in the ENDF/B-VIII.0.

The impact of the shift on the rotation band at high temperatures on reactor calculations were investigated by observing the ratio of the total cross section at high temperature with respect to the room temperature data. In general, this ratio should increase with increasing temperatures due to an increase in the probability of the up scattering of neutrons. The total cross section obtained using the JEFF-3.3 TSL evaluation showed that the ratio increases with increasing temperature, whereas it decreases in the neutron energy range of 15-50 meV when using the ENDF/B-VIII.0 TSL evaluation. This energy range (15-50 meV) is important in reactor physics applications as the majority of thermal nuclear systems (including PWRs) operate in this energy region. Such difference in the total cross section in thermal neutron energy region can have an impact on reactors operating at high temperatures. Since high temperature TSL data are utilized for PWR applications, care must be taken when using TSL from the ENDF/B-VIII.0 evaluation. However, it will be appropriate to develop clean critical integral benchmark at several temperatures to quantify the TSL temperature effects.

A new TSL evaluation named as $S(\alpha,\beta)_{\text{JEFF-3.3-MOD}}$ was evaluated based on this investigation and knowledge of the limitations of both JEFF-3.3 and ENDF/B-VIII.0. The JEFF-3.3 evaluation was modified, keeping the same frequency spectrum as in the original evaluation, but the molecular diffusion was described using the Egelstaff and Schofield model instead of free gas model. This new evaluation showed improvements when compared to double differential and total cross section data even at low incident neutron energies.

In order to verify these discrepancies observed in the existing TSL libraries, especially at high temperatures and to study the impact of pressure on the TSL new TOF measurements for light water were carried out at ILL. Double differential cross section measurements for light water were performed for a series of temperatures and pressures. The measured data was translated to the dynamic structure factor and the frequency spectrum. From the analysis of the measured data, an important conclusion is that the impact of pressure on the frequency spectrum, double differential cross section and total cross section is negligible.

The frequency spectrum measured experimentally were also qualitatively compared with the one utilized in the JEFF-3.3 and ENDF/B-VIII.0 TSL evaluations. The position of the rotational band at room temperature, both in the JEFF-3.3 and ENDF/B-VIII.0 is in close agreement with the new TOF measurements. It was found that the shape of the frequency spectrum at high temperatures is in agreement with the JEFF-3.3 even for higher temperatures (no down shift in energy of the rotation bands, as seen in ENDF/B-VIII.0, was observed). A new TSL evaluation named as $S(\alpha,\beta)_{\text{ILL}}$ was prepared at the experimental temperatures using the new frequency spectrum measured at ILL. The ratio of total cross section at the experimental temperatures generated using $S(\alpha,\beta)_{\text{ILL}}$ showed agreement with the JEFF-3.3, i.e. the ratio increases with increasing temperatures.

Since the TOF experiments were carried out at limited temperatures and pressures covering a small range of energy and momentum transfer, new MD simulations were carried out to complement the experimental data. Instead of a non polarizable water potential (TIP4P/2005f), like the one utilized in ENDF/B-VIII.0, a polarizable water potential with explicit hydrogen bond interaction (TCPE) was used to perform light water simulations using the PolarisMD code for a series of temperatures and pressures.

In the frequency spectrum obtained from the new MD simulations, a very slight shift in the energy of the rotational band with increasing temperature was observed, as opposed to the ENDF/B-VIII.0 where this shift is significantly larger. Finally a new TSL library was prepared using the frequency spectrum obtained from the PolarisMD simulations named as $S(\alpha,\beta)_{\text{TCPE}}$.

It has been demonstrated that choosing water potential without testing its limitations for high temperature and pressure conditions is not a viable option. Pointing out the best water potential is a difficult task as different potentials reflect various different properties at different thermodynamic conditions. A non-polarizable model such as TIP4P/2005f that is parametrized at ambient conditions might fail to predict the change in the hydrogen bond at high temperatures and pressures. The studies carried out in this PhD work indicate that the use of a water potential for applications, in particular reactor applications, requires thorough tests for all the thermodynamic properties of water at the required temperatures and pressures. Failure to do so may lead to misleading results and conclusions. In this respect PolarisMD simulations using the TCPE water potential seem promising.

Finally, the SAB module of the GAIA code was developed with capabilities to generate TSL libraries for light water at the desired temperature requested by the user. It was highlighted that even though a series of temperatures are tabulated in existing TSL evaluations, in certain cases one might need the TSL data at some specific temperature not available in the evaluations. For instance, in the French plutonium temperature effect experimental program, instead of a positive temperature effect (measured experimentally) a negative temperature effect was observed when using TSL data at the closest temperature available in the TSL evaluations. The SAB module was tested by generating new TSL evaluations at the desired temperatures to simulate the experimental program. This was the first time that a positive reactivity effect was validated using new TSL data at correct temperatures developed using the SAB module.

The performance of all the newly developed TSL evaluations, i.e. $S(\alpha,\beta)_{\text{JEFF-3.3-MOD}}$, $S(\alpha,\beta)_{\text{ILL}}$ and $S(\alpha,\beta)_{\text{TCPE}}$ were tested on a series of differential, double differential and total cross section measurements available in the literature. Also, a series of critical benchmarks available in the ICSBEP data base, sensitive to thermal scattering energy region were chosen and the new TSL libraries were tested to evaluate their performances.

In addition, new IRSN ^{16}O, ^{235}U evaluations along with ^{235}U PFNS from ENDF/B-VIII.0 were tested in conjunction with the new TSL evaluations and a global improvement in these benchmark results were observed. The addition of both ^{16}O and ^{235}U, from evaluations performed at IRSN, show great improvement in the k_{eff} results and improves the C-E value for a majority of benchmarks.

Further improvements are still needed to prepare better evaluations of TSL for light water. New experiments were carried out at the SNS facility in the US and the data will be analyzed in the near future. After observing the performance of all the new TSL evaluations, it is suggested to utilize $S(\alpha,\beta)_{\text{TCPE}}$ developed during this thesis, until newly acquired experimental data at SNS is fully analyzed.

Future work and perspectives

The present research work has its own limitations both in the experimental approach dealing with TOF experiments and the theoretical approach dealing with MD simulations. Due to the restricted time frame during this PhD thesis, there is still much room for improvements in both the approaches. Also, the SAB module discussed in **Chapter 6**, though tested, is still in its preliminary phase to generate TSL. Hereby, a brief perspective is presented to define how this research work could be extended to obtain improved TSLs and better confidence in the methodologies adapted for their generation.

Experimental approach

The experimental approach adapted in this thesis to generate TSL was by performing TOF experiments with light water at the ILL. The TSL libraries generated during this work based on the TOF data, i.e. $S(\alpha,\beta)_{\mathrm{ILL}}$ was derived using the measured frequency spectrum. However, the frequency spectrum obtained from both the the IN4c and IN6 spectra can only reveal information about the rotational band due to the chosen incident energy of the neutron which limits the energy transfer range. Due to this limitation the high energy modes, i.e. the bending and the stretching modes were not accessible in the measured spectra and these modes were approximated using harmonic oscillators while preparing the LEAPR parameters to generate the TSL. This approximation works quite well, but poses a challenge to define the energy of these oscillators, which is not well known experimentally for high temperatures. To avoid these approximations, using the full frequency spectrum of light water extending to higher energy transfers would be more reliable.

There is still a need for high resolution differential and total cross section data for light water at high temperatures and pressures on a broad energy and momentum transfer range. Figure. 7.16 represents a pictorial sketch of the frequency spectrum that can be accessed depending on the choice of incident neutron energies. As it can be seen, the entire frequency spectrum can be accessible by choosing a high incident neutron energy, which makes facilities like the Spallation Neutron Source (SNS) at the Oak Ridge National Laboratory (ORNL), a favorable option to carry out TOF experiments. Also, high resolution measurements of energy and momentum transfers are required to study the dynamical structure properties of light water with a satisfactory signal to noise ratio. The SEQUOIA spectrometer at the SNS allows inelastic neutron scattering studies with fine three-dimensional momentum and energy transfer measurements. Also, the availability of different high incident energies by choosing the appropriate Fermi chopper speed makes it a favorable machine for cross section data measurements. TOF measurements for light water at thermodynamic conditions of the PWR operating conditions in wide range

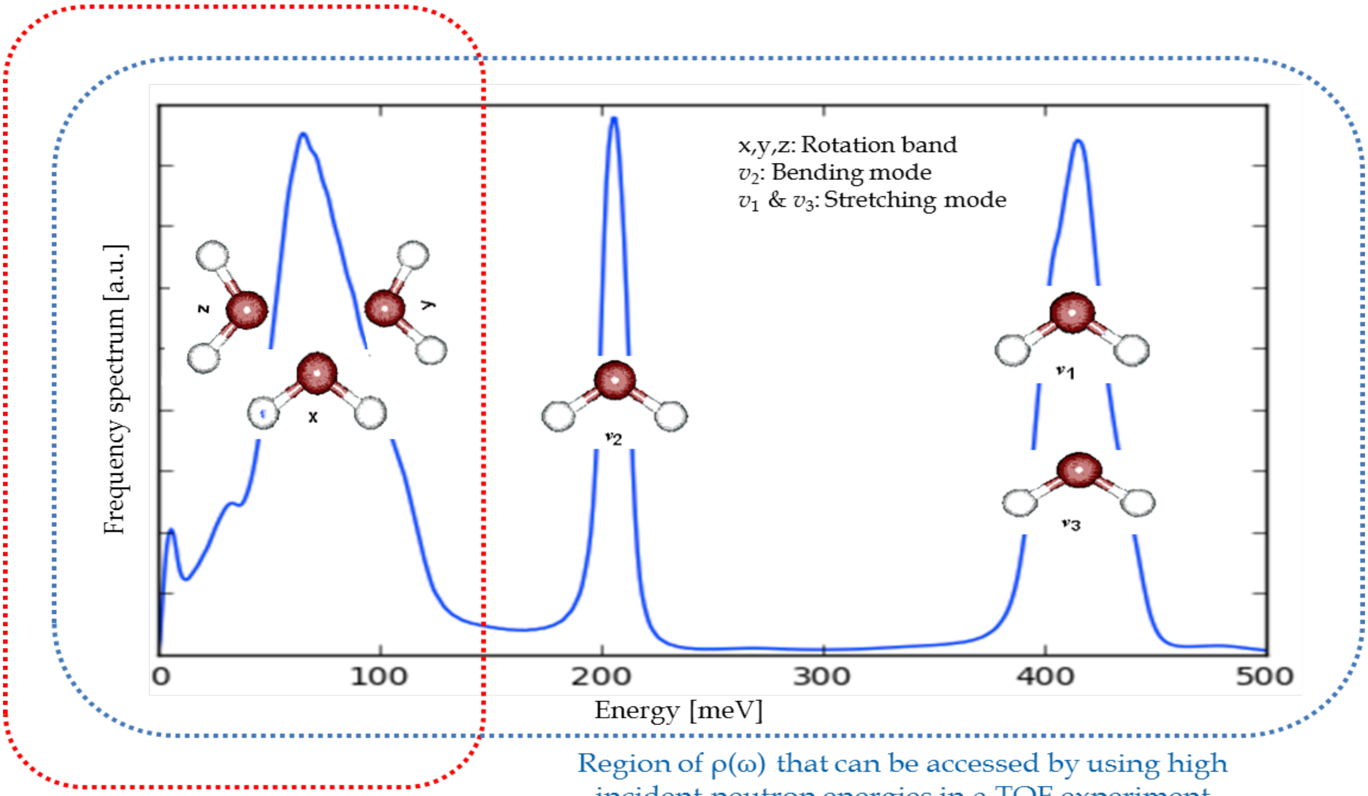

Region of ρ(ω) that can be accessed by using high incident neutron energies in a TOF experiment

Region of ρ(ω) accessible from the TOF experiments performed at the ILL

FIGURE 7.16: Pictorial diagram representing the different energy bands in the frequency spectrum that can be accessible depending on the choice of incident neutron energy. The data for this particular frequency spectrum has been taken from Ref. [6].

of energy transfer have been carried out using the SEQUOIA spectrometer at the SNS in the last week of July

2018. The measurements have been performed at reasonably high incident energy without compromising the resolution, to investigate the full frequency spectrum domain obtained from the $S(\vec{q}, \omega)$. The temperature range that has been measured lies between 295 K and 600 K and pressure range between 1 bar and 150 bar. Five different sets of measurements at incident neutron energies (800 meV, 280 meV, 160 meV, 60 meV and 8 meV) have been carried out for each thermodynamic conditions. These incident energies would help exploring different regions of the frequency spectrum of light water, optimizing resolution and energy and momentum transfer range. Multiple scattering effect which is an unavoidable characteristics of such kind of data measurements, was optimized to keep it as minimum as possible by choosing a thin sample.

Also, the evaluation of the new SNS data would provide the grounds to obtain the uncertainties associated with the experimental conditions in connection with the measurements, namely, the systematic and the statistical uncertainties. While existing nuclear data libraries contains TSL evaluation for water for certain PWR operational condition it should be noted that no uncertainty information exists based on actual experimental data. This uncertainty quantification based from the data measured at the ILL, was unrealistic due to high multiple scattering.

The obtained anticipated results, once fully analyzed can be compared with the MD simulations and with the experimental data at ILL (in a smaller energy range). Two different experimental data (ILL and SNS) would facilitate the development of a new model-free and more accurate TSL for water, knowledge of which is very important to design moderators in modern thermal nuclear systems. The outcome of this study will not only help in comparing the MD and experimental results but will also lead to a better interpretation of the impact of temperature and pressure on the $S(\alpha, \beta)$. The experiments carried out at the SNS will be of great benefit to better understand the thermal scattering behavior of light water which will have a direct impact on nuclear systems that use light water as the moderator under high temperature and pressure conditions.

The data measured at the SNS for light water at high temperatures and pressures is related to reactor applications. However, for criticality safety studies low temperature measurements (< 293.6 K) for moderators like ice, polyethylene, etc., would be of interest to enhance our present knowledge.

Theoretical approach

Due to time limitations integral benchmark tests were not carried out using the $S(\alpha, \beta)_{\text{TCPE}}$ and $S(\alpha, \beta)_{\text{ENDF/B-VIII.0}}$. Fig. 7.17 shows the C-E values obtained using these two TSLs, i.e. both generated using MD simulations, the former based on the TCPE rigid water model and the latter based on the TIP4P/2005f flexible non-polarizable model. No significant conclusion can be drawn based on Fig. 7.17 about the performance of these water

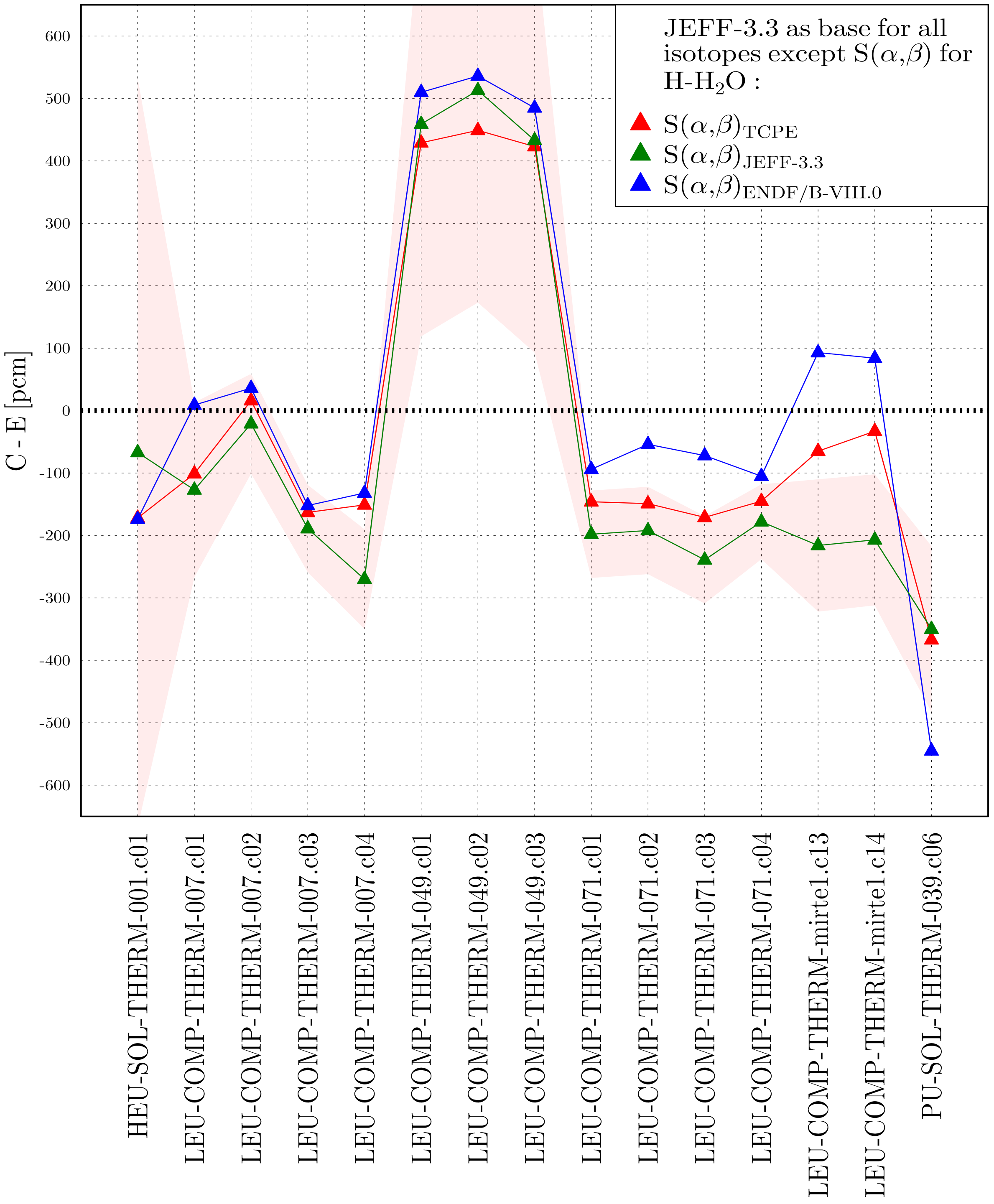

FIGURE 7.17: Calculated - Experimental (C-E) results for the selected ICSBEP benchmark using different TSL evaluations.

models as a mixed agreement is observed between the two. C-E value improves for some benchmarks using the $S(\alpha,\beta)_{\mathrm{TCPE}}$, whereas $S(\alpha,\beta)_{\mathrm{ENDF/B\text{-}VIII.0}}$ shows better agreement with some specific benchmarks. Also, the chosen benchmarks are at ambient temperatures and it would be important to test it with high temperature benchmarks, if available in the future. As already discussed, using an MD water model without testing its limitations at higher temperatures and pressure is not a viable option for reactor physics community. This implies further studies to reassess or parametrize water models at high temperatures and pressures so as to correctly reproduce the properties of light water.

There is also a need for developing new processing methodologies to improve thermal scattering data evaluations and expand their applicability. Using better physics models and MD simulations, the accuracy and reliability of the existing cross section data can be improved and the uncertainties in the cross sections can be quantified. Significant work is still to be done in revisiting the limitations of the LEAPR module of the NJOY code. Implementation of new robust methodologies to generate TSLs within the framework of IRSN nuclear data processing code GAIA, which is under development, would be an important step in this direction. This would provide an opportunity to explore mechanisms to address issues regarding TSL determination at any temperature within a reasonable amount of time for Monte Carlo applications (for example, Doppler on-the-fly). The developed methodology can then be implemented into Monte Carlo neutron transport codes to generate TSL on-the-fly within the Monte Carlo environment. The viability of the approach for generating TSL on the fly needs be thoroughly examined so as to ensure its practicality.

References

[1] D. E. Cullen, R Blomquist, M Greene, E Lent, R MacFarlane, S McKinley, E Plechaty, and J. C. Sublet. *How Accurately Can We Calculate Neutrons Slowing Down In Water ?* en. Tech. rep. UCRL-TR-220605, 889442. Mar. 2006. DOI: `10.2172/889442` (cit. on p. 1).

[2] *JEFF-3.3* (cit. on pp. 2, 25, 26, 136).

[3] Z. Ge, H. Wu, G. Chen, and R. Xu. “CENDL project, the chinese evaluated nuclear data library”. en. In: *EPJ Web of Conferences* 146 (2017), p. 02002. ISSN: 2100-014X. DOI: `10.1051/epjconf/201714602002` (cit. on p. 2).

[4] *JENDL-4.0: A New Library for Nuclear Science and Engineering: Journal of Nuclear Science and Technology: Vol 48, No 1* (cit. on p. 2).

[5] L. Leal. *Role of Nuclear Data in Response to Practical Applications*. Tech. rep. (cit. on p. 2).

[6] J. Marquez Damian and V. Semkova. *Compilation of Thermal Neutron Scattering Data for Experimental Nuclear Reaction Data Library (EXFOR)*. Apr. 2016 (cit. on pp. 3, 26, 146).

[7] L. Van Hove. “Correlations in Space and Time and Born Approximation Scattering in Systems of Interacting Particles”. In: *Physical Review* 95.1 (July 1954), pp. 249–262. DOI: `10.1103/PhysRev.95.249` (cit. on pp. 3, 5, 16, 19).

[8] G. L. Squires. *Introduction to the Theory of Thermal Neutron Scattering by G. L. Squires*. en. Mar. 2012. DOI: `10.1017/CBO9781139107808` (cit. on pp. 3, 11).

[9] A. Santamarina, D. Bernard, P. Blaise, M. Coste, A. Courcelle, T. D. Huynh, C. Jouanne, P. Leconte, O. Litaize, and S. Mengelle. "The JEFF-3.1. 1 nuclear data library". In: *JEFF report* 22.10.2 (2009), p. 2 (cit. on p. 5).

[10] K. N. Zaitsev, V. N. Petrov, S. P. Kuznetsov, O. A. Langer, I. V. Meshkov, and A. D. Perekrestenko. "The total cross sections of the interaction of ultracold neutrons with H2O and D2O". en. In: *Soviet Atomic Energy* 70.3 (Mar. 1991), pp. 238–242. ISSN: 1573-8205. DOI: `10.1007/BF01126475` (cit. on pp. 5, 61).

[11] S. B. Herdade. *Progress Report on Nuclear Data in Brazil*. Tech. rep. Institute International Atomic Energy Agency, Vienna, Austria, 1972 (cit. on p. 5).

[12] S. B. Stepanov and V. E. Zhitarev. "Total cross section for the interaction of cold neutrons with water". en. In: *Soviet Atomic Energy* 41.2 (Aug. 1976), pp. 743–743. ISSN: 1573-8205. DOI: `10.1007/BF01132657` (cit. on p. 5).

[13] *NEA Data Bank Nuclear Data Services: Experimental Data* (cit. on p. 5).

[14] *THE JEFF3.1.1 LIBRARY FOR ACCURATE CRITICALITY-SAFETY CALCULATIONS*. en (cit. on p. 5).

[15] M. B. Chadwick et al. "ENDF/B-VII.1 Nuclear Data for Science and Technology: Cross Sections, Covariances, Fission Product Yields and Decay Data". In: *Nuclear Data Sheets*. Special Issue on ENDF/B-VII.1 Library 112.12 (Dec. 2011), pp. 2887–2996. ISSN: 0090-3752. DOI: `10.1016/j.nds.2011.11.002` (cit. on pp. 5, 27).

[16] A. C. S. Kahler III and R. Macfarlane. *NJOY2016*. en. Tech. rep. NJOY, NJOY16; 005075MLTPL00. Los Alamos National Lab. (LANL), Los Alamos, NM (United States), Aug. 2016 (cit. on p. 5).

[17] R. MacFarlane. *New Thermal Neutron Scattering Files for ENDF/B-VI, Release 2*. Tech. rep. LA-12639-MS (ENDF-356). Mar. 1994 (cit. on pp. 5, 16, 21, 22, 27).

[18] M. Mattes and J. Keinert. *Thermal Neutron Scattering Data for the Moderator Materials H2O, D2O and ZrH in ENDF-6 Format and as ACE Library for MCNP(X) Codes*. Tech. rep. INDC(NDS)-0470. International Nuclear Data Committee, 2005 (cit. on pp. 5, 7, 29).

[19] J. Koppel and D. Houston. *Reference manual for ENDF thermal neutron scattering data*. Tech. rep. GA-8774, ENDF-269. General Atomics, 1978 (cit. on pp. 5, 27).

[20] B. C. Haywood. "The spectral density of hydrogen in water". In: *Journal of Nuclear Energy* 21.3 (Jan. 1967), pp. 249–262. ISSN: 0022-3107. DOI: `10.1016/S0022-3107(67)90072-X` (cit. on pp. 6, 37).

[21] B. Haywood and I. Thorson. “The Scattering Law for Light and Heavy Water at 20 C and 150 C”. In: *Proceedings of the Brookhaven Conference on Neutron thermalization, IAEA*. 1962 (cit. on pp. 6, 7, 27, 28, 33, 37, 88, 89).

[22] E. Farhi, G. Ferran, W. Haeck, E. Pellegrini, and Y. Calzavara. “Light and heavy water dynamic structure factor for neutron transport codes”. en. In: *Journal of Nuclear Science and Technology* 52.6 (June 2015), pp. 844–856. ISSN: 0022-3131, 1881-1248. DOI: `10.1080/00223131.2014.984002` (cit. on pp. 7, 33).

[23] B. Haywood and D. Page. “Scattering Laws for Heavy Water at 540K and Light Water at 550K”. In: *Proc. of the Symp. on Neutron Thermalization and Reactor Spectra*. Vol. Vol. I. 1967 (cit. on p. 7).

[24] J. I. Márquez Damián, J. R. Granada, and D. C. Malaspina. “CAB models for water: A new evaluation of the thermal neutron scattering laws for light and heavy water in ENDF-6 format”. In: *Annals of Nuclear Energy* 65 (Mar. 2014), pp. 280–289. ISSN: 0306-4549. DOI: `10.1016/j.anucene.2013.11.014` (cit. on pp. 7, 27, 33, 34, 82, 102).

[25] W. Haeck and N. Leclaire. “Thermal scattering data and criticality safety”. In: vol. 1. Sept. 2008 (cit. on pp. 7, 113).

[26] J. P. Scotta. “Amélioration des données neutroniques de diffusion thermique et épithermique pour l’interprétation des mesures intégrales”. PhD Thesis. 2017 (cit. on p. 11).

[27] J. I. M. Damián. “Desarrollo y aplicaciones de nuevas bibliotecas de secciones eficaces neutrónicas para H2O, D2O y HDO”. PhD thesis (cit. on pp. 11, 23).

[28] A.-Q. Iyad Ibrahim. “Thermal Neutron Scattering in Graphite”. PhD thesis. NC State University, 2008 (cit. on p. 11).

[29] R. MacFarlane and D. Muir. *The NJOY Nuclear Data Processing System*. Tech. rep. LA-12470-M. USA: Los Alamos National Laboratory, 1994 (cit. on p. 16).

[30] P. A. Egelstaff. “Neutron scattering studies of liquid diffusion”. In: *Advances in Physics* 11.43 (July 1962), pp. 203–232. ISSN: 0001-8732. DOI: `10.1080/00018736200101282` (cit. on pp. 21, 35).

[31] D. A. Brown et al. “ENDF/B-VIII.0: The 8th Major Release of the Nuclear Reaction Data Library with CIELO-project Cross Sections, New Standards and Thermal Scattering Data”. In: *Nuclear Data Sheets*. Special Issue on Nuclear Reaction Data 148 (Feb. 2018), pp. 1–142. ISSN: 0090-3752. DOI: `10.1016/j.nds.2018.02.001` (cit. on pp. 25, 26).

[32] H. B.C. and P. D.I. “Scattering law for heavy water at 540 K and light water at 550 K”. In: *Proceedings f a Symposium, Ann Arbor, 17-21 July 1967*. Vol. Vol. I. INTERNATIONAL ATOMIC ENERGY AGENCY, VIENNA, 1968 (cit. on p. 28).

[33] Y. Abe and S. Tasaki. “Molecular dynamics analysis of incoherent neutron scattering from light water via the Van Hove space–time self-correlation function with a new quantum correction”. In: *Annals of Nuclear Energy* 83 (Sept. 2015), pp. 302–308. ISSN: 0306-4549. DOI: `10.1016/j.anucene.2015.04.024` (cit. on pp. 33, 43).

[34] I. Shvab and R. J. Sadus. “Atomistic water models: Aqueous thermodynamic properties from ambient to supercritical conditions”. In: *Fluid Phase Equilibria*. Aqueous Solutions 407 (Jan. 2016), pp. 7–30. ISSN: 0378-3812. DOI: `10.1016/j.fluid.2015.07.040` (cit. on pp. 33, 39, 97, 101).

[35] M. A. González and J. L. F. Abascal. “A flexible model for water based on TIP4P/2005”. eng. In: *The Journal of Chemical Physics* 135.22 (Dec. 2011), p. 224516. ISSN: 1089-7690. DOI: `10.1063/1.3663219` (cit. on pp. 33, 39, 98).

[36] A. G. Novikov, A. A. Van’kov, and L. S. Gosteva. “Temperature dependence of the general spectrum for water”. en. In: *Journal of Structural Chemistry* 31.1 (Jan. 1990), pp. 77–85. ISSN: 0022-4766, 1573-8779. DOI: `10.1007/BF00752017` (cit. on pp. 35, 38).

[37] P. Schofield. “Space-Time Correlation Function Formalism for Slow Neutron Scattering”. In: *Physical Review Letters* 4.5 (Mar. 1960), pp. 239–240. DOI: `10.1103/PhysRevLett.4.239` (cit. on pp. 35, 81).

[38] S. E. Lappi, B. Smith, and S. Franzen. “Infrared spectra of , and D2O in the liquid phase by single-pass attenuated total internal reflection spectroscopy”. en. In: *Spectrochimica Acta Part A: Molecular and Biomolecular Spectroscopy* 60.11 (Sept. 2004), pp. 2611–2619. ISSN: 13861425. DOI: `10.1016/j.saa.2003.12.042` (cit. on p. 35).

[39] L. J. Esch, M. L. Yeater, W. E. Moore, and K. W. Seemann. “The Temperature Dependence of Neutron Inelastic Scattering from Water”. In: *Nuclear Science and Engineering* 46.2 (1971), pp. 223–235. DOI: `10.13182/NSE71-A22356` (cit. on p. 37).

[40] K. E. Larsson and U. Dahlborg. “A Study of the Diffusive Atomic Motions in Glycerol and of the Vibratory Motions in Glycerol and Light and Heavy Water by Cold Neutron Scattering”. In: *Inelastic Scattering of Neutrons in Solids and Liquids. VI Proceedings of the Symposium on Inelastic Scattering of Neurons in Solids and Liquids*. 1963 (cit. on pp. 37, 38).

[41] R. B. Smith. *Some Measurements of the Neutron Scattering Law for Light Water at 95 C*. Tech. rep. BNWL-345. Pacific Northwest Laboratories, 1967 (cit. on p. 37).

[42] D. K. Ross, F. P. Szabo, and Y. Sanalan. “Inelastic Scattering of Neutrons from Benzene and Water”. In: *Neutron Thermalization and Reactor Spectra. Vol. I. Proceedings of the Symposium on Neutron Thermalization and Reactor Spectra*. 1968 (cit. on pp. 37, 38).

[43] F. Bischoff, W. Bryant, L. Esch, C. Lajeunesse, W. Moore, S. Pan, S. Purohit, and M. Yeater. *Low Energy Neutron Inelastic Scattering (LENIS) in Linear Accelerator Project Progress Report*. Tech. rep. RPI-328-27. RPI, 1967 (cit. on pp. 43, 122).

[44] O. K. Harling. “Slow Neutron Inelastic Scattering Study of Light Water and Ice”. In: *The Journal of Chemical Physics* 50.12 (June 1969), pp. 5279–5296. ISSN: 0021-9606. DOI: `10.1063/1.1671047` (cit. on pp. 46, 122).

[45] *ISIS Neutron Training Course* (cit. on p. 68).

[46] *Time-of-flight spectrometers IN4 and IN6, Guide to the Neutron Research Facilities*. Tech. rep. Institut Laue-Langevin, Grenoble, France, 2008 (cit. on pp. 71, 72).

[47] G Cicognani, H Mutka, and F Sacchetti. “The thermal neutron time-of-flight spectrometer IN4C”. In: *Physica B: Condensed Matter* 276-278 (Mar. 2000), pp. 83–84. ISSN: 0921-4526. DOI: `10.1016/S0921-4526(99)01366-6` (cit. on p. 71).

[48] D. Richard, M. Ferrand, and G. J. Kearley. “Analysis and Visualisation of Neutron-Scattering Data”. en. In: *Journal of Neutron Research* 4.1-4 (Jan. 1996), pp. 33–39. ISSN: 1023-8166. DOI: `10.1080/10238169608200065` (cit. on p. 77).

[49] B. D. Hehr. “Development of the Thermal Neutron Scattering Cross Sections of Graphitic Systems using Classical Molecular Dynamics Simulations.” PhD thesis. 2010 (cit. on pp. 81, 112).

[50] J. S. Bader and B. J. Berne. “Quantum and classical relaxation rates from classical simulations”. In: *The Journal of Chemical Physics* 100.11 (June 1994), pp. 8359–8366. ISSN: 0021-9606. DOI: `10.1063/1.466780` (cit. on p. 82).

[51] L. Frommhold. *Collision-induced Absorption in Gases*. Feb. 1994 (cit. on p. 82).

[52] S. A. Egorov, K. F. Everitt, and J. L. Skinner. “Quantum Dynamics and Vibrational Relaxation”. In: *The Journal of Physical Chemistry A* 103.47 (Nov. 1999), pp. 9494–9499. ISSN: 1089-5639. DOI: `10.1021/jp9919314` (cit. on p. 82).

[53] J. C. Phillips, R. Braun, W. Wang, J. Gumbart, E. Tajkhorshid, E. Villa, C. Chipot, R. D. Skeel, L. Kalé, and K. Schulten. "Scalable molecular dynamics with NAMD". en. In: *Journal of Computational Chemistry* 26.16 (Dec. 2005), pp. 1781–1802. ISSN: 1096-987X. DOI: `10.1002/jcc.20289` (cit. on p. 96).

[54] S. Plimpton. "Fast Parallel Algorithms for Short-Range Molecular Dynamics". In: *Journal of Computational Physics* 117.1 (Mar. 1995), pp. 1–19. ISSN: 0021-9991. DOI: `10.1006/jcph.1995.1039` (cit. on p. 96).

[55] I. T. Todorov, W. Smith, K. Trachenko, and M. T. Dove. "DL_POLY_3: new dimensions in molecular dynamics simulations via massive parallelism". en. In: *Journal of Materials Chemistry* 16.20 (May 2006), pp. 1911–1918. ISSN: 1364-5501. DOI: `10.1039/B517931A` (cit. on p. 96).

[56] D. Van Der Spoel, E. Lindahl, B. Hess, G. Groenhof, A. E. Mark, and H. J. C. Berendsen. "GROMACS: fast, flexible, and free". eng. In: *Journal of Computational Chemistry* 26.16 (Dec. 2005), pp. 1701–1718. ISSN: 0192-8651. DOI: `10.1002/jcc.20291` (cit. on pp. 96, 102).

[57] F. Réal, V. Vallet, J.-P. Flament, and M. Masella. "Revisiting a many-body model for water based on a single polarizable site: From gas phase clusters to liquid and air/liquid water systems". In: *The Journal of Chemical Physics* 139.11 (Sept. 2013), p. 114502. ISSN: 0021-9606. DOI: `10.1063/1.4821166` (cit. on pp. 96, 99, 101).

[58] J. L. F. Abascal and C. Vega. "A general purpose model for the condensed phases of water: TIP4P/2005". In: *The Journal of Chemical Physics* 123.23 (Dec. 2005), p. 234505. ISSN: 0021-9606. DOI: `10.1063/1.2121687` (cit. on p. 98).

[59] M. Masella and J. P. Flament. "A pairwise and two many-body models for water: Influence of nonpairwise effects upon the stability and geometry of (H2O)n cyclic (n=3–6) and cagelike (n=6–20) clusters". In: *The Journal of Chemical Physics* 107.21 (Dec. 1997), pp. 9105–9116. ISSN: 0021-9606. DOI: `10.1063/1.475202` (cit. on pp. 99, 101).

[60] W. W. Engle. "Cross Section Processing Codes and Data Bases (AMPX)". en. In: *Computer Techniques in Radiation Transport and Dosimetry*. Ed. by W. R. Nelson and T. M. Jenkins. Ettore Majorana International Science Series. Boston, MA: Springer US, 1980, pp. 123–124. ISBN: 978-1-4684-3608-2. DOI: `10.1007/978-1-4684-3608-2_8` (cit. on p. 107).

[61] *PREPRO 2018* (cit. on p. 107).

[62] G. Ferran. "Nouvelles méthodes numériques pour le traitement des sections efficaces nucléaires." PhD thesis. 2015 (cit. on p. 109).

[63] T. Yamamoto and Y. Miyoshi. “Mechanisms of Positive Temperature Reactivity Coefficients of Dilute Plutonium Solutions”. In: *Nuclear Science and Engineering* 142.3 (Nov. 2002), pp. 305–314. ISSN: 0029-5639. DOI: `10.13182/NSE02-A2309` (cit. on p. 113).

[64] *ICSBEP Benchmark, PU-SOL-THERM-038*. International Handbook of Evaluated Criticality Safety Benchmark Experiments, 2016 edition NEA/NSC/DOC/(95)03/I, Volume 1 (cit. on p. 113).

[65] *ICSBEP Benchmark, PU-SOL-THERM-039*. Tech. rep. NEA/NSC/DOC/(95)03/I, Volume 1 (cit. on pp. 113, 115).

[66] ICSBEP. *ICSBEP-2016, International Criticality Safety Benchmark Experiment Handbook*. Tech. rep. (cit. on pp. 113, 114).

[67] H. Wim and L. Nicolas. *Thermal scattering data and criticality safety*. en (cit. on p. 114).

[68] J. R. Beyster. “Neutron Scattering from Light Water”. In: *Nuclear Science and Engineering* 31.2 (Feb. 1968), pp. 254–271. ISSN: 0029-5639. DOI: `10.13182/NSE68-A18238` (cit. on p. 126).

[69] L. Leal, E. Ivanov, G. Noguere, A. Plompen, and S. Kopecky. “Resonance parameter and covariance evaluation for 16O up to 6 MeV”. en. In: *EPJ Nuclear Sciences & Technologies* 2 (2016), p. 43. ISSN: 2491-9292. DOI: `10.1051/epjn/2016036` (cit. on p. 133).

[70] L. Leal, G. Noguere, C. Paradela, I. Durán, L. Tassan-Got, Y. Danon, and M. Jandel. “Evaluation of the 235U resonance parameters to fit the standard recommended values”. en. In: *EPJ Web of Conferences* 146 (2017), p. 02021. ISSN: 2100-014X. DOI: `10.1051/epjconf/201714602021` (cit. on pp. 134, 136).

Publications and oral presentations

Publications:

1. **V. Jaiswal**, N. Leclaire, L. Leal, F. Réal, V. Vallet, “Impact of Thermal Scattering Law of Light Water on the French Plutonium Temperature Effect Experimental Program”, **WONDER 2018: 5th International Workshop On Nuclear Data Evaluation for Reactor applications, 8th October – 12th October, 2018 Aix-en-Provence, France** (2018) (In progress).

2. **V. Jaiswal**, L. Leal, N. Leclaire, F. Réal, V. Vallet, “Evaluation of thermal scattering law for light water based on new time-of-flight measurements at the Institut Laue-Langevin (ILL)”, **PHYTRA4 - The Fourth International Conference on Physics and Technology of Reactors and Applications. Marrakech, Morocco, September 17-19, 2018, on CD-ROM, GMTR, Rabat, Morocco** (2018) (In progress).

3. **V. Jaiswal**, L. Leal, “Investigation of frequency spectrum of light water to generate thermal scattering law”, **PHYSOR 2018: Reactor Physics paving the way towards more efficient systems, Mexico** (2018).

4. **V. Jaiswal**, L. Leal *et al.* “Measurement of double differential cross-section of light water at high temperature and pressure to generate $S(\alpha, \beta)$”, **EPJ Web of Conferences 146, 13006** (2017).

Oral presentations:

1. Oral presentation, “Need for new TOF experiments for light water to generate improved TSL evaluations at high temperature and pressure”, **Spallation Neutron Source, Oak Ridge National Laboratory, Knoxville, United States** (2018).
2. Oral presentation, "Evaluation of thermal scattering law of light water based on experimental data at ILL and improved physics model", **RMD department, Oak Ridge National Laboratory, Knoxville, United States** (2018).
3. Oral presentation, “Thermal scattering law at high temperature and pressure” at Service d’Études de Réacteurs et de Mathématiques Appliquées (SERMA) laboratory, **CEA-Saclay, Saclay, France** (2018).
4. Oral presentation, “Investigation of frequency spectrum of light water to generate thermal scattering law”, **PHYSOR 2018: Reactor Physics paving the way towards more efficient systems, Mexico** (2018).
5. Oral presentation, “Journees des theses”, **Annecy, IRSN, France** (2018).
6. Oral presentation, **SG-42, WPEC meeting**, **OECD/NEA, Paris, France** (2018).
7. Oral presentation, “NAUSICAA Workshop”, **ILL, Grenoble, France** (2018).
8. Oral presentation, “Journees des theses”, **IRSN, France** (2017).
9. Oral presentation, **SG-42, WPEC meeting, OECD/NEA, Paris, France** (2017).
10. Oral presentation, “NAUSICAA Workshop”, **ILL, Grenoble, France** (2017).
11. Oral presentation, “Journees des theses”, **IRSN, France** (2016).
12. Oral presentation, **SG-42, WPEC meeting, OECD/NEA, Paris, France** (2016).
13. Oral presentation, “Measurement of double differential cross-section of light water at high temperature and pressure to generate $S(\alpha,\beta)$”, **ND2016 International conference on nuclear data, Bruges, Belgium** (2016).
14. Oral presentation, “NAUSICAA Workshop”, **ILL, Grenoble, France** (2016).

Appendix A

INS data reduction procedure

INS data collected at the ILL for both the IN4c and IN6 are treated using a data reduction software called as LAMP which is based on IDL language. The entire procedure starting from measured number of neutrons in the detector to transform it to double differential cross section and then to the dynamic structure factor and frequency spectrum is taken care by LAMP. Below are the .prox file while is used to treat the INS data for both the spectrometers.

A.1. Data reduction procedure for the IN4c TOF spectrometer

.prox file IN4c

```
;; Data treatment for 1-04-90 (IN4); H2O
;; lambda = 2.41 A (14 meV) ITF -50 meV ratio 2
;;---------------------------------------------------------------
;; Vana Cyl 10 mm
;;Load the raw data to LAMP by specifying the
;;directory of the data
rdset,inst='in4',path='data␣path',/raw
;;Load data files of vanadium (60m measurement)
a='83869>83877'
w1=rdopr(a)
;;Normalization to monitor
;;(monitor peak is found by least square Gaussian fit)
w1=normalise(w1,/monitor)
```

```
;;Extract sectors of the detector
;;bank (wide=extracts wide angle bank,bad=removes bad detectors)
w1=in4strip(w1,/wide,/bad)
w2=corr_tof(w1,/det_eff,/bkgd_trans)
w2=sumbank(w2)
w3=in5_t2e(w2)
w4=in5_sqw_rebin(w3,dQ=0.01,emin=-200)
write_lamp,'vanadium_in4_in_time',w=2, format='hdf'
write_lamp,'vanadium_in4_t2e', w=3, format='hdf'
write_lamp,'vanadium_in4_sqw', w=4, format='hdf'

;--------------------------------------------------
;Processing the empty cell at ~520K
;Load data files of measured empty cell (8h measurement)
a='83896>83911'
w5=rdopr(a)
w5=normalise(w5,/monitor)
w5=in4strip(w5,/wide,/bad)
w6=corr_tof(w5,/det_eff,/bkgd_trans)
w6=sumbank(w6)
w7=in5_t2e(w6)
w8=in5_sqw_rebin(w7,dQ =0.01,emin = -200)
write_lamp,'ec_in4_in_time', w=6, format='hdf'
write_lamp,'ec_in4_t2e', w=7, format='hdf'
write_lamp,'ec_in4_sqw', w=8, format='hdf'

;------------------------------------------------
;;Load data files of measured H2O sample;
;;Cylinder of H=70mm, Dint=6mm (mass = 1.9723g
;;Uncomment a particular value of 'b' and 'a' for
;;which you want to do a data treatment
;;------------------------------------------------------------------------------

;;; H2o RTRP
;b='t300_P1'  & a='83651>83655',& w9=rdopr(a) ;& @process_in4
;;;-----------------------------------------------
;;;--H2o T=300K P=100-88b
;b='t300_p94' & a='83660>83663' ;& @process_in4
;;;-----------------------------------------------
;;;--H2o T=350K P=115b
;b='t350_p115'& a='83664>83667' ;& @process_in4
;;;-----------------------------------------------
;;;--H2o T=392-466K P=128-165b
;b='t430_p147'& a='83668>83677' ;& @process_in4
;;;-----------------------------------------------
;;;;--H2o T=479-485K P=172-180b
;b='t482_p176' &a='83678>83681' ;& @process_in4
;;;;-----------------------------------------------
;;;;--H2o T=490-497K P=185b
;b='t494_p185'& a='83682>83702' ;& @process_in4
```

```
;;;;------------------------------------------------
;;;; --H2o T=517K P=42b
;b='t517_p42' &a='83703>83708' ;& @process_in4
```

Data reduction for IN4c (process file)

```
w9=normalise(w9,/monitor)
w9=in4strip(w9,/wide,/bad)
w10=corr_tof(w9,/det_eff,/bkgd_trans)
w10=sumbank(w10)
;;;Sample-Empty Cell, i.e. (sample - t*EC)
t=0.6 ; transmission of water
w11=w10-(t*w6)
;;;Propagate Errors
e11 = sqrt(e10^2+(t*e6)^2)
;;;Normalize by the elastic peak of the vanadium
w12=in5_vnorm(w11,w2)
w13=in5_t2e(w12,w2)
w14=in5_sqw_rebin(w13,emin=-200,dq=0.01)
write_lamp, b, w=14, format='hdf'
rdset,inst='in5'
w15=in5_gdos(w13,nbbins=300)
write_lamp, b+'gdos', w=15, format='hdf'
output,w15,b
rdset,inst='in4'
w16=in5_sqw_rebin(w13,emin=-200,dq=0.05)
w17=transpose(w16)
output_allqs,w17,file=b
;;fine hw grid and then sqw fine
w18 = reb(w13,dE=0.01)
w19=in5_sqw_rebin(w18,emin=-200,dq=0.01)
write_lamp, b+'fine_grid_sqw', w=19, format='hdf'
```

A.2. Data reduction procedure for the IN6 TOF spectrometer

.prox file IN6

```
; Data treatment for 1-04-90 (IN6)
; lambda = 5.1 ITF ratio 1
;-------------------------------------------------------------
rdset,inst='in6'
path='D:\Users\JAISWAL-VAI\Desktop\experiment\data_H2O\in6',noraw

;List of bad detectors
M=[75,90,93,95,97,123,176,177,178,179,
   191,200,202,212,214,215,216,217,224,229]

;-------------------------------------------------------------
; Vana Cyl 8 mm
```

```
a='180564>180566'
w1=rdopr(a)
w1=remove_spectra(w1,M)
w1=normalise(w1,/monitor)
w2=corr_tof(w1,/b,propb=0.9)
w2=sumbank(w2)
w3=in5_t2e(w2)
w4=in5_sqw_rebin(w3,dQ =0.01,emin = -10)
 write_lamp, 'vanadium_in6_in_time', w=2, format='hdf'
 write_lamp, 'vanadium_in6_t2e', w=3, format='hdf'
 write_lamp, 'vanadium_in6_sqw', w=4, format='hdf'
;;;------------------------------------------------------------

 ;;;Empty cell at 494.5K
a='180633>180661'
w5=rdopr(a)
w5=remove_spectra(w5,M)
w5=normalise(w5,/monitor)
w6=corr_tof(w5,/b,propb=0.9)
w6=sumbank(w6)
w7=in5_t2e(w6)
w8=in5_sqw_rebin(w7,dQ =0.01,emin = -200)
 write_lamp, 'ec_in6_in_time', w=6, format='hdf'
 write_lamp, 'ec_in6_t2e', w=7, format='hdf'
 write_lamp, 'ec_in6_sqw', w=8, format='hdf'
;;;-------------------------------------------------------------

 ;;
 ;;;  ******** H2O ********
 ;;
 ;;;  H2o T~350K P~5b
b='t350_p1_in6' & a='180582>180589' & @process_in6
 ;;
;;;-------------------------------------------------
 ;;;  H2o T=494K P~70b
 ;b='t494_p70_in6' & a='180595>180612' & @process_in6
 ;;
;;;-------------------------------------------------
 ;;;  H2o T=494K P=600b--340b
 ;b='t494_p600_in6' & a='180614>180622' & @process_in6
```

Data reduction for IN6 (process file)

```
w9=rdopr(a)
w9=remove_spectra(w9,M)
w9=normalise(w9,/monitor)
w10=corr_tof(w9,/b,propb=0.9)
w10=sumbank(w10)
 ;;;Sample-Empty Cell, i.e. (sample - t*EC)
t=0.6 ; transmission of water
w11=w10-(t*w6)
```

```
;;;Propagate Errors
e11 = sqrt(e10^2+(t*e6)^2)

;;;Normalize by the elastic peak of the vanadium
w12=in5_vnorm(w11,w2)
w13=in5_t2e(w12,w2)
w14=in5_sqw_rebin(w13,emin=-200,dq=0.01)
write_lamp, b, w=14, format='hdf'
w15=in5_gdos(w13,nbbins=300)
write_lamp, b+'gdos', w=15, format='hdf'
output,w15,b
w16=in5_sqw_rebin(w13,emin=-200,dq=0.05)
w17=transpose(w16)
output_allqs,w17,file=b
;;fine hw grid and then sqw fine
w18 = reb(w13,dE=0.01)
w19=in5_sqw_rebin(w18,emin=-200,dq=0.01)
write_lamp, b+'fine_grid_sqw', w=19, format='hdf'
```

Appendix B

Frequency spectrum from thermal scattering law

There are two methods to transform the TSL to frequency spectrum depending on the type of TSL,i.e, classical thermal scattering law like the one obtained from molecular dynamics simulations or quantum scattering law obtained from TOF experiments.

B.1. $\rho(\omega)$ from the classical TSL

The classical intermediate scattering function in the Gaussian approximation is written as:

$$I_s^{cl}(q,t) = \exp\left[-\frac{1}{2}q^2\sigma^2(t)\right] \tag{B.1}$$

where,

$$\sigma^2(t) = \frac{1}{3}\langle r^2(t)\rangle \tag{B.2}$$

The mean squared displacement $\langle r^2(t)\rangle$ can be expressed as:

$$\langle r^2(t)\rangle = 2\int_0^t dt'(t-t')\langle v(0)\cdot v(t')\rangle \tag{B.3}$$

Thus, the second order derivative of the mean squared displacement can then be written as:

$$\frac{d^2\langle r^2(t)\rangle}{dt^2} = 2\langle v(0)\cdot v(t)\rangle \tag{B.4}$$

Since the velocity autocorrelation is a Fourier conjugate of the frequency spectrum, the velocity autocorrelation can be written as:

$$\langle v(0)\cdot v(t)\rangle = \frac{3}{2}\frac{k_BT}{M}\int_{-\infty}^{\infty} d\omega\rho(\omega)\exp(i\omega t) \tag{B.5}$$

Thus, we obtain:

$$\frac{d^2\langle r^2(t)\rangle}{dt^2} = \frac{3k_BT}{M}\int_{-\infty}^{\infty} d\omega\rho(\omega)\exp(i\omega t) \tag{B.6}$$

Now, q being very small, applying the limits on q, Eq. B.1 becomes:

$$\lim_{|q|\to 0}[I_s^{cl}(q,t)] = 1 - \frac{1}{2}q^2\sigma^2(t) \tag{B.7}$$

From this Eq. $\sigma^2(t)$ can be written as

$$\sigma^2(t) = \lim_{|q|\to 0}\left\{\frac{2[1 - I_s^{cl}(q,t)]}{q^2}\right\} \tag{B.8}$$

Now, differentiating twice both the sides of Eq. B.8 with respect to time, we obtain:

$$\frac{d^2\sigma^2(t)}{dt^2} = \lim_{|q|\to 0}\left\{\frac{-2}{q^2}\frac{d^2[I_s^{cl}(q,t)]}{dt^2}\right\} \tag{B.9}$$

Calculating double differential of σ^2 from Eq. B.2 and Eq. B.6 and substituting it in Eq. B.9, the expression between the intermediate function and the density of states deduces to:

$$\lim_{|q|\to 0}\left\{\frac{-2}{q^2}\frac{d^2[I_s^{cl}(q,t)]}{dt^2}\right\} = \frac{k_BT}{M}\int_{-\infty}^{\infty} d\omega\rho(\omega)\exp(i\omega t) \tag{B.10}$$

Now, upon differentiating the backward Fourier transform of the classical Van Hove scattering law, we obtain:

$$\begin{aligned}\frac{d^2[I_s^{cl}(q,t)]}{dt^2} &= \frac{d^2}{dt^2}\left\{\hbar\int_{-\infty}^{\infty} d\omega S_s^{cl}(q,\omega)\exp(i\omega t)\right\}\\ &= \hbar(i\omega)^2\int_{-\infty}^{\infty} d\omega S_s^{cl}(q,\omega)\exp(i\omega t)\\ &= -\hbar\omega^2\int_{-\infty}^{\infty} d\omega S_s^{cl}(q,\omega)\exp(i\omega t)\end{aligned} \tag{B.11}$$

Substituting this is Eq. B.10 and solving the equation:

$$\rho(\omega) = \frac{2M\hbar\omega^2}{k_B T} \lim_{|q|\to 0} \left[\frac{S_s^{cl}(q,\omega)}{q^2} \right] \tag{B.12}$$

and in the dimensionless form, it reduces to:

$$\rho(\omega) = \beta^2 \lim_{\alpha\to 0} \left[\frac{S_s^{cl}(\alpha,\beta)}{\alpha} \right] \tag{B.13}$$

This equation defines the relation between density of states and the classical symmetric scattering law.

B.2. $\rho(\omega)$ from the quantum TSL

$S_s(q,\omega)$, the quantum scattering law can be written in terms of $\rho(\omega)$ as:

$$S_s(q,\omega) = \frac{1}{2\pi} \int_{-\infty}^{\infty} \exp\left(\frac{\hbar q^2}{2M} \int_{-\infty}^{\infty} \frac{\rho(\omega)\exp(\frac{\hbar\omega}{2k_BT})}{2\omega \sinh(\frac{\hbar\omega}{2k_BT})} [\exp(i\omega t) - 1] d\omega \right) \exp(-i\omega' t) \tag{B.14}$$

Applying limit $|q| \to 0$, and expanding the first exponential term on the right side of Eq. B.14:

$$\begin{aligned} \lim_{|q|\to 0} S_s(q,\omega) &= \frac{1}{2\pi} \int_{-\infty}^{\infty} \exp(-i\omega' t) dt \\ &+ \frac{1}{2\pi} \frac{\hbar q^2}{2M} \int_{-\infty}^{\infty} \left(\int_{-\infty}^{\infty} \frac{\rho(\omega)\exp(\frac{\hbar\omega}{2k_BT})}{2\omega \sinh(\frac{\hbar\omega}{2k_BT})} [\exp(i\omega t) - 1] d\omega \right) \exp(-i\omega' t) dt \end{aligned} \tag{B.15}$$

Since, $\delta(\omega')$ can be expressed as:

$$\delta(\omega') = \frac{1}{2\pi} \int_{-\infty}^{\infty} \exp(-i\omega' t) dt \tag{B.16}$$

In the case of solids where, $\rho(\omega) \to 0$ as $\omega \to 0$, the first term on the right of Eq. B.15 can be treated as zero. Also, in the case of inelastic scattering $\omega \neq 0$. Integrating the remaining term, one obtains:

$$\lim_{|q|\to 0} S_s(q,\omega) = \frac{\rho(\omega)\hbar q^2 \exp(\frac{\hbar\omega}{2k_BT})}{4M\omega \sinh \frac{\hbar\omega}{2k_BT}} \tag{B.17}$$

Converting the $S_s(q,\omega)$ from an asymmetric form to a symmetric $S_s^{sym}(q,\omega)$, Eq. B.17 transforms to:

$$\lim_{|q|\to 0} S_s^{sym}(q,\omega) = \frac{\rho(\omega)\hbar q^2}{4M\omega \sinh(\frac{\hbar\omega}{2k_BT})} \tag{B.18}$$

And hence,

$$\rho(\omega) = \frac{4M\omega}{\hbar} \sinh\left(\frac{\hbar\omega}{2k_BT}\right) \lim_{|q|\to 0} \left\{ \frac{S_s^{sym}(q,\omega)}{q^2} \right\} \tag{B.19}$$

This symmetric scattering law in Eq. B.18 can be written in terms of α and β as:

$$\lim_{\alpha\to 0} S_s^{sym}(\alpha,\beta) = \frac{\alpha\rho(\beta)}{2\beta\sinh(\frac{\beta}{2})} \tag{B.20}$$

and the corresponding frequency spectrum,

$$\rho(\omega) = 2\beta\sinh\left(\frac{\beta}{2}\right) \lim_{\alpha\to 0} \left\{ \frac{S_s^{sym}(\alpha,\beta)}{\alpha} \right\} \tag{B.21}$$